Inversion for reservoir pressure change using overburden strain measurements determined from 4D seismic

Neil Hodgson

A Thesis Submitted for the Degree of Doctor of Philosophy
Heriot-Watt Institute of Petroleum Engineering,
Heriot-Watt University, Edinburgh, Scotland.

November, 2009

Abstract

When significant pore pressure changes occur because of production from a hydrocarbon reservoir the rocks both inside and outside of the reservoir deform. This deformation results in traveltime changes between reflection events on time-lapse seismic data, because the distance between reflection events is altered and the seismic velocity changes with the strain. These traveltime differences are referred to as time-lapse time shifts.

In this thesis, time-lapse time shifts observed in the overburden are used as an input to a linear inversion for reservoir pressure. Measurements from the overburden are used because, in general, time shift estimates are more stable, the strain deformations can be considered linear, and fluid effects are negligible, compared to the reservoir-level signal.

A critical examination of methods currently available to measure time-lapse time shifts is offered. It is found that available methods are most accurate when the time shifts are slowly varying with pressure and changes in the seismic reflectivity are negligible. While both of these conditions are generally met in the overburden they are rarely met at reservoir level.

Next, a geomechanical model that linearly relates the overburden time-lapse time shifts to reservoir pressure is considered. This model takes a semi-analytical approach by numerical integration of a nucleus of strain in a homogeneous poroelastic halfspace. Although this model has the potentially limiting assumption of a homogenous medium, it allows for reservoirs of arbitrary geometries, and, in contrast to the complex numerical approaches, it is simple to parameterise and compututationally efficient.

This model is used to create a linear inversion scheme which is first tested on synthetic data output from complex finite-element model. Despite the simplifications of the

inversion operator the pressure change is recovered to within ±10% normalised error of the true pressure distribution.

Next, the inversion scheme is applied to two real data cases in different geological settings. First to a sector of the Valhall Field, a compacting chalk reservoir in the Norwegian Sea, and then the Genesis Field, a stacked turbidite in the Gulf of Mexico. In both cases the results give good qualitative matches to existing reservoir simulator estimates of compaction or pressure depletion. It is possible that updating of the simulation model may be assisted by these results. Further avenues of investigation are proposed to test the robustness of the simplified geomechanical approach in the presence of more complex geomechanical features such as faults and strong material contrasts.

This thesis is dedicated to S.K.H.

Acknowledgements

How did I end up studying for a PhD in Geophysics? Well the person I need to thank (or blame?) for this is Dr Roger Clark of Leeds University, who took chance and accepted a Chemical Physicist onto the Exploration Geophysics course and later employed me as a research assistant. In addition to working on time-lapse QVO, which sparked my interest in 4D seismic, he encouraged me to do fun stuff, like drive out to the middle of a wood and hit the ground with a sledgehammer. While I was at Leeds Dr Andrew Carter kindly put up with my seemingly endless questions, and I learnt a lot from his answers. My time there was invaluable, thank you both.

The next person to take a chance on me was Prof. Colin MacBeth. Thank you for the encouragement and guidance. Colin started the Edinburgh Time-Lapse Project which is a unique and exciting place to do research and something I am proud to be a part of. At ETLP I made some great friends, some of whom I was lucky enough to be flatmates with. Thanks to: Mariano Floricich, Margarita Corzo, Jesus Nunez, Fabian Domes, Said Al-Busaidi, Faisal Al-Kindi, Asghar Shams, Karl Stephen, Houshang Mansouri. Thanks also go to all at Heriot-Watt Institute of Petroleum who helped me out or were just a friendly face. I am also grateful for the financial support of the ETLP sponsors: BG Group, BP, Chevron, ConocoPhillips, ExxonMobil, Fairfield, Landmark, Maersk, Shell, Statoil-Hydro and Total. Additional financial support was gratefully received from the SEG Foundation which awarded me the Leon Thompson/BP Scholarship.

In 2005 I did an internship with Chevron in San Ramon, California. The advice and encouragement I received from Luca Duranti, James Rickett and Kurt Nihei was a turning point. I returned with the ideas that form the foundation of this thesis, thank you.

Shell have been in the background of my geophysical career since the beginning, sponsoring the Leeds QVO work, ETLP and time I spent in Aberdeen on internship

in 2007. Thanks to, Joel Ita, Jon Brain, Rob Staples, Peter Schutjens, Peter Rowthbotham and Rebecca Nash. Thanks also to Rhian and Joe (I owe you guys!), Jane and Mariano for making my time in Aberdeen a memorable one.

Special thanks go to Margarita Corzo who I worked with a lot when we both started investigating time-lapse seismic and geomechanics. Margarita kindly provided the model used to test the inversion scheme in Chapter 3.

Also, many thanks to my examiners Olav Barkved and Ingo Pecher, for taking the time to carefully read this thesis and making helpful suggestions for improvement (small details can make big differences).

Whenever this PhD seemed like hard work I have drawn endless inspiration my Mam (that's my Mum to non-Geordies). I watched her graduate with her degree in Nursing with great pride and realise that education is something it is all too easy to take for granted. Your love, encouragement, support and guidance over the years has been invaluable. Thanks to David, Janis, Joan, Richard and Florence for everything, I couldn't have done this without such supportive families.

Finally I would like to thank Sarah. Her love, friendship, honesty and patience enriches everything I do and the person I am. This thesis would not have been written without her. It's done, let's get on with life!

Neil Hodgson, November 2009

Publications

Part of the work presented in this thesis is also presented in the following publications:

1. Rickett, J., Duranti, L., Hudson, T. and **Hodgson, N.** (2006), *Compaction and 4-D time strain at the Genesis Field.* 76th Annual International Meeting, SEG, Expanded Abstracts.

2. **Hodgson, N.**, MacBeth, C., Duranti, L., Rickett, J. and Nihei, K. (2007), *Inverting for reservoir pressure change using time-lapse time strain: Application to Genesis Field, Gulf of Mexico.* The Leading Edge, 26(5), 649-652, SEG.

3. **Hodgson, N.**, MacBeth, C., Duranti, L., Rickett, J. and Nihei, K. (2007), *Inverting for pressure using time-lapse time-strain: Application to a compacting GOM reservoir.* 67th Meeting, EAGE, Expanded Abstracts, A009

4. Rickett, J., Duranti, L., Hudson, T., Regel, B. and **Hodgson, N.** (2007), *4D time strain and the seismic signature of geomechanical compaction at Genesis.* The Leading Edge, 26(5), 644-647, SEG.

5. Rickett, J., Duranti, L., Hudson, T., Regel, B., **Hodgson, N.** (2007), *4D time strain and the seismic signature of geomechanical compaction at Genesis*, 67th Meeting, EAGE, Expanded Abstracts, A009

Contents

1 Introduction **1**

1.1 The role of time-lapse seismic in production optimization 2

1.1.1 Understanding a hydrocarbon reservoir 2

1.1.2 How good are our predictions? 3

1.2 Time-lapse seismic 7

1.2.1 Some time-lapse examples 9

1.2.2 An established technique 11

1.2.3 Time-lapse seismic - imaging more than just the reservoir . . . 14

1.3 Compaction due to hydrocarbon production and why monitoring it is important 15

1.3.1 Surface subsidence 16

1.3.2 Well integrity 17

1.3.3 Reservoir compaction 18

1.4 Geomechanics - monitoring and modelling 18

1.5 Monitoring the whole earth 20

1.6 Thesis aims and outline 22

2 4D seismic and compacting reservoirs: An overview 24

2.1 4D seismic monitoring of compacting reservoirs 25

2.1.1 Early observations 25

2.1.2 A growing number of published examples 26

2.2 Reservoir geomechanics: An overview 29

2.2.1 Stress and strain around a compacting reservoir 30

2.2.2 Integrating geomechanics and time-lapse seismic 35

2.3 Velocity stress/strain relationships 39

2.3.1 Rock physics models: A brief overview 39

2.3.2 Static and dynamic moduli 42

2.3.3 The reliability of core data 43

2.3.4 The R factor 45

2.3.5 Independent calibration of stress sensitivity by 4D seismic . . 49

2.4 Summary of published techniques that use overburden time-shifts for reservoir management 52

3 Measuring time-lapse time shifts around compacting reservoirs 56

3.1 Introduction 57

3.2 The time-lapse seismic signature of compaction 57

3.3 Problems with determining compaction from the reservoir-level signal 60

3.4 Time-lapse seismic data quality and time shift measurements 63

3.5 Why do we need to improve current methods of time shift estimation? 66

3.5.1 Cross-correlation 66
3.5.2 Problems with the cross-correlation approach 69
3.6 Developments in time shift estimation 75
3.6.1 Fast local cross-correlation 75
3.6.2 Inversion-based methods 77
3.7 Time shifts and time strains 78
3.8 Summary 84

4 Inverting for reservoir strain using time-lapse time shifts and time strains 87

4.1 Introduction 88
4.2 Deformation in a poroelastic medium 91
4.2.1 Governing equations 91
4.2.2 A Green's function solution 95
4.2.3 Nucleus of strain in a linear poroelastic homogeneous halfspace 96
4.2.4 Forming arbitrary reservoir shapes by numerical discretization 98
4.3 Validation of the discretization procedure 99
4.4 Inversion for reservoir pressure change 102
4.5 Why 4D seismic offers more 103
4.6 Inversion method 104
4.7 Experimental design analysis 105
4.8 Assessing the impact of uncertainties 111
4.8.1 Uncertainties in material properties 113

4.9 Test inversion . . . 117
4.9.1 Description of the model . . . 117
4.9.2 Depletion scenario and compaction . . . 118
4.9.3 Inversion for reservoir pressure . . . 120
4.10 Conclusions and discussion . . . 125

5 Inverting for reservoir compaction at Valhall field, North Sea 128

5.1 Description of Valhall Field . . . 129
5.1.1 Background . . . 129
5.1.2 Compaction . . . 129
5.1.3 Life of Field Seismic . . . 131
5.2 Motivation . . . 132
5.2.1 Scope of the study . . . 134
5.2.2 Study area . . . 134
5.3 Building a model of the area of interest . . . 134
5.4 An linear equation relating time shifts to reservoir strain . . . 136
5.5 Forward modelling overburden time-lapse time shifts . . . 138
5.5.1 Reservoir strain estimate . . . 138
5.5.2 Visual comparison . . . 138
5.5.3 Investigating the sensitivity to R and ν . . . 141
5.5.4 Interpreting the value of C . . . 143
5.6 The effect of residual multiple energy on overburden time-lapse time shifts . . . 143

5.7 Inversion for reservoir strain from time-lapse time shifts 149

5.7.1 Inversion results 150

5.7.2 Investigating uncertainty in reservoir thickness 153

5.8 Summary 154

6 Inverting for reservoir compaction using time-lapse time strains: Application to the Genesis Field 157

6.1 Introduction 158

6.2 The Genesis Field 158

6.2.1 Location and geology 158

6.2.2 Production history and compaction 159

6.2.3 Description of the time-lapse surveys 161

6.2.4 Initial 4D observations 161

6.2.5 Cross-equalization over compacting reservoirs 162

6.3 Time shifts and time strains at Genesis 163

6.3.1 Time shift resolution at reservoir level 164

6.4 Inversion for reservoir pressure change 167

6.4.1 Inversion of a vertically stacked reservoir 167

6.4.2 Data preparation 172

6.4.3 Results 174

6.4.4 Discussion 181

6.4.5 Conclusion 183

7 Conclusions and recommendations for future research 184

7.1 Conclusions 185

7.2 Suggestions for further research 188

7.2.1 Further investigation of the limitations of the geomechanical model 188

7.2.2 Understanding the reservoir level signal 190

7.2.3 Geomechanically consistent seismic warping 190

A Time shift estimation by non-linear inversion **193**

B Strain field around a nucleus of strain in a poroelastic half-space **196**

B.1 Introduction 196

B.2 Displacements 196

B.3 The strain tensor 199

B.4 The stress tensor 199

B.5 Numerical Tests 200

C Beyond the R-factor **207**

C.1 Introduction 207

C.2 Example: Relating velocity to vertical stress 208

List of Figures

1.1 The relationship between seismic, the geological model and the reservoir model 6

1.2 A simple representation of physical principles of time-lapse seismic . . 8

1.3 A time-lapse example from Gannet C 10

1.4 A time-lapse example from Norne 12

1.5 The global propagation of 4D programmes 13

1.6 A comparison between geomechanical modeling and 4D seismic at Valhall 15

1.7 A cartoon of reservoir compaction-related effects 16

1.8 Subsidence at the Ekofisk platform. 17

1.9 Localised deformation of well damaged at Wilmington Field 18

1.10 Casing damage scenarios inside a compacting reservoir 19

1.11 InSAR measurements over Lost Hills Reservoir, California 21

1.12 Work flow for inverting for reservoir pressure from time-lapse time strains as outlined in this thesis. 23

2.1 Number of abstracts published at the EAGE and SEG annual conferences concerning the use of time-lapse seismic to monitor compacting reservoirs. 27

2.2 Cartoon of subsidence and compaction 31

2.3 Vertical stress around a disk-shaped reservoir in a halfspace for a range of reservoir depths and radii 33

2.4 Horizontal stress path around a disk-shaped reservoir in a halfspace for a range of reservoir depths and radii 34

2.5 Predicted and observed time-shifts 36

2.6 Predicted and observed shear wave splitting 38

2.7 Schematic illustration of the effect of core damage 45

2.8 Stress path effects on Berea sandstone 46

2.9 Stress-sensitivity derived directly from the 4D seismic at the Schiehallion Field 51

3.1 An idealised time shift signature through the centre of a depleting disk-shaped reservoir 59

3.2 An example of cross-correlation 67

3.3 Time shifts measured using various size windows 68

3.4 Time shifts measured using various size windows to demonstrate some of the limitations of the cross-correlation technique. 70

3.5 Ricker wavelet before and after tapering. 72

3.6 The effect of dominent frequency, taper type and magnitude of the time shift on the time shift estimated by cross-correlation. 74

3.7 Comparison between time shifts estimated using an inversion approach compared with those estimated by local cross-correlations 79

3.8 Time shifts and time strains at Genesis Field 80

3.9 Synthetic test of time shift estimation algorithms 81

3.10 Synthetic test of time shift estimation algorithms 82

3.11 Testing the effect of smoothing parameter weight on the time shift inversion result 83

4.1 Compaction predicted by uncoupled versus coupled modeling. 94

4.2 The geometry used for the Geerstma model 98

4.3 A reservoir composed of four blocks 100

4.4 Test of the effect of grid discretization 101

4.5 Cartoon showing the use of an L-curve to choose the optimum regularization parameter 106

4.6 Impulse test for three different observation geometries. 108

4.7 3D seismic, 4D seismic differences and measured time shifts at Shearwater. 109

4.8 Impulse test for three different observation geometries over a dipping reservoir. 110

4.9 Errors due to depth conversion uncertainty. 112

4.10 Effect of reservoir geometry on errors in vertical strain caused by uncertainties in Poisson's ratio. 115

4.11 Effect of the observation location relative to the reservoir on errors caused by uncertainties in Poisson's ratio. 116

4.12 Geometry and properties of the Valhall sector model 118

4.13 Changes in reservoir pressure and porosity in the Valhall model after 10 years of production 119

4.14 Profile of U_{zz} and E_{zz} through the cell with the largest depletion in the Valhall model. 121

4.15 Comparison of the vertical strain predicted by the semi-analytical model compared to that predicted by the FEM model. 122

4.16 Comparison of the vertical strain predicted by the semi-analytical model compared to that predicted by the FEM model after scaling . . 123

4.17 The reservoir pressure change inverted from strains output from the Valhall reservoir model 124

4.18 Comparison of the normalised difference between the vertical strain predicted by semi-analytical and finite element models. 126

4.19 Laplacian of the Valhall depletion pattern 126

5.1 Location of the Valhall Field 130

5.2 A simplified geological cross-section of Valhall Field 130

5.3 Reflectivity changes in the reservoir zone at Valhall 133

5.4 The sub-area selected for the study 135

5.5 Reservoir strain in the area of interest 139

5.6 Comparison of modelled and measured time shifts at the area of interest in Valhall 140

5.7 Seasonal variations in water velocity at Valhall 144

5.8 Investigating the overburden time-lapse time shift anomaly. 145

5.9 Plot of time shift against water velocity variations at Valhall 147

5.10 Results of an inversion for reservoir strain. 152

5.11 Inversion residuals. 152

5.12 Receiver line striping 153

5.13 Effect of uncertainty of the reservoir thickness. 155

6.1 Location of the Genesis Field 158

6.2 Genesis schematic cross-section and log. 160

6.3 Initial published time-lapse differences at Genesis Field 163

6.4 Time shifts and time strains at Genesis Field 164

6.5 Baseline seismic at Genesis 165

6.6 Geomechanical modeling of compacting turbidite reservoir 166

6.7 Spike test showing resolution leakage between stacked reservoirs . . . 169

6.8 Upscaling of a vertically stacked reservoir 170

6.9 Displacement and strain caused by a series of depleting vertically stacked sands compared with the displacement and strain due to an upscaled layer. 171

6.10 Time strains at a horizon 350m above and parallel to the top N1 sands.173

6.11 Pressure from the N1, N2 and N3 sands upscaled to a single layer. . . 175

6.12 Inversion result 178

6.13 Downhole pressure measurements in the N2 sands 179

6.14 Modelled and observed time strains 180

7.1 Work flow for inverting for reservoir pressure from time-lapse time strains as outlined in this thesis. 186

B.1 Figure taken from Geertsma (1966) defining the geometry used in subsequent equations 197

B.2 Numerical and analytical derivatives of u_x 204

B.3 Numerical and analytical derivatives of u_y. 205

B.4 Numerical and analytical derivatives of u_z. 206

List of Tables

2.1 Published examples of observed time-lapse time-shifts in the overburden above compacting reservoirs 28

2.2 Reservoir properties used to create Figures 2.3 and 2.4 32

2.3 Summary of published methods which use compaction-induced overburden time shifts to infer dynamic reservoir changes (compaction or pressure changes) 54

2.3 Summary of published methods which use compaction-induced overburden time shifts to infer dynamic reservoir changes (compaction or pressure changes) 55

4.1 The geomechanical properties of the Valhall sector model 119

5.1 Determining the Poisson's ratio for the half-space 142

5.2 Water velocities at the time of the Valhall LoFS surveys 148

6.1 Acquisition parameters for the base and monitor surveys at Genesis . 162

6.2 Determining the Poisson's ratio and shear modulus for the half-space used in the Genesis inversion 176

B.1 Derivatives of u_x. All expressions require multiplication by a factor of $C_m/4\pi$ which is omitted for ease of notation 201

B.2 Derivatives of u_y. 202

B.3 Derivatives of u_z. 203

List of Symbols

Geomechanical

U_i	Displacement
σ_{ij}	Stress tensor
ε_{ij}	Strain tensor
ε_{vol}	volumetric strain
μ	Shear modulus
ν	Poisson's ratio
m	fluid mass
V	Volume
E	Young's modulus
K	Bulk modulus
K_g	Grain bulk modulus
ρ	Density
α	Biot's coefficient
B	Skemptons's coefficient
C_m	Uniaxial compaction coefficient
Δp	Change in reservoir pressure
γ_v	Vertical stress path $\gamma_v = \Delta\sigma_v/\Delta p$
γ_h	Horizontal stress path $\gamma_h = \Delta\sigma_h/\Delta p$
G	Green's function relating reservoir changes to subsurface deformation

Geophysical

t	two-way seismic travel time
R	factor relating change in velocity to change in vertical strain
τ	time-lapse time shift

V_p and v	Seismic P-wave velocity
V_s	Seismic S-wave velocity

Abbreviations

4D	Multiple 3D seismic surveys at taken at different times
AI	Acoustic Impedance
BHP	Bottom Hole Pressure
CNS	Central North Sea
DHI	Direct Hydrocarbon Indicator
EAGE	European Association of Geoscientists and Engineers
FEM	Finite Element Modelling
GWC	Gas-water contact
GOM	Gulf of Mexico
HPHT	High Pressure High Temperature
LoFS	Life of Field Seismic
NRMS	Normalized root-mean square
NRMSD	Normalized root-mean squared deviation
NTG	Net-to-gross
OWC	Oil-water contact
PVT	Pressure Volume Temperature
RFT	Repeat Formation Tester
RMS	Root-mean square
SEG	Society of Exploration Geophysics
SIBHP	Shut-in Bottom Hole Pressure
TLE	The Leading Edge (SEG Publication)

CHAPTER

ONE

Introduction

This chapter frames the main topics discussed in this thesis. First, time-lapse seismic and its use as a reservoir management tool is introduced. Next, I discuss this in the context of reservoir compaction. Finally, I give an overview of the content of this thesis.

1.1 The role of time-lapse seismic in production optimization

1.1.1 Understanding a hydrocarbon reservoir

It is widely acknowledged that the majority of the world's easily accessible hydrocarbons have been discovered. The hydrocarbons of the coming century will be challenging to find and extract, geographically, geopolitically, environmentally and technologically. At the same time it is expected that demand for oil and gas is expected to grow over the coming decades, such is the modern economy's dependence on fossil fuels. It is therefore crucial that we find ways of producing both existing and future discoveries optimally. As discussed by Calvert (2005), optimization can encompass many aspects of production, including safety, environmental impact, recovery factor (the final amount of oil produced as a fraction of the total estimated reserves), timeliness, cost and profit.

So how can we optimize production? A hydrocarbon reservoir is a complex system generally situated thousands of metres below the Earth's surface. It is impossible to see the reservoir, so its properties are inferred from diverse sources of data. Seismic data provides the main technique for imaging the subsurface in three dimensions and can be termed *soft data* as it is not a direct measurement of subsurface properties, but is instead used to infer them. Significantly, just a few sparsely located measurements are made within the reservoir. These downhole measurements, such as wireline logs and formation tests, provide the only direct measurements of reservoir properties and as such can be termed *hard data*. These data, hard and soft, are used to build a computer model which is used to predict how the reservoir will produce.

During production the predictions from the model are compared with observations. Unfortunately, we often find that our predictions do not match our observations - our initial model is not a sufficiently adequate reflection of the physics of the system. In what is often a cyclic process, an initial model is used to predict a set of observations (production history at a well or change in seismic amplitude for example) and is revised if there is a mismatch with the real data observations. Hopefully, these mismatches will provide clues about what part of the model needs to be improved.

A great deal of effort is put into the construction of these models because the ability to accurately forward model the reservoir allows us to assess the impact and added

value of future production strategies and drilling programmes with more confidence. In this context, optimization is achieved by understanding how the reservoir will behave as we produce it.

1.1.2 How good are our predictions?

One measure of performance is how much oil we recover in relation to the total estimated amount of oil in place, which is termed the recovery factor. Recovery factors of oil reservoirs are generally around 30-40%, which many in the oil industry instinctively feel should and could be improved upon with the appropriate application of optimization technologies. It should be noted that a simple numerical measure such as the recovery factor can not tell the full story. The geological setting combined with the physics of production will determine the maximum amount of recoverable hydrocarbons. In addition, it may be necessary to abandon a reservoir before the all the technically recoverable hydrocarbons are extracted because it is unsafe or uneconomic to continue production. Within these constraints, if optimization is to be achieved by increasingly accurate predictions of production behaviour then we first need to understand how these predictions are made, and if the uncertainties involved can be reduced.

Building a reservoir model

The main tool for making forward predictions is the numerical reservoir simulation model. Built from hundreds of thousands of cells, each assigned with individual properties, this representation of the reservoir is used to solve the flow equations and simulate production and recovery of fluids from porous rock. As the reservoir goes through the various stages of field development (development, reservoir management through to abandonment) the simulation model is used at each stage to help make decisions. But how is this model built and how certain is it?

Sources of data

When developing a reservoir, the key data is well data, such as petrophysical, geological and wireline logs. They provide our only direct measurement of *in*

situ properties. For economic and safety reasons we generally aim to produce the maximum amount of oil with as few wells as possible and as a result these measurements are sparse. If the only available data were well data, we are reduced to playing a sophisticated game of joining the dots in order to determine properties inbetween wells.

Fortunately, in addition to well data, there is also seismic data. The seismic method consists of propagating an acoustic wave through the ground, by creating an explosion with dynamite for example, and recording the arrival time and amplitude of the reflections and refractions of the wave as it travels through the subsurface. A good analogy is the use of ultrasound in medicine to make images of inside the body.

In the early days of oil exploration seismic surveys were conducted by setting out sources and receivers in simple 2D lines. In the 1980s the 3D seismic revolution occurred and sources and receivers where instead set out in grids, greatly improving absolute spatial resolution and relative accuracy in image positioning compared to 2D data (Yilmaz and Doherty, 2001). This resulted in improvements such as better stratigraphic imaging, better structural imaging of dips, improved mapping of fault systems and continuous mapping of surfaces and seismic attributes. These new data provide a 3D picture of the subsurface and help to 'fill in' the gaps between well observations.

3D seismic is not without pitfalls or problems. Acquisition, processing, noise, tuning effects and complex geological settings can all impact the validity of the seismic result. Crucially, seismic images still need to be calibrated with borehole observations in order to convert between the time and depth domains. Nevertheless, to date the 3D seismic data has proven the best method of imaging the subsurface in three dimensions.

Putting it all together

Taking these diverse sources of data geoscientists work together to build a model of the reservoir. First, the 3D seismic data and well observations are used to define the geometry (top, base, boundaries, etc.). Faults and other structural features are also delimited from the 3D seismic data. The character of the 3D seismic data can be used to define different lithological units and determine properties such as porosity and net-to-gross. Statistical methods are utilized along with the known

characteristics of the geological setting to map well data to stochastic models of the reservoir properties. In addition, it may be possible to identify the seismic signature of fluid contacts, often called direct hydrocarbon indicators (DHIs), which allow the mapping of the oil-water contact for example. The result is a finely-gridded geological model, often made up of millions of cells, which defines the best estimate of the geology and structure of the reservoir.

In order to simulate fluid flow as hydrocarbons are produced the characteristics of the rock such as permeability, need to be estimated. These values can be derived from laboratory measurements on cores extracted from the wells. The distribution of these properties between wells, may be estimated using geostatistical techniques, along with analysis of the 3D seismic data. Initial pressures and fluid contact positions come from downhole measurements such as RFTs (repeat formation testers) and wireline logs. The chemical properties such as the pressure-volume-temperature (PVT) behaviour, come from laboratory tests of fluids extracted from the well. Once all these properties have been assigned the geological model is then often up-scaled (i.e. the grid is made coarser) because the geological grid is too fine for flow computations to be conducted in realistic time frames.

Uncertainty in the model

It is clear to see, with only the most cursory of glances, that there are a large number of unknowns which are constrained only by a small amount of spatially coarse data from wells. Some properties such as fault transmissibility (the degree to which a fault allows fluid to flow across it) may not be known at all until the reservoir is producing and well interference tests can be conducted. In some cases, high permeability layers may dominate the flow but may not have been identified in the initial model because they did not intersect a well or were undetectable in the seismic data.

When production data become available a process called history matching is used to constrain these unknowns by attempting to match the data observed at the well, such production rates and changes in pressures and saturation, to the predictions from the simulator. Using the previous examples, the reservoir engineer may find that a fault that was thought to be sealing is not, or that the only way to explain early water breakthrough is the addition of a high-permeability layer. However, this is a highly non-unique process. Many different changes to the model might result in

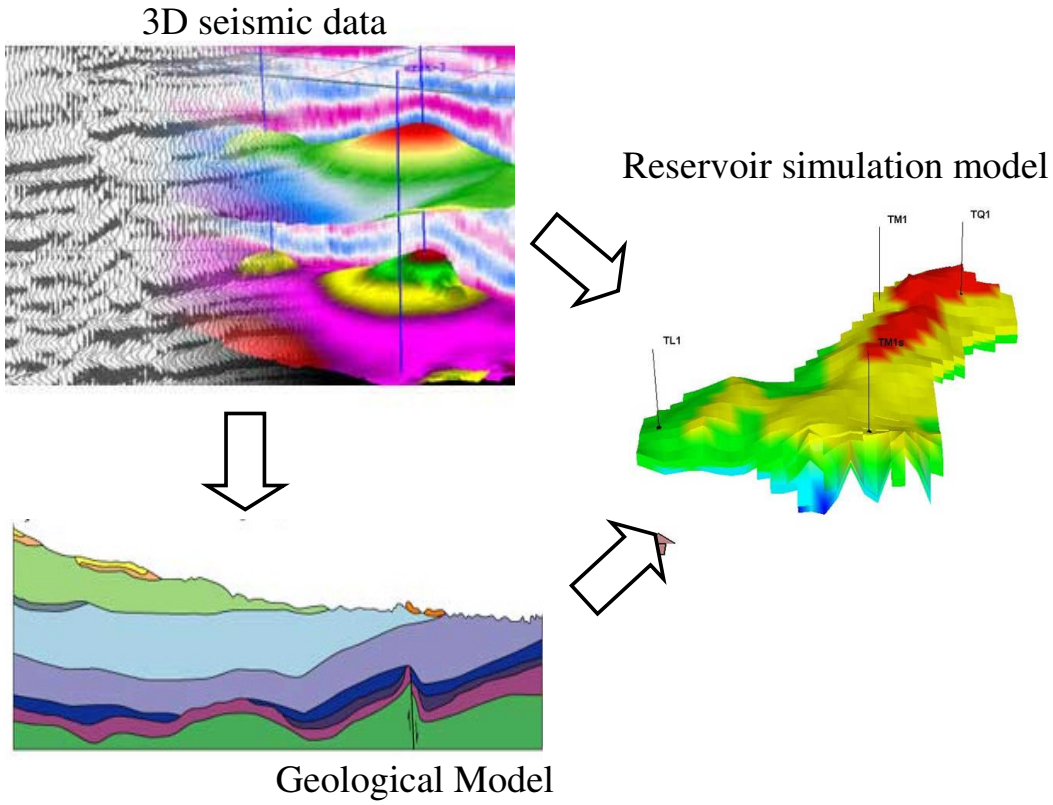

Figure 1.1: *This schematic diagram shows the relationship between seismic, the geological model and the reservoir model. Seismic provides both the structural framework and property variations to populate the reservoir model. In the figure, horizons showing the boundaries between different rock types are shown. Geological understanding provides realism to this construction and controls the inherent nonuniqueness of seismic data, by understanding the observations in terms of the rock types (shown as different colors on the geological cross-section above), deposition history and the wider structural setting for example. The end goal is to produce a numerical reservoir simulation model that will correctly predict flow, such as a change in fluid saturation as shown in the reservoir model above.*

an equally good match to the production data, only one of which will match reality.

So, even after careful analysis of the available data before and during production, there are still many unknowns and large uncertainties. 3D seismic has emerged as the best tool geoscience has to extrapolate the static properties of the reservoir between wells. If we wish to improve the predictive capability of simulation models by reducing the uncertainty and the non-uniqueness of the problem, we also need some way of monitoring dynamic changes between wells, something for which seismic technology is proving a valuable tool.

1.2 Time-lapse seismic

Just as the move from 2D to 3D seismic had a major impact on the improvement of the static model so the addition of time-lapse seismic is making great contributions to the understanding of the dynamic behavior of the reservoir. Time-lapse seismic is the practice of repeating two seismic measurements at different times and comparing them. When two 3D seismic surveys are compared the practice is often termed *4D seismic* or simply *4D*, where the fourth dimension is the time between surveys.

A simple representation of the principles of time-lapse seismic is given in Figure 1.2. The elastic properties of a porous reservoir rock are primarily a function of the rock type, the fluids contained within the rock pores and the current stress state of the rock (which is related to the fluid pressure). Production will affect the fluid saturations and pressures, which will change the acoustic properties of the reservoir rock, and will in turn change the seismic signature.

The ability to see a change will depend on three controlling factors. First, the geology which controls properties such as porosity, dry-frame modulus and the contrast between the compressibility of the fluids, will dictate the magnitude of the changes that result from changes in pressures and fluid saturations. Second, the quality of the seismic will ultimately determine whether theses changes can be resolved or seen above noise. Finally, there must be a significant change to observe!

Before proposing a time-lapse survey the geophysicist must work with the reservoir engineer to define the uncertainties in the simulation model. Together they ask if time-lapse seismic is able to provide information that will constrain those

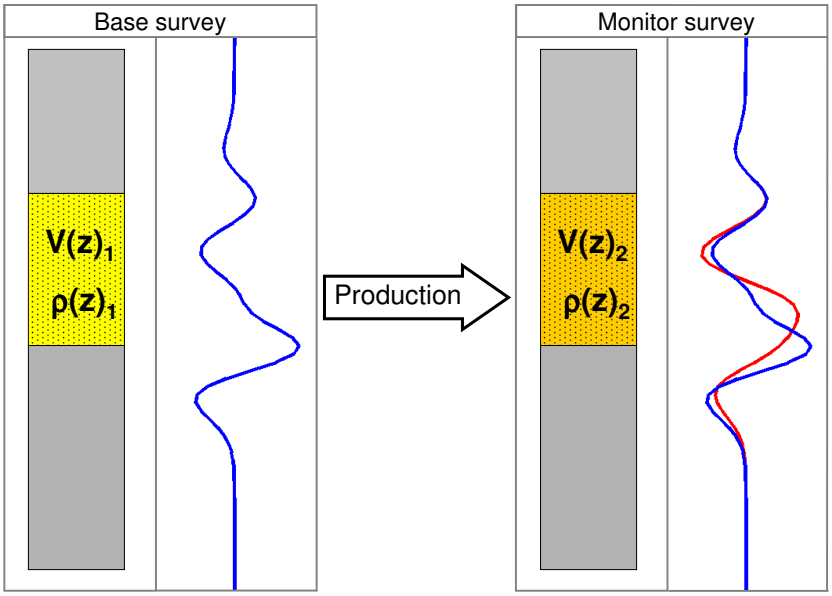

Figure 1.2: *A schematic representation of physical principles of time-lapse seismic. In the base line survey (left), the contrast of elastic properties, V_p, V_s (compressional and shear wave velocity) and ρ (density), between the reservoir and the over and underburden (shown in gray) create reflection events, which are recorded by on seismic trace (shown in blue). Changes due to production cause changes in the elastic properties of the reservoir, changing the timing and amplitude of the reflected seismic pulse (compare the blue seismic trace from the base survey to the red seismic trace from monitor survey).*

uncertainties. Usually this question will be answered using forward modeling of the 4D response, a so-called feasibility study, which will estimate the ability of 4D seismic to provide the information needed.

1.2.1 Some time-lapse examples

Gannet C

One of the many examples that could be used to demonstrate the value of time-lapse is the Shell-operated Gannet C Field, in the UK Central North Sea (Staples et al., 2006). The field is a ring-shaped structure created by salt diapir growth. Figure 1.3 shows the original model of the field structure. The red line shows where the oil-water contact (OWC) was originally thought to be. However, when the 4D seismic data were analyzed, 4D amplitude differences, which are qualitatively indicative of where water has replaced oil, were found outside the field boundary, as shown in the second panel of Figure 1.3. It was realized that within the uncertainties of the seismic time-depth conversion it was plausible to extend the area of the field to the south, suggesting a substantial increase in reserves.

Well data also suggested that some oil-bearing sands may lie above the main reservoir sands, but that these sands were thin and the volume of oil contained within them was too small to be of any real significance. These sands where also difficult to interpret on the original 3D seismic data. However, quantitative interpretation of the additional 4D data suggested that these sands where in fact in the order of 150ft thick, and therefore contained commercially viable quantities of oil. Interestingly, the 4D seismic signature was able to see what the original 3D seismic could not. This new information, which is a direct result of the 4D analysis, was used to make major updates to the static model (the addition of connected volume in the south and the addition of the new layers).

The 4D seismic also helped provide dynamic information on fault block communication and an interpretation of how water was approaching the wells. This new information was used to guide model updates in a process called history matching, in which the most uncertain aspects of the dynamic model are adjusted to obtain a better match to observed data. The observed data came from pressure measurements at wells, water/gas cut data (the time at which water or gas starts to be produced

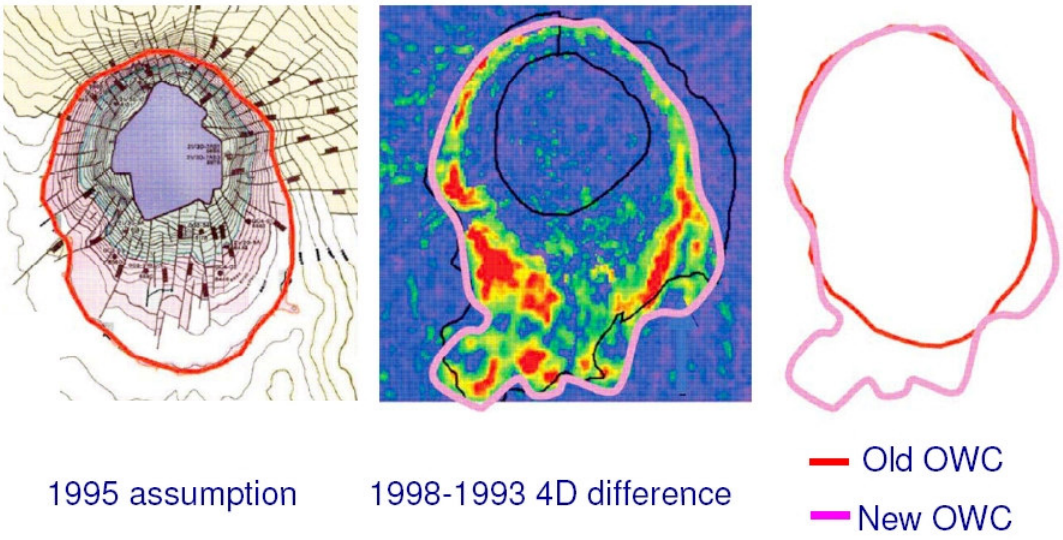

Figure 1.3: *Oil-water contact (OWC) assumptions compared before (red) and after 4D seismic (pink). After Staples et al. (2006)*

at the well), and the 4D-derived oil-water contact movements. In addition, aquifer strengths in each sector, fault transmissibility, well skins, and intra-reservoir shale transmissibilities were varied to achieve a better match to the observed data. The improvements to the static and dynamic models, as evidenced by the improved history match, allowed the identification of two opportunities for two infill wells to produce bypassed oil and prompted a workover (converting a gas injector to an oil producer). In total, Staples et al. estimate that the 4D seismic results were instrumental in approximately trebling the field oil production.

Norne

Gannet C is a relatively old example of 4D seismic in the North Sea. Acquisition and processing are improving all the time. One area in which companies are looking to improve is the so-called turn-around time between acquisition and processing/interpretation. This allows 4D to contribute to time-critical decisions. The development of fast-track processing, which can provide an unrefined 4D product in a short time, is made possible by improved source and receiver positioning, which

is crucial for time-lapse repeatability (Calvert, 2005). Fast-track 4D processing was used at the Statoil-operated Norne Field where Boutte (2007) reports that time-lapse seismic contributed to the decision to revise a well trajectory within a month of the acquisition of the monitor survey.

Figure 1.4 shows the original development plan to drill into the Ile reservoir (shown by the black well trajectory). A carbonate-cemented barrier, which pressure data from several offset wells indicated to be sealing, was previously thought to lie between the lower Tilje and upper Ile formations. A 3D geobody of acoustic impedance (AI) differences between the baseline and the monitor survey was created. Increases in AI where shown to be indicative of water replacing the oil. It was clear that the proposed well path was very close to the new oil-water contact and in some places entered the water zone. The water encroachment through the carbonate barrier was believed to be caused by several sub-seismic faults that allowed vertical communication. This theory was tested by inserting several small-scale faults into the simulation model, which was found to improve the match between the observed and predicted 4D data. As a result of this fast-track processing and interpretation, Statoil revised the well track, placing it in the same reservoir but above the indicated new water level, as shown by the grey well trajectory. The well was drilled on the new trajectory and flowed at a rate of 25,157 b/d of oil with no water on start up. This greatly improved the productive life of the well.

1.2.2 An established technique

These specific examples highlight the unique information that time-lapse can provide:

- **Areal coverage** – 4D seismic provides information on dynamic changes between coarsely spaced wells.
- **4D insight on 3D problems** – The 4D measurement is fundamentally different to the 3D one. Uncertainties or ambiguities that exist in the 3D data may be resolved by the 4D data.
- **Constraints on the history match** – Even a qualitative 4D interpretation can provide enough spatio-temporal information to significantly constrain some on the non-uniqueness of the history match. Successful efforts have been made

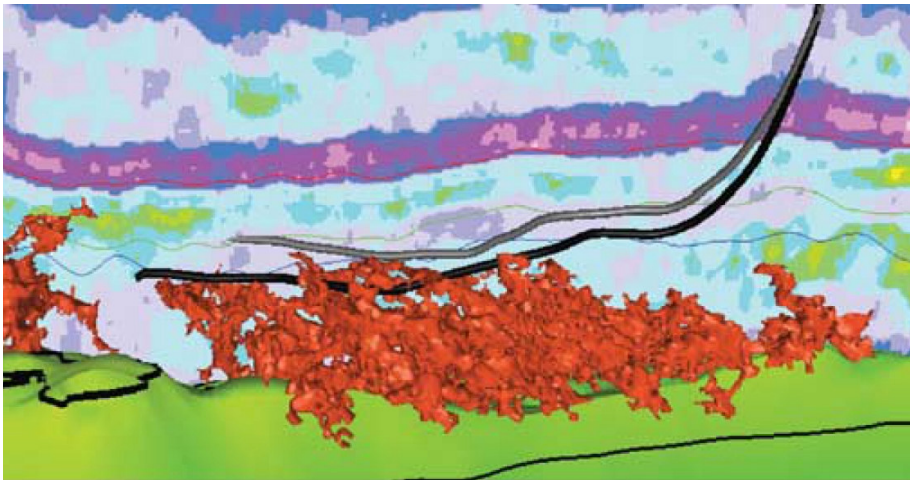

Figure 1.4: *Differences in AI signaled localized water encroachment through a leaking barrier and caused the operator to redesign the proposed horizontal well. The original well plan (black) was too close to the water. The revised well plan (gray) will add to the productive life of the reservoir.*

to integrate quantitative 4D information into the history match and this is an area of active research.

- **Improved seismic imaging** – Technological improvements are increasing exponentially. In the years between surveys new technologies become available, such as improvements in seismic migration algorithms, that mean that the 3D image is improved as a by-product of the 4D objectives.

- **The element of surprise** – As we have seen, reservoirs are complex systems. When the 4D results arrive it may often be the case that entirely unexpected issues are identified. Additional data always has the potential to add to our understanding of the reservoir.

As with the Gannet C and Norne examples, the majority of published material about the application of time-lapse seismic is from surveys carried out in the North Sea. In the North Sea, over the period 2000-2003 more than 80% of the total expenditure on time-lapse services (Lumley, 2004), defined as acquisition, processing and interpretation by service companies and contractors. The North Sea has played a crucial role in proving the efficacy of time-lapse technology. National governments,

Figure 1.5: *The global propagation of 4D programmes. After Tang et al. (2007).*

recognising the need to optimize recovery of their finite natural resources, made the North Sea an attractive place for long-term investment in research and development by establishing favorable financial conditions. The initial investment paid off and there are now numerous 4D success stories.

Shell Expro, for example, reported a saving of approximately US$27 million by showing a single injection well was not needed, for an investment of approximately US$3 million in time-lapse seismic over their Gannet fields (Kloosterman et al., 2003). At the well-known Gulfaks Field the added value of 4D seismic has so far been estimated to be approximately US$950M (El Ouair and Strønen, 2006).

Some basic effects that time-lapse has been shown to successfully detect are: reservoir compartmentalisation (and hence bypassed oil); lateral movement of injected gas and water; upward fluid contact movement (gas-oil contact, oil-water contact); pressure changes, especially pressure increases due to fluid injection; exsolved gas; and changes in fluid saturations away from the wells.

Having proven itself in the North Sea, both technically and economically, time-lapse seismic is being gradually deployed on a global scale. Figure 1.5 shows the major new areas of 4D activity around the globe. Tang et al. (2007) report that a study by Institut Français du Pétrole (IFP) has shown that the global 4D market grew by over 95% in the period 2003-2006.

1.2.3 Time-lapse seismic - imaging more than just the reservoir

In the previous section I identified that one of the advantages of time-lapse seismic as being its ability to surprise geoscientists by presenting phenomena that had not previously been considered. So far, we have only considered dynamic changes inside the reservoir. The dominant conceptual model of a time-lapse experiment is one in which the acoustic properties of the reservoir rock change with production and those of the surrounding earth are considered static. Indeed, the assumption of a dynamic reservoir isolated from the surrounding earth is also made by reservoir engineers in most reservoir simulations. The assumption that only production-related changes are occurring inside the reservoir is often a good one. However, when geophysicists observed significant unexpected 4D signatures outside the reservoir at certain fields this assumption was challenged.

It is recognised that when reservoir compaction occurs, the stress around the reservoir will change in response to changes the reservoir volume. With the exception the Valhall and Ekofisk fields, where severe reservoir compaction led to massive surface subsidence, the possibility that significant and detectable changes would occur outside the reservoir was never a consideration in early time-lapse studies. In any case, early time-lapse seismic data where generally not of sufficient quality to resolve these changes even if their existence had been predicted. As a result of constantly improving data quality and an increasing awareness among 4D practitioners of a new *whole-earth* approach, there is now a increasing collection of published examples where compaction-related acoustic changes outside the reservoir are observed as coherent signals on time-lapse seismic surveys (Guilbot and Smith, 2002; Hall et al., 2002; Hatchell et al., 2003; Herwanger and Horne, 2005; Rickett et al., 2006; Hawkins et al., 2007).

Figure 1.6 shows a comparison of forward modeled volumetric strain above the compacting Valhall reservoir and time-lapse seismic time delay. The two show good agreement but most importantly they show that time-lapse data can image coherent changes in the whole earth and not just the reservoir zone. While these non-reservoir changes add complexity to the interpretation of the time-lapse seismic response, they can also be used to provide information on the dynamic changes inside the reservoir. Utilising these non-reservoir time-lapse changes to infer dynamic changes inside the compacting reservoir will be the main focus of this thesis.

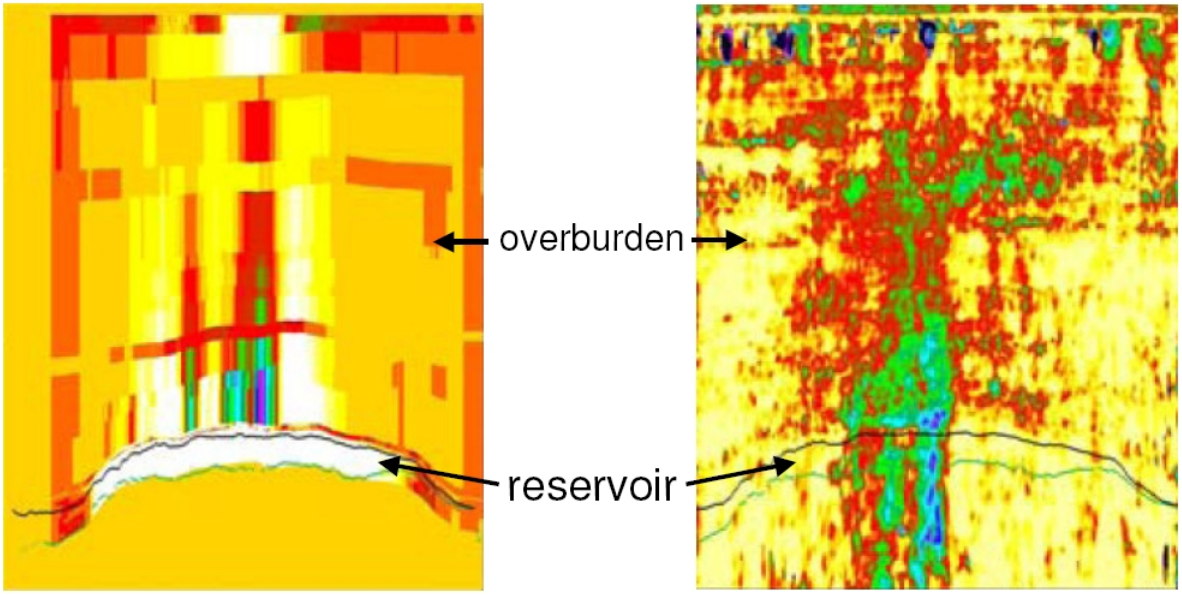

Figure 1.6: *A qualitative comparison of modeled volumetric strain above the compacting Valhall reservoir (left) and time-lapse seismic time delay (right) showing good agreement (green/blue colours represent decreasing volumetric strain/increasing time delay, while orange colors represent no change). The time-lapse data images changes in the whole earth and not just the reservoir zone. After Kristiansen et al. (2005).*

1.3 Compaction due to hydrocarbon production and why monitoring it is important

All bounded reservoirs will show pore pressure depletion unless pressure is supported naturally, by a strong aquifer for example, or artificially, by the injection of fluids. If the reservoir rock is a compressible material, such as an unconsolidated clastic or a weak chalk, then the reduction in pore pressure will result in compaction of the reservoir. Compaction can also be induced by chemical weakening of the reservoir rock and by thermal effects. Reservoir compaction has been observed in a wide range of geographical locations and reservoir types, such as the North Sea, the Gulf of Mexico, California, Canada, South America and Southeast Asia (Bruno, 2002). It can be a positive phenomenon because the compaction mechanism can provide significant energy to drive production, analogous to squeezing water from a sponge. Indeed, there are several examples where compaction is recognised as the predominant drive mechanism (Setarri, 2002). Unfortunately, the majority of compaction-related effects are negative. Figure 1.7 is a cartoon showing several possible effects of reservoir

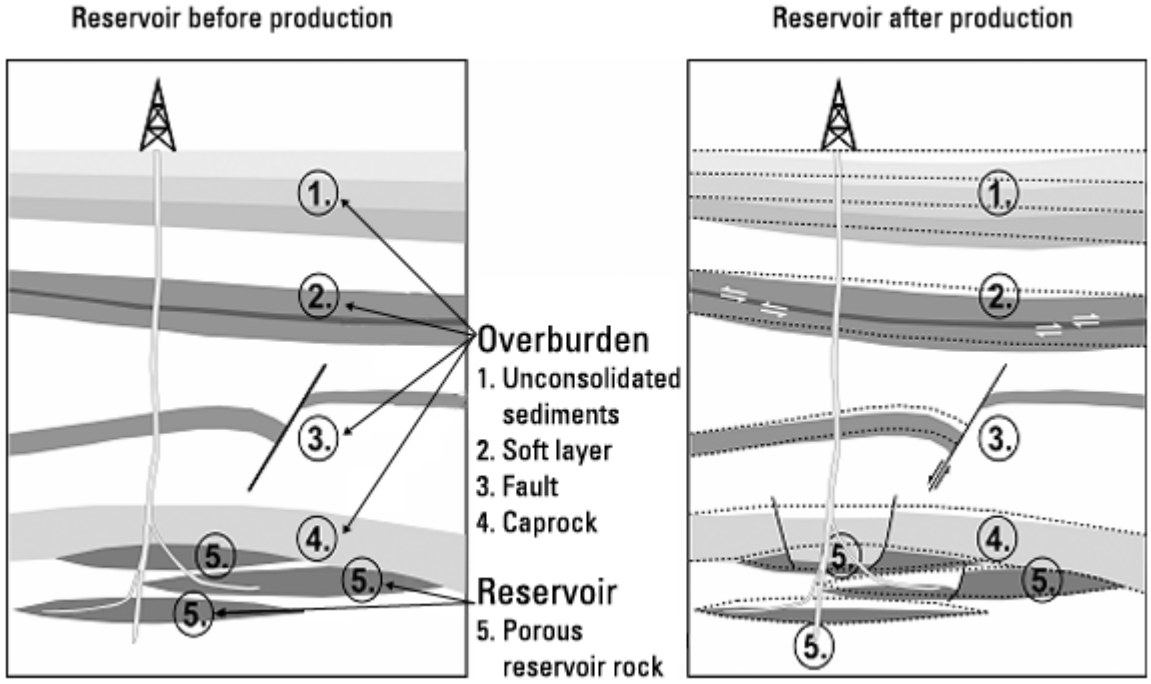

Figure 1.7: *A cartoon of reservoir compaction-related effects (courtesy of www.westerngeco.com)*

compaction, which will be discussed in the coming sections.

1.3.1 Surface subsidence

Reservoir compaction will result in surface subsidence in certain geological situations, such as highly compacting reservoirs that are laterally extensive in comparison to their depth. Two well-known and dramatic cases of surface subsidence are the Wilmington oil field in California and Ekofisk in the North Sea. At Wilmington depletion due to hydrocarbon production between 1926 and 1967 caused a subsidence bowl covering 75km^2 which showed a maximum subsidence of approximately 9m and differential horizontal movements of up to 3m, causing significant damage to infrastructure, such as bridges, rail tracks and utilities (Allen and Mayuga, 1969). At Ekofisk, seafloor subsidence of several metres has been observed since production began in 1974, which jeopardised the integrity of the platform (Sulak, 1991), as shown in Figure 1.8. A temporary solution was found, the re-elevation of the platform and construction of a protective barrier, at a cost of approximately US$1 billion

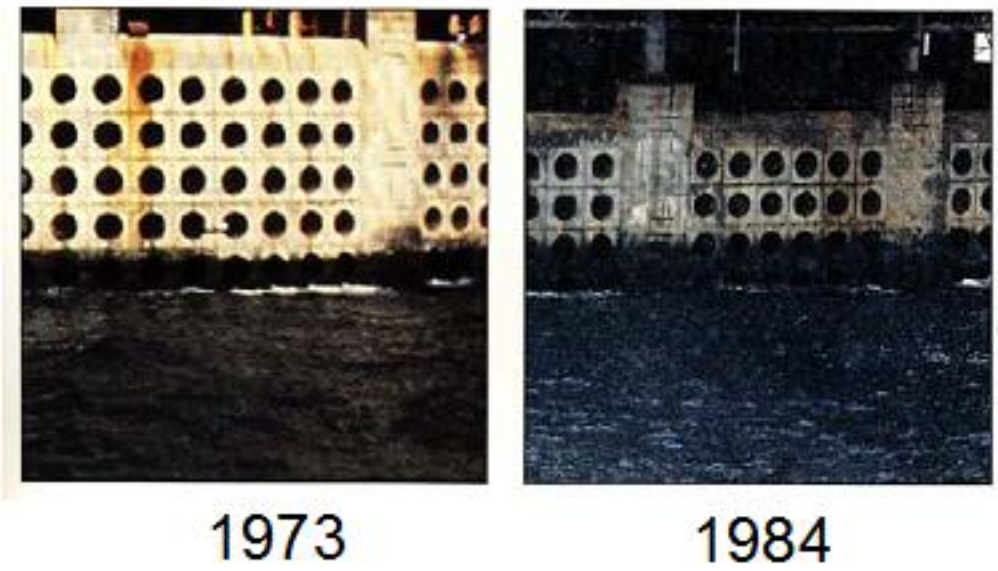

Figure 1.8: *Subsidence at the Ekofisk platform.*

(Hermansen et al., 1997). A subsequent review of the facilities and production strategy resulted in the construction of a new platform, which came online in October 1996.

1.3.2 Well integrity

Moving deeper into the overburden the major problems are related to well integrity. Weak lithological interfaces can cause localised shear (Bruno, 2002) and changes in overburden stress can cause the reactivation of existing faults (Segall, 1989). Just above the reservoir there is a danger of fracturing the reservoir seal, which could lead to hydrocarbon leakage into the overburden. In this region wells can also fail due to extensional forces (Dusseault et al., 2001). A well recovered from Wilmington Field shows how localised the damage can be (Figure 1.9).

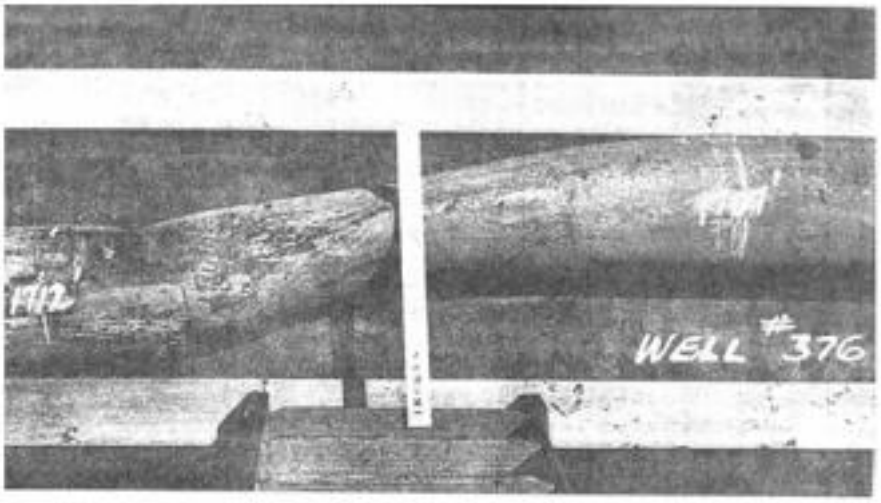

Figure 1.9: *Localised deformation in a well damaged in the overburden at Wilmington Field, CA, USA showing approximately* 10" *lateral offset on* $10\frac{3}{4}$" *casing over a 5ft interval. After Bruno (2002)*

1.3.3 Reservoir compaction

Inside the reservoir strong compaction can lead to a reduction of porosity and loss of permeability, resulting in lower production. At the Genesis Field, an over-pressured, unconsolidated turbidite reservoir in the Gulf of Mexico, several wells displayed permeability losses of between 80-95% as a result of depletion-induced reservoir compaction (Pourciau et al., 2005). Large deformations inside the reservoir can result in buckling-induced casing damage. Figure 1.10 shows five casing damage scenarios as outlined by Veeken et al. (1994).

1.4 Geomechanics - monitoring and modelling

Geomechanics is concerned with the mechanics (deformation and failure) of the earth and is the main discipline which studies the effects related to the compaction of reservoirs. In the oil industry typical problems that come into the sphere of geomechanics are pore pressure prediction, sand production prediction, well bore stability, fracture analysis, fault seal analysis and reservoir compaction analysis. The aim is to gather data to determine *in situ* stresses, rock failure mechanisms and rock mechanical parameters in order to make forward predictions which can be used to

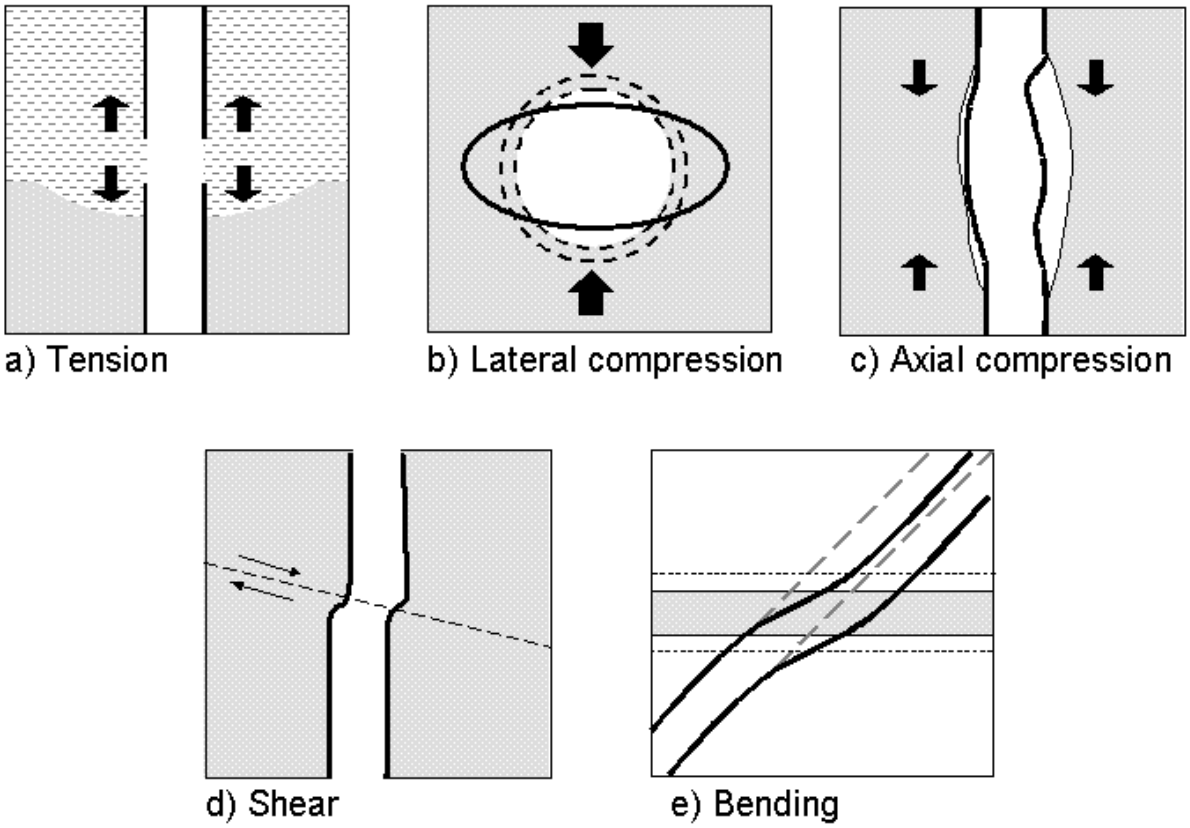

Figure 1.10: *Casing damage scenarios inside a compacting reservoir (after Veeken et al. (1994))*

mitigate the effects of rock deformation and failure.

As emphasized earlier in this chapter, the only *in situ* measurements available are from borehole data. Cores may be extracted from the well and tested in the laboratory to determine the constitutive relationship between stress and strain, or the reduction of porosity or permeability under compaction for example. Down-hole measurements can also taken, for example compaction logging, where radioactive bullets are injected into the formation and repeated logging measures changes in their depth. However, dense spatial measurements are generally restricted to the surface expression of reservoir compaction.

Leveling surveys and global positioning system (GPS) measurements provide centimetre to millimetre accuracy and if the conditions are favorable (e.g. on accessible land or on a oil platform) can be carried out at regular intervals and at sea regular bathymetry surveys can be used to monitor seafloor subsidence (e.g. Guilbot and Smith, 2002). Displacement gradients (tilts) can also be measured using tiltmeters, which can make high precision measurements with a resolution of $10^5 m$ Vasco et al. (e.g. 2000). Remote-sensing technologies such as InSAR (interferometric synthetic aperture radar) are providing opportunities to survey large areas (e.g. Xu, 2002).

Figure 1.11 shows InSAR measurements over the Lost Hills reservoir in California. Lost Hills is situated approximately 700m below the surface and has dimensions of approximately 1.5×3.5km. The interferometric measurements show changes composed primarily of vertical surface subsidence, with purple indicating no change and the brightest red showing highest subsidence levels (white areas are where the radar measurements were unobtainable, mostly in the agricultural fields where surface disruption (such as ploughing) alters radar properties). The images show four measurements in 1995, 1996, 1998 and 1999. It is clear to see that subsidence in the central part of the field reduced over this time, which is a consequence of a water flood programme introduced in 1992 to improve recovery and mitigate subsidence (Fielding et al., 2002).

1.5 Monitoring the whole earth

We can conclude that field development of compacting reservoirs is substantially more complex than that of conventional reservoirs. Production optimization in this context

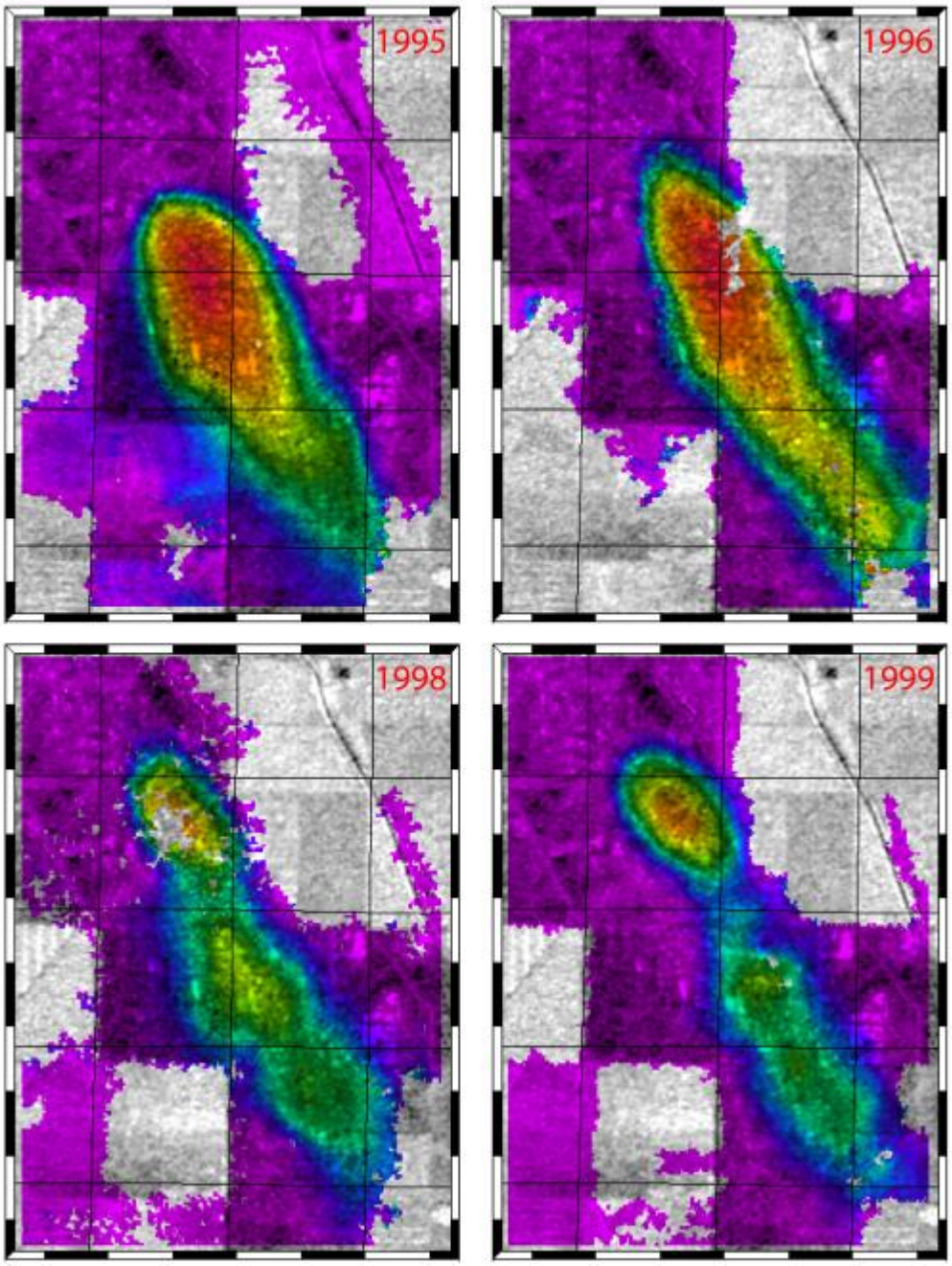

Figure 1.11: *InSAR measurements over Lost Hills Reservoir California, showing changes composed primarily of vertical surface subsidence. Purple indicates no change and the brightest red indicates the highest subsidence levels (white areas are where the radar measurements were unobtainable, mostly in agricultural fields where surface disruption (such as ploughing) alters radar properties). Source: NASA/JPL-Caltec, Producer ID:MRPS97478*

must give additional consideration to the geomechanics of production. The stakes are high, as the example of Ekofisk clearly demonstrates. Monitoring technologies will be required to help pinpoint where model updates are required and help guide the nature of these updates. As we have seen, time-lapse seismic is unique among the many monitoring options available because it opens up the possibility of imaging changes in the whole earth.

1.6 Thesis aims and outline

This thesis will develop the idea of monitoring changes inside the reservoir by analysing time-lapse seismic observations from outside the reservoir. I will develop the workflow presented in Figure 1.12 and apply it to two real-world examples.

The remainder of this thesis consists of six chapters:

Chapter 2 provides an overview of the evolution of methods which use time-lapse seismic to monitor reservoir compaction. Specific attention is given to deformations outside the reservoir and how they can be monitored by time-lapse seismic. An overview of reservoir geomechanics also is given, along with some current rock-physics models of how velocity changes with stress and strain, both of which aid interpretation of observed non-reservoir time-lapse anomalies.

Chapter 3 makes the case for using time-lapse observations above the reservoir as part of the 4D analysis. Techniques to establish stable estimates of time-lapse time shifts and their derivatives, time strains, are critically examined.

Chapter 4 builds on Chapters 2 and 3, which show how time-lapse time shifts and there derivatives (time strains) can be transformed into representations of the strain earth around compacting reservoirs. I show how, under appropriate assumptions, 3D estimates of strain deformation can be related to changes in reservoir pressure via a linear system of equations.

Chapter 5 applies the inversion scheme set out in Chapter 4 to data from the Valhall Field, in the Norwegian North Sea.

Chapter 6 applies inversion scheme in a different geological setting, the Genesis Field in the Gulf of Mexico.

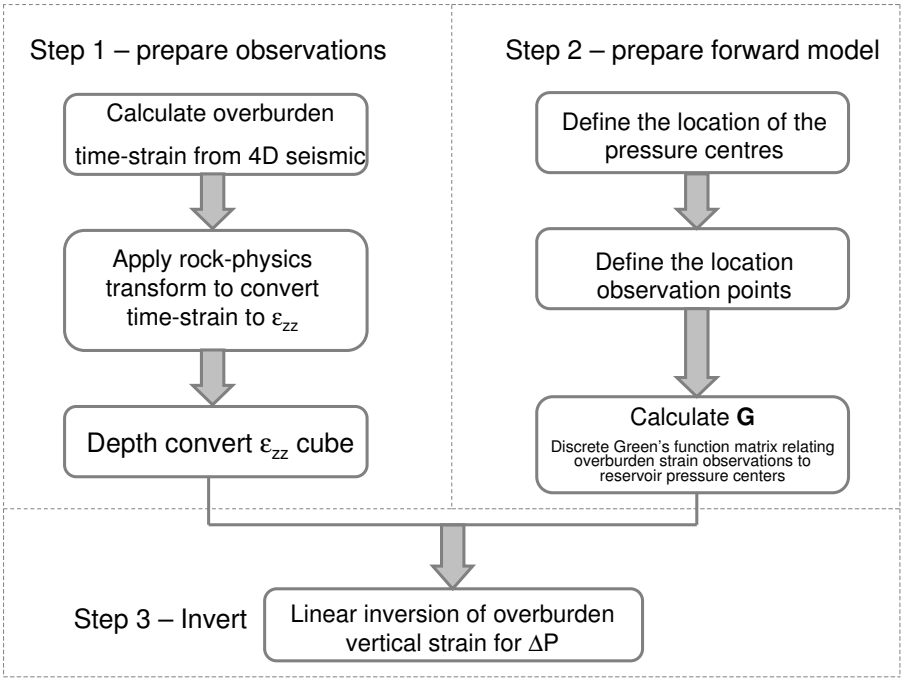

Figure 1.12: *The work flow for inverting for reservoir pressure from time-lapse time strains as outlined in this thesis.*

Chapter 7 presents a summary of the thesis. In addition, recommendations for further development of the ideas presented in this thesis are made.

CHAPTER

TWO

4D seismic and compacting reservoirs: An overview

This chapter provides an overview of the evolution of methods which use time-lapse seismic to monitor reservoir compaction. Specific attention is given to deformations outside the reservoir and how they can be monitored by time-lapse seismic. An overview of reservoir geomechanics also is given, along with some current rock physics models of how velocity changes with stress and strain, both of which aid the interpretation of observed non-reservoir time-lapse anomalies.

2.1 4D seismic monitoring of compacting reservoirs

2.1.1 Early observations

Reservoir compaction is balanced by changes in the stress state of the overburden. Above a compacting reservoir the overburden stress will decrease as the overburden expands to accommodate the reduction in reservoir volume. This is accompanied by a reduction in acoustic velocity of the overburden rock. To this author's knowledge, the first published example of 4D seismic being used to as a tool for monitoring compaction of a hydrocarbon reservoir is as recent as 2002 when the article *"4-D constrained depth conversion for reservoir compaction estimation: Application to Ekofisk Field"* (Guilbot and Smith, 2002) was published in the Society of Exploration Geophysics (SEG) publication *The Leading Edge*. Guilbot and Smith (2002) suggest that the time shifts at top reservoir could not be produced by the physical displacement of top reservoir alone, as this assumption would result in compaction estimates of 2-4 times greater than the reservoir model-based prediction.

The assertion that stretching the overburden will reduce the velocity is an entirely reasonable one. It is a well-documented phenomenon that acoustic velocities of sedimentary rocks are dependent on the stress state of the rock (e.g. Wyllie et al. (1958); Freund (1992); Han et al. (1986)). Typical laboratory measurements of velocity versus effective stress (defined as the external stress on the rock minus the pore fluid pressure, see Fjær et al. (1992) for more details) show a nonlinear relationship, in which velocity increases rapidly at low effective stress. The rate of increase gradually reduces until, at high effective stress, it reaches a plateau.

Later in 2002 Hall et al. published observations from Valhall, a compacting North Sea reservoir with similarities to Ekofisk, that support the idea that stretching in the overburden is likely to be accompanied by a reduction in velocity. This work was based on seismic warping technology, first developed as part of the Edinburgh Time-Lapse Project (ETLP), which will be discussed in greater depth in Chapter 3. The method uses image processing techniques to warp, in three dimensions, a monitor survey back onto a base survey, from which time shifts and apparent lateral displacements can be derived. At the Valhall Field, time shifts as large as 20ms down-shift are observed at top reservoir, which is far larger than those the observed 5-10m of compaction would produce with no accompanying velocity change. The

authors suggest that a velocity decrease as subtle as 0.8%, in combination with horizon displacements, would account for the observed time-shift.

A simple 1D perturbation formula was first published the same year by Landrø and Janssen (2002) and later by Landrø and Stammeijer (2004). It aids the interpretation of the observations made by Guilbot and Smith (2002) and Hall et al. (2002) by relating the fractional change in travel time to a fractional change in velocity and a fractional change in thickness.

$$\frac{\Delta t}{t} \approx \frac{\Delta z}{z} - \frac{\Delta v}{v} \tag{2.1}$$

In the reservoir, where the rock is compacted, the path length is decreased, which will decrease travel time through the reservoir zone. At the same time, compaction will increase the effective stress inside the reservoir, which generally increases velocity. The net effect is a decrease in the travel time through the reservoir. The opposite is true if the rock is dilated (stretched), as is the case in the overburden. The path length will increase, which will increase the travel time. Generally, dilation will cause the velocity to decrease, which will also have the effect of increasing the travel time. So for stretching, the net effect is an increase in travel time. The two effects of velocity and thickness change reinforce each other to produce time-lapse time shifts. The large time shifts at top reservoir observed by Guilbot and Smith (2002) and Hall et al. (2002) are due to the fact that although the changes in thickness and velocity in the overburden are relatively small, the effect is integrated over a large path length. The total time shift observed at top reservoir is an integration of Equation 2.1 over the whole overburden.

2.1.2 A growing number of published examples

Around 2005 there was a notable increase in the number of publications investigating the use of time-lapse seismic to monitor compacting reservoirs. Figure 2.1 shows the number of abstracts on the subject published at the EAGE (European Association of Geoscientists and Engineers) and SEG (Society of Exploration Geophysics) annual conferences between 1999-2007, which represents a good indication of the level of research activity in the reservoir geophysics community. There have also been two special editions of The Leading Edge (TLE), the SEG gateway publication that

highlights emerging technologies on this subject. The first was in December 2005 and titled *Rocks under stress* and the second in May 2007 titled *Geomechanics*. Table 2.1 gives an overview of publications showing observations of coherent time-lapse signal in the overburden above compacting reservoirs.

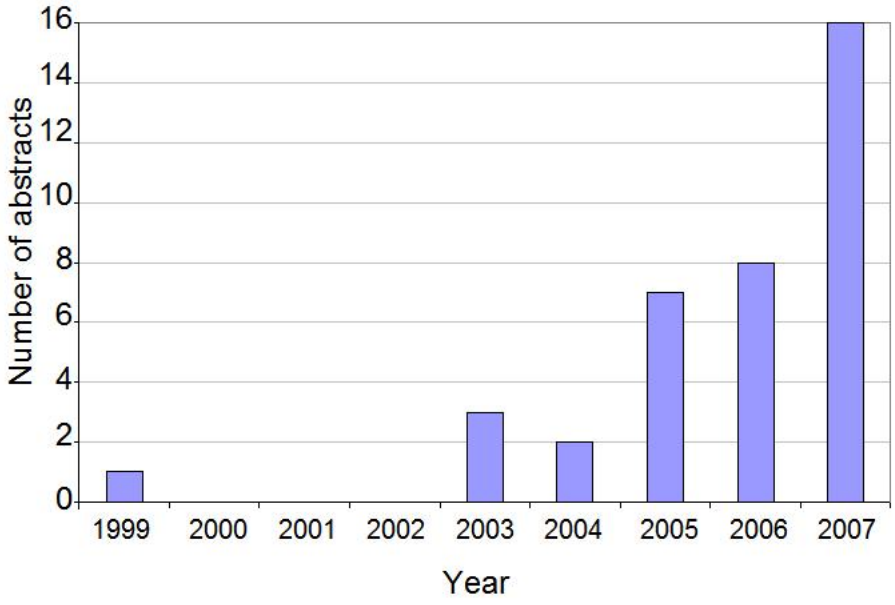

Figure 2.1: *The number of abstracts published at the EAGE and SEG annual conferences that on the topic of using time-lapse seismic to monitor compacting reservoirs.*

Table 2.1 show that the majority of examples are currently from the North Sea and Gulf of Mexico. However, it is no coincidence that these are also the areas with the highest number of time-lapse surveys. As the application of time-lapse seismic becomes more widespread and the number of surveys increase it is anticipated that a growing number of non-reservoir time-lapse observations will be made. The commonality between the reservoirs in Table 2.1 is that most are soft rocks, such as the unconsolidated deepwater turbidite sands in the Gulf of Mexico or North Sea chalk, often with high initial porosities ($> 30\%$), which are highly over-pressured.

The examples given in Table 2.1 give us an idea of the type of reservoir that might show non-reservoir time-lapse changes. Guilbot and Smith (2002) and Landrø and Stammeijer (2004) provide some methods for interpreting them, but they do not attempt explain the physical origins of these changes. We understand that stretching

Field	Area	Operator	Notes	Reference
Mars	GOM	Shell	Deepwater turbidite	Tura et al. (2005)
Europa	GOM	Shell	Deepwater turbidite	Tura et al. (2005)
Genesis	GOM	Chevron	Deepwater turbidite	Hudson et al. (2006)
Valhall	North Sea	BP	Chalk	Hall et al. (2002)
Ekofisk	North Sea	Conoco-Phillips	Chalk	Guilbot and Smith (2002)
South Arne	North Sea	Hess	Chalk	Herwanger et al. (2007)
Dan	North Sea	Maersk	Chalk	Hatchell and Bourne (2005b)
Shearwater	North Sea	Shell	HPHT	Staples et al. (2007)
Skua	North Sea	Shell	HPHT	Staples et al. (2007)
Egret	North Sea	Shell	HPHT	Staples et al. (2007)
Heron	North Sea	Shell	HPHT	Staples et al. (2007)
Elgin/Franklin	North Sea	Total	HPHT	Hawkins et al. (2007)
Offshore Sarawak	SE Asia	Shell	Carbonates	Hatchell and Bourne (2005a)

Table 2.1: *Published examples of observed time-lapse time-shifts in the overburden above compacting reservoirs*

a rock is likely to slow its acoustic velocity, but by how much? Are we able to predict if an observable time shift signal is likely at a given time, in order to predict if a time-lapse survey will be of value? Are time shifts able to distinguish if the reservoir depletion is compartmentalized?

As discussed in Chapter 1 the aim of this thesis is to quantitatively relate our time-lapse seismic observations to the dynamic changes in the reservoir. To fully understand how a compacting reservoir interacts with its surroundings and how that manifests itself on time-lapse seismic, the geomechanics of production must be also be understood and accounted for.

2.2 Reservoir geomechanics: An overview

Geomechanics is a discipline concerned with the mechanics (deformation and failure) of the Earth. In the oil industry typical problems that enter the sphere of geomechanics are pore pressure prediction, sand production prediction, well bore stability, fracture analysis, fault seal analysis and reservoir compaction analysis. If a reservoir is predicted to compact or found to be compacting, then it is likely that there will be some form of geomechanical analysis. As an established discipline geomechanics has a substantial back catalogue of literature and expert knowledge to draw upon.

Approaches to geomechanics can be roughly classified as empirical, analytical or numerical. The empirical approach is based on a company's in-house knowledge and published empirical observations. The analytical approach aims to describe deformation and stress change with precise mathematical equations. The complexity of such solutions means that they require the subsurface to be represented by simplified geometries, depletion patterns and mechanical properties. A well known analytical solution is the depletion of a disk-shaped reservoir in an semi-infinite linear elastic medium (Geertsma, 1973b). In many cases, analytical models provide a good first-order approximation to the problem. Finally, the availability of cheaper and increasingly powerful computers with large memory capacity means that numerical methods have become more accessible and popular. Using techniques such as the finite element method (FEM) to solve the governing equations, computer models allow for a more realistic representation of the subsurface (e.g. variations in material

properties, realistic geological structures). The problem with these models is that they require calibration to *in-situ* data before they can be used as a predictive tool. As discussed in Chapter 1, *in-situ* data is often unavailable because it is costly or difficult to obtain and is a sparse representation of the subsurface. Poorly calibrated numerical geomechanical models populated with highly uncertain properties can give potentially inaccurate and at worst misleading results.

The analytic and numerical approaches require a constitutive model, the simplest being linear elasticity, in which it is assumed that the stress and strain of an material element are linearly related and deformation is completely reversible with the removal of applied forces (see Fjær et al., 1992). Linear poroelasticity is the study of porous materials and therefore also includes the effects of fluid-filled pores on deformation (e.g. Rice and Cleary, 1976). More complex constitutive models incorporate non-linearity, such as the poroplasticity model which deals with post-yield deformation (e.g. Couples et al., 2007).

2.2.1 Stress and strain around a compacting reservoir

A 1D analytical solution for a compacting reservoir can be derived by considering a reservoir of thickness h that compacts uniaxially (only in the vertical direction) in an linear elastic way with no change in vertical stress. If the reservoir pressure depletes by an amount Δp, then the compaction Δh and textcolorredvertical strain ε_{zz} is given by the following equation (Fjær et al., 1992):

$$\varepsilon_{zz} = \frac{\Delta h}{h} = C_m \Delta p \tag{2.2}$$

where C_m is the uniaxial compaction coefficient, which is the rock compressibility under uniaxial conditions. Even in this idealized scenario an important observation can be made: Compaction tends to be larger for thicker intervals. Figure 2.2 shows an idealised scenario in which all the reservoir compaction is transferred to the surface subsidence so that $\Delta h = \Delta h_s$. In reality, the finite extent of reservoir means that compaction will be smaller at the edges than in the centre because of the constraining effect of the side-burden, and the surface subsidence will take the form of a subsidence bowl. This constraining effect is known as arching. Arching is the phenomenon whereby when a reservoir of finite extent compacts, the overburden vertical stress

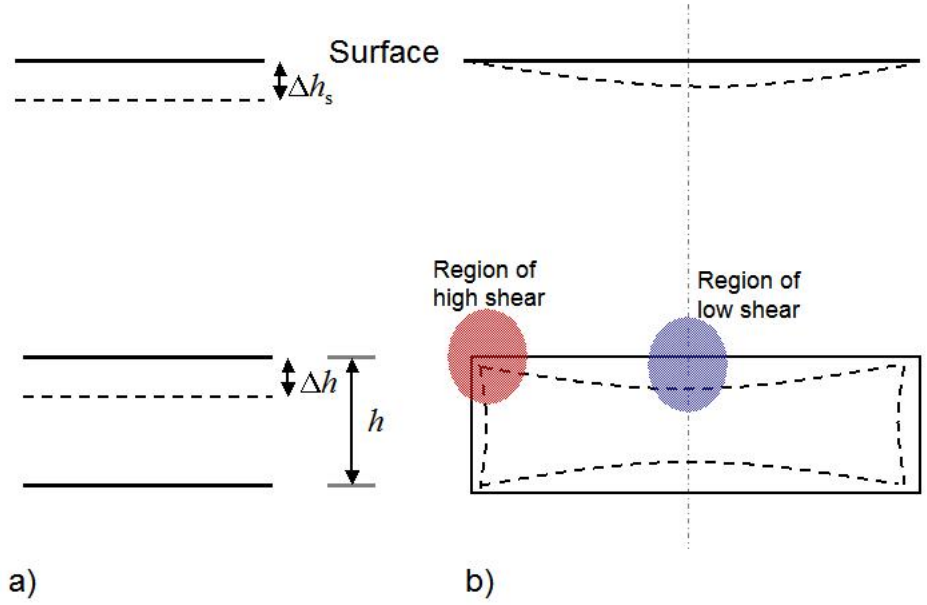

Figure 2.2: *Subsidence and compaction: (a) idealised model and (b) cartoon of realistic behaviour (adapted from Setarri (2002).)*

is reduced but the horizontal stress is increased, as the restrictive effect of the side-burden takes some of the overburden load. This is the principle was used by the Romans when building arches, and the provenance of the term arching effect.

The amount of arching will depend on the geometry of the reservoir and the depletion pattern. Thus, there is a spectrum of reservoir types ranges from shallow, laterally extensive reservoirs, that show a small arching effect, textcolorredto deep, narrow reservoirs, that show a large arching effect and very little surface subsidence.

A useful model to understand the general geomechanical behaviour of a compacting reservoir is the so-called nucleus of strain model by Geertsma (1973a). In this model the displacement caused by a nucleus of strain in a linear poroelastic halfspace is calculated. The effect of many nuclei can be integrated over the area of a reservoir to calculate the displacements, stresses and strains caused by reservoir depletion. Unfortunately the complexity of the integration means that only simple reservoir geometries can be accounted for analytically. Geertsma (1973a) integrates over a disk shape whilst Segall (1992) provides a more general solution for axisymmetric shapes, recovering the disk as a special case. Although the method is based on

Poisson's ratio	ν	0.25
Shear modulus	μ	2 GPa
Biot's coefficient	α	1
Reservoir thickness	h	100m
Reservoir depletion	$\Delta\overline{P}$	-10MPa

Table 2.2: *Reservoir properties used to create Figures 2.3 and 2.4*

constant elastic properties (i.e. no distinction between the reservoir and bounding rock properties) the solution gives a good general insight into the problem of stress and strain around a compacting reservoir. To illustrate the concepts discussed above the concept of stress path introduced by Hettema et al. (2000) is adopted. The stress evolution may be defined as the ratio of the principal stress components to the average reservoir pressure change, presented here in cylindrical coordinates:

$$\gamma_v = \frac{\Delta\sigma_v}{\Delta\overline{P}} \quad , \quad \gamma_\theta = \frac{\Delta\sigma_\theta}{\Delta\overline{P}} \quad , \quad \gamma_r = \frac{\Delta\sigma_r}{\Delta\overline{P}} \tag{2.3}$$

where γ_v is termed the vertical stress path, which relates the change in reservoir pressure ($\overline{\Delta P}$) to the change in vertical stress ($\Delta\sigma_v$). The same relationship between change in reservoir pressure and stress can be defined in the axial (θ) and radial (r) directions. The vertical and the radial stress paths are shown in Figures 2.3 and 2.4 for a range of reservoir depths and radii. The properties of the linear poroelastic halfspace along with reservoir thickness and depletion are given in Table 2.2.1. The grid shows reservoirs located at increasing depths (1000m, 2000m and 4000m) and increasing radii (1000m, 2000m and 4000m).

From the plots it is clear to see that the arching effect increases as the reservoir gets narrower and deeper. The arching becomes greater as more overburden and side burden are present to restrict the propagation of the vertical relaxation by increasing the radial stress above the reservoir (increasing γ_v, decreasing γ_r). As I will discuss, it is important for 4D seismic that, even when the expression of reservoir compaction at the surface is small, significant stress perturbations may extend well into the overburden. For these types of reservoirs even though surface subsidence cannot be used to monitor reservoir depletion then 4D seismic may still 'see' the arching effect.

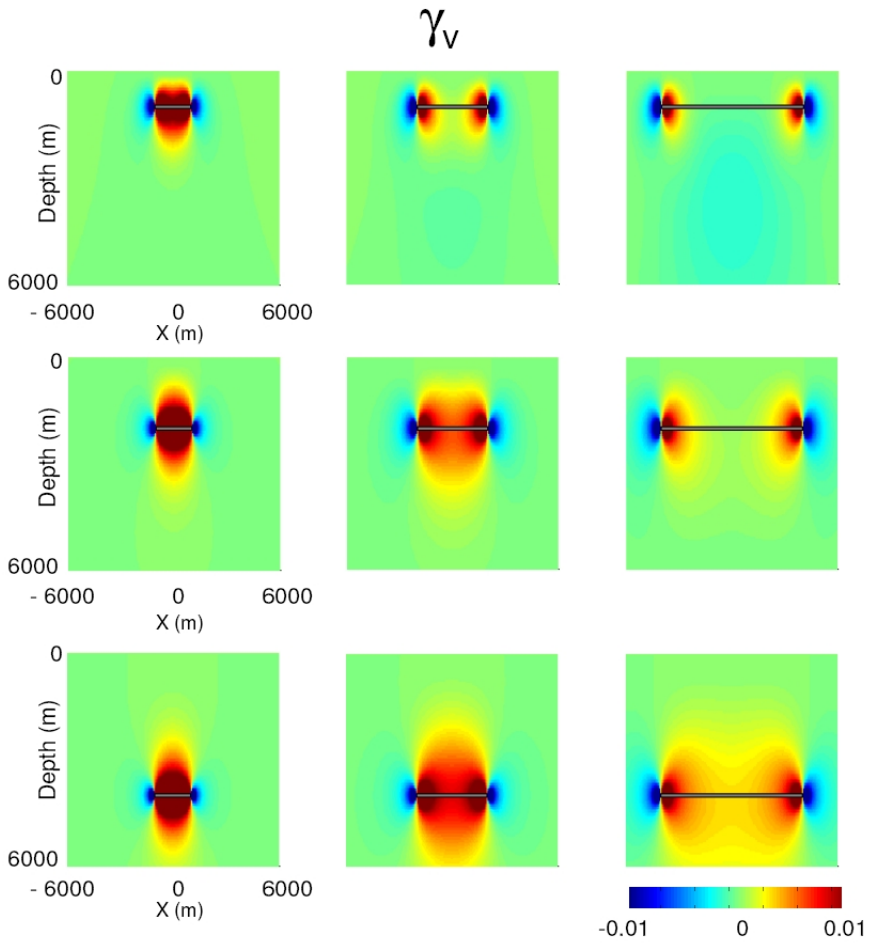

Figure 2.3: *Vertical stress path around a disk-shaped reservoir in a half space for a range of reservoir depths and radii. The properties of the half space are found in Table 2.2.1. The depths and radii are 1000m, 2000m and 4000m. See Equation 2.3 for definition of* γ_v .

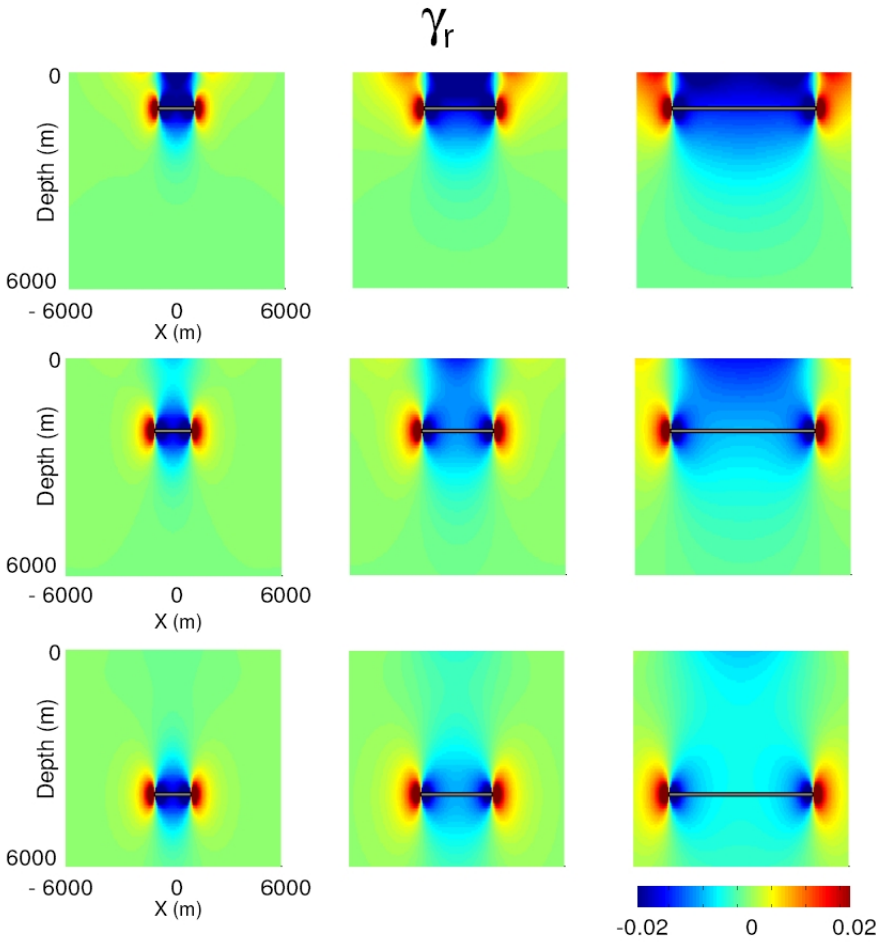

Figure 2.4: *Horizontal stress path around a disk-shaped reservoir in a half space for a range of reservoir depths and radii. The properties of the half space are found in Table 2.2.1. The depths and radii are 1000m, 2000m and 4000m.*
See Equation 2.3 for definition of γ_r.

2.2.2 Integrating geomechanics and time-lapse seismic

In 2003 Hatchell et al. published the abstract *'Whole earth 4D: reservoir monitoring geomechanics'*. This abstract is significant because, while the basic observations and concepts proposed within it are similar to those suggested by Guilbot and Smith (2002) and Landrø and Janssen (2002), it also includes the use of geomechanical modelling to forward predict the distribution and magnitude of the 4D time shifts. In contrast to the simple 1D (uniaxial) approach of Guilbot and Smith (2002) and Landrø and Janssen (2002) the authors recognise that the strain is not uniformly distributed above the reservoir, but spatially variable in a manner that is dependent on a number of factors, such as the shape of the reservoir or the mechanical properties of the rocks for example. Hatchell et al. (2003) show that by combining the use of geomechanics to predict the change in stress distribution in the overburden with a model of how velocity changes with stress, they were able to get a reasonable match between the observed and predicted travel time change at top reservoir as seen in Figure 2.5.

The abstract contained no specific details of the method, but rather outlined the concept of integrating geomechanics with time-lapse seismic. The link was further emphasized in a later abstract which utilized the same data (Stammeijer et al., 2004). Earlier publications anticipate combining geomechanical modeling and time-lapse seismic by conducting synthetic feasibility studies, (see Minkoff et al. (1999); Olden et al. (2001); Vidal et al. (2002)), however the overburden is only acknowledged for its role in the geomechanics of production, and forward modeling of the time-lapse seismic in these studies assumes the acoustic properties of the overburden are unaffected by changes in overburden stress.

Hatchell et al. (2005) expanded on the earlier work of Hatchell et al. (2003) and published details of a method using geomechanical models to predict time-lapse time shifts, taking the pragmatic approach of coupling the change in velocity to strain. textcolorredRelating velocity to strain, as opposed to stress, was a new approach which will be discussed in greater detail in Section 2.3.4. For a zero offset seismic ray, one can relate, to first order, the fractional change in travel-time to a fractional change in velocity and a fractional change in thickness (Landrø and Stammeijer (2004), see Equation 2.1). When 4D seismic time shifts are our only observations then there is a fundamental non-uniqueness; there are two unknowns for only one set of observations. In 2003 Røste et al. (2005) and Hatchell et al. (2005) independently

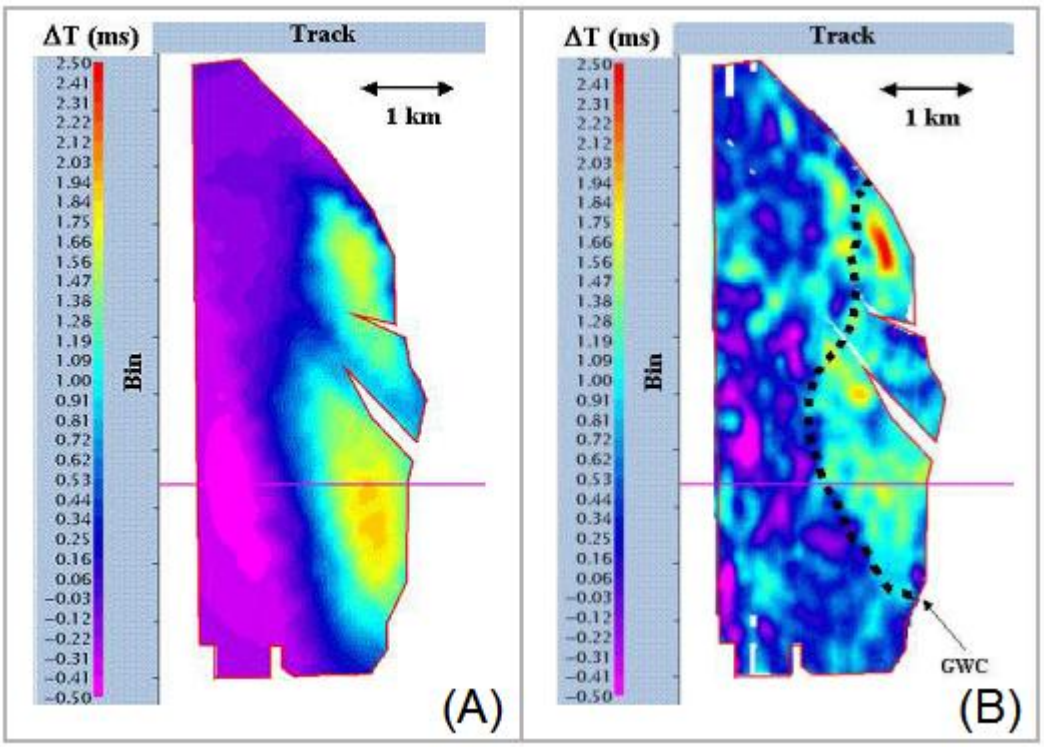

Figure 2.5: *(a) Predicted and (b) observed time-lapse time-shifts at top reservoir. The predictions were made by combining the predicted change in stress from a geomechanical simulation and a model of how velocity will change with changing stress. After Hatchell et al. (2003).*

proposed that changes in velocity could be linearly related to vertical strain via a constant of proportionality which Røste et al. termed α and Hatchell et al. termed R. For various reasons R has become the popular terminology, so it will be used from herein. By writing the change in velocity as proportional to vertical strain (Equation 2.4a), where the sign convention is that compression causes velocity increase and dilation causes a velocity decrease, then Equation 2.1 can be rewritten as Equation 2.4b.

$$\frac{\Delta v}{v} \approx -R\varepsilon_{zz} \tag{2.4a}$$

$$\frac{\Delta t}{t} \approx (1+R)\varepsilon_{zz} \tag{2.4b}$$

where the term $\Delta z/z$ from Equation 2.1 has been replaced by ε_{zz}, signifying the vertical component of the strain tensor. Of course, this linearisation does not solve the problem of having more unknowns than observations. However, by coupling the two factors contributing to the observations, it presents the problem in a new light. If the value of R could be somehow obtained independently (theoretically or experimentally) then vertical strain can be determined from zero offset time shifts and vice versa. Hatchell et al. (2005) took the approach of obtaining estimates of vertical strain as an output from a geomechanical model and calculating the value of R that gave the optimal match between observed time shifts and time shifts calculated using the integral form of Equation 2.4b. This approach was applied to data from a number of compacting fields around the world and Hatchell and Bourne (2005b) report that the value of R was found to be approximately 5 for the overburden. This approach makes the assumption that the estimates of vertical strain from the geomechanical models are accurate.

A similar workflow was proposed by Herwanger and Horne (2005). However, instead of linking changes in velocity changes to vertical strain, the authors chose to use an anisotropic model for how velocity changes with using the full triaxial stress state of the rock (Prioul et al., 2004). The forward modelling workflow was used to predict changes in shear wave splitting in the overburden. Changes in shear wave splitting can only be explained by anisotropy changes in velocity, because the phenomenon is unique to anisotropic materials. When a shear wave enters an anisotropic medium it splits into two approximately orthogonal polarizations, which propagate at different

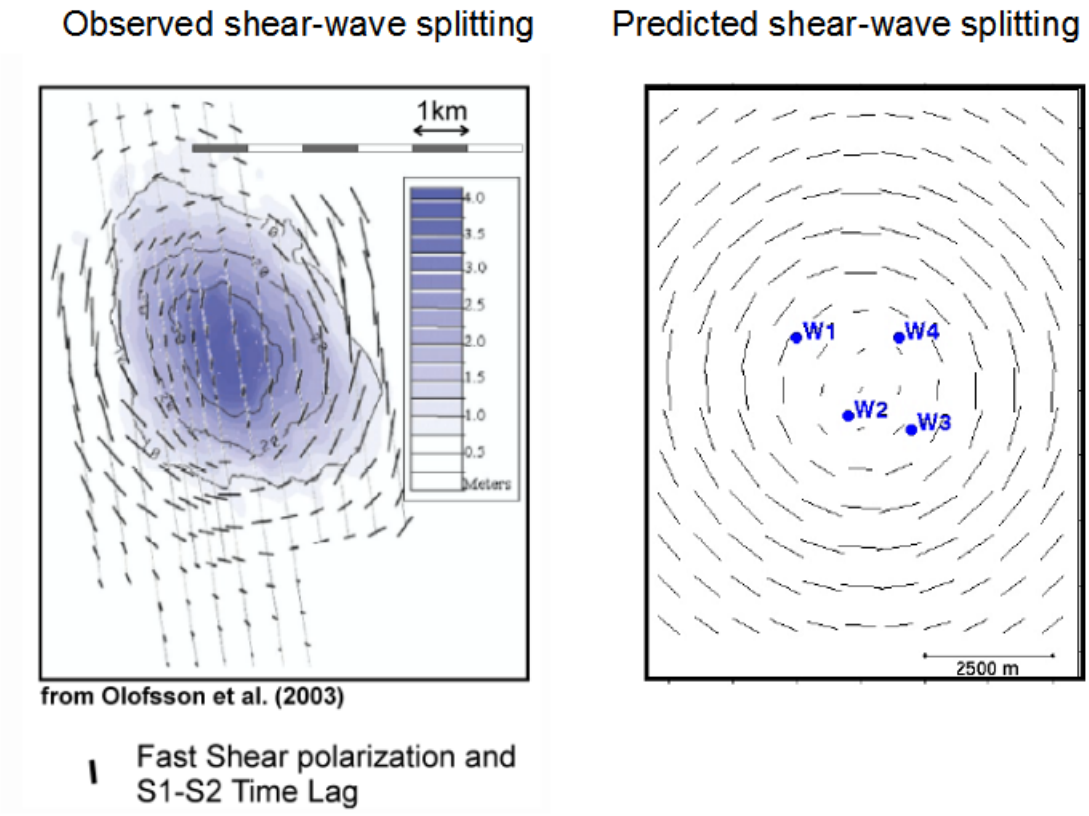

Figure 2.6: *(a) Predicted and (b) observed time-lapse changes in shear-wave splitting in the shallow overburden at Valhall (after Herwanger (2007)). Arrows represent the polorization and magnitude (travel time delay between the fast (S_1) and slow (S_2) shearwaves) of the splitting. In (a) the blue colours show the observed magnitude of subsidence.*

velocities. This can result in a measurable time delay between the so-called *fast* and *slow* shear waves. Herwanger and Horne (2005) proposed that if the seismic anisotropy of a overburden changed, due to changes in the triaxial stress state, then this could be observed on multi-component seismic data. The authors compare observed shear wave splitting from Valhall with their predictions, made using an analogue geomechanical model based on the Valhall Field which was assembled from published data on geometry and rock properties. The result, shown in Figure 2.6, suggests a good agreement between the predicted and the observed response.

Clearly a key step the workflow that integrates geomechanics and time-lapse seismic is the transformation of the changes in the stress/strain state of the earth into changes in seismic velocity. The next section gives an overview of the main approaches to

this transformation.

2.3 Velocity stress/strain relationships

As we have established, a change in the stress state of a rock will cause the acoustic velocity to change. As outlined earlier, laboratory data shows that velocities initially increase rapidly at low effective stresses, but that this increase will gradually reach a plateau at high stresses. Many rock models exist to describe the variation of various of rock properties under a host of different conditions, however, many of these models require the parametrization of a large number of unknowns. The complexity and uncertainty of rock models is one explanation for the prevalence of empirical relationships in the oil industry. This does not imply that all rock models are not always useful. For example, Biot-Gassmann theory (Gassmann, 1951), which describes the variation of the rock modulus with changing pore fluid properties, has been the foundation for amplitude-versus-offset (AVO) fluid discrimination and 4D seismic feasibility studies. It has proved to be extremely accurate in many sandstone reservoirs.

The observed mechanical properties of a rock will depend largely on the length scale at which the observation is made relative to the heterogeneities present. Rocks have heterogeneities on many different length scales. For example, layering and faulting exist on macroscopic scales, while microcracks, mineralogy and porosity exist on the microscopic scale. For seismic properties we are interested in length scales on the order of tens of metres which are generally described in terms of continuum mechanics, i.e. the rock is described as a homogeneous elastic material. The aim of microscopic rock models is to describe the macroscopic properties based on the microscopic behaviour. Theories adopting this approach are commonly called *effective medium* theories.

2.3.1 Rock physics models: A brief overview

The observed stress dependency of acoustic wave velocities implies a non-linear stress-strain relationship, because for a linear material the acoustic velocity would be constant. Holt et al. (2005) give an overview of the sources of non-linearity in

sedimentary rocks: Change in porosity with stress, the existence of sharp grain contacts and the presence of cracks and fractures. These nonlinearities can be incorporated in macroscopic models, that use the framework of continuum mechanics, or microscopic models which deal with nonlinearities on the scale of particles or microscopic inclusions.

Macroscopic models

The propagation of an elastic wave through the earth is often described by solid linear elastic theory. However, since porous rocks also generally contain fluids then poroelasticity is required. Solid linear elasticity does not allow for the variation of elastic velocity with stress, instead higher order stress-strain relationships are required which we will discuss later. Poroelasticity does allow for a change of velocity with stress, but the magnitude of the effect is not large enough to explain laboratory or field observations.

Under the framework of poroelasticity both the fluid and the rock grain components of the rock contribute to the seismic velocity. Since the porosity changes as a function of effective stress it is tempting to assume that changes in porosity can account for observed changes in seismic velocity with stress. On the application of external stress σ the pore fluid pressure P_{pore} will resist the change, resulting in a effective stress σ_{eff} that is defined as $\sigma_{eff} = \sigma - nP_{pore}$. The factor n, the effective stress coefficient, weights the contribution of the pore-pressure and will be discussed in more detail later. In the theory of linear poroelasticity porosity is a function of the mean effective stress while the rock framework and grain moduli remain stress insensitive. Velocity will change as a function of porosity (and therefore stress) because of changes in the ratio of the volume occupied by pore fluid and solid rock. However, when the stress sensitivity of velocity is calculated on this basis it is found to be negligible in comparison to the large stress sensitivity displayed by most rock laboratory experiments or field observations (from 4D seismic) (Fjær et al., 2008). In order to obtain the magnitude of stress sensitivity seen in the laboratory we need to incorporate nonlinear elasticity.

In contrast to conventional linear elasticity where the potential energy is defined as a quadratic (second-order) function of strain, *third-order* or *nonlinear* elasticity includes cubic (third-order) terms that account for the change in acoustic properties

with stress (Thurston and Brugger, 1964; Prioul et al., 2004). As noted by Prioul et al. (2004) this approach is only valid for relatively small stress deviations about a reference stress state since the model predicts that linear changes in velocity with stress, compared with linear elasticity which predicts velocity is constant with stress. Since a power-law or exponential type behaviour of velocity with stress is observed in the laboratory, third-order elasticity cannot explain the full range of observations.

Microscopic models

Two popular approaches can be made to effective mediums: Grain pack models and inclusion models. Grain pack models describe microscopic behaviour by imagining the material as a collection of grains with varying degrees of contact. Inclusion models, on the other hand, imagine the rock to be a solid with inclusions imbedded within it. The classic example of a grain pack model is a collection of uncemented spherical particles. The contact area between the particles will increase with an increasing external force normal to the contact. This forms the basis of Hertz-Mindlin theory (Mindlin, 1949; Walton, 1987), which predicts that the macroscopic behaviour of a collection of these contacts will lead to a velocity-stress sensitivity that is proportional to $\sigma^{1/6}$, where *sigma* is the effective stress. Comparison with laboratory tests on loose sands and glass beads (e.g. Domenico, 1977; Holt et al., 2005) show that in reality the stress sensitivity is more likely to be proportional to σ^n where n has a value of 0.20-0.25. There are several possible explanations for this discrepancy. Analytical models cannot account for partial slip or grain rotation. The force also is assumed to taken equally at all grain contacts. In addition, the coordination number, which characterises the average number of contacts per grain is not well-known. Of course the assumption of spherical particles is also not accurate for natural minerals. Nevertheless, many refinements have been made to Hertz-Mindlin theory, such as accounting for various packing orders, adding the effect of a saturating fluid or describing cemented rather than pressurized contacts.

In contrast to the above approach, inclusion theories treat the rock as a solid which contains inclusions such as open cracks or fractures. Models differ by the types and orientation of the inclusions. Kuster and Toksöz (1974), for example, investigate ellipsoidal inclusions. Another crack-based approach is to assume that the stress dependence of the rock matrix is caused by internal discontinuities, such as graingrain contacts, micro-cracks, clay content or any regions of internal damage.

The stress-sensitivity of these internal weaknesses can be collectively accounted for by introducing the concept of excess-compliance (Sayers and Kachanov, 1995). In a homogeneous isotropic elastic medium this is a function of the confining pressure loading the rock. At high confining pressures, the rock matrix will have a finite compliance, because any excess-compliance will tend to zero when only incompressible pore space exists and all internal weaknesses are closed. Then, as pressure is relaxed, excess-compliance is formed due to the opening of these internal weaknesses. This formulation can describe stress induced changes in anisotropy. MacBeth (2004) used this concept to derive a semi-empirical law to describe the dependency of the sandstone rock frame moduli under hydrostatic loading.

2.3.2 Static and dynamic moduli

If we measure the compressional and shear wave velocities of a rock, from well logs or seismic data, along with the density, we can calculate the elastic moduli of the rocks as experienced by the acoustic wave. We could reasonably expect this to match the elastic moduli calculated from stress and strain measurements in rock mechanics tests. In general, the two do not match. Moduli obtained from rock mechanical tests, the so-called static moduli, are often found to be substantially lower than those obtained by acoustic measurements, the so-called dynamic moduli. The origins of this difference are likely to be differences in strain amplitude and the heterogeneous nature of the rock microstructure (Fjær et al., 2008). The strain amplitudes for seismic waves are on the order of 10^{-6}–10^{-7}, while in a rock mechanical test they are typically 10^{-2}–10^{-3}. Tests have shown that when the rock mechanical tests are conducted in such a way that strain amplitudes are lowered, by performing a short unloading-reloading cycle, then static moduli moduli measured from under these conditions tend towards the dynamic moduli (Fjær et al., 2008). The effect of the heterogeneous microstructure is implied by observation that for a homogeneous elastic material, such as steel, there is no difference between the dynamic and static moduli.

In the preceding sections we have considered stress changes in a medium and changes in acoustic wave velocities resulting from those changes. In a typical geomechanical model constructed for the oil industry all but the reservoir zone (and certain special cases such as salt) will be assumed to behave as linear elastic materials. The resulting stress changes from these models are then used to calculate velocity changes.

However, a linear elastic material has constant elastic moduli and therefore its velocity is also constant with stress. The deformations of linear elastic materials are used to predict nonlinear changes in wave propagation. The approach appears fundamentally inconsistent. This inconsistency may be reconciled by quantifying the relationship between static and dynamic moduli. More research is required in this area, but it is problematic because many geophysicists are sceptical about the validity of laboratory data, as I will discuss next.

2.3.3 The reliability of core data

We have discussed the general behaviour of velocities with stress in the context of observations made in the laboratory on cores extracted from wells or outcrops. How confident are we that these are representative of the *in situ* response of rocks? With the advent of time-lapse seismic our predictions of how velocity will change with stress are being increasingly tested. In general, it has been found that the response due to pore pressure increases, around an injection well for example, is usually within the uncertainty of our predictions (**?**). In the case of pore pressure depletion however there are many examples in which the velocity change is much smaller than expected (**?**). These results have lead to doubts about the validity of core data used to characterise the velocity stress relationship. The main concerns are:

Representation As discussed in Chapter 1, wells are, in general, sparsely located. Each core measurement is costly and time consuming so a limited number of cores are sampled from an already sparse dataset. As a consequence cores do not provide a statistically meaningful representation of the heterogeneities in the earth. For example, in highly unconsolidated reservoirs often the most competent rock is sampled due to the practicalities of handling core.

Core damage Damage caused by stress unloading during and after coring could significantly change the stress velocity response. The change from *in situ* stress to atmospheric conditions may be sufficient to induce micro-cracks and broken grain bonds, reducing the elastic stiffness and acoustic velocity. The damage to the core plug is irreversible and reloading in the laboratory, back to the in situ stress state, will not give the same velocity stress response. Nes et al. (2002) showed the effect of core damage by conducting controlled

laboratory tests on synthetic sandstones cemented under stress to simulate *in situ* stress conditions. Starting at initial reservoir pressure the velocity of the synthetic core was measured during unloading to simulate coring and reloading to simulate a laboratory test on cored material. Figure 2.7 shows a schematic that illustrates the findings. The stress sensitivity (slope of the curve) is greater on reloading. This suggests that a significant part of the stress dependency measured in the lab is actually related to core damage effects.

Stress path The stress path that a rock undergoes during production can be shown to have a significant impact on the stress dependency of acoustic velocities. Scott Jr (2007) shows that a uniaxial deformation test on Berea sandstone resulted in very little change in velocity with stress, whereas a applying a triaxial stress path, where axial stress is increased and lateral stresses are held constant, showed changes in both velocity and anisotropy as a function of stress. Figure 2.8 shows the triaxial test (a) and the uniaxial test (b). Testing the rock along the appropriate stress path is therefore important to understand the stress dependance of velocity. Unfortunately, determining the stress path that a rock will follow is difficult. The stress path is dependent on many factors such as the geometry of the reservoir and the geomechanicial properties of the reservoir and its surroundings. Furthermore, the stress path will depend on the region of interest. For example, the stress path inside the reservoir may differ substantially from that of the overburden.

Effective stress coefficient In a porous rock the principle of effective stress is also required. On the application of external stress σ the pore fluid pressure P_{pore} will resist the change, resulting in a effective stress σ_{eff} that is defined as $\sigma_{eff} = \sigma - nP_{pore}$. This concept originated in the study of deformations in linear poroelastic rocks (see Chapter 4). However, the internal processes involved in deformation and wave propagation may be inherently different (see discussion on static and dynamic moduli). The concept of effective stress is not as well understood in the context of wave velocities compared to the concept as applied to the deformation of a linear poroelastic medium. A further complication is that velocity also depends on the pore fluid, which depends on pore pressure but not external stress. To decouple the contribution of the pore fluid to wave velocities the stress dependance of the dry-frame moduli is often examined, rather than velocity, by adding or subtracting the fluid contribution using Gassmann's equation (Gassmann, 1951). In the absence of a working theory or

clear empirical relationships the value of n is often taken to be unity, although experiments have identified a range of values above and below unity.

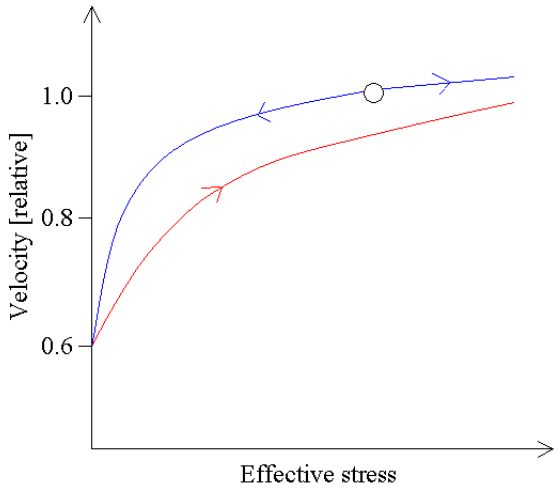

Figure 2.7: *Schematic illustration of the effect of core damage. The cementation state (marked with circle) represents the in situ conditions. Changing the stress from that point represents loading (reservoir depletion) or unloading (injection or coring) under in situ conditions (blue curve). When core is taken it is unloaded to zero effective stress. Upon reloading in the lab the velocity-stress relationship will follow the red curve and the stress sensitivity will be over-estimated. Figure adapted from Fjær et al. (2008).*

2.3.4 The R factor

The single parameter empirical relationship between velocity and strain proposed by Hatchell and Bourne (2005a) (Equation 2.4a) has been widely adopted by geophysicists investigating overburden stretching. This pragmatic and empirical approach has appeared, to first order, to be extremely effective. However, there has been some discussion about the applicability of such a relationship.

Theoretically a relationship between vertical strain and velocity changes can be justified in the context of either macroscopic or microscopic rock physics models. On the macroscopic scale Herwanger (2007) and Fuck et al. (2007) independently show that, under certain reasonable assumptions, third-order elasticity described earlier reduces to the velocity-strain relationship proposed by Hatchell and Bourne

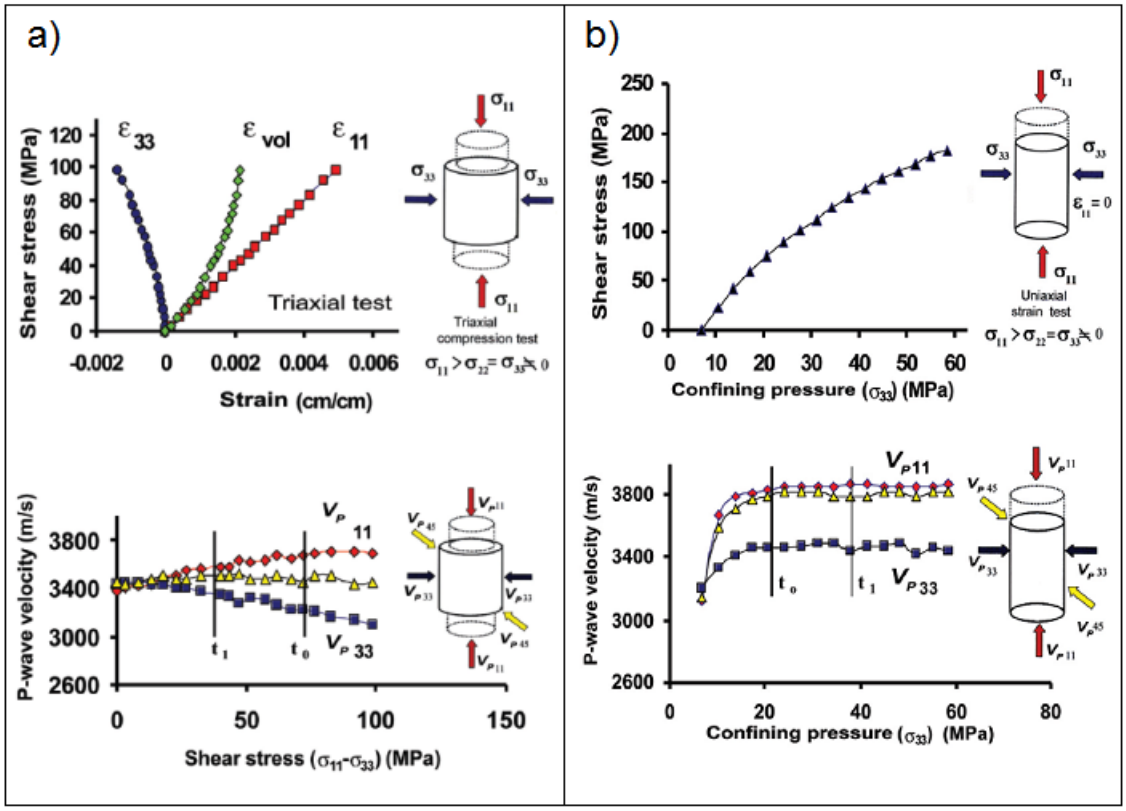

Figure 2.8: *Stress path effects on Berea sandstone. (a) A triaxial stress path, where axial stress is increased and lateral stresses are held constant (b) uniaxial stress path, where both axial and lateral stresses are raised to allow one-dimensional compaction. Significant changes in velocity and anisotropy are induced by triaxial loading between the time of the base line (t1) and monitor (t2). Under uniaxial loading velocity and anisotropy show little sensitivity to stress. After Scott Jr (2007)*

(2005a) for zero-offset seismic rays. On a microscopic scale Hatchell and Bourne (2005a) justify the R factor model using the effective medium approach of Sayers and Kachanov (1995).

The adoption of a linear relationship between vertical strain and velocity changes by Hatchell and Bourne (2005a) seems natural when examining Equation 2.4a which gives the relationship between time shifts, velocity changes and vertical strain. However, it is a notable departure from the norm, as almost all measurements of dynamic properties are reported as a function of stress rather than strain. There are some good arguments in favour of linking velocity to strain. Referring to the poro-plastic deformation of rocks, Couples et al. (2007) state "it does not make sense to attempt to relate properties to stress, since the stress state is not uniquely associated with a particular strain". Staples et al. (2007) argues that, as many models propose that the velocity change is caused by crack opening and closure, it is natural to link velocity changes to strain. Of course, strain is a relative property so this relies on us being able to define the correct original stress state of the rock before measuring strain, which, as we have discussed, can be a difficult task in the laboratory.

The fact that strain is relative does have some practical benefits. As noted by Staples et al. (2007) by defining the velocity as a function of strain the constant of proportionality R is unitless and is the same for metric or imperial systems. Using strain also has a normalizing effect. If we consider the equivalent relationship in stress:

$$\Delta V_p = U\Delta\sigma \tag{2.5}$$

Schutjens (2005) shows that the constant of proportionality R covers a much smaller range of numbers than U. Caution is required when defining the component of stress to make it proportional to velocity. Defining the change in velocity proportional to the vertical strain, as done by Hatchell and Bourne (2005a), is not equivalent to making it proportional to the vertical stress. If we cast the time shift perturbation equation (Equation 2.4b) in terms of stress then in a linear elastic medium we get:

$$\frac{\Delta t}{t} = (1+R)\varepsilon_{zz} = \frac{(1+R)}{E}(\Delta\sigma_{zz} - \nu(\Delta\sigma_{xx} + \Delta\sigma_{yy})) \tag{2.6}$$

Several things can be noted from this equation. Firstly, for the stress formulation the static Young's modulus E and Poisson's ratio ν are required. While Poisson's ratio

will, in general, be well constrained, the estimated value of E may contain a larger degree of uncertainty. Secondly, it also requires knowledge of the triaxial stress state. Some researchers have proposed linking velocity changes to changes in vertical stress (e.g. Tura et al. (2005)). Unless the stress changes can be approximated as uniaxial then it is important to note that $\varepsilon_{zz} \neq \Delta\sigma_{zz}/E$.

So far assuming a linear relationship between velocity and vertical strain has proved an effective approach which can be theoretically justified and has yielded a good match between forward models and observed data for zero offset seismic data. Caution is required, however, if we wish to cast the velocity change as a function of other components of the stress or strain tensor or look at pre-stack seismic data. In these cases the simple formulation of Hatchell and Bourne (2005a) may become unsuitable.

Anisotropic velocity changes

As we have seen, in general velocity changes will be lithology dependent and anisotropic. Triaxial stress changes may cause stress-induced anisotropy, but, at present, our ability to use these changes is limited. Offshore it is only at fields such as Valhall, where four component (4C) ocean bottom cable (OBC) is deployed, that shear wave or converted wave information is recorded. Although permanent OBC data is an aspiration for reservoir management it is along way from becoming standard because of the high costs involved (Calvert, 2005). Research is still being undertaken into the sensitivity of 4D overburden time shifts on conventional P-wave stacked data to anisotropic velocity changes and there are few published studies. As discussed earlier, Herwanger (2007) bases the calculation of stress-induced anisotropy on analogue core data and the results, although they show a promising qualitative match, are not yet at a quantitative stage. A modelling study by Fuck et al. (2007) notes that the main difficulty in the practical assessment of travel time shifts using this method is that they rely on the calibration of three independent parameters. Fuck et al. (2007) also note that stress-induced anisotropy has the largest impact in the pre-stack seismic domain and suggest measuring time shifts as a function of offset. As we will discuss later, researchers have already proposed and tested (to varying degrees of success), models that suggest time-shifts increase as a function of offset even assuming isotropic velocity changes (Landrø and Stammeijer, 2004; Røste et al., 2005; Hawkins et al., 2007). These issues will need to be accounted for

in prestack processing of the time-lapse seismic data. It could be that our current lack of understanding of these issues is leading us to "processes away" these effects. Although these anisotropic changes have the potential to further constrain our understanding of the overburden response and indirectly aid reservoir management, until multi-component data becomes more readily available and we can calibrate rock physics models in the laboratory with more confidence, it seems reasonable to proceed using a simple model.

2.3.5 Independent calibration of stress sensitivity by 4D seismic

In recent years time-lapse seismic has afforded geophysicists the unique opportunity to test the petroelastic model, which defines the transformation of rock physical properties to acoustic properties. This is primarily built around Biot-Gassmann theory (Gassmann, 1951). As we discussed earlier, stress sensitivity enters these macroscopic equations as by defining the rock frame modulus (K_{fr}) as a stress dependent function. The reliability of the petroelastic model is especially important because it not only effects our ability to interpret time-lapse seismic data, but also to predict a future time-lapse response. In general, for sandstone reservoirs, the petroelastic model is found to be accurate and good agreement is observed when reservoir pressure is increased. However, in the case of reservoir pressure depletion, there are several examples where over prediction of the velocity-stress sensitivity has resulted in and the time-lapse signature being smaller than predicted, which can render the 4D survey useless for reservoir management.

Eiken and Tøndel (2005) report on their experiences at two fields in the Norwegian North Sea: Troll Øst and Sleipner Vest. Troll Øst is a large, gas-filled reservoir on the eastern part of the larger Troll Field, which consists of an alternation of clean and mica-rich sands with an average porosity of 30%. The reservoir is at a depth of 1290-1550 m below sea level, with a maximum gas column height of about 260m above a thin (0-4 m) oil zone, and an aquifer providing moderate water drive. Pressure depletion averaging 1.5 MPa was observed. A time-lapse signature consisting of a time delay below the reservoir was recorded, caused by an increase in reservoir velocity as a result of rock frame stiffening. The velocity-pressure sensitivity of was found by making a linear approximation of the velocity change with pressure and examining the time-lapse time shift versus the gas-column height. The pressure sensitivity was found to be 2-3 times lower than that predicted

by hydrostatic laboratory tests. In this instance, even though the pressure sensitivity was lower than predicted, the time-lapse signature was still a useful tool for reservoir management.

At Sleipner Vest, a gas condensate reservoir, the velocity stress sensitivity was also found to be much lower than predicted. In contrast to Troll Øst the reservoir is much deeper (3500-3600m). The sands range in thickness between 50-200m and have an average porosity of 17%. Despite reservoir depletion of up to 10MPa, for which laboratory-based data predicted several milliseconds time-lapse time shift, and excellent quality time-lapse data, no time-lapse signature was observable.

In another North Sea example, Floricich et al. (2006) performed a Bayesian inversion based on a relationship between time-lapse attributes and changes in gas saturation, water saturation and reservoir pressure at the Schiehallion Field. It was found that the relationship between acoustic impedance (AI) changes in gas and water saturation behaved as expected. However, the pressure sensitivity of the AI changes (and therefore the rock velocity, in the absence of large density changes) was dramatically different from that predicted in the laboratory. This result was independently confirmed by Stephen and MacBeth (2006a) using the seismic history matching methodology (Stephen and MacBeth, 2006b). It was found that the only way to match the time-lapse seismic data was to allow the stress-sensitivity to vary as part of the history matching process. The authors found the history match was significantly improved by the reduction of the velocity-stress sensitivity. Both papers assumed no more than the functional form of the velocity stress relationship. The results are summarized in Figure 2.9.

4D seismic is also driving the understanding of velocity-stress (or strain) relationships. In the absence of reliable core data geophysicists are turning to methods that seek to calibrate the petroelastic model using 4D data from other domains (such as the engineering domain), or even use this information to bypass the petroelastic model altogether.

The examples given so far have been for the stress sensitivity of the reservoir rock, but what about the overburden? As we have discussed, the same issues exist when trying to define the stress sensitivity of the overburden. Even though shale is the most abundant overburden rock (Holt et al., 2005) shales (and overburden rocks in general) are rarely cored and tested because the main focus of any coring programme

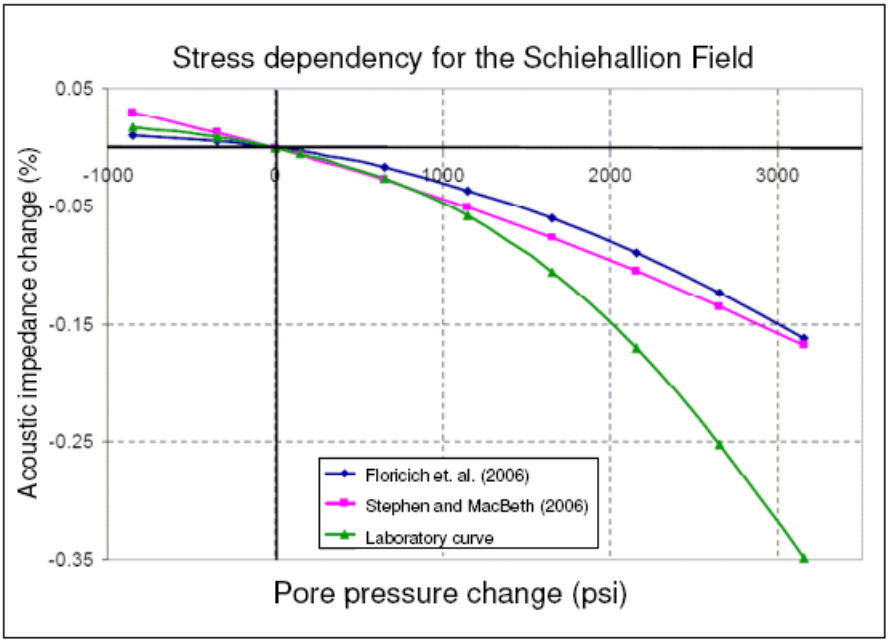

Figure 2.9: *Stress-sensitivity derived directly from the 4D seismic at the Schiehallion Field. The green line shows the original stress-dependency curve used, derived from laboratory measurements. The pink line shows the best history matched stress-dependency for sands after Stephen and MacBeth (2006a). The blue line is the the stress-dependency derived from the non-linear Bayesian inversion by Floricich et al. (2006). The two agree well as show markedly less stress-dependency than the laboratory data. After Floricich (2006).*

is to determine the properties of the reservoir. In addition, shale is a difficult material to handle in the laboratory because of its extremely low permeability and chemical sensitivity to water. This sensitivity to water also poses challenges for the testing equipment. To measure wave velocities the transducer must transmit through a water proof loading apparatus (Sarout et al., 2007).

Difficulties with laboratory testing of shales mean that theoretical models are difficult to verify with any statistical confidence. Whereas MacBeth (2004), for example, was able to collect measurements from 179 sets of openly published hydrostatic measurements on sandstones, the equivalent material on shales is rare. Furthermore, most dynamic experiments on shale are performed under hydrostatic loading conditions. As shale is inherently anisotropic, due to the alignment of the clay platelets, hydrostatic experiments prevent the quantification of that anisotropy. This means that, along with the questions of the reliability of core data discussed earlier, rigorously verifying theories of velocity-stress dependency against laboratory data is, at present, not a practical option. Like the earlier examples, one option is to employ methods which bypass any reliance on laboratory data and instead use 4D seismic data and constrains from other disciplines, such as engineering or geomechanics, to calibrate these relationships.

2.4 Summary of published techniques that use overburden time-shifts for reservoir management

While there is a growing number of observations of time-lapse time shifts related to overburden stress changes above compacting reservoir (see Table 2.1 and Figure 2.1) the number of methods using them for reservoir management (i.e. predicting compaction or pressure change) is relatively small. The methods all adopt the approach linearising the relationship between velocity and strain but they differ in their approach to resolving the non-uniqueness in this relationship, essentially by constraining the R factor.

The approach of Røste et al. (2005) and Hawkins et al. (2007) is to use the 4D time shift information contained in prestack P-wave data to make the problem over determined. Another approach is to use the strain output from a geomechanical model and vary the R factor to match observed 4D time-shift data. Differences

between the predictions and observations suggest that either the model needs updating or that there is a break down in the assumptions used in modeling. Finally, the approach taken by Bourne and Hatchell (2005) uses geomechanical concepts to pose a linear relationship that directly links reservoir compaction to the strain in the overburden, so that a linear inversion can be performed. This linear inversion can bring in suitable constraints as they are available or appropriate. A similar approached that will be explored further in this thesis was published independently in Hodgson et al. (2007). These methods are summarised in Table 2.3.

Paper	Method	Output	Field
Guilbot and Smith (2002)	A model for change in porosity with strain along with a two parameter model of how velocity varies with porosity (calibrated in the lab) is used to perform time-lapse tomography. The model requires two constraints (1) uniaxial compaction and (2) the assumption that the base reservoir is fixed.	Estimate of reservoir compaction	Ekofisk, North Sea
Hatchell and Bourne (2005a), Hatchell et al. (2005), Tigrek and Hatchell (2006), Staples et al. (2007), Hatchell et al. (2007)	All these papers present variations on comparing observed overburden time-lapse time shifts with those calculated using the equation $\Delta t/t = (1 + R)\varepsilon_{zz}$ in conjunction with geomechanical models.	Estimates of 4D time shifts from geomechanical modeling. Mismatch used to update reservoir compaction model.	Various, North Sea
Røste et al. (2005)	Derives a formula for time shift as a function of offset in pre-stack P-wave seismic data. Independently of Hatchell et al. (2005) proposes a linear relationship between velocity and vertical strain.	Estimate of reservoir compaction and the constant of proportionality between ΔV and ε_{zz}.	Valhall, North Sea

Table 2.3: *Summary of published methods which use compaction-induced overburden time shifts to infer dynamic reservoir changes (compaction or pressure changes)*

Paper	Method	Output	Field
Herwanger and Horne (2005); Herwanger et al. (2007); Herwanger (2007)	Similar approach to Hatchell and Bourne (2005a) but instead uses an anisotropic model of velocity changes with stress/strain	Estimates of time-shifts and shear wave splitting from geomechanical modeling. Mismatch can potentially be used to update reservoir compaction model.	Valhall, North Sea
Bourne and Hatchell (2005)	A Green's function approach based on linear elasticity theory is used to perform a joint inversion for top reservoir time shifts and surface subsidence.	Estimate of reservoir compaction.	Valhall, North Sea
Hawkins et al. (2007)	An inversion for stress is presented using the variation of time shift with offset in pre-stack P-wave seismic data. The relationship with stress is derived using the linear relationship $\Delta V/V = -R\varepsilon_{zz}$. No prior knowledge of R is required. Other constraints are needed, such as overburden density and pore pressure profiles with depth.	Estimate of stress changes.	Elgin/Franklin, North Sea

Table 2.3: *Summary of published methods which use compaction-induced overburden time shifts to infer dynamic reservoir changes (compaction or pressure changes)*

CHAPTER

THREE

Measuring time-lapse time shifts around compacting reservoirs

This chapter makes the case for using the overburden time shift instead of the reservoir-level time shift to determine reservoir compaction. In addition, a critical examination of methods currently available to measure time-lapse time shifts is offered.

3.1 Introduction

In the previous chapter I reviewed how reservoir compaction causes changes in stress around the reservoir, which can alter the path length and the seismic velocity and hence the seismic travel time. On the timescales suitable for reservoir management (a few years or less) the magnitude of these time-lapse time shifts is often only a few samples (or around 4-12ms on 4ms sampled data). To confidently recover these subtle time shifts we require highly repeatable time-lapse seismic. I will review the advances in the acquisition and processing of time-lapse seismic data have resulted in a steady improvement in repeatability. The methods by which we estimate time shifts have been found to be problematic, producing noisy and uncertain products. In this chapter I review current methods of time shift estimation and discuss how they may be improved. In addition, I discuss the interpretation of time shifts in terms of vertical strain and fractional change in velocity.

3.2 The time-lapse seismic signature of compaction

In Chapter 2 I showed how reservoir compaction causes changes in the stress and strain both inside and outside the reservoir. I also reviewed how seismic wave velocities are sensitive to changes in stress and strain. The combination of these effects causes changes in zero offset travel times with depth, which I refer to as time-lapse time shift. I also identified several published real data observations of time shifts in and around compacting reservoirs. All these examples share common characteristics which describe a basic time shift signal through the centre of compacting reservoirs.

In general, compaction-induced time shifts have opposite gradients inside and outside of the reservoir. There will be an increasing time-delay with depth, because the overburden rocks have stretched and their velocity has decreased. At top reservoir there is an change in the gradient of the time shift, where rocks change from being stretched to being compacted. This compaction causes an increase in velocity and a reduction in travel-time. It is generally observed that this reduction in travel time through the reservoir is not larger than the accumulated time shift through the overburden because in most settings the reservoir is relatively thin, in relation to the distance of overburden affected by stress changes. The result is that the total

time shift at base-reservoir is still positive. In the underburden further relaxation is expected to occur, resulting in a further accumulation of time shift.

To demonstrate the above concept I forward model time shifts through the centre of a 30m thick disk-shaped reservoir buried in a homogeneous halfspace (Poisson's ratio of 0.25 and a shear modulus of 1GPa), using methods that will be discussed in more detail in Chapter 4. The reservoir is buried at a depth of $D = 2500$m and has a radius of 1000m ($D/R = 2.5$). The pressure is reduced so that reservoir compaction totals 1m (i.e. a strain of 3.3%). I assume an initially constant velocity throughout the half-space of $v_0 = 2000ms^{-1}$. To calculate time shifts I use the R factor approach, introduced in the previous chapter, which relates velocity change to strain:

$$\Delta t(z) \approx \frac{2}{v_0}(1+R)\int_0^d \varepsilon_{zz}(z)dz \tag{3.1}$$

Other models of how velocity varies with stress or strain could be used, but for the purposes of a simple example the R factor model is sufficient. Hatchell and Bourne (2005a) suggest that different R factors are required for rocks in compression compared with those in expansion, otherwise the predicted time shift through the reservoir layer is too large and makes the time shifts below the reservoir negative, which disagrees with published observations. This is in agreement with the general observation of an asymmetry between the velocity-stress response of rocks under dilation, compared with those under compaction. Figure 3.1 shows the calculated vertical displacement, vertical strain and zero offset time shift through the reservoir described earlier. When the rocks are expanding (positive strain) I use $R^+ = 5$, where the plus sign denotes that this value is used in areas of positive strain. Inside the reservoir where the rock is compacting I use six different R values ranging monotonically from $R^- = 0$ to $R^- = 5$, where the negative sign denotes that these value are used for where strain is negative (compaction). In this example I have removed the constant offset time shift caused by surface subsidence.

Figure 3.1 shows the time shifts created using the different R factors inside the reservoir. Obviously, down to top reservoir the time shift in all examples are the same because $R^- = 5$ in the overburden for all cases. For $R^+ = R^- = 5$ the time shift through the reservoir is large enough to reverse the sign of the time shifts below the reservoir. As the value of R^+ increases, the time shifts below the reservoir are shifted towards the positive as the magnitude of compaction-induced speed-up through the reservoir is decreased.

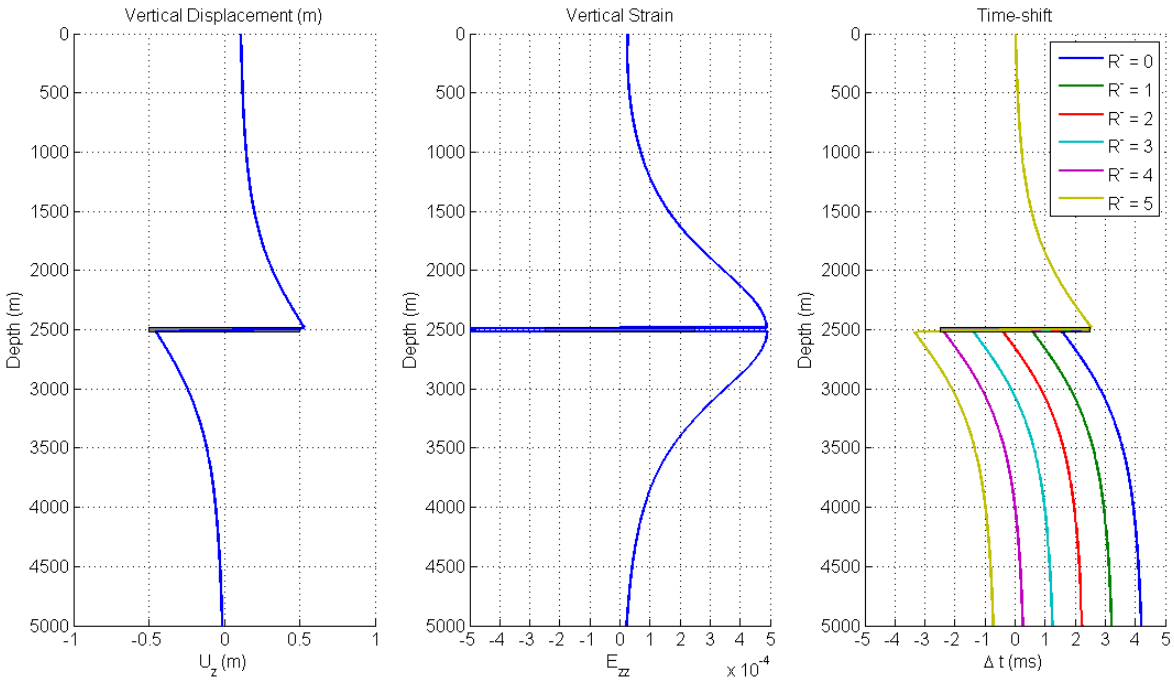

Figure 3.1: *The displacement, strain and calculated time shift though a disk-shaped reservoir with a radius of 1000m buried at 2500m depth in a homogeneous half-space ($\nu = 0.25, \mu = 1 GPa$). The time shift was calculated by assuming the velocity is a linear function of strain. Outside the reservoir the R^- factor, which relates velocity changes to strain under dilation is $R^- = 5$. A range of R^- factors were used inside the reservoir.*

The simple example above shows how knowledge of the velocity change inside the reservoir is crucial to our understanding of the time-lapse signal at reservoir level and below it. In the next section I elaborate on some of the complexities of determining reservoir compaction using the reservoir-level time-lapse signature.

3.3 Problems with determining compaction from the reservoir-level signal

In Chapter 2 I introduced the equation $\Delta t/t = \Delta z/z - \Delta v/v$ which relates the time strain ($\Delta t/t$) to the fractional changes in vertical thickness ($\Delta z/z$) and velocity ($\Delta v/v$). This equation has been widely adopted to interpret time-lapse time shift measurements in and around compacting reservoirs. The assumption that the fractional change in velocity can be linearly related to vertical strain is also often adopted, so that $\Delta v/v = -R\varepsilon_{zz}$ (e.g. Røste et al., 2005; Hatchell et al., 2003; Bourne and Hatchell, 2005; Staples et al., 2007; Hawkins et al., 2007). Both equations are derived using simplifying assumptions which rely on small changes in thickness and velocity. In addition, by relating fractional change in velocity to vertical strain it is assumed that there are no additional factors which contribute to the velocity change. I will argue that these assumptions are invalid inside the reservoir, but are valid in the overburden. By restricting our analysis to how overburden deformation relates to reservoir strain, we can find an alternative route to estimating reservoir compaction.

Fluid effects

Adopting the approach of Hatchell and Bourne (2005a) and using different R-factors under extension and compression to account for the smaller than expected observed speed-up in the reservoir assumes that the sole contributing factor to the reservoir velocity change is reservoir strain, which is generally not the case. In all but the simplest of production scenarios the velocity change will be made up from a fluid component, such as the variation of fluid properties with pressure (e.g. gas out of solution, fluid compressibility) and changes in fluid saturations (the relative mixture of gas, oil and water). If we wish to decouple the compaction and fluid components of the velocity change in the reservoir we require knowledge of the fluid distribution and fluid properties, in addition to the reservoir strain.

For example, Staples et al. (2007) calculate an effective $R^- = 3 - 5$ for the reservoir at Shearwater Field, North Sea, by estimating vertical strain from radioactive bullet data and the time shift through the reservoir from 4D seismic. However, when the fluid effect of the gas condensate pore-fill was accounted for, the R^- value attributed to strain alone was estimated to be in the much higher range of $R^- = 5 - 10$. This is because at Shearwater the gas bulk modulus decreases with reservoir depletion, counteracting the speed up in the rock frame modulus caused by compaction.

Separating the pressure and saturation related components from reservoir level time-lapse signal, such as amplitude changes, has been a major goal for time-lapse seismic community (see for example Landrø et al., 2001; Floricich, 2006). The addition of compaction-related effects further complicates this (e.g. Corzo and MacBeth, 2006).

Velocity changes due to compaction

In addition to the fluid effect, there is a high degree of uncertainty around determining the actual velocity changes due to rock compaction. There have now been many examples of a simple R-factor model being used to explain the time shifts observed through the overburden. However, there is significant controversy over whether such a simple model can be applicable in the reservoir.

Using the R factor model, Hatchell and Bourne (2005b) proposed that an asymmetry exists between the velocity-stress dependency under compaction and under extension. I used this assumption earlier for forward modelling. While this asymmetry can be used practically to help to explain time-lapse observations and improve the match with geomechanical models, as Bauer et al. (2008) note, this model implies a sharp discontinuity of the slope of $\Delta V_p/\varepsilon_{zz}$ at zero strain, which is unlikely.

Instead this apparent asymmetry may be explained by a number of factors. First, the linearisation of velocity and strain used in the R factor model is based on small strain perturbations. Outside the reservoir, strains are typically in the order of 10^{-3} compared with inside the compacting reservoir where they may be an order of magnitude larger (up to a few percent).

Some authors have suggested this asymmetry may be due to the different stress-paths followed by the overburden and the underburden (e.g. Sayers, 2007; Scott Jr, 2007).

In addition, if the rock fails and enters the plastic regime as may happen in the reservoir (e.g. Kristiansen et al., 2005; Fjær et al., 2008) then post-failure velocity-stress is not a phenomenon that is easily (or usually) measured in the laboratory and therefore not well understood.

If it were possible to understand the rock velocity changes inside the reservoir, which would be required to decouple the fluid changes from the rock changes, one would also have to be able to confidently measure the time shift at top and base reservoir, which can be problematic.

The time shift across the reservoir is difficult to measure

Measuring time shifts at top and base reservoir can be very difficult, especially if the reservoir is thin. Several factors complicate time shift measurements at the reservoir level. Firstly, Figure 3.1 shows that we expect an instantaneous change in gradient of the time shifts at top and base reservoir, where velocity reduction above and below the reservoir is interrupted by speed-up inside the reservoir. Usually, time shifts are measured using a windowed cross-correlation measurement. The windowed nature of cross-correlation means that if the window used is too long it will contain areas of both positive and negative time shift and these sharp changes will be lost (e.g. Tigrek and Hatchell, 2006; Staples et al., 2007). This is especially a problem when the reservoir is has a relatively small time-thickness in which case even the shortest practical correlation windows can contain signal from both top and base reservoir. Furthermore, if the reflectivity is strongly changed because of the reservoir acoustic impedance changes or tuning effects, methods which rely on comparing the similarity of time-lapse traces to estimate the time shift will be invalid (Williamson et al., 2007). In contrast, we expect the overburden to be free from both these problems. Strain is predicted to vary gradually in the overburden and because velocity changes are small we expect negligible reflectivity changes. I will discuss this issue in further detail later in this chapter in relation to the specific techniques used to measure time shifts.

3.4 Time-lapse seismic data quality and time shift measurements

So far I have identified a generalized time-lapse time shift signal above, inside and below the centre of a compacting reservoir. Our ability to use these time shifts qualitatively for reservoir management relies on our ability to confidently and accurately measure them. Before discussing in detail specific methods of estimating time shifts I first discuss how improvements in time-lapse seismic data quality has lead to our ability to detect these small time shifts in the first place.

It is now widely accepted that we can observe subtle (often <2 samples) time-lapse time shifts around geomechanically active reservoirs. Our confidence that these observations are real comes from a growing confidence in the quality of time-lapse seismic data and the fact that we are increasingly able to forward predict the gross features of our observations. However, such subtle measurements were not always possible because production-related time shifts were contaminated by noise.

In the earliest days of time-lapse seismic, so-called *legacy data* was typical. In this case, the baseline survey may have been an old exploration or development seismic survey. The legacy survey often had different acquisition and processing parameters to the monitor, leading to significant differences between the base and monitor which were unrelated to dynamic reservoir changes. To account for these differences a process known as cross-equalization was developed. This broad term encompasses several signal processing techniques that were used to compensate for differences in processing and acquisition such as trace interpolation onto a common grid, amplitude balancing, spectral balancing and image warping. For an overview of cross-equalization see Ross and Cunningham (1996).

As part of the cross-equalization process image warping was commonly used as a final step, to correct for gross vertical misalignments (time shifts) and horizontal misalignments between the data sets (Rickett and Lumley, 2001; Hall et al., 2002) possibly in a cyclic sequence of cross equalization. However, improvements in data quality due to dedicated 4D acquisition and processing mean that warping is now rarely required as part of the cross-equalization process, because the sources of noise that cause non production-related misalignments have been eliminated or greatly reduced. Indeed, warping is now more commonly used to study the more subtle

production-induced misalignments between time-lapse surveys (Hall et al., 2002; Hall, 2006; Rickett et al., 2006; Williamson et al., 2007).

So, how much has data quality improved since the earliest 4D experiments? As the technological and economic benefits of 4D seismic data became more apparent there was a drive for better quality time-lapse images. Big leaps were made when the geophysical community realized that dedicated parallel processing was needed. Whereas early 4D processing tried to correct for differences in acquisition and processing in the post-stack domain (e.g. Rickett and Lumley, 2001), processors instead started with the raw pre-stack seismic data and processed the base and monitor in parallel (e.g. Magesan et al., 2005). This greatly reduced processing errors (differing algorithms or migration velocity fields, for example) and allowed quality control at every stage of the processing sequence. A second step-change in data quality can be attributed to recent efforts to repeat source and receiver positions as accurately as possible. Calvert (2005) suggests that:

$$(\text{Monitor} + \text{Error}_2) - (\text{Base} + \text{Error}_1) = \text{small production-related change}$$

where the definition of Error can include a host of phenomenon that will damage the time-lapse seismic signal, such as random noise, water velocity variations, source and receiver positioning errors, overburden heterogeneities and the effects of processing. Where we are unable to eliminate sources of error, a second approach suggested by Calvert is to repeat errors as accurately as possible, so that they are differenced away. One source of the errors is non-repeatability of the ray path, which is controlled by source and receiver position repeatability. For example, in the case of distortions caused by overburden heterogeneity, if the seismic ray paths between base and monitor surveys are repeated with enough accuracy, then distortions due to these heterogeneities will be differenced away.

Most time-lapse seismic surveys are now dedicated to the purpose of reservoir management, so that the base survey acquisition and processing are designed with future monitor surveys in mind. For marine seismic data steerable streamers are now commonly used to repeat the acquisition geometry as closely as possible (e.g. Eiken et al., 2003). A further development is at the Valhall Field where permanent Ocean Bottom Cable (OBC) has been used with excellent results in the BP Life of Field Seismic (LOFS) project. Errors in receiver positions are essentially eliminated

because the receiver cables are trenched in the seabed at a depth of 1m (Kommedal et al., 2005). Careful source positioning has resulted in such good repeatability that automated workflows can be used to produce a rapid turnaround between acquisition and processing. van Gestel et al. (2008b) report achieving fully processed time-lapse data just three weeks after the last shot of the survey.

One measure of the quality of time-lapse data can be quantified by examining the now common metric NRMS (normalized root-mean-square) given by:

$$\text{NRMS} = 2\frac{RMS(a(t) - b(t))}{RMS(a(t)) + RMS(b(t))} \tag{3.2}$$

where RMS is defined as:

$$\text{RMS} = \sqrt{\frac{\sum_{t_1}^{t_2} a(t)^2}{N}} \tag{3.3}$$

and N is the number of samples in the interval $[t_1, t_2]$ (Kragh and Christie, 2002). The value of NRMS tells us how similar the two traces a and b are over the time interval $[t_1, t_2]$. Numerically it varies between 0 and 2. If the two traces are identical, NRMS = 0. If the two traces are anti-correlated (i.e. $b = -a$) then NRMS = 2. When the two traces are entirely made of random noise, NRMS = $\sqrt{2}$. Multiplying by 100 then gives what is commonly termed the percentage NRMS, although the term percentage is misleading as NRMS ranges from 0 to 200%! NRMS is a common metric used to judge the improvement due to cross-equalization. While NRMS is not an absolute metric, it can give a qualitative idea of the general level of repeatability. A literature survey reveals that in the North Sea early legacy time-lapse surveys had NRMS values of 60% or higher, while the NRMS values for more recent 4D-specific surveys were generally below 40%. More recently, where emphasis has been placed on repeating source and receiver positioning with a high degree of accuracy, NRMS values of 20% or lower are typically achieved (e.g. Eiken et al., 2003; Staples et al., 2006; Osdal et al., 2006; Furre et al., 2006).

3.5 Why do we need to improve current methods of time shift estimation?

Even though the quality of time lapse seismic data is constantly being improved, there remain inherent limitations on the accurate measurement of time-lapse time shifts using the most common methods. In this section I review these limitations.

3.5.1 Cross-correlation

By far the most common technique used at present to estimate time shifts is local window cross-correlation. The cross-correlation of two time sequences a and b is defined as:

$$c_j = \frac{1}{N+M-1} \sum_i a_i b_{i+j} \tag{3.4}$$

where j is called the *lag*, N and M are the lengths of a and b respectively and the sum is taken over all $N + M - 1$ possible products (Gubbins, 2004). Often, the correlation coefficient is normalised so that $c_j = 1$ when $a = b$ and $c_j = -1$ when $a = -b$. The normalised cross-correlation is given by:

$$c_j = \frac{\sum_i a_i b_{i+j}}{\sqrt{\sum a_i a_i \sum b_i b_i}} \tag{3.5}$$

Normalisation makes the correlation coefficients insensitive to variations in local amplitudes. As I discussed in earlier chapters, time shifts around compacting reservoirs are spatially variable. To capture this variability cross-correlation is performed in local windows of data. The window is often multiplied by a taper to mitigate the influence of strong events entering the window edge. Figure 3.2 shows an example of a local cross-correlation performed on a 101 sample section of two traces, x_1 and x_2, which have been tapered with a Hanning window. The traces are taken from a real time-lapse dataset.

The time shift is identified by finding the lag with the maximum cross-correlation coefficient. However, as can clearly seen on Figure 3.2, which shows the cross-correlation function, the peak is not resolved because of the discrete sampling of

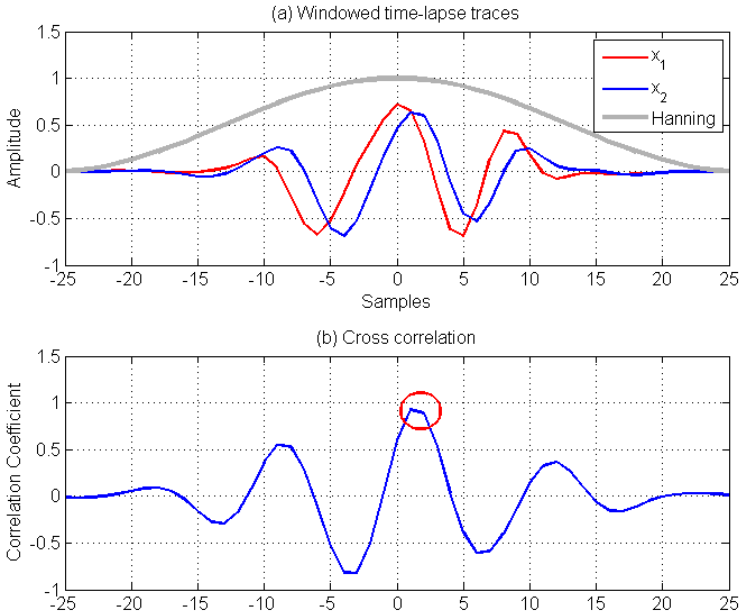

Figure 3.2: *(a) Two time series x_1 and x_2 with in a 51 sample (204ms) window centered on sample 26 which have been tapered with a Hanning window. (b) The normalised cross correlation of the two sequences. Note that the peak is not fully resolved because of the discrete nature of the signal.*

the time series, which is usually $4ms$ for seismic data. Sub-sample resolution is possible by (a) resampling either the seismic data or the cross-correlation function to some desired resolution or by (b) fitting a function in the vicinity of the maximum cross correlation value. Of these two options a fitting procedure is often used because resampling is a comparatively costly computation process and provides only a marginal improvement in accuracy. If we chose the two points either side of the cross-correlation maximum value then it is trivial to exactly fit a parabola and calculate the lag and cross correlation value associated with the peak.

When significant time shifts occur outside the reservoir in a spatially variable pattern it is more natural to examine a time shift cube, where the time shift has been evaluated at every sample of the seismic trace. This can be viewed in standard seismic visualization packages which allow the extraction of arbitrary slices and horizons, potentially greatly aiding our interpretation capability. However, measuring the time shift at every sample using cross-correlation is not without pitfalls. The windowed nature of the cross correlation measurement means that there are inherent limitations of resolution and accuracy. I will illustrate these limitations by examining an example from a real time-lapse dataset. Figure 5.2 shows two real time-lapse traces from a

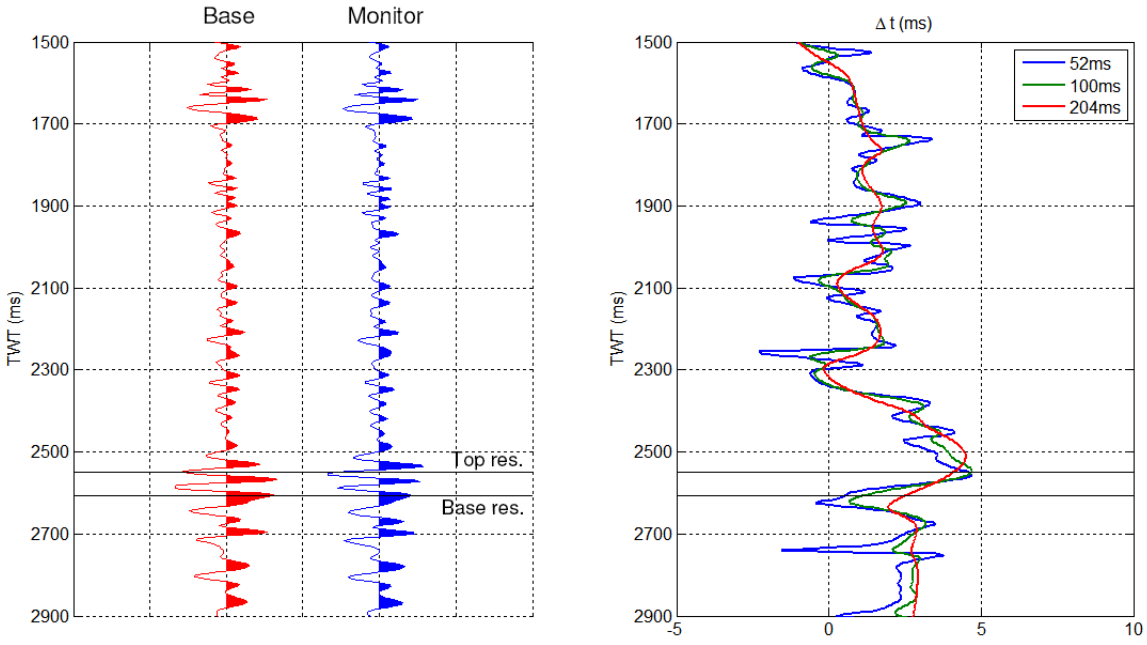

Figure 3.3: *Time shifts between two time-lapse traces measured in local windows at every sample. Three different size windows 13, 25, 51 samples (52, 100, 204ms) were used. Top and base reservoir are shown.*

time-lapse survey over a compacting reservoir. The time shift is estimated at every sample using three different sized local windows (tapered using a Hanning taper).

The time shifts show the general characteristics of the time shift signal through a compacting reservoir. Time shifts accumulate through the overburden, reaching a maximum at top reservoir. A reduction in travel time can clearly be seen through the reservoir zone. In the underburden time shifts start to accumulate again, before levelling off. Clearly, in the overburden the time shift estimates show more variability as the window length decreases. At top reservoir the breakpoint, where the time shifts start to decrease because of reservoir speed-up, is less well defined. As the window size increases the breakpoint appears earlier. In addition the base reservoir breakpoint is also not well defined for the same reason. This makes measuring the time strain ($\Delta t/t$) over the reservoir zone difficult and prone to error. I will explore these points further.

3.5.2 Problems with the cross-correlation approach

To demonstrate inherent problems with the windowed nature of cross-correlation methods I create a seismic trace by imbedding two large reflections (to simulate top and base reservoir) in an otherwise random reflectivity. I have create a second "time-lapse" trace by applying a time-variant time shift which follows our conceptual model of compaction-induced time shifts (Figure 3.4). Next, I try to recover these shifts using sliding window cross correlation. I have used window lengths of 52, 100 and 204ms and show the results with and without the application of a Hanning taper.

Several main points can be observed from this example:

- Tapering and increasing window length stabilizes the time shift estimation.
- Resolution decreases with increasing window size.
- Short windows tend to underestimate the actual time shift.

Resolution

One obvious consequence of windowed measurements is that the length of the window determines the ultimate resolution. For long window lengths rapid changes in the time shift gradient will be averaged within the window. For this reason the time shift at top and base reservoir is not measured correctly by the 204 or 100ms windows and the reduction in time shift over the reservoir zone is smeared. The 52ms does a better job of delineating the reservoir zone, but clearly underestimates the time shift in several places. This is result of window bias, which I will discuss later.

Tapering

One way to understand how tapering helps to stabilize the time shift estimate is to consider cross-correlation in the frequency domain, although the analysis is relevant regardless of whether the calculation is done in the time or frequency domains. If we let f and g be the seismic traces in the time domain then the cross-correlation is defined as $c = f \star g = f(-t) * g(t)$, where the star denotes the correlation and the

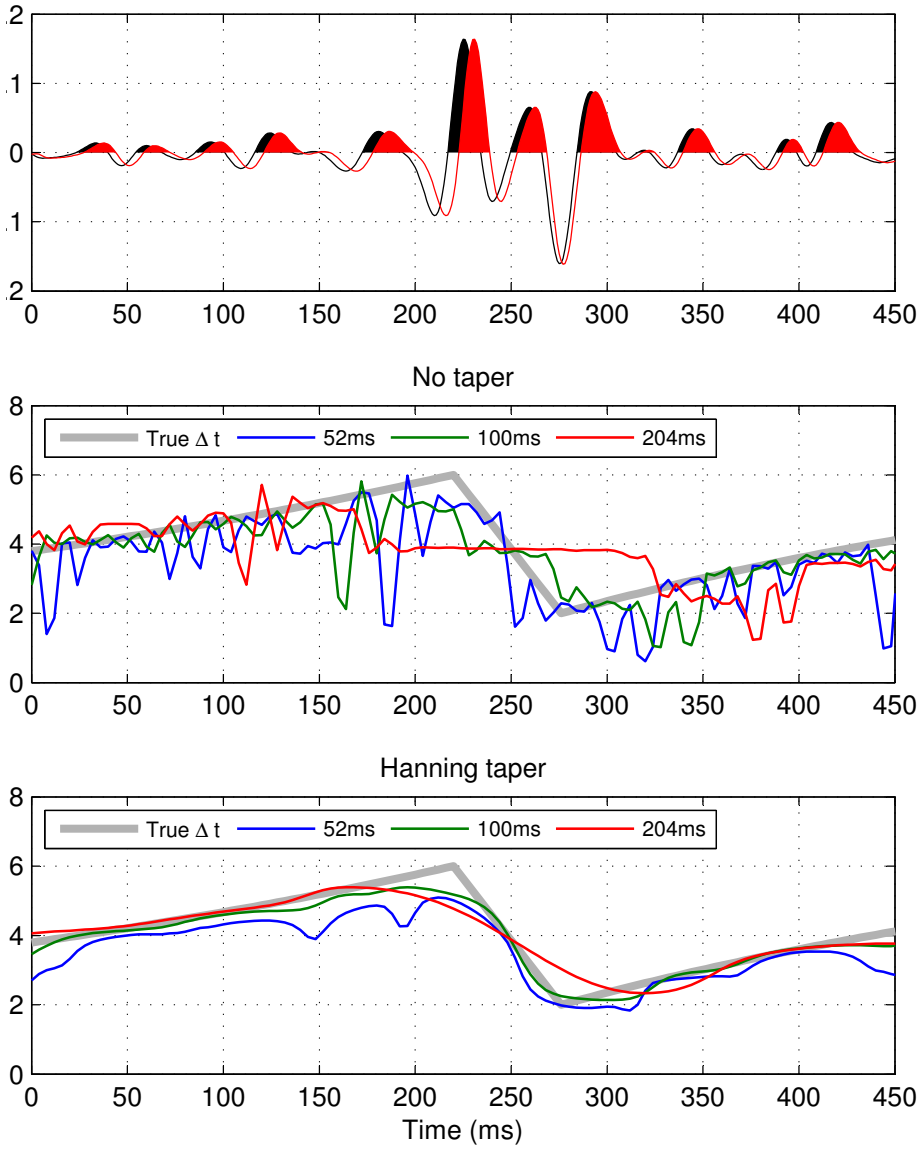

Figure 3.4: *Time shifts measured using various size windows to demonstrate some of the limitations with the cross-correlation technique.*

asterisk denotes convolution. The cross-correlation is the convolution of the time-reversed f with g. Using convolution theorem and the fact that time reversal is equivalent to complex conjugation in the frequency domain, the cross-correlation is defined as $C = F^* \cdot G$ in the frequency domain, where F^* is the complex conjugate of F. Therefore, the accuracy of the cross-correlation can be related to the accuracy of the spectra of our two locally windowed time-series.

Without applying a taper we are multiplying our seismic trace by a boxcar in order to take a local cross-correlation. A boxcar function suffers from considerable spectral leakage (Gubbins, 2004) meaning the energy in the spectrum is spread across a range of frequencies around the actual central frequency. Tapering reduces spectral leakage but effectively smooths the amplitude spectrum, reducing the resolution of individual frequencies. The positive side of this smoothing is that noise is attenuated. It also has the effect of equalizing end points of the data to zero, avoiding discontinuities in the convolution. These positive effects result in the more stable estimation shown in Figure 3.4(c).

Prediction bias in short tapered windows

An often overlooked aspect of using short tapered windows is the bias it produces in the cross-correlation. Imagine a reflection event situated at 2000ms (the base line seismic) and the same event shifted by +6ms so that it is situated at 2006ms (the monitor seismic). In a standard cross-correlation approach we would window and taper both the base and monitor seismic at 2000ms, the location of the original event. For large windows the whole event is captured in the window. However, for increasingly smaller windows the event is gradually shaped by the taper, which has its maximum 6ms earlier than the reflection event. The effect is to bias the cross-correlation and make the time shift appear smaller than it is. The exact amount of bias will be determined by the frequency content of the seismic data and the type of taper that is used to window the data.

To demonstrate this I create a baseline event situated at 0ms and a time-lapse event delayed by 6ms. In accordance with usual practice the cross-correlation window is centered at 0ms in both the base and monitor traces. Figure 3.5 shows a 25Hz Ricker wavelet centred at 6ms before and after tapering the data using a 52ms Hanning window. Both the boxcar and the Hanning taper are centred on 0ms. This example

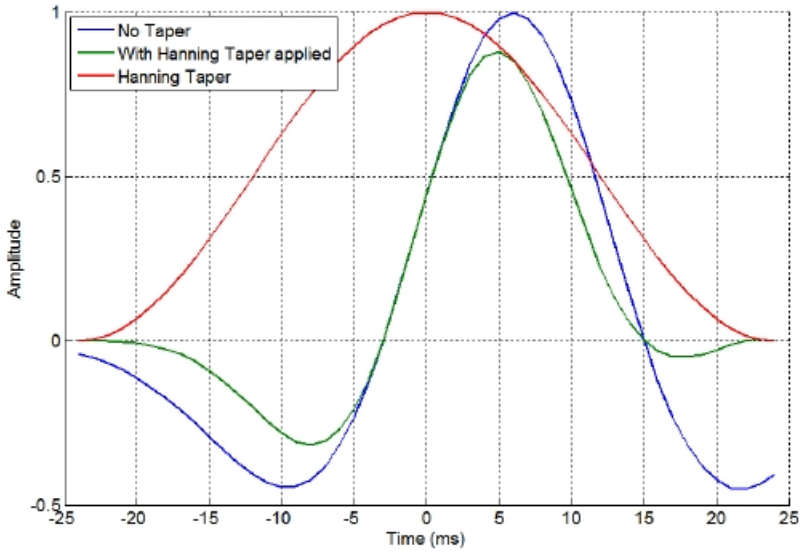

Figure 3.5: *A Ricker wavelet centered on 6ms before and after tapering with a Hanning taper centred on 0ms. The wavelet peak is biased towards 0ms after tapering because the centre of the taper is displaced in relation to the centre of the wavelet.*

clearly shows how the wavelet peak is biased towards 0ms after tapering because the centre of the taper is displaced in relation to the centre of the wavelet. If I cross-correlate the Hanning tapered monitor with baseline (also tapered using a Hanning window) then the calculated time shift is 5.17ms, nearly nearly 1ms less than the actual 6ms time shift.

The amount of bias will depend on the following factors,

- Frequency content (higher frequencies, less bias)
- Magnitude of the time shift (smaller time shift, less bias)
- Taper type
- Window size (longer windows, less bias)

To demonstrate the frequency dependency I repeat the above example using Ricker wavelets with several different central frequencies. Figure 3.6(a) is a plot of bias (defined as $\Delta t_{true} - \Delta t_{est}$) against the central frequency of the Ricker wavelet. As predicted, as the central frequency increases the bias is reduced. However, even at

30Hz the bias is still as high as 0.5ms, which could add significant uncertainty to the time shift estimation.

Figure 3.6(b) shows the impact of the taper length on the bias. In this example the central frequency of the Ricker wavelets was kept at 25Hz, but an increasingly large taper was used to window the data. As expected, as the length of the taper increases the bias is reduced, so that for windows of 200ms the bias is less than 0.1ms, which is well below the noise level for real data. However, as we saw in the earlier examples, in order to capture sharp changes in time shift we require small windows. In addition to the trade-off between noise and resolution, there is also the window-bias effect to consider.

The magnitude of the time shift is also an important factor. The bias increases with the magnitude of the time shift. This can be significant as time shifts as large as 12ms have been observed over some compacting reservoirs (e.g. Magesan et al., 2005). To demonstrate this I have time shifted a 25Hz Ricker wavelet by an increasing amount, from 0ms to 12ms. I then calculate the time shift by cross-correlation, first windowing and tapering the data with a 52ms Hanning window. Figure 3.6(c) shows the result. The bias increases with increasing time shift. One approach adopted by many processors is to use smaller windows then to smooth the result after. Ironically this means that the bias will be made even worse, since smoothing also tends degrade the magnitude of the true signal.

The type of taper also makes a difference. As noted by Gubbins (2004), a whole menagerie of tapers are used in signal processing, many without physical basis. Commonly used tapers are the Hanning, Cosine, Bartlett and Gaussian. Different windows have optimal properties depending on the application. To show the effect of window choice on the cross-correlation time shift estimate, I taper two 25Hz Ricker wavelets delayed by 6ms with a Hanning, Cosine and Bartlett tapers. The bias cause by the windows is 0.63ms, 0.51ms and 0.91ms respectively.

Conclusion

The standard method of measuring time shifts, using locally windowed cross-correlation, has many pitfalls. All the synthetic examples I have shown have been noise-free with no reflectivity changes between the base and monitor times, demonstrating that these problems are inherent to the local cross-correlation method.

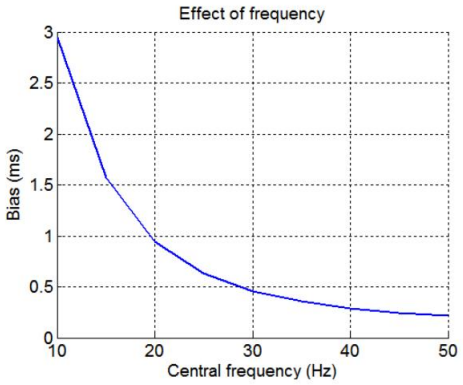

(a) The effect of the central frequency of the Ricker wavelet on the bias.

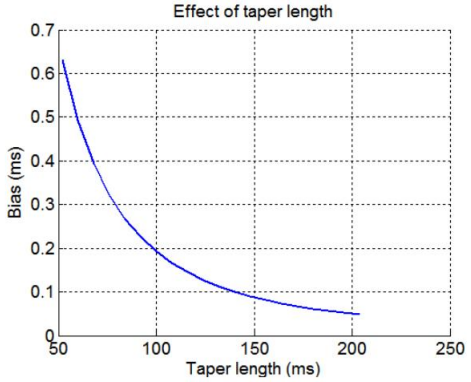

(b) The effect of the length of the Hanning taper on the bias.

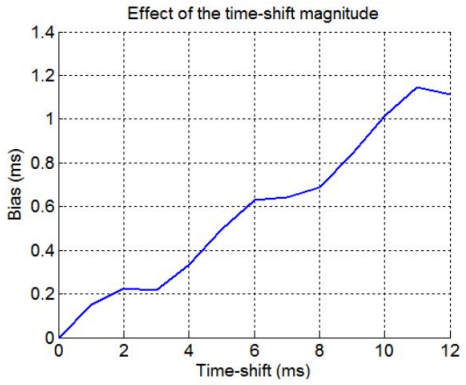

(c) The effect of the magnitude of the time shift on the bias. The time shift between two Ricker wavelets estimated using a 52ms Hanning tapered window for varying time shifts. The bias is the actual time shift minus the estimated time shift

Figure 3.6

At the heart of these problems is a trade-off between long windows, which are less sensitive to bias but lack the desired resolution, and short windows which provide resolution but are prone to biasing the result.

An additional factor is the effect of 4D noise. The exact nature of 4D noise is complex to understand but it is almost certainly not random (ref). For that reason I have not investigated the effect of noise. However, I can readily conclude conclude based on the published experience of the 4D community that short windows suffer much more from 4D noise than long windows (e.g. Tigrek and Hatchell, 2006; Staples et al., 2007; De Gennaro et al., 2008). The effect of window length and noise is also readily observed in the real data example shown in Figure 5.2.

The implication for time-lapse time shift estimation is that improvements or new methods are needed to address these limitations. However, where the time shift is slowly varying, long windows provide stable cross-correlation results as shown in Figures 3.3 and 3.4. For compacting reservoirs, where overburden velocity slowdown is observed, this implies that we can measure the slowly varying overburden time shift with considerable confidence. However, near or inside the reservoir zone time shift estimates measured by cross-correlation are often unreliable, depending on the time-thickness of the reservoir and frequency content of the seismic data.

3.6 Developments in time shift estimation

The recognition that time-lapse time shifts hold valuable information has led to a drive to develop improved methods of estimating them.

3.6.1 Fast local cross-correlation

The equation for a local cross-correlation between two windows of data a and b was defined earlier as:

$$c_j = \frac{1}{N+M-1} \sum_i a_i b_{i+j} \tag{3.6}$$

where j is called the *lag*, N and M are the lengths of a and b respectively and the sum is taken over all $N + M - 1$ possible products.

As noted by Rickett et al. (2006) the computational cost of calculating c_j for k samples in a seismic volume is $O(N_k \times N_l \times N_w)$, where N_k is the number of local correlations, N_l the number of lags and N_w the number of samples in the window. For 3-D datasets, which commonly contain tens of millions of samples it is easy to see that this is a very computationally expensive process. Recently two papers Rickett et al. (2006) and Hale (2007) have addressed the issue of reducing the computational cost of performing cross-correlations. Their approaches are different but both reduce the cost of computing local cross-correlations at every sample to $O(N_k \times N_l)$ by removing the dependence on the window length.

Speeding up the cross-correlation process alone is not an improvement to time shift estimation, since the inherent problems discussed in Section 3.5.2 remain. However, one thing faster execution times do make practical is the cross-correlation of 3D patches of data, instead of individual traces. The cross-correlation of a 3D patch of data in the time-direction is defined as:

$$c^{(3D)}_{j_x,j_y,j_z} = \sum_{p_x} \sum_{p_y} \sum_{p_z} a_{p_x,p_y,p_z} b_{p_x+j_x,p_y+j_y,p_z+j_z} \tag{3.7}$$

where j_x is the lag in the x direction, j_y the lag in the y direction and j_z the lag in the z direction. Note that this is not the same as warping, which finds the maximum cross-correlation in a 3D sense to estimate a 3D shift that aligns the data. Instead the maximum correlation in the vertical sense (i.e. time) is only found for a 3D patch of data. The method of fast cross-correlation proposed by Hale (2007) uses Gaussian tapers so that 3D 'blobs' of data are cross-correlated, whereas the method proposed by Rickett et al. (2006) uses a boxcar window (i.e. no taper) so that rectangular blocks of data are cross-correlated. As discussed earlier, tapering is necessary, meaning that the algorithm proposed by Hale (2007) is of more practical value for field data.

Cross-correlating 3D patches of data has the apparent effect of smoothing, but it is different to simply smoothing the time shifts calculated from trace-to-trace local cross-correlations. Instead the effect is to average the cross-correlation functions in the 3D patch *before* calculating the time shift by calculation of the maximum cross-correlation.

3.6.2 Inversion-based methods

A different approach to finding the time shift is to use an inversion approach. In this approach an inversion problem is set up to find a time shift that, once applied, minimizes the misfit between two seismic volumes.

The least-squares objective function that describes this problem is:

$$E = |\mathbf{d} - f(\mathbf{m})|^2 \tag{3.8}$$

where the data vector $\mathbf{d}$ contains the baseline seismic data volume, $x_1(x, y, t)$, the model vector $\mathbf{m}$ contains the time shift volume, $\tau(x, y, t)$, and the function $f(\mathbf{m})$ applies these shifts to the monitor survey to give $x_2(x, y, t + \tau(x, y, t))$. As the time shifts are themselves a function of time the inversion is a non-linear problem.

The function f that applies time shifts to the seismic survey is typically an interpolation algorithm. Applying a time shift to a seismic trace involves first shifting the amplitudes by the time shift then, reconstructing the trace at the regular sampling interval. This reconstruction is usually by numerical interpolation such as cubic spline interpolation or sinc interpolation.

There are various options for solving nonlinear least-squares problems. Rickett et al. (2007a) chose the Gauss-Newton method which, proves to be efficient for small time shifts. Gauss-Newton works by linearizing the nonlinear operator around the current model, solving the resulting linear problem, updating the model, and iterating (see Aster et al., 2005, for example).

Additional constraints can be put into the objective function in order to regularize the inverse problem and give the solution some desired characteristics. A common form of regularization is to minimize the first or second gradient of a solution. Rickett et al. (2007a) choose to minimize the second derivative of the time shift estimate, in order that the first derivative be stable. I will address the reasons for this later in this chapter. Adding in this regularisation, our objective function becomes:

$$E = |\mathbf{d} - f(\mathbf{m})|^2 + \alpha^2 |\nabla_t^2 \mathbf{m}| \tag{3.9}$$

where α^2 controls the relative importance of the smoothness in the inverse solution. A more detailed derivation of the inversion method can be found in Appendix A.

To demonstrate how the inversion presented can offer potential improvements compared to local cross-correlations I use the same synthetic example presented earlier in Figure 3.4. I recover the time shifts using the inversion scheme presented above. The result shown in Figure 3.7 is a clear improvement on the local cross-correlation approach.

3.7 Time shifts and time strains

So far, I have described approaches to estimate time shift. In addition to time shifts, time strains, the vertical derivatives of time shifts are of great interest. Time shifts accumulate along the seismic ray path. For a vertical ray path the time shift at a particular point is the sum of travel time differences due to all the layers above. To assess what is happening at a particular point in the subsurface, we need to differentiate this integrated measurement to give the fractional change in travel time at that location. For example, consider two reflection events, A and B, with travel times t_A and t_B on the base trace and have times $t_A + \tau(t_A)$ and $t_B + \tau(t_B)$ on the monitor trace. The fractional change in travel time between these two events on the two surveys is given by:

$$\frac{\Delta t_{AB}}{t_{AB}} = \frac{\tau(t_B) - \tau(t_A)}{t_B - t_A} \tag{3.10}$$

in the limit that the distance between A and B becomes very small, then the right side of Equation 3.10 becomes a differential:

$$\frac{\Delta t}{t} = \frac{\partial \tau}{\partial t} \tag{3.11}$$

Equation 3.11 indicates that by taking the vertical derivative of the time shift volume, we can produce a volume that describes the fractional change in travel time. I showed in Chapter 2 that this fractional change in travel time can be decomposed into a vertical strain component and a fractional change in velocity:

$$\frac{\Delta t}{t} \approx \frac{\Delta z}{z} - \frac{\Delta v}{v} \tag{3.12}$$

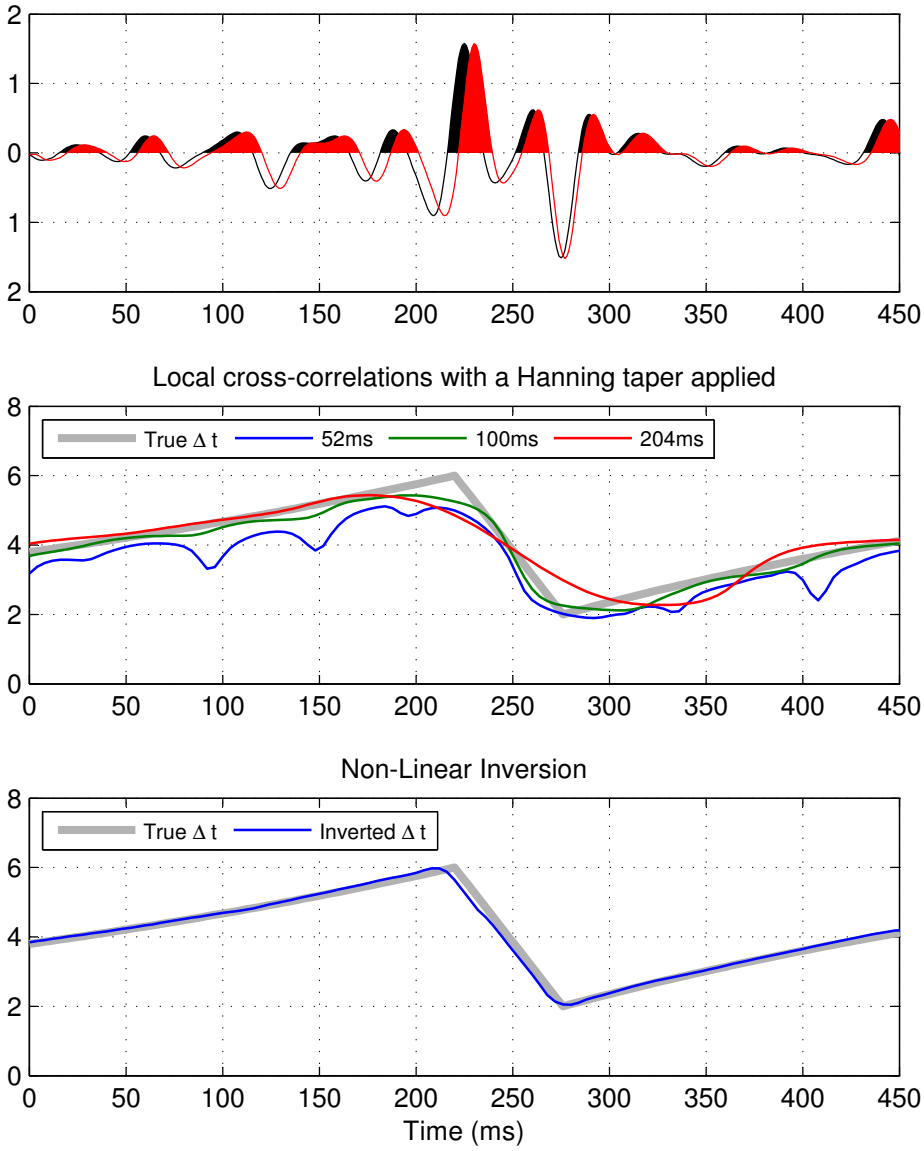

Figure 3.7: *Time shifts estimated using an inversion approach compared with those estimated by local cross-correlations*

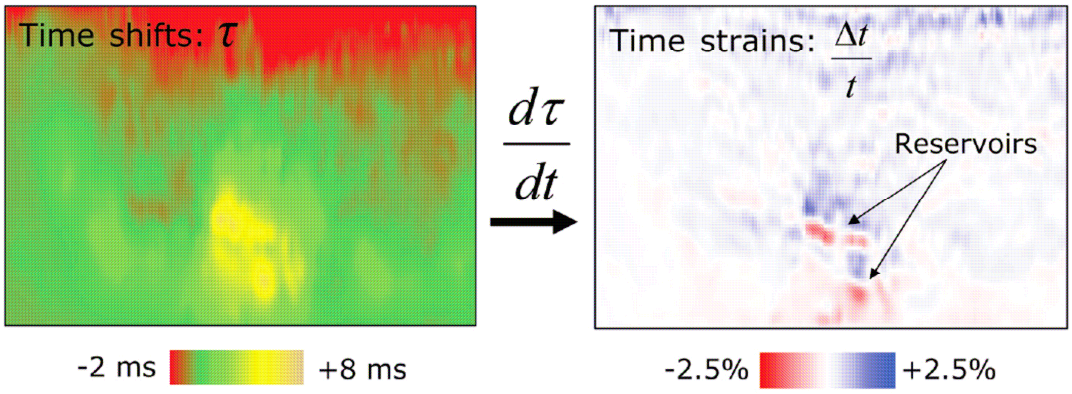

Figure 3.8: *(a) Time shifts calculated at a cross-line through the Genesis reservoir, (b) time strains. Note how the time strain is instantly more interpretable. A clear distinction can be made between velocity slow-down in the overburden (blue) and the speed-up in the reservoir (red). From Rickett et al. (2007b).*

In an analogy with physical strain, the fraction change in travel time may be called *time strain*. The derivative of the time-lapse time shifts is essentially a layer-stripping process that converts the averaged time shift measurement into the interval time strain. By converting the time shift into an interval property, it can be interpreted more directly than accumulated time shifts. Figure 6.4 shows the interpretive potential of time strains. Time shifts at the Genesis Field, a compacting turbidite reservoir in the Gulf of Mexico, are shown on the left and the time strains on the right. The time strains are instantly more interpretable. A distinction can be made between the stretching and accompanying velocity slow-down in overburden (blue) and compaction and velocity increase in the reservoir (red). In addition to the improved interpretation value, time strains have attractive physical properties. I will show in the next chapter how time strain (but not time shifts) can be linearly related to reservoir pressure changes. Unfortunately, taking the derivative of the time shift volume tends to boost noise. As a consequence time strain estimates are generally noisier and less robust than time shift estimates.

In the paper *4D time strain and the seismic signature of geomechanical compaction at Genesis* Rickett et al. (2007a) show that the inversion approach to time shift estimation can yield superior estimates to time strain compared to local cross-correlation methods. This is because, in the inversion approach, the stability of

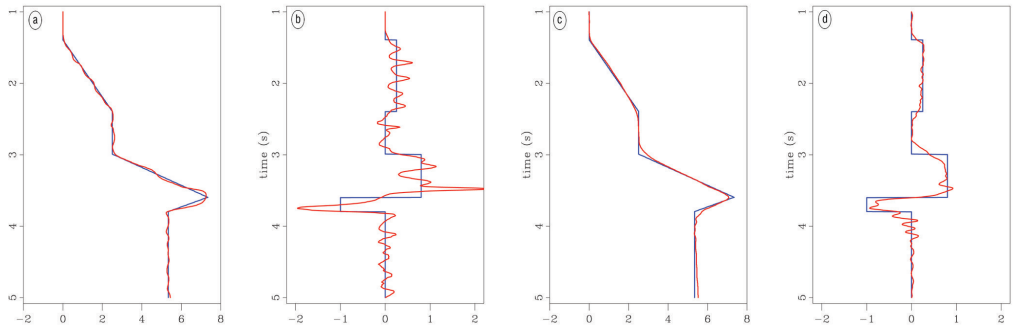

Figure 3.9: *Synthetic test of time shift estimation algorithms. A 1D synthetic data set was created with time shifts given by the blue curves in (a) and (c), and time strains given by the blue curves in (b) and (d). The red curves show the recovered functions with the cross-correlation technique, panels (a) and (b), and the nonlinear inversion, panels (c) and (d). After Rickett et al. (2007a)*

the time shift derivative can be built-in to the objective function, ensuring that the time shift estimate also gives a stable time strain.

The examples given in Rickett et al. (2007a) are shown in Figure 3.9. Indeed, the time strain estimates generated by inversion are far superior to those generated by local cross-correlations. However, the time shift examples in Figure 3.9 are not very representative of a true compaction-induced time-lapse time shifts. The time shifts between zones all change monotonically and the smallest zone has a thickness of ∼200ms two-way-time. At the beginning of this chapter I showed time shifts generated from a geomechanical model, albeit a very simple one. That model showed a 30ms-thick reservoir. The time shift accumulates smoothly through the reservoir before reducing sharply in the reservoir zone and then continuing smoothly in the overburden. This simple model, even though idealized, is more similar to observations from field data. This reservoir time-thickness is more representative of Genesis, where the stacked turbidite reservoirs are at most ∼50ms thick and also Valhall, where the compacting zone is approximately 30ms thick.

Therefore, I conduct a similar comparison of local cross-correlation versus inversion using the time shifts from the model presented at the beginning of the chapter. The difference from the earlier time shift estimation examples is that we are now interested in the ability to recover time strain in addition to time shifts.

To conduct this experiment I create a base seismic trace by convolving a random reflectivity with a Ricker wavelet which has a central frequency of 25Hz. I then

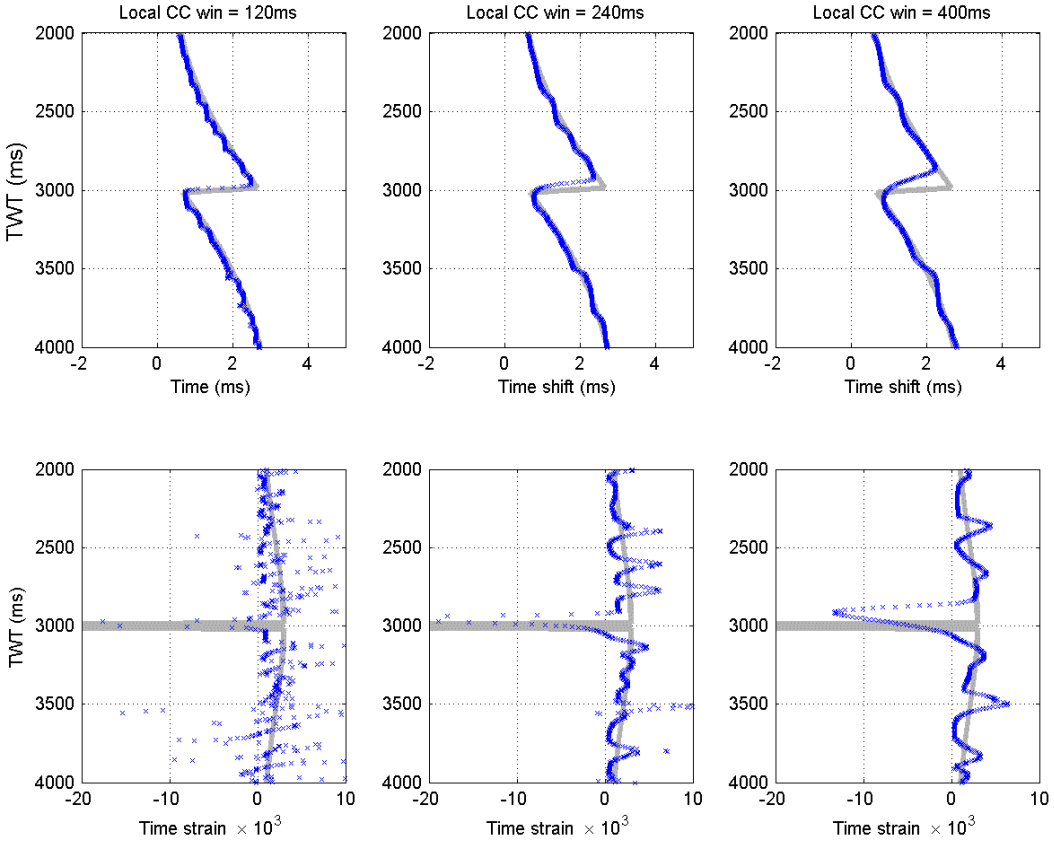

Figure 3.10: *Synthetic test of time shift estimation algorithms. A 1D synthetic data set was created with time shifts and time strains given by the grey curves. The blue crosses show the recovered functions using the cross-correlation technique using a cosine tapered window with lengths of 120ms, 240ms and 400ms.*

create the monitor trace by applying the time shifts through the centre of a depleting disk-shaped reservoir, which I generated earlier in the chapter.

The time shifts were estimated using local cross-correlations with three different window lengths (120ms, 240ms and 400ms) all with Hanning tapers applied, and with the inversion scheme. For the inversion scheme the α value, which in the objective function weights the importance given to the minimization of the second derivative, is set to 10, 100 and 1000. The time strain is calculated using the numerical derivative i.e. $(\tau_{i+1} - \tau_i)/s$, where τ is the time shift at sample i and s is the sampling rate of the seismic data, which in this case is 4ms. Figures 3.10 and 3.11 show the result of the test.

Clearly, as was originally found by Rickett et al. (2007a), the time strains produced by the inversion technique are far superior to the local cross-correlation technique, even

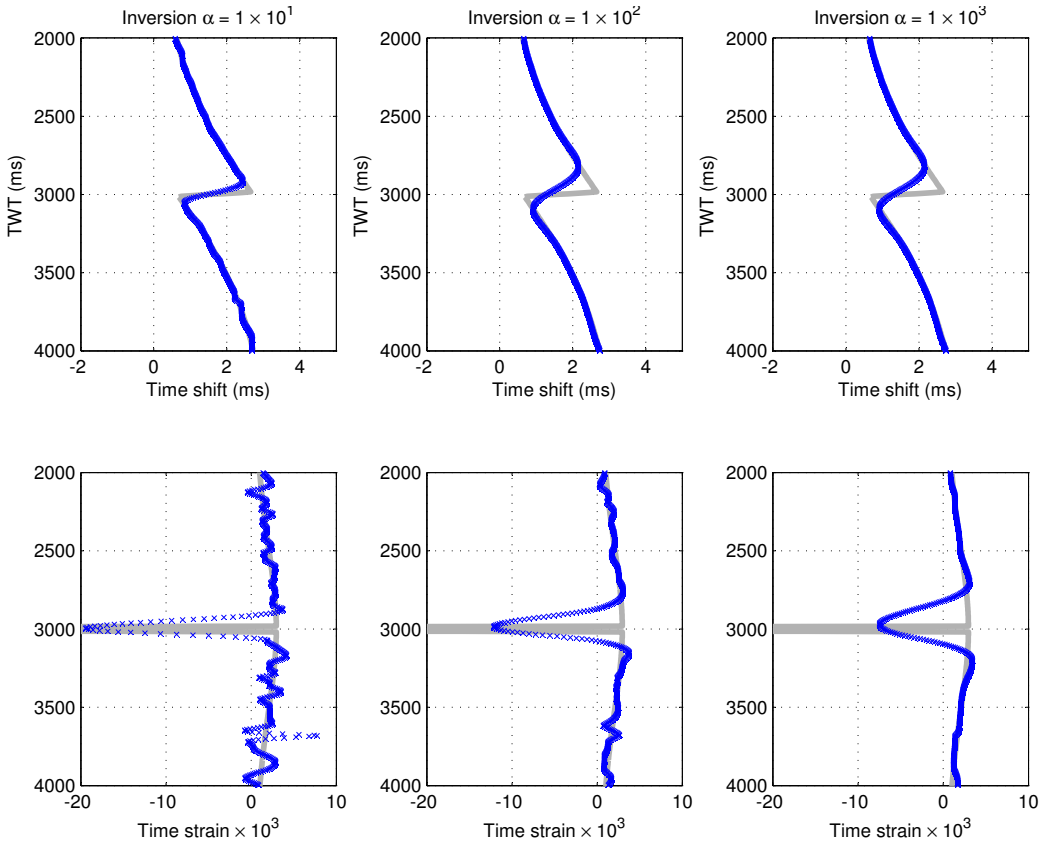

Figure 3.11: *Synthetic test of time shift estimation algorithms. A 1D synthetic data set was created with time shifts and time strains given by the grey curves. The blue crosses show the recovered functions using the inversion technique with α values (weighting the importance of the second derivative in the objective function) set at 1, 100 and 1000.*

for the lowest α value. In this geomechanically-based example however we are made aware that the inversion approach does have some of the limitations of the cross-correlation technique. I find a similar trade-off between the stability and resolution of the time shifts and time strains. Clearly if we strongly weight the importance of the second derivative in the objective function then we achieve more accurate time shifts and time strains away from the reservoir, at the expense of resolution inside the reservoir zone. This is a result of the underlying assumption in the inversion that the time strain is slowly varying, which in reality is not the case.

3.8 Summary

This chapter has investigated the time shift signature around a compacting reservoir. I have taken a very simple example of a compacting disk in a homogeneous half-space and used simple strain-velocity transforms to give the time shift for a seismic trace through the centre of the reservoir.

In the first section of this chapter I focused on how different models of velocity change inside the reservoir can dramatically change our predictions of time shifts at reservoir level and in the underburden, because of the cumulative nature of time shifts. In general, a large amount of uncertainty remains when calculating the velocity change inside the reservoir because of the many complex contributing factors. In the overburden, however, for zero offset traces, a simple linear relationship between velocity change and strain has proved effective when matching modelled time shifts from geomechanical models to several field examples. In this thesis I will suggest ways of using the overburden time shift signature to infer changes in the reservoir zone. By using the overburden signal we avoid the complexities involved in separating all the components contributing to the reservoir level signature.

Next, I investigated how accurately time shifts can be estimated. Despite the ever-increasing quality of time-lapse seismic data there remain some inherent problems with the standard methods used to estimate time shifts, which means even with noise-free synthetic data our ability to accurately recover time shift estimates is limited. I investigated the method of local cross-correlations and found that there is a trade-off between long windows, which are less sensitive to bias but lack the desired resolution, and short windows which provide resolution but are prone to bias the result. I also

found that tapering the local window is necessary, but that the taper chosen can also influence the result. I concluded that these problems were significant where time shifts vary slowly, such as in the overburden. Again the using the overburden time shifts we avoid the complexities in and around the reservoir zone.

I also introduced the concept of time strain, which will be important feature in the next chapters of this thesis. Time strains are the derivative of time shifts and convert time shifts into an interval property, which can be interpreted more directly than accumulated time shifts. Unfortunately, taking the derivative of the time shift volume tends to boost noise. As a consequence, time strain estimates are generally noisier and less robust than time shift estimates.

An inversion-based time shift estimation scheme first presented by Rickett et al. (2007a) offers an alternative route to the calculation of time-shifts. This method maximizes the smoothness of the time strain function as part of the objective function and as a result produces more stable estimates of time strain. However, I was critical of the examples presented in Rickett et al. (2007a) because they were not based on realistic geomechanical modelling. I repeated the experiment based on a simple geomechanical model of a thin compacting reservoir. I found that in general the inversion method was indeed superior to the local cross-correlation method. However, there is a also a trade-off with this method: We again sacrifice resolution in the reservoir zone for stability outside of it.

I have shown that when the reservoir zone of is included in our analysis we introduce several complexities. Firstly, the velocity change is hard to characterize because of the complex processes inside the reservoir. Secondly, all our current time shift estimation methods struggle to correctly estimate the time shift around the reservoir zone.

I stress that the pursuit of understanding the reservoir level signature is an important goal. However, studying the reservoir changes in terms of time shifts through the reservoir alone is not sufficient. To characterize the sharp changes around the reservoir zone alternative methods are required such as those being investigated by Corzo and MacBeth (2006) where geomechanical and reservoir engineering information is integrated into the reservoir level interpretation. With the tools available at present the overburden offers one alternative way to characterize changes inside the reservoir, without the complication of the reservoir-level signal. The rest

of this thesis will develop this idea further.

CHAPTER

FOUR

Inverting for reservoir strain using time-lapse time shifts and time strains

In previous chapters I have shown how time-lapse time shifts are observed throughout the 4D seismic volume around compacting reservoirs. I have also suggested that these time shifts can be transformed to 3D estimates of vertical strain, under appropriate assumptions. In this chapter I will establish a linear relationship between time shifts in the overburden and reservoir strain, using simple geomechanical models. This linear relationship forms the basis for a linear inversion to estimate reservoir strain directly from 4D seismic measurements.

4.1 Introduction

In the first two chapters we have seen how reservoir depletion of certain reservoirs can lead to reservoir compaction and can cause significant time-lapse changes in the rocks surrounding the reservoir. While these non-reservoir 4D seismic changes can potentially obscure or contribute to the reservoir-level signal, making the 4D interpretation uncertain, if used appropriately they may also provide information on the actual reservoir pressure changes. In this chapter I will formulate a linear inversion for reservoir pressure change using these non-reservoir changes.

My starting point is the linear relationship between fractional change in time-lapse time shift, which I will term *time strain*, and physical strain in the earth, which was proposed by Hatchell and Bourne (2005a) and was derived in the previous chapter.

$$\frac{\Delta t}{t} \approx (1+R)\varepsilon_{zz} \tag{4.1}$$

This equation shows that if we can estimate the value of R and vertical strain ε_{zz} then we can directly estimate time-lapse time strains. It also shows that we can do the inverse and estimate vertical strain from time-lapse time strains. As seen in the previous chapter, the earth around the reservoir strains as a direct result of reservoir pressure changes. In this chapter I will show that we can rewrite vertical strains as a linear function of the reservoir pressure changes that caused them, allowing us to perform a linear inversion for reservoir pressure directly from 4D seismic data. Note the distinction between time shift and time strain. Time strain and vertical strain are instantaneous properties, whereas the time shift is a cumulative property. To recast Equation 4.1 in terms of time shift we need to integrate the time strain between the surface and a depth of interest z.

$$\Delta t(z) \approx 2(1+R)\int_0^d \frac{\varepsilon_{zz}(z)}{V_o(z)}dz + t_0 \tag{4.2}$$

where t_0 is a static time shift, such as that created by sea floor surface subsidence. The relationship between depth and time is defined by the initial velocity function $V_0(z)$ (i.e. the velocity before any strain-induced velocity changes caused by reservoir production).

On first inspection it is easy to see that working with the instantaneous properties of vertical strain and time strain greatly simplifies the problem and is a more natural choice over the cumulative properties of time shifts. However, there may be cases where it is preferable to work with time shifts rather than time strains, for example when time strains are difficult to measure. In this case we need to evaluate the integral in Equation 5.2 which means we are only able to preserve a linear relationship between the time shift and strain when the initial velocity function $V(z)$ can be assumed to be constant. Regardless of whether we use time shifts or time strains, in both cases we wish to relate the induced strain in the overburden directly to reservoir pressure.

The formulation of an inversion for reservoir pressure from overburden changes can be split into two components. One component is the identification of a suitable forward operator that can describe observed strain as a linear function of reservoir pressure, which will be investigated in this chapter. The second component is the estimation of 4D seismic time shifts and time strains, which form the input data to our inversion, as discussed in the previous chapter of this thesis.

Relating reservoir pressure changes to observed strains is a geomechanical problem. Geomechanical approaches that tackle this problem can be split into three categories; analytical, semi-analytical and numerical.

Analytical: Estimating strain due to reservoir pressure changes using analytical methods quickly becomes a complex problem for anything other than very simple geometries and material properties. Analytical solutions are only feasible in homogeneous linear-poroelastic (HLP) whole or halfspaces for reservoirs which simple geometries. A commonly used analytical solution is a uniformly disk-shaped reservoir situated in a HLP halfspace, commonly known as the Geertsma model (Geertsma, 1966). This model was later recovered as a special case by Segall (1992), who provides an analytical solution for axisymmetric depletion patterns and reservoir shapes (such as a dome structure) in a HLP halfspace. While these models are useful for insights into the stress, stain and displacement around reservoirs (Fjær et al., 2008) they rarely represent real reservoir geometries or depletion scenarios.

Semi-analytical: The analytical solutions described above use the nucleus of strain approach. Deformation due to a point source (a nucleus of strain) is described

analytically and then integrated over the area of the reservoir. Deriving the expression for a point-source deformation and performing an analytical integration of this over a volume is only tractable for simple media and reservoir shapes. If we wish to include arbitrary reservoir shapes or more complex material properties, such as a layered media, then these solutions quickly become too complex to be solved analytically. Semi-analytical models are models that are rooted in the analytical approach. They aim to maintain as much simplicity as possible, but employ numerical methods where necessary.

Numerical: For complex problems with arbitrary material properties and complex geometries the problem can only be solved using fully numerical methods. The standard method to solve complex deformation problems is the finite element method (e.g. Smith and Griffiths (2004)). The finite element method is a powerful tool. However, there is a cost associated with the increased complexity. Models are time-consuming to build and computationally expensive to run. Also, while finite element modeling may correctly capture some degree of the earths heterogeneity, the misparameterisation of such models can give misleading results. As we discussed in Chapter 2, the parametrisation of geomechanical properties is a difficult problem because of the sparse nature of hard data measurements.

My approach will take the semi-analytical route. This route provides a compromise between the inflexibility of analytical solutions and the complexity, uncertainty and time-consuming nature of numerical modeling. In many cases semi-analytical solutions can give a good approximation of the fully numerical solution, capturing the essential phenomena but not the fine detail of the problem, with the advantage of requiring minimal parametrization and being computationally fast. The philosophy I adopt is to start simply and only add complexity if we find that our simplifying assumptions break down.

In the next section I use the governing equations for deformation in a poroelastic media as a framework to obtain a semi-analytical linear relationship between reservoir pressure change and vertical strain.

4.2 Deformation in a poroelastic medium

4.2.1 Governing equations

Biot (1941) derived constitutive equations for a linear-poroelastic material which relate solid stress σ_{ij}, solid strain ε_{ij}, changes in fluid mass Δm and fluid pressure p in a porous medium:

$$\sigma_{ij} = 2\mu\varepsilon_{ij} + \frac{2\mu\nu}{1-2\nu}\varepsilon_{kk}\delta_{ij} - \alpha p\delta_{ij} \tag{4.3a}$$

$$\Delta m = m - m_0 = \frac{\alpha(1-2\nu)\rho_0}{2\mu(1+\nu)}\left[\sigma_{kk} + \frac{3}{B}p\right] \tag{4.3b}$$

In addition to the standard elastic parameters, Poisson's ratio ν and shear modulus μ, for a solid linear elastic medium, there are two additional parameters that describe the fluid interaction with the rock: Biot's coefficient α and Skempton's coefficient B.

Biot's coefficient can be thought of as the load taken by the rock grains. Imagine all pore space is filled with fluid and that all the solid phase consists of material elements which respond isotropically with the same bulk modulus K_g. If we simultaneously apply a pore pressure $p = p_0$ and external stresses amounting to compression by p_0 on all faces, then the result is a local stress state of $-p_0\delta_{ij}$ on each point of the solid phase. The induced local stresses will cause the solid phase to strain by an amount $-p_0\delta_{ij}/3K_g$. Using this concept the definition of Biot's coefficient can be derived (Biot and Willis, 1957; Nur and Byerlee, 1971):

$$\alpha = 1 - \frac{K}{K_g} \tag{4.4}$$

where K is the bulk modulus of the rock mass under *drained conditions* i.e. fluid is allowed to flow in and out of a martial element in a manner that maintains pore pressure. Biot's coefficient varies between 0 and 1.

Skempton's pore pressure coefficient relates the pore-pressure to induced mean stress under *undrained conditions*, i.e. the fluid is constrained from flowing in or out of the material element during deformation. Its value lies between zero and one and is a

measure of how the applied stress is distributed between the skeletal framework and the fluid. It will tend toward one for saturated soils because the fluid will support the load and tend toward zero for gas-filled pores because the pore framework will take the load.

$$p = -\frac{B\sigma_{kk}}{3} \tag{4.5}$$

Rice and Cleary (1976) formulate equations 4.3a and 4.3b with emphasis on the two limiting behaviours described above, drained and undrained. They introduce the undrained elastic constants, ν_u, λ_u and K_u. The undrained Poisson's ratio ν_u has the standard definition of Poisson's ratio, but is measured under undrained conditions (i.e. $\delta m = 0$ in equation 4.3b). As the shear modulus μ is unaffected by the fluid pore fill then λ_u and K_u can be calculated using the standard relationships by inserting ν_u.

Using these constitutive relationships we can derive the equations that give the displacements induced in a poroelastic medium by a change in pore-fluid mass (reservoir depletion or inflation). Assuming the material can be treated as continuum and neglecting inertial forces, then conservation of linear momentum leads to the equilibrium equation:

$$\frac{\partial \sigma_{ij}}{\partial x_j} - b_i = 0 \tag{4.6}$$

where b_i are external body forces (e.g. gravity). Strain ε_{ij} and displacement u_i are related by

$$\varepsilon_{ij} = \frac{1}{2}\left(\frac{\partial u_i}{\partial x_j} + \frac{\partial u_j}{\partial x_j}\right) \tag{4.7}$$

The equilibrium equation (Equation 4.6) can be rewritten in terms of stress and strain by using the strain and displacement relation (Equation. 4.7) together with the constitutive equations (Equation. 4.3a) to give the governing equation:

$$\frac{\partial}{\partial x_j}\left[\mu\left(\frac{\partial u_i}{\partial x_j} + \frac{\partial u_j}{\partial x_i}\right)\right] + \frac{\partial}{\partial x_j}\left[\lambda_u \frac{\partial u_k}{\partial x_k}\right]\delta_{ij} = \alpha\frac{\partial p}{\partial x_i} + b_i \tag{4.8}$$

Solving the forward problem involves finding the pore-pressure distribution on the righthand side of Equation 4.8. This can be obtained by combining Darcy's law with the conservation of fluid mass. For an isotropic material, ignoring body forces acting on the fluid, Darcy's law states:

$$q_i = -\frac{\rho_0 \kappa}{\eta} \frac{\partial p}{\partial x_i} \tag{4.9}$$

where q_i is the fluid mass flux, κ permeability, ρ_0 fluid density and η fluid viscosity. Conservation of fluid mass requires

$$\frac{\partial q_i}{\partial x_i} + \frac{\partial m}{\partial t} = 0 \tag{4.10}$$

Combining equations Equation 4.9 and Equation 4.10 yields the diffusion equation:

$$c(\mathbf{x})\nabla^2 m = \frac{\partial m}{\partial t} \tag{4.11}$$

where $c(\mathbf{x})$ is the hydraulic diffusivity which is a spatially variable function of porosity, permeability, fluid compressibility and fluid viscosity.

Coupled fluid flow and deformation

The preceding equations clearly show that changes in fluid mass and displacements are coupled in a linear poroelastic medium. Generally, in reservoir engineering, the flow equation (Equation 4.11) is solved independently of the stress equations, which makes the problem theoretically simpler, less computationally expensive and in most cases where stress changes in the reservoir are small, is a good approximation. Pseudo-coupling is often used to account for reservoir compaction . The overburden stress σ_{ob} is assumed to be constant and is used to calculate the reservoir effective stress which is defined as $\sigma_{eff} = \sigma_{ob} - \alpha P_{pore}$, where P_{pore} is the pore pressure. Porosity is then assumed to be some function of effective stress, which may be theoretical or based on laboratory tests, and is recalculated as the effective stress in the reservoir changes.

This approach is incorrect in strongly compacting reservoirs. The coupled poroelastic equations show that we expect overburden stress to change as the reservoir compacts

and, therefore, the assumption of constant overburden stress used in pseudo-coupling is invalid. This can lead to incorrect estimates of effective stress and reservoir compaction. Figure 4.1 compares the compaction predicted using the pseudo-coupling with a fully-coupled approach, for an idealized North Sea reservoir (Sen and Settari, 2005). Compaction is predicted by pseudo-coupled modeling and the fully coupled modeling under two depletion scenarios: depletion for 25 years and partial depletion for 15 years followed by repressurization by water flood. Ignoring the coupling leads to significant errors in the predictions.

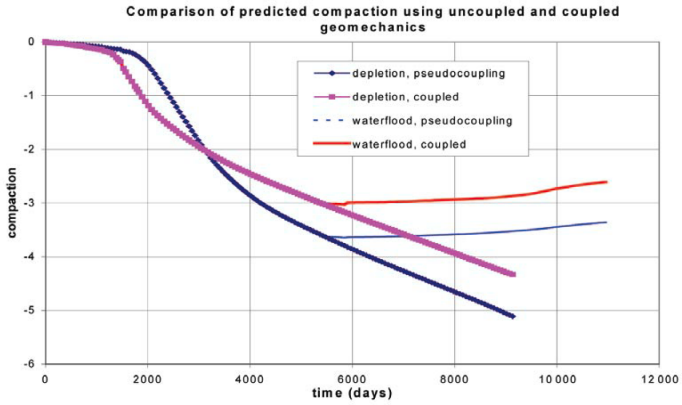

Figure 4.1: *Compaction predicted by uncoupled versus coupled modeling. After Sen and Settari (2005).*

A linear model for deformation

The problem of predicting deformations due to reservoir pressure changes and it's inverse can be cast as linear if we treat it as quasi-static, i.e. we can assume a steady state has been achieved. If the pressure source term is no longer taken to have a time dependency then it appears on the righthand side only. Since it does not multiply the displacement field both the forward and inverse problems are linear. As noted by Vasco et al. (2000), with the exception of the righthand side Equation 4.8 is identical to the equation governing static displacements in an elastic medium (Aki and Richards, 2002). This linearity means that given a pressure change distribution we can calculate the resultant displacements or given overburden strains we can invert for reservoir pressure changes.

Pressure or volume changes?

In the above approach the equations are set out in terms of pressure sources but can equally be recast to be in terms of volume changes. Whatever the choice, it is important to recognise that they are mathematically equivalent because in a linear-elastic system pressure and volume change are linearly related. The choice does not effect the nature of the solution to equation 4.8. If we define the source term (the right-hand side of Equation 4.8) as $f_i(\boldsymbol{x})$ then the source can be written as a function of pressure:

$$f_i(\boldsymbol{x}) = -\frac{\partial}{\partial x_j}\left[\alpha \Delta p\right]\delta_{ij} - b_i(\boldsymbol{x}) \tag{4.12}$$

or in terms of volume change:

$$f_i(\boldsymbol{x}) = -\frac{\partial}{\partial x_j}\left[B \Delta v\right]\delta_{ij} - b_i(\boldsymbol{x}) \tag{4.13}$$

where volume change is derived from the change in fluid mass, $\Delta v = K_u \Delta m/\rho_0$. K_u is the undrained bulk modulus and ρ_0 is the initial density. The important thing to realize is that under a linear elastic system swapping between strain and pressure is only a matter of scaling. In reality, however, the relationship between strain and pore pressure is most likely non-linear.

4.2.2 A Green's function solution

Segall (1992) shows that the displacement in a poroelastic medium can be generated by a distribution of centres of dilatation with a magnitude proportional to $\alpha \Delta p(\zeta, t)$. This provides a solution to the governing equations of linear poroelasticity (Equation 4.8). The ith component of the displacement tensor u_i at an observation point $\boldsymbol{x}$ in the subsurface, given by a center of dilatation located at $\boldsymbol{\zeta}$ is given by:

$$u_i(\boldsymbol{x}, t) = \frac{\alpha}{\mu}\int_v \Delta p(\zeta, t) g_i(\boldsymbol{x}, \boldsymbol{\zeta}) dV_{\boldsymbol{\zeta}} \tag{4.14}$$

Following this approach the problem becomes one of finding a suitable displacement Green's function, $g_i(\boldsymbol{x}, \boldsymbol{\zeta})$. Given a displacement Green's function the strain Green's functions are found by taking the appropriate derivatives:

$$\varepsilon_{ij} = \frac{1}{2}\left(\frac{\partial u_i}{\partial x_j} + \frac{\partial u_j}{\partial x_j}\right) \tag{4.15}$$

where the subscripts i and j can be the numbers 1, 2, 3, representing the x-, y- and z-axis respectively. The stress tensor is easily calculated by combining elements of the strain tensor and the elastic properties of the material. Assuming undrained conditions (i.e. no pore pressure change in the material surrounding the nucleus) the stress tensor is related to strain by:

$$\sigma_{ij} = 2\mu\varepsilon_{ij} + \frac{2\mu\upsilon}{1-2\upsilon}\varepsilon_{kk}\delta_{ij} \tag{4.16}$$

The displacement Green's function in Equation 4.14 could be calculated in various ways. As discussed at the beginning of this chapter, there is a trade-off between the advantages of simple solutions, such as the nucleus of strain method for a homogeneous elastic whole-space (Fjær et al., 1992) or halfspace (Geertsma, 1966), which are easy to implement, computationally fast and require little parametrisation, and the complexity of more sophisticated numerical techniques, such as finite element methods, which require a greater number of parameters and are computationally expensive. In keeping with the philosophy outlined in the introduction to this chapter I explore the simplest solution that is representative the problem, the superposition of point sources in a homogeneous linear poroelastic halfspace.

4.2.3 Nucleus of strain in a linear poroelastic homogeneous halfspace

A general solution to this problem was first presented independently by Mindlin and Cheng (1950) and Sen (1943) within the framework of thermoelasticity and adapted to poroelasticity by Geertsma (1966), who provides an analytical Green's function for a nucleus of strain in a homogeneous linear poroelastic halfspace. The general expression for displacement at the radial distance r and depth z due to an

infinitesimal nucleus of strain located at $(0, 0, c)$ is given by:

$$\overrightarrow{u_l^*} = \frac{C_m \Delta p}{4\pi} \left[\frac{\overrightarrow{R}}{R_1^3} + \frac{(3-4\upsilon)\overrightarrow{R_2}}{R_i^3} - \frac{6z(z+c)\overrightarrow{R_2}}{R_2^5} - \frac{\overrightarrow{2k}}{R_2} \left\{ (3-4\upsilon)(z+c) - z \right\} \right] \quad (4.17)$$

where $R_1^2 = r^2 + (z-c)^2$, $R_2^2 = r^2 + (z+c)^2$ which relates to the image source and is introduced to create a traction-free surface, $\overrightarrow{k}$ is the unit vector in the z-direction and C_m is the uniaxial compaction coefficient, which is given by:

$$C_m = \frac{\alpha(1-2\nu)}{2\mu(1-\nu)} \quad (4.18)$$

Uniaxial deformation?

Referring to the previous discussion on the interchangeability of pressure and volume change in a linear elastic system we see that:

$$C_m \Delta p = \frac{\Delta V}{V} = \varepsilon_v \quad (4.19)$$

The solution of the fundamental equations result in the finding that the volumetric strain caused by a unit dilatation (pressure sink) is not proportional to the material bulk compressibility (C_b) as one might intuitively expect, but rather proportional to another constant C_m. For typical values of Poisson's ratio and shear modulus in rocks $C_b > C_m$ The physical reason for this is the way that stress is distributed around the nuclei (Fjær et al., 2008).

As I showed earlier, the total strain due to reservoir depletion is found by integrating the contributions of individual strain nuclei of the volume of the reservoir. Geertsma gave C_m the term *uniaxial compaction coefficient* because for horizontal reservoirs of *infinite lateral extent* the total deformation is indeed uniaxial (i.e. all the deformation is in the vertical direction). This is often the source of much confusion. In Geertsma's terminology the volumetric strain of a strain nucleus is given by the product of the uniaxial compaction coefficient and pressure change. However, it is not the case that the sum of contributions of individual nuclei results in the uniaxial deformation of the reservoir, except in the case of a horizontal reservoir of infinite lateral extent. Indeed,

it is obvious from the Green's function (Equation 4.17) that the lateral components of deformation are non-zero.

The geometry relating to Equation 4.17 is shown in Figure 4.2. It should be noted that Geertsma uses the convention that z is positive downwards.

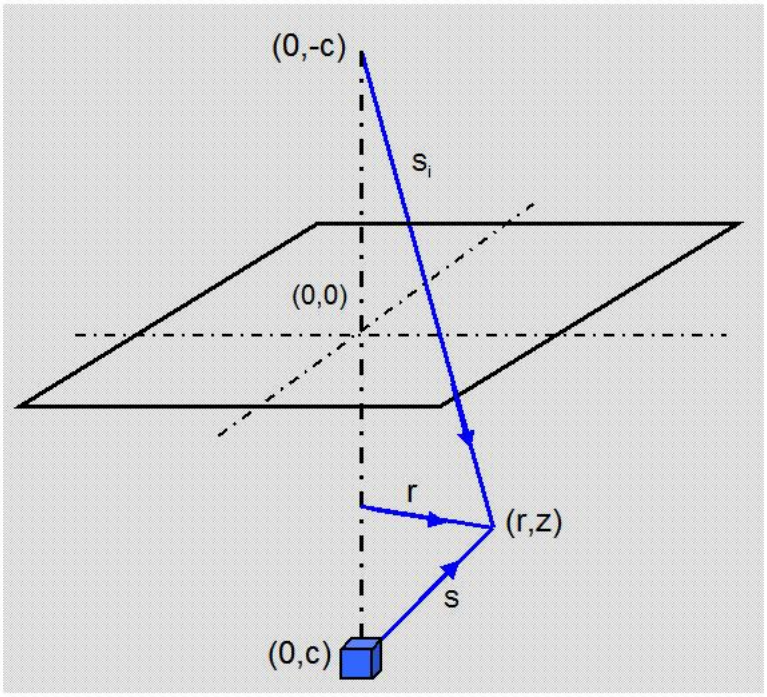

Figure 4.2: *The geometry to which Equation* **??** *is applied. Note that Geertsma uses z positive downward.*

The components of the strain tensor are found by taking the appropriate derivative of the displacement Green's function. A derivation of the Green's functions for displacement vector, stress tensor and strain tensor based on Equation 4.17 is provided in Appendix B. These expressions contain the Green's function's that will be used for this particular work.

4.2.4 Forming arbitrary reservoir shapes by numerical discretization

Geertsma (1966) analytically integrated Equation 4.17 over the volume of a thin disk, enabling displacements, stresses and strains to be calculated due to a constant pressure change over that disk. Segall (1992) later recovered Geertsma's solution as

a special case of a more general solution that includes axisymmetric geometries and pressure distributions, allowing the creation of dome structures for example.

The more general approach, that enables us to account for an arbitrary reservoir geometry, takes advantage of the linearity of Equation 4.14 with respect to pressure change. This linearity allows us to represent the reservoir as a linear sum of N prescribed orthogonal basis functions (Vasco et al., 2000). For practical applications, the most convenient basis functions are non-overlapping cuboids (for example, it is common practice for the reservoir model to be composed of cells). We can therefore write Equation 4.14 as a summation over N cuboids:

$$u_i = \frac{\alpha}{\mu} \sum_{n=1}^{N} \Delta p_n \int_{V_n} G_i(\boldsymbol{x}, \zeta) dV_n \tag{4.20}$$

where V_n signifies the volume occupied by the nth cuboid. The change in pressure represents an average in each cuboid and the volume integral is taken over the volume of each cuboid. As we have derived expressions for the Green's functions for displacement, stress and strain then Equation 4.20 can be applied to any component of interest by using the appropriate Green's function. The volume integral can be achieved using an appropriate numerical method (I use an algorithm set out by Stroud (1971)). Assuming the volume integral has been performed as part of the Green's function calculation, we can express the vertical strain as a linear system of equations:

$$\varepsilon_{zz,M} = \sum_{n=1}^{N} \Delta p_n G_{n,M}^{\varepsilon_{zz}} \tag{4.21}$$

where $\varepsilon_{zz,M}$ is the Mth strain observation and Δp are the reservoir pressure changes. Figure 4.3 gives a pictorial representation of how equation C.2 is applied for a rectangular reservoir split into four cuboids.

4.3 Validation of the discretization procedure

The forward model is validated against the analytical solutions of Geertsma (1966) and Geertsma (1973b). First, the vertical displacement is calculated along the z-

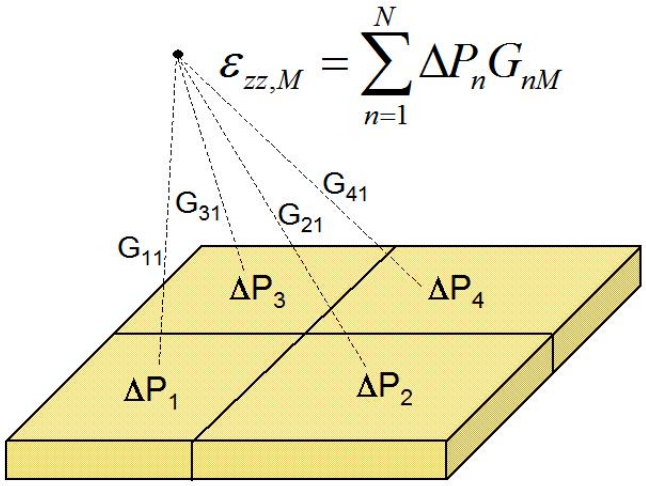

Figure 4.3: *A pictorial representation of Equation C.2 for a rectangular reservoir split into four cuboids. The pressure change in each cube contributes to the observed strain.*

axis at the centre of a thin disk-shaped reservoir of radius R and height h for which Geertsma (1966) gives an analytical solution:

$$\frac{u_z(0,0,z)}{C_m h \Delta p} =$$

$$-\frac{1}{2}\left[\frac{C(Z-1)}{[1+C^2(Z-1)]^{\frac{1}{2}}} - \frac{(3-4\nu)C(Z+1)}{[1+C^2(Z+1)]^{\frac{1}{2}}} - \frac{2CZ}{[1+C^2(Z+1)]^{\frac{3}{2}}}\right] + (3-4\nu+\varepsilon) \tag{4.22}$$

where $C = D/R$, $Z = z/D$, D is the reservoir depth and $\varepsilon = -1$ when $z \geq D$ and $\varepsilon = +1$ when $z < D$. Figure 4.4 shows a comparison between the numerical and analytical solution for normalized vertical displacement for a 30m thick reservoir with an average depth of 1000m, a radius of 3000m and a Poisson's ratio of $\nu = 0.25$. Observations are made at regular intervals of 15m, except for inside and on the boundaries of the reservoir where the numerical integration is invalid.

To show the effect of the numerical integration two grid spacings are used, 10×10m and 100×100m. Because a disk shape cannot be fully reconstructed from cuboids it

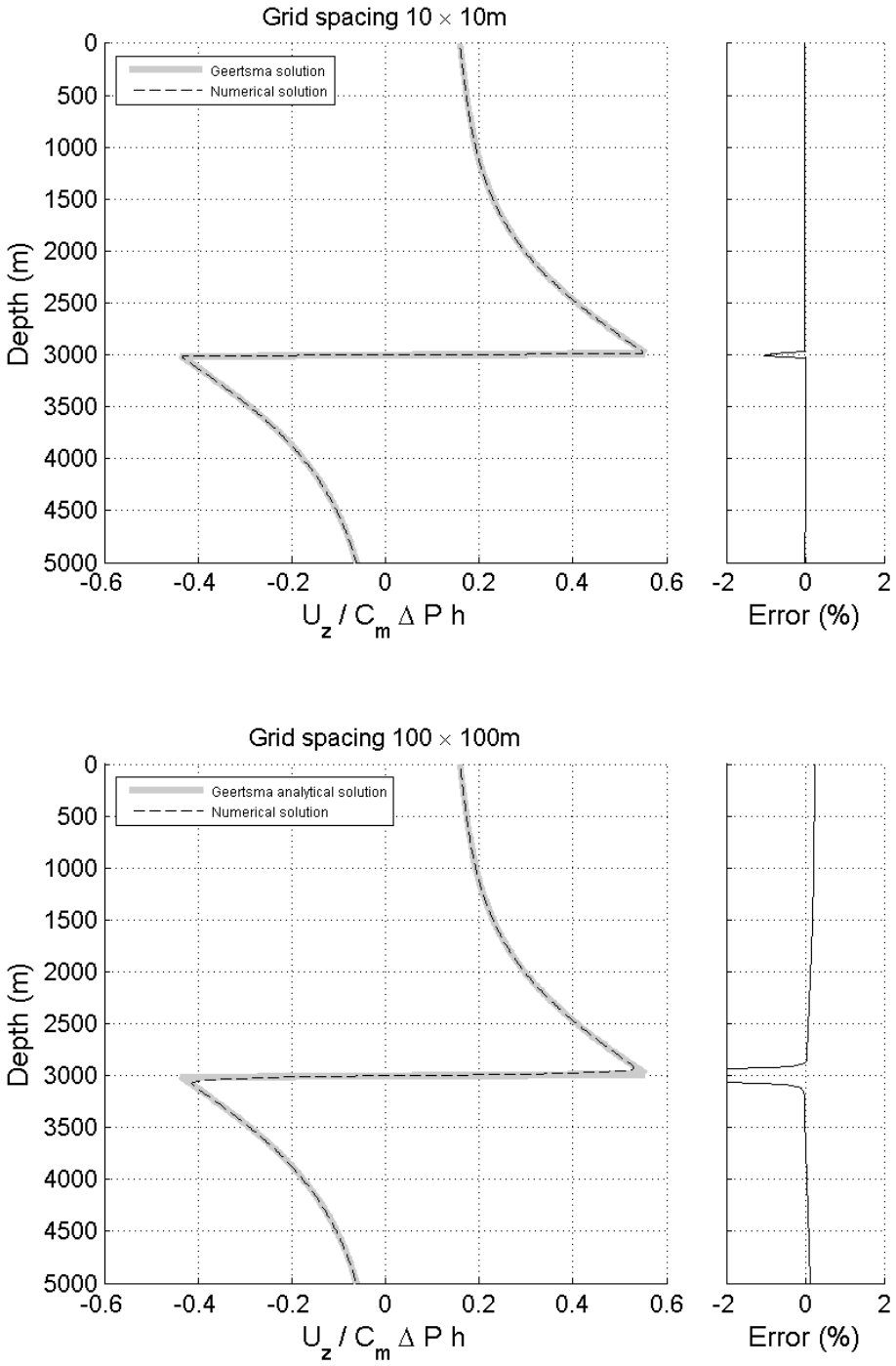

Figure 4.4: *A comparison between the analytical solution of $U_z(0,0,z)$ for a thin disk-shaped reservoir (Geertsma, 1966) and the numerical solution for two different discretization grids.*

is natural to expect some error. The difference in area between the disk and the disk constructed of cuboids is 0.007% for the fine grid and 0.303% for the coarse grid. As can be seen clearly in Figure 4.4, the error between the analytical and numerical solutions is small. For the fine grid the mean absolute error is 0.002% and for the coarse grid it is 0.316%. There is clearly a problem when the observations points are in close proximity to the reservoir. For the fine grid the maximum error is still only 0.004%. The problem is more acute for the coarser grid, where the error is as large as 23% 30m above the reservoir. However, the error quickly reduces as the distance from the reservoir increases and it reduces to $> 0.3\%$ when the observation points are situated > 75m above or below the reservoir.

As expected, the results show a common phenomenon associated with the discretization of continuous functions, the finer the discretization the more accurate the solution in comparison to the analytic one. The greatest error related to coarse gridding occurs nearest the reservoir and that we should treat the numerical solution with caution in this region.

4.4 Inversion for reservoir pressure change

Using our forward model we can now write our time-lapse time strains as a linear function of reservoir pressure. Given a time strain measurement located at an observation point M then rewriting the vertical strain term in Equation C.2 using the relationship of Hatchell and Bourne (2005a) we have:

$$\left(\frac{\Delta t}{t}\right)_M = (1+R)\sum_{n=1}^{N} \Delta p_n G_{n,M}^{\varepsilon_{zz}} \tag{4.23}$$

We can build a discrete vertical strain Green's function matrix $\mathbf{G}$ with dimensions $n \times k$ where n is the number of observation points, and k is the number of reservoir blocks. The data matrix $\mathbf{d}$ will contain time strain observations and is of length n. The vector $\mathbf{p}$ is the unknown average reservoir pressure changes in each cuboid and has a length k. The least-squares (L_2) objective function can be written as follows:

$$E = \|\boldsymbol{G\Delta p} - \boldsymbol{d}\|^2 \tag{4.24}$$

4.5 Why 4D seismic offers more

In this section we see why the ability of time-lapse seismic to see inside the Earth offers a distinct advantage over inverting for reservoir pressure changes from surface subsidence methods. In doing so I also show why this is an ill-posed inverse problem that requires regularization to stabilize the solution.

The Green's function for vertical displacement in a homogeneous linear poroelastic halfspace at the Earth's surface due to a nucleus of strain at depth c is given by:

$$g_z(x, y, c) = -\frac{C_m(1-\upsilon)}{\pi}\frac{c}{(x^2+y^2+c^2)^{3/2}} \tag{4.25}$$

Assuming a 2D pressure distribution located on a plane at depth c then the total surface displacement is given by a two-dimensional convolution between the pressure distribution $\Delta P(x, y, c)$ and the Green's function, $g_z(x, y, c)$ in the (x, y) plane:

$$g_z(c, x, y) = \int_{-\infty}^{\infty}\int_{-\infty}^{\infty} \Delta P(\zeta_1 - x, \zeta_2 - y, c) \cdot \frac{c}{(\zeta_1^2+\zeta_2^2+c^2)^{3/2}} d\zeta_1 d\zeta_2 \tag{4.26}$$

The convolution in the spatial domain can be written as a multiplication in the frequency domain so that Equation 4.27 can be written:

$$g_z^{'}(k_x, k_y) = \Delta\mathcal{P}(k_x, k_y) * \mathcal{G}(k_x, k_y) \tag{4.27}$$

Using the Fourier basis functions $e^{ik_x x}$ and $e^{ik_y y}$, where $k = 2\pi/\lambda$, then the transfer function of the Green's function $\mathcal{G}(k_x, k_y)$ can be written in the Fourier domain:

$$\mathcal{G}(k_x, k_y) = \int_{-\infty}^{\infty}\int_{-\infty}^{\infty} \frac{c \cdot e^{-ik_x x} e^{-ik_y y}}{(\zeta_1^2+\zeta_2^2+c^2)^{3/2}} dxdy = e^{-c(k_x^2+k_y^2)^{1/2}} \tag{4.28}$$

Equation 4.28 shows that the Green's function acts as a low pass filter. The higher wavenumber (large k) spatial basis functions, which represent the frequency components of the surface displacement, have their amplitudes attenuated exponentially. The parameter that controls the rate of decay of the transfer function is the depth c. The surface displacement becomes smoother as the reservoir is located at greater

depths. In solving the inverse problem we are performing a deconvolution, for which the transfer function is given by:

$$[\mathcal{G}(k_x, k_y)]^{-1} = e^{c(k_x^2+k_y^2)^{1/2}} \tag{4.29}$$

Equation 4.29 reveals a fundamental problem: The spatial frequencies of the deconvolution operator grow without bound as spatial frequencies grow. Thus small components of high frequency noise will make the inverse problem severely unstable. Problems of this kind are ill-posed inversion problems and frequently require regularization (Hansen, 1998), such as smoothness or inequality constrains.

The above equations illustrate the additional information that time-lapse seismic data can potentially offer. Although I gave the example of vertical surface displacement (because the mathematics is more compact for the purpose of an example), the principles hold true for measurements of the vertical strain. We can only hope to better resolve the features of the reservoir pressure change distribution by taking measurements closer to the reservoir, i.e. capturing higher frequency information before it is attenuated. As I have shown, time-lapse seismic has the potential to deliver estimates of strain inside the earth and so offer higher frequency information than surface displacements, which at present are the most common data used for inversion of reservoir pressure changes (e.g. Vasco et al., 2000; Du and Olson, 2001; Vasco and Ferretti, 2006).

4.6 Inversion method

To perform the inversion I will use well established techniques based on SVD (singular value decomposition) and use regularization to constrain the ill-posed nature of the problem. The objective function I will solve is:

$$E = \|\mathbf{G}\Delta\mathbf{p} - \mathbf{d}\|^2 + \gamma^2\|\mathbf{L}\Delta\mathbf{p}\|^2 \tag{4.30}$$

where $\boldsymbol{G}$ is the forward operator connecting the pressure changes $\Delta\boldsymbol{p}$ to the observation data $\boldsymbol{d}$. The second term in the objective function is the regularization term which makes certain pressure change distributions more favourable than others.

Zero order Tikhonov solutions use $\mathbf{L} = \mathbf{I}$ where $\mathbf{I}$ is the identity matrix. Higher order Tikhonov solutions use discrete finite difference approximations of derivatives. A commonly used matrix for $\mathbf{L}$ is the Lapacian operator which in two dimensions approximates

$$\mathbf{L} = \frac{\partial^2}{\partial x^2} + \frac{\partial^2}{\partial y^2} \tag{4.31}$$

Minimizing $\gamma^2 \|\mathbf{L}\Delta\mathbf{p}\|^2$ penalizes pressure change distributions that are rough in the second derivative sense, meaning that we expect the solution to be smoothly varying, but not flat. Tikhonov regularization can be solved using generalized singular value decomposition techniques (Hansen, 1998).

Selecting the smoothing weight γ is an important problem in both theory and practice (Aster et al., 2005). When there is only a single regularization term, as in Equation 4.30, then a commonly used method is the trade-off or "L-curve" method (Hansen, 1998). If we plot the model norm $|Gm - d|$ against the smoothness norm, which in the case of Equation 4.30 is $\gamma^2|Lm|$, as a log-log plot then we generally get a characteristic L-shaped curve. As we increase the value of γ, so that greater importance is placed on minimizing the smoothness norm, the model misfit becomes greater. Conversely, if we allow too little smoothing then the inversion will provide the best fit with both the noise and the data (see figure 4.5). The optimum value of γ is, therefore, a trade-off between model smoothness and data fit.

4.7 Experimental design analysis

Seismic data is commonly sampled on a lateral grid of a 25×25m and sampled every 4 milliseconds. If we calculate time strain at every data sample then for a seismic survey covering 5×5km area with a trace length of 4 seconds we would have over 40 million data points. Using this sort of volume of data in the inversion would be impractical because of the computational expense. In general, we will select a subset of the data to use as an input, such as the time shift or time strain at a particular seismic horizon in the overburden or on an arbitrary slice through the volume. This leads us to ask which subset of data is optimal to resolve the reservoir pressure changes from 4D seismic. I will show that the answer to this question depends on

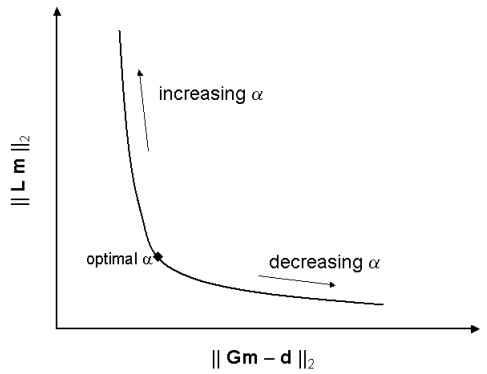

Figure 4.5: *A cartoon showing the use of an L-curve used to choose the optimum regularization parameter. If the model norm, $|Gm - d|$, is plot against the smoothness norm, $\alpha|Lm|$, on a log-log scale then one generally sees a characteristic L-shaped curve. As the value of α is increase greater importance is placed on minimizing the smoothness and norm the model misfit becomes greater. Conversely, if we impose no smoothing at all then the model will provide the best fit with the both noise and the data increasing the smoothness norm.*

the reservoir in question because it is a function of the geometric relationship between the reservoir and observation data. As a consequence there will be and optimized solution for every reservoir geometry, but by looking a some simple examples we can draw some general conclusions.

We can characterize the resolution offered by a certain configuration of observation points by examining the model resolution matrix. For Tikhinov regularization the model resolution matrix is given by:

$$\boldsymbol{R_{m,\gamma,L}} = \boldsymbol{G^{\dagger}G} \tag{4.32}$$

where $\boldsymbol{G^{\dagger}}$ is the generalized inverse (Aster et al., 2005). The important thing to note is that the resolution matrix is independent of the data. The resolution matrix is only dependent on the forward operator matrix $\boldsymbol{G}$, the order of regularization used (the $\boldsymbol{L}$ matrix) and the weight given to the regularization (γ).

We can compare the relative resolution of different experimental setups by examining the impulse response of the model resolution matrix. The model resolution matrix multiplied by a model consisting of a unit amplitude spike at a single location would return the same model if the resolution was perfect. However, the geometry of the

horizons and the use of regularization will mean that the model can never be fully recovered with perfect resolution. While we have complete control over the geometry of the observation data, the regularization term is dictated by the noise level in the data. Because noise will always be present in the system, the regularization term will be large enough that the resolution is substantially affected by regularization. The order of the regularization and the magnitude of γ will determine the smearing of the recovered reservoir strain. Therefore, the absolute resolution will be determined by the magnitude of γ, which will be ultimately dictated by the signal to noise ratio of the data. However, we can compare the relative resolution of different observation geometries by fixing the value of γ.

Which horizons?

First, I will show that, if we have several horizons in the overburden the ultimate resolution is controlled by the horizon nearest to the reservoir. To show this I use a deep narrow reservoir buried at 4km depth, which is rectangular in shape, has dimensions of 6×2km and a thickness of 100m. This is an approximation of the geometry of the Genesis Field, which will be studied later in this thesis. In this example the reservoir is perfectly horizontal.

Three scenarios are tested: two horizons located at 3250m and 3500m depth, one horizon located at 3500m depth and finally two horizons located at 3500m and 3750m depth. The overburden horizons are assumed to be perfectly horizontal in depth and cover an area of 8×8km. The observations are located on a 100×100m grid. An impulse test is carried out with the unit impulse located in the centre of the reservoir. In all cases second order Tikhinov regularization is used ($\boldsymbol{L}$ is the discrete Laplacian) and the value of α is held at 1×10^{-5}.

Figure 4.6 shows the consequence of the low pass filter nature of the Green's function, which was demonstrated earlier. We can only improve resolution by making measurements closer to the reservoir. Adding a shallower horizon to the horizon at 3500m has little effect on the resolution. However, adding a deeper horizon improves the resolution.

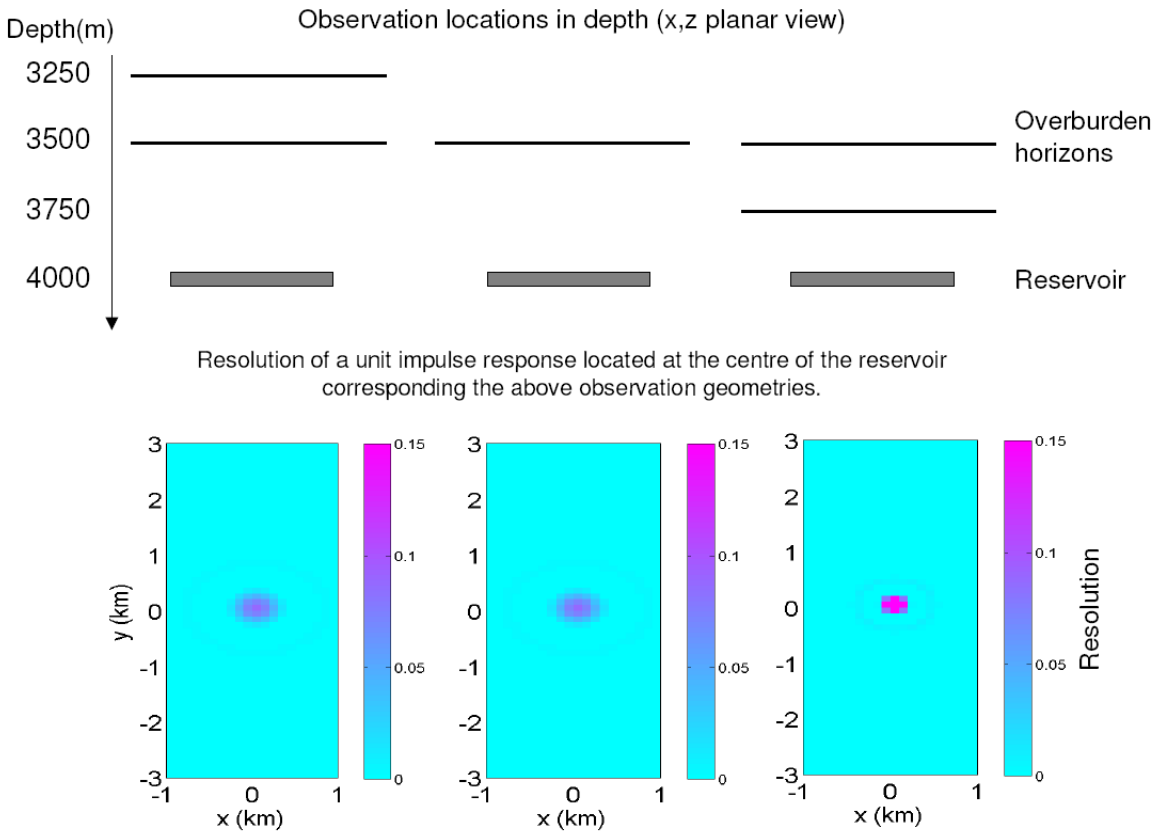

Figure 4.6: *An impulse response test to characterize the resolution of different observation geometries. Three scenarios are tested. Horizons with lateral dimensions of 8×8km containing observations points every 100×100m are placed at depths of (a) 3250m and 3500m (b) 3500m and (c) 3500m and 3750m. The reservoir is horizontal with lateral dimensions of 6×2km, is 100m thick and located at a depth of 4000m and discretized into 100×100×100m blocks. Clearly the depth of the horizon closest to the reservoir controls the resolution.*

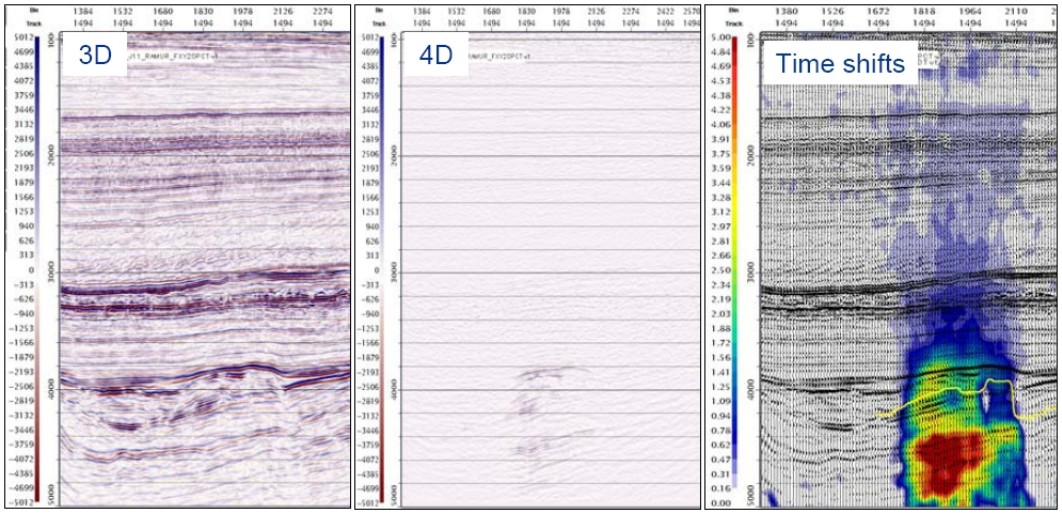

Figure 4.7: *3D seismic, 4D seismic differences and measured time shifts at Shearwater. The reservoir has undergone significant compaction and displays a strong overburden slow-down response, with time shifts extending considerably above the reservoir. After Staples et al. (2006). Top reservoir is marked by the yellow horizon on the time shift section.*

Dipping reservoirs

I have examined the effect of using horizons located at different depths on the resolution of the recovered reservoir pressure change using a horizontal reservoir and horizontal overburden horizons as an example. However, a common scenario is a dipping reservoir with approximately horizontal layering in the overburden. Two published examples of compacting reservoirs with this geometry are the Genesis Field in the Gulf of Mexico, and Shearwater in the North Sea. Figure 4.7 shows the 3D seismic, 4D seismic difference and measured time shifts at Shearwater (Staples et al., 2006). The reservoir and some overburden layers display moderate dip before being truncated by the Base Cretaceous Unconformity, whereafter the overburden layers are conformable and approximately horizontal. The reservoir has undergone significant compaction and displays a strong overburden slow-down response, with time shifts extending considerably above the reservoir.

The question is, which horizons offer more resolution, those parallel to the reservoir or horizontal horizons? To address this I take the same approach as earlier and examine the model resolution matrix for three different scenarios. The model is based on the Shearwater Field, a deeply buried narrow reservoir with a moderate dip of 15^o. The reservoir has lateral dimensions of 6×2km, is 100m thick and is

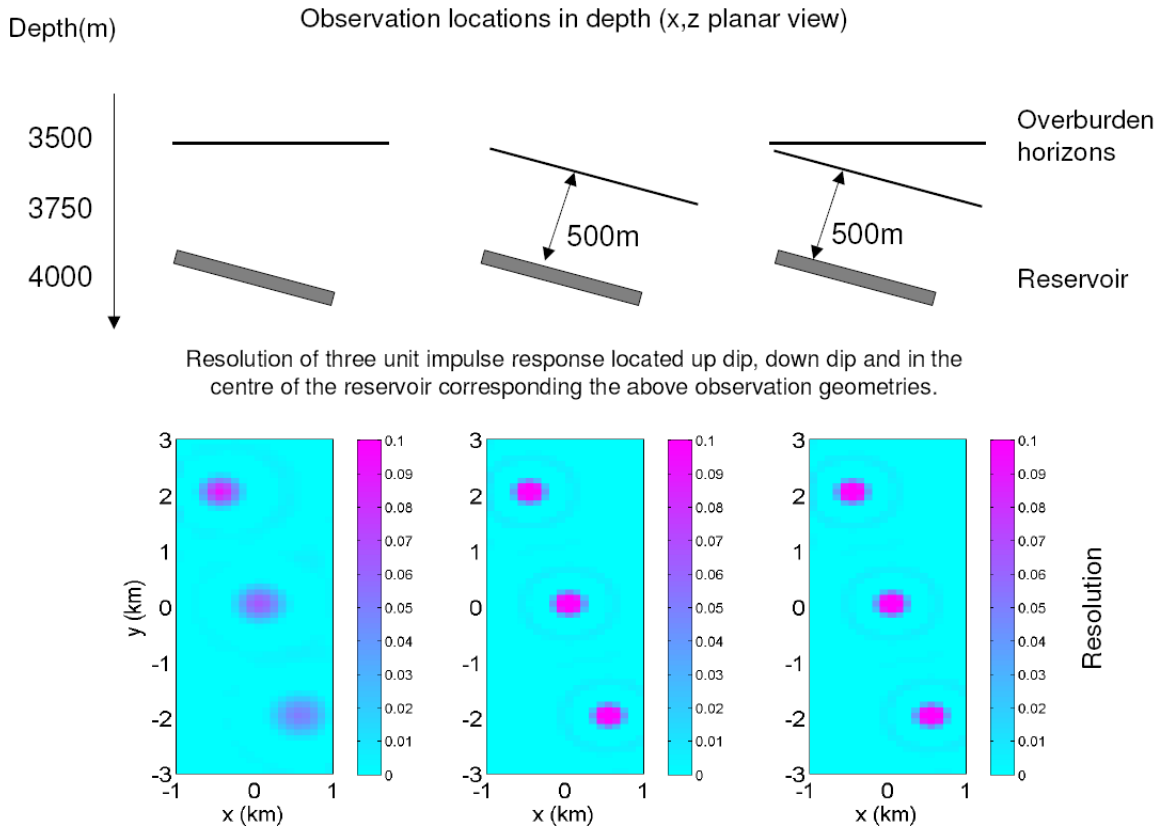

Figure 4.8: *An impulse response test to characterize the resolution of different observation geometries over a reservoir with a dip of* 15^o*. The reservoir is horizontal with lateral dimensions of 6×2km, is 100m thick and located at a depth of 4000m and discretized into 100×100×100m blocks. Three scenarios are tested. Horizons with lateral dimensions of 8×2.5km containing observations points every 100×100m are placed (a) horizontally 500m above the reservoir and (b) parallel to the reservoir 500m above it. In the third scenario both horizons are used.*

constructed from 100×100×100m blocks. I investigate three experimental setups: (a) An observation plane located horizontally 500m above the reservoir; (b) a observation plane located parallel to the reservoir 500m above it; and (c) both the dipping and horizontal horizons are used. The horizons have lateral dimensions of 8×2.5km and have observations every 100×100m. In all cases second order Tikhinov regularization is used ($\boldsymbol{L}$ is the discrete Laplacian) and the value of α is held at 1×10^{-5}. I test the resolution of three different impulse responses located up dip, in the centre of the reservoir and down dip.

Figure 4.8 is in agreement with the earlier observation that resolution is controlled

by the observation points closest to the reservoir. In the case where the observations are parallel to the reservoir all locations in the reservoir are equally resolved. In the case of a horizonal horizon resolution is lost down dip, as the distance between the pressure centre and the observations becomes greater. The final scenario of using both horizons shows that the resolution is determined by the observations parallel to the reservoir and adding the shallower horizon has no effect. This means that for strongly dipping reservoirs we should choose data aligned parallel to the top reservoir surface.

4.8 Assessing the impact of uncertainties

So far I have addressed resolution, which is dictated by the experimental geometry and which is independent of the data. We will also wish to assess the impact of uncertainties on our input data. Uncertainties in the time-lapse derived strain estimation will be discussed in the next chapter. However, there will be uncertainties in the location of the observation points, caused by uncertainty in the depth conversion, and in the material properties, which I will address in this section.

Depth conversion uncertainties

The 3D strain estimates from time-lapse seismic data must be converted into the depth domain because the geomechanical domain is depth, not two-way time. To convert between time and depth the velocity structure of the earth must be known. The seismic industry devotes a huge amount of time and effort to building accurate velocity models that transform the data between the time and depth domains. Accurate depth converted models are needed to define the geometry of the reservoir and plan wells. Absolute errors in depth conversion will depend on many factors, such as the complexity of the geological setting or the quality of the pre-stack seismic data used in velocity analysis.

The severity of depth conversion errors on the inversion result will depend on the rate of change of vertical strain at the observation point. In areas where the rate of change is high the error due to an incorrect depth estimate will be most severe. The vertical distribution of strain in the overburden will depend primarily on the geometry of the

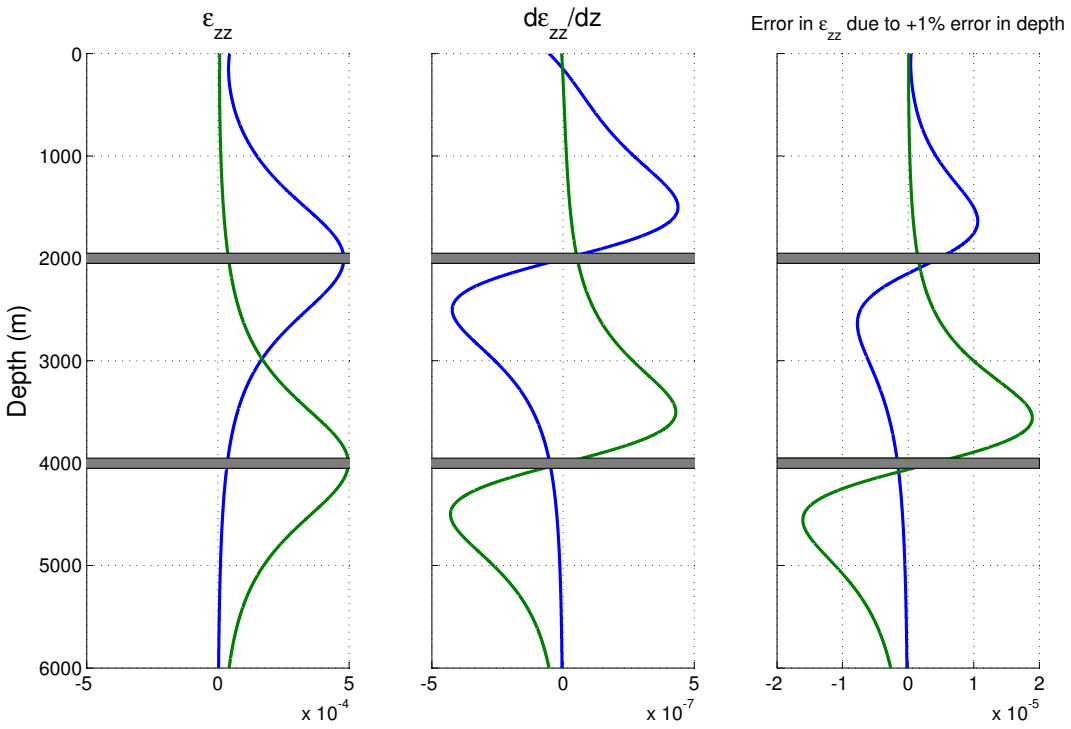

Figure 4.9: *The errors in vertical strain estimates caused by a* 1% *error in the true depth. Errors are greatest when the gradient of the vertical strain is greatest. Two examples are given for two thin disk-shaped reservoirs located at 2000m (blue lines) and 4000m depth (green lines).*

reservoir, depth of burial and the depletion pattern, therefore, potential errors will be unique to the model.

To demonstrate this I examine the vertical strain in the overburden caused by a uniform depletion of two a thin, disk-shaped reservoirs, at observation points along a vertical cross section through the centre of the reservoir. The first reservoir is buried at 2000m and the second at 4000m. Errors are calculated by comparing the strain at the true depth, d, and at $d + 0.01d$, i.e. 1% error in depth. Figure 4.9 shows that the error is correlated with the the gradient of the vertical strain.

It is important to remember that we expect depth conversion errors will, in most cases, be of low spatial frequency (see Brown, 2004, for example). Therefore, if depth errors exist, we expect them to introduce a systematic low frequency bias to the inversion result, since errors in the forward model linearly map into the inverse.

4.8.1 Uncertainties in material properties

The Green's function for vertical strain in a linear poroelastic halfspace (LPH) is a function of very few variables:

- The relative position of the source $\boldsymbol{\zeta}$ and the observation $\boldsymbol{x}$
- The material properties, which can be fully characterized by three poroelastic constants: Poisson's ratio, ν; the shear modulus, μ; and the Biot's coefficient, α.

The vertical strain due to the unit depletion of a nucleus of strain in a LPH can be written as follows:

$$\varepsilon_{zz}(\boldsymbol{x}, \boldsymbol{\zeta}, \mu, \nu, \alpha) = \frac{\alpha(1-2\nu)}{8\pi\mu(1-\nu)} G(\boldsymbol{x}, \boldsymbol{\zeta}, \nu) \tag{4.33}$$

where $G(\boldsymbol{x}, \boldsymbol{\zeta}, \nu)$ is a geometrical term which is only dependent on the Poisson's ratio along with the spatial locations of the source and observation. Equation 4.33 reveals that the controlling geomechanical parameter is the Poisson's ratio, because the constants μ and α linearly scale the strain. This means that if we imagine two halfspaces with different values of shear modulus and Biot's coefficient, but identical Poisson's ratios, then the spatial distribution of the strain with be exactly the same. However, the magnitude at every location will differ by a constant. For two materials with the same Poisson's ratio ν but shear moduli μ_1 and μ_2 and Biot's coefficients α_1 and α_2 this ratio is given by:

$$\frac{\varepsilon_{zz}(\boldsymbol{x}, \boldsymbol{\zeta}, \mu_1, \nu, \alpha_1)}{\varepsilon_{zz}(\boldsymbol{x}, \boldsymbol{\zeta}, \mu_2, \nu, \alpha_2))} = \frac{\alpha_1}{\alpha_2} \frac{\mu_2}{\mu_1} \tag{4.34}$$

This means that if the Poisson's ratio is correct but there are errors in μ and α, then the magnitude of the inverted depletion pattern will simply be under or over-estimated, but the spatial pattern will remain unaffected.

I have identified that the Poisson's ratio is the controlling geomechanical factor. How big is the uncertainty on the Poisson's ratio and how does this uncertainty feed into our inversion? Poisson's ratio is a measure of lateral expansion relative

to longitudinal contraction. For an isotropic linear elastic material the laws of thermodynamics give theoretical bounds of -1 $< \nu <$ 1/2 and in general the value in rocks is typically 0.15-0.25 (Fjær et al., 2008).

I will show that the error in vertical strain caused by an uncertainty in the Poisson's ratio is both non-linear and dependent on the geometry of the reservoir and the location of the observation relative to the reservoir.

First, I study the effect the reservoir geometry. To do this I use the analytical solution for a uniformly depleting disk-shaped reservoir in a homogeneous halfspace. Two reservoirs are used: A shallow reservoir and buried at $D = 2000m$ with a radius of $R = 4000m$ ($D/R = 0.5$) and a deep reservoir buried at $D = 4000m$ with a radius of $R = 2000m$ ($D/R = 2$). I study the error in predicted strain at an observation point 500m above the centre of each reservoir relative to a true Poisson's ratio of 0.15. The result is shown in Figure 4.10.

Clearly for the two different reservoirs the errors are dramatically different. This shows that we can not generalize the error due to uncertainties in Poisson's ratio because they will depend on the geometry of the reservoir.

Next, to show that the error is also dependent on the position of the observation to point relative to the reservoir I conduct the same experiment but this time fixing the reservoir geometry to that of the shallow reservoir, but testing two difference observations; 500m and 1000m above the centre of the reservoir. The result is shown in Figure 4.11 which shows the error is clearly dependent on position of the observation to point relative to the reservoir.

In conclusion, we cannot generalize the sensitivity of the inversion to uncertainties in Poisson's ratio. This will depend on the geometry of the reservoir and location of the strain data we choose to use as an input to the inversion. This should be incorporated into the inversion or a sensitivity study should be carried out if the uncertainty in the Poisson's ratio is high. In addition, these errors may be small compared with the assumption of a homogeneous halfspace.

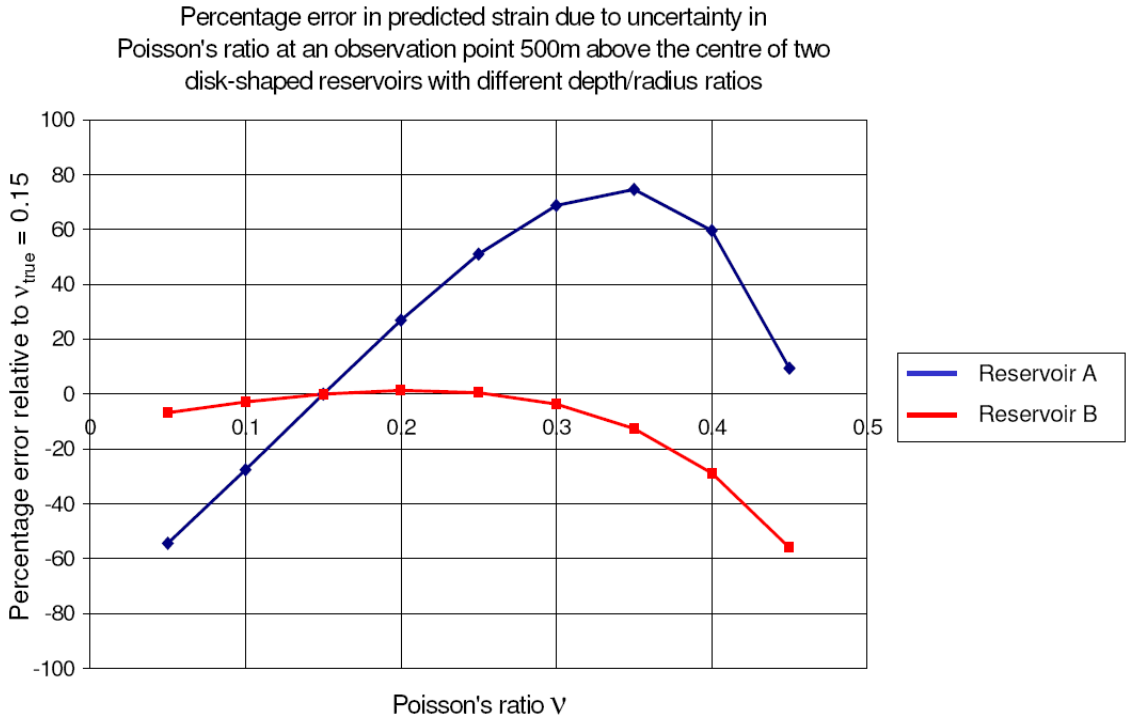

Figure 4.10: *The effect of reservoir geometry on errors in vertical strain caused by uncertainties in Poisson's ratio. The analytical solution for a uniformly depleting disk-shaped reservoir in a homogeneous halfspace is used to measure the strain 500m above the centre of two different reservoirs. Reservoir A is a shallow reservoir buried at $D = 2000m$ with a radius of $R = 4000m$ $(D/R = 0.5)$. Reservoir B is a deep reservoir buried at $D = 4000m$ with a radius of $R = 2000m$ $(D/R = 2)$. The error in predicted strain is given relative to a true Poisson's ratio of 0.15.*

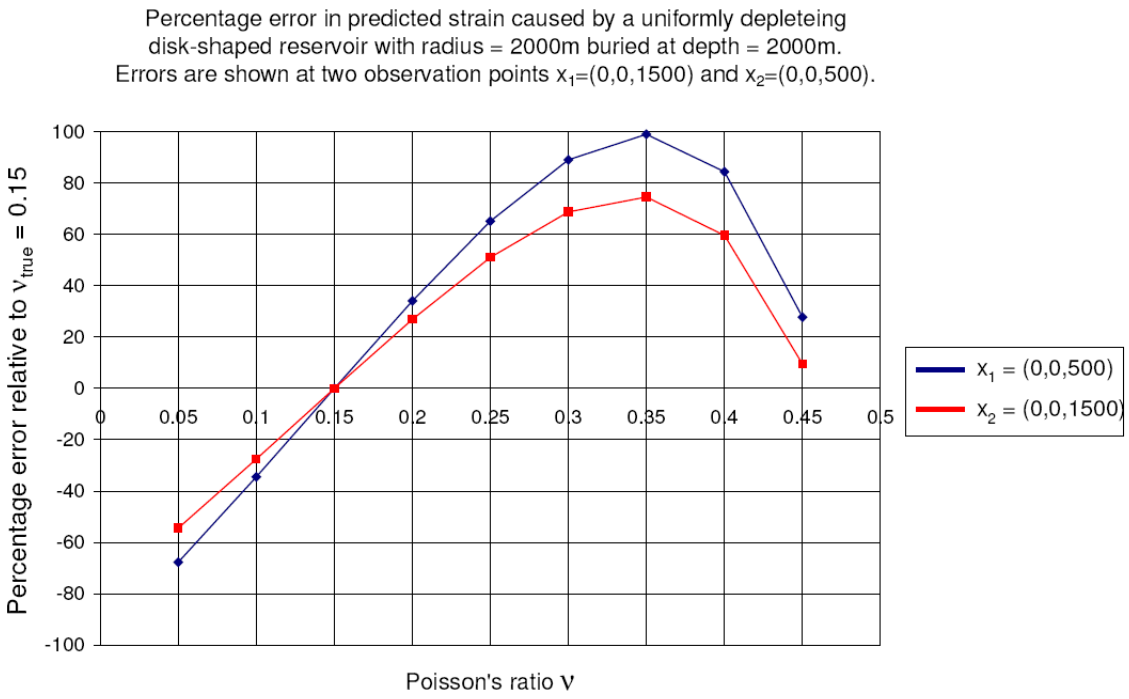

Figure 4.11: *The effect of the observation location relative to the reservoir on errors in vertical strain caused by uncertainties in Poisson's ratio. Vertical strain is measured 500m and 1000m above a uniformly depleting reservoir buried in at 2000m with a radius of 4000m.*

4.9 Test inversion

In this section I explore several of the issues involved in the inversion scheme. Rather than conducting an inversion of synthetic data forward modelled by the simple semi-analytic methods explored so far, in this chapter I will use data from an iteratively coupled (fluid flow and deformation) model of a compacting reservoir, created using the finite element method (FEM). The model was created by Margarita Corzo and is based on a sector of the Valhall Field (Corzo and MacBeth, 2006).

4.9.1 Description of the model

The following description is based on details from Corzo and MacBeth (2006) and directly from Margarita Corzo (pers. comm.).

The model is based on the geological structure of the southeastern part of Valhall field. A horizontal well is located in the thickest part of the producing layer. The model has 23 layers in total that includes: Nine overburden layers, 13 reservoir layers and one underburden layer. A horizontal well is located in the 12th layer of the reservoir zone. The overburden and underburden are comprised of nine linear elastic materials, with varying geomechanical properties. The input fluid and reservoir rock properties, such as porosity, oil density, and relative/matrix permeabilities, used in the model are similar to those observed in the field. Reservoir permeability is held constant (i.e. there is no compaction related permeability loss) during simulation but porosity is allowed to vary and is updated as a function of the reservoir effective stress.

Two sets of initial porosities are used: 40% initial porosity in the upper high porosity zone (the first four reservoir layers) and 15% for the remaining reservoir layers. The initial porosity is an important factor for the model as rocks with higher initial porosities have been shown to compact more that those with lower ones. Compaction curves published by Barkved et al. (2003) were used to calculate the linear elastic parameters for the two porosity families. For layers with porosities of 40%, two linear elastic behaviors are used, before and after a yield-point. The Youngs modulus after yield-point (E_2) is smaller than the Youngs modulus before the rock yields (E_1), which approximates the non-linear properties of the rock. For the low porosity layers, a single value of Youngs modulus is used. Figure 4.12 shows the geometry of

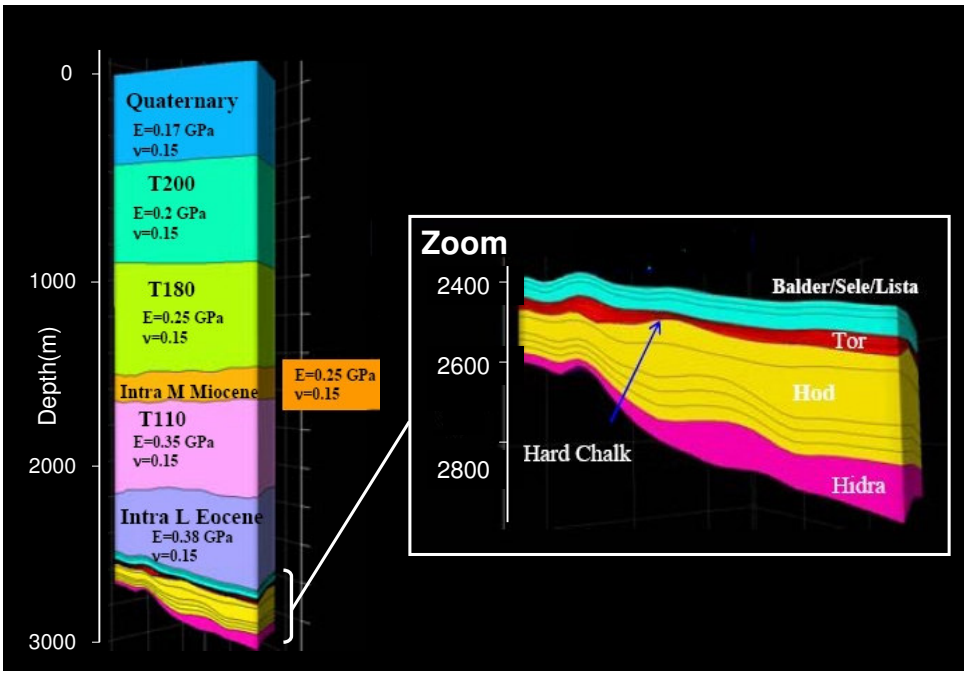

Figure 4.12: *The geometry and properties assigned to the Valhall sector model. Geomechanical properties are fully tabulated in Table 4.1. After Corzo and MacBeth (2006)*

the whole model and of the reservoir and some of the elastic properties assigned to the overburden. The geomechanical properties assigned throughout the model are given in Table 4.1.

4.9.2 Depletion scenario and compaction

The initial reservoir pressure was 41.4MPa at a depth of 2500m. A horizontal well was placed along the centre of the reservoir and was set to produce 3100bb/day for 10 years. Primary depletion was assumed, with no aquifer support. After 10 years the pressure depleted by approximately 12MPa at the well location (Figure 4.13). Although the pressure drops uniformly throughout the reservoir, the greatest porosity loss, and hence the majority of reservoir compaction, occurs in the mechanically softer high-porosity layers in the upper part of the reservoir (Figure 4.13).

Layer Distribution		Young's Modulus (GPa)	Poisson's Ratio
Overburden	Quaternary/T200	0.17	0.15
	T180	0.2	0.15
	Intra M Miocene	0.25	0.15
	T110	0.35	0.15
	Intra L Eocene	0.38	0.15
	Balda/Sele/Lista	1	0.2
Reservoir	Tor	$E_1 = 2.43$	0.18
		$E_2 = 1.65$	0.18
	Hod	9	0.18
Underburden	Hidra	6	0.17

Table 4.1: *The linear elastic geomechanical properties assigned to the Valhall model. After Corzo and MacBeth (2006)*

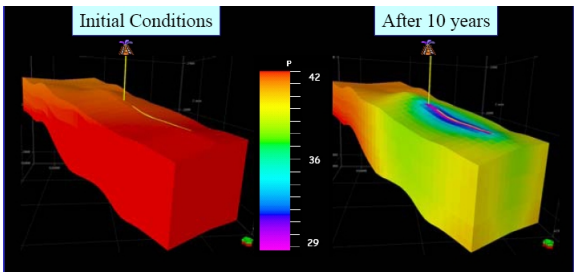

(a) Change in reservoir pressure

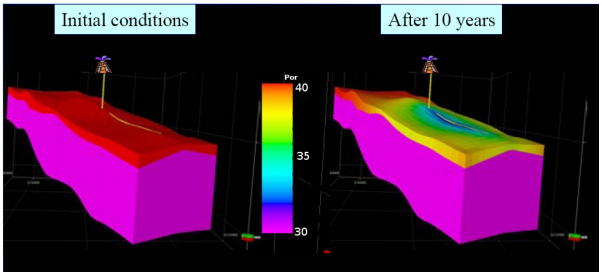

(b) Change in porosity

Figure 4.13: *Changes in reservoir pressure and porosity in the Valhall model after 10 years of production Corzo and MacBeth (2006)*

4.9.3 Inversion for reservoir pressure

Given our simple semi-analytic geomechanical model, is it possible to recover reservoir pressure from overburden strain from a much more complex geomechanical model that includes contrasts in the mechanical properties of layers? In this section I answer this question by performing the inversion using data output from the Valhall model as an input to the inversion.

Inversion setup

To perform the inversion we need very little information. The first step is to form the semi-analytic discrete linear poroelastic vertical strain Green's function for a halfspace. This is a function of only three required parameters: The relative position of the reservoir grid to the observation grid, the thickness profile of the reservoir, and the poroelastic properties of the halfspace (the shear modulus, Poission's ratio and Biot coefficient). I assign a shear modulus of 1GPa, Poisson's ratio of 0.15 and Biot coefficient of 1, which are the averaged overburden properties. The reservoir grid used is the same as in the geomechanical model, which has a lateral spacing of 100×100m in the reservoir.

The observation data in this case is the strain output from the Valhall finite element model. The finite element model calculates the displacement at element nodes. Changes and stress and strain are calculated from displacements and the material properties of the cells. In the case of the Valhall model there are only nine layers in the overburden, with one cell per layer in the vertical direction. The coarse discretization of the overburden means that the strain profile is not well characterized. To calculate the strain at a given point we must assume an interpolation function. If we assume that this is a linear function, then the vertical strain due to displacements at nodes on layer n and layer $n+1$ is given by:

$$\varepsilon_{zz}[z_n + D/2] = \frac{U_z[z_{n+1}] - U_z[z_n]}{D} \tag{4.35}$$

where D is the vertical distance between the two nodes which are located at depths z_n and z_{n+1}. The strain observation is located halfway between the nodes at the depth $z_n + D/2$. The square brackets indicate that we are working with a discretised function.

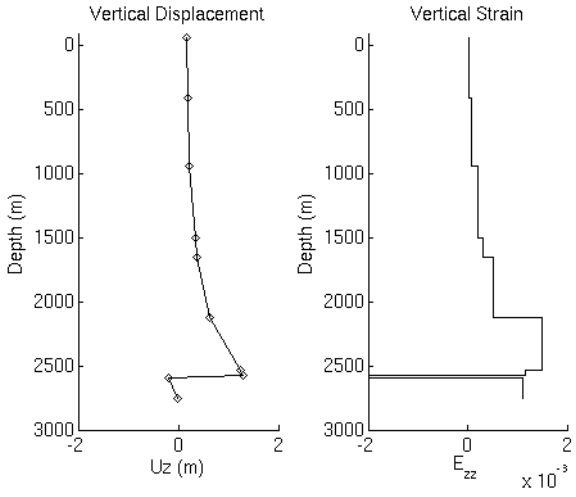

Figure 4.14: *A profile of U_{zz} and E_{zz} through the cell with the largest depletion in the Valhall model. Each diamond represents a node in the FEM model. The coarse discretization in the overburden means that the non-linear decay of the vertical displacement and strain is not fully characterized. If linear interpolation is used between the displacements the result is a blocky strain model. In reality strain is expected to vary more smoothly in the overburden. This can only be remedied by finer discretization of the overburden.*

I use the strain between layers 6 and 7 on a 100×100m grid, which is the lateral grid spacing in the reservoir zone of the finite element model. I use the strain between layers 6 and 7 rather than layers closer to the reservoir to avoid any near-reservoir numerical effects in the semi-analytic calculation, which I identified earlier in the chapter.

Forward modelling and calibration

Once the discrete Green's function is calculated it is possible to perform both the forward and inverse operations. Since the depletion pattern is known we can forward model the overburden strain using the semi-analytic method and compare it to the strain given by the Valhall finite element model.

Figure 4.15 shows the vertical strain between layers 6 and 7 forward modelled by the semi-analytical method calculated by the Valhall finite element model.

The agreement between the spatial distribution is very good. The most obvious difference is the magnitude. The ratio of root mean square (RMS) energy between

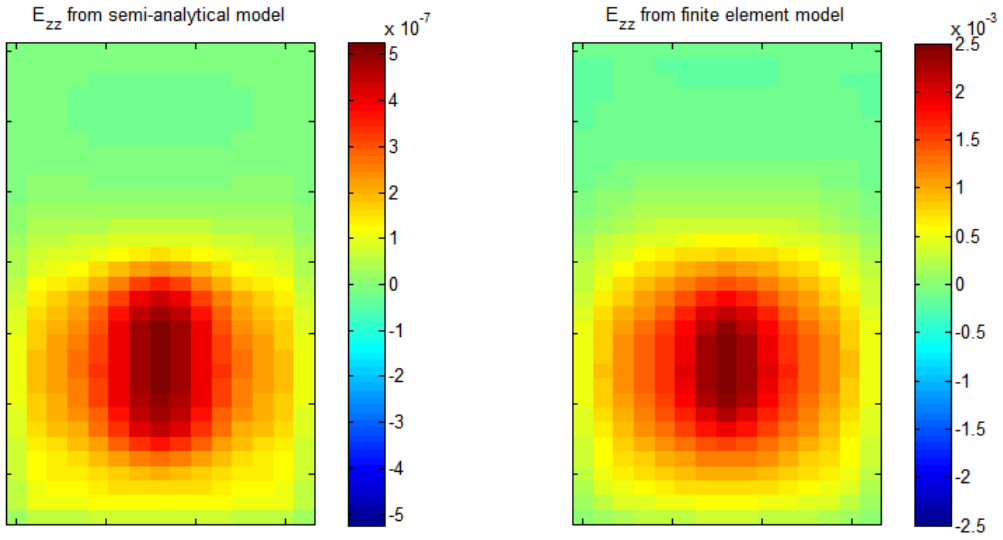

Figure 4.15: *Strain between layers 6 and 7 predicted using the semi-analytical model for a homogeneous halfspace ($\mu = 0.2$ GPa and $\nu = 0.15$) compared with the strain calculated from the Valhall FEM model. Note the scalebars differ by a factor of* 10^4.

the FEM result and the semi-analytic result is approximately 4800, which can be attributed to fact that the semi-analytical model doesn't account for the heterogeneous layering of materials with different mechanical properties. For example, the reservoir is stiffer than the overburden but the semi-analytic model uses the same properties in the reservoir as the overburden. As the reservoir is less compressible than the overburden the amount of reservoir strain per unit depletion is under-estimated.

This difference means that we will need to calibrate the inverted solution against known pressures, or average pressure changes. Figure 4.16 shows the strain maps after calibration. Both strain maps are now on the same colour scale. The normalized difference is also shown, which is defined as the difference between to two maps divided by the RMS energy of the Valhall model strain map. The agreement is good, showing that a single scaler can account for much of the difference. However, some differences remain, especially above the area of main drawdown.

Another area of consideration when analysing the differences between the maps is the coarseness of the Valhall finite element model, which I discussed earlier. There is tendency to assume that numerical models are 'truth'. In reality many factors such as the density and type of elements or the boundary conditions for example

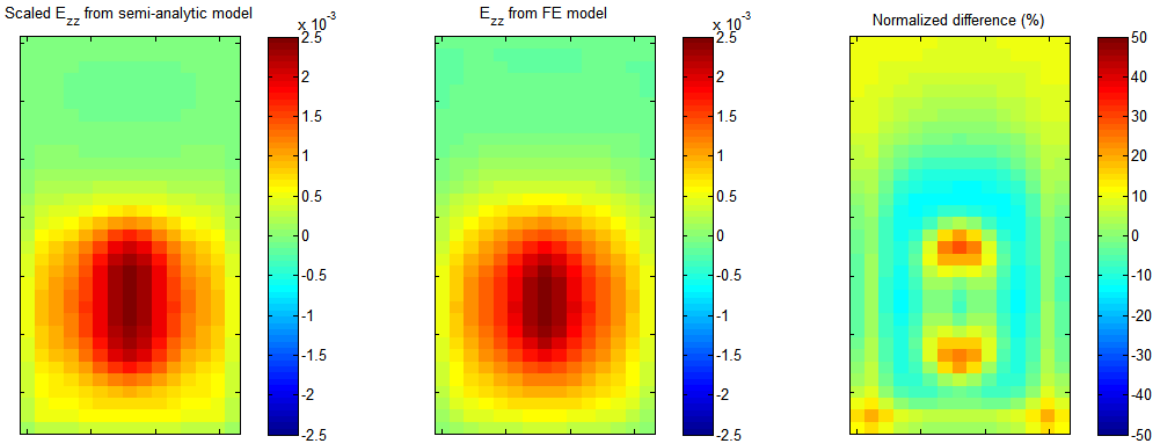

Figure 4.16: *Strain between layers 6 and 7 predicted using the semi-analytical model for a homogeneous halfspace (μ = 0.2 GPa and ν = 0.15) compared with the strain calculated from the Valhall FEM model, after scaling the semi-analytical result to account for differences in magnitude. After scaling two maps visually correlate very well (also, note that in comparison to Figure 4.15 both images are now shown on the same colour scale.) The normalized difference reveals that there are still significant differences.*

all contribute to the quality of the solution. In this example, we saw in how coarse discretization in the vertical direction results in a blocky strain model (Figure 4.14), which does not fully capture the decay of vertical strain through the overburden. This coarse discretization will also effect the lateral distribution of the vertical strain.

Performing the inversion

I now invert for reservoir pressure using the Valhall model strain data. The discrete Green's function matrix is formed using a shear modulus of 1GPa, a Poisson's ratio of 0.15 and a Biot coefficient of 1. In addition, the Green's function is scaled by a calibration factor of 4800, which was as identified earlier. For now this calibration is possible because we know the pressure changes and can compare the forward modeled and observed strain. I will address how this calibration can be performed on real data in later Chapters, when I apply the technique to the Genesis and Valhall Field data. The inversion is solved using standard numerical techniques.

In general the gross features and magnitude of the pressure depletion pattern are recovered well. Rather than calculate the percentage error I use the normalized error (NRMS), which is defined as the difference between the inverted and synthetic

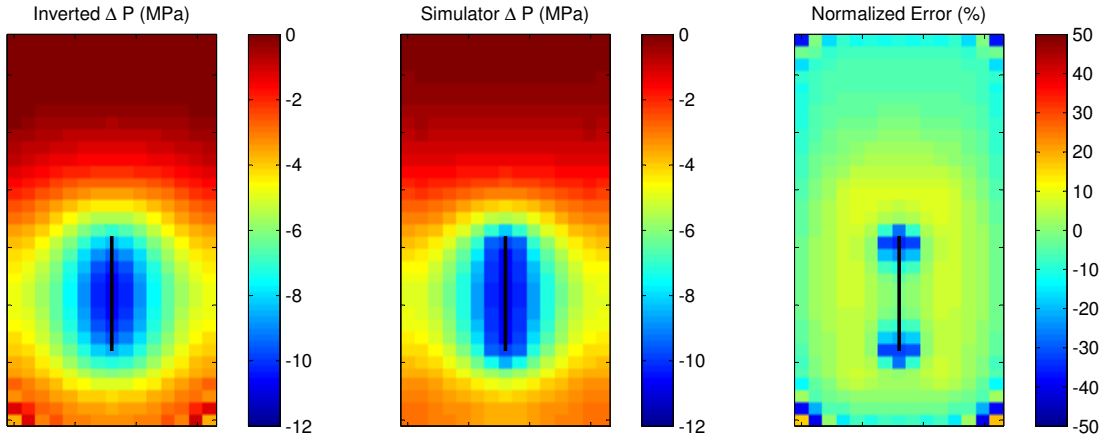

Figure 4.17: *The reservoir pressure change inverted from strains output from the Valhall reservoir model.*

pressure changes normalized by the RMS energy of the synthetic depletion map. This avoids instabilities in the denominator in the traditional percentage error calculation, which will occur when the pressure is very small. Errors are largest at the edges of the well-track. Elsewhere the depletion is predicted within ±10% NRMS of the actual solution. So what are the cause of these errors?

Earlier I showed that there are significant differences between observed strains from the Valhall model and the strain predicted by the semi-analytical model. A scaling factor was needed to account for an order of magnitude difference between the two. After the scaling factor was applied differences remained. Figure 4.18 shows the normalized difference between the forward modeled strain created using the semi-analytic method and FE model alongside the errors in the inverted pressure.

There is a clear correlation in the difference between the semi-analytic and FEM strain data and the errors in pressure, which is expected since the two are linearly related.

Another source of error will be related to the depletion pattern. In the case of a horizontal well the drawdown at the well decays sharply. To regularize the inversion I used second order Tihkinov regularization, which makes the assumption that the Laplacian of the depletion pattern is zero. This assumption is invalid near the region of the well, as shown in Figure 4.19. This means that there is a trade-off between

preserving the sharp gradient in this region and the stability of the rest of the solution. This explains why the inverted depletion pattern is slightly broader than the actual depletion pattern in the central region.

4.10 Conclusions and discussion

This chapter began with the assumption that we can relate overburden time-lapse time shifts or there derivative time strains to overburden strain. The aim of the remainder of this chapter was to try to identify a link between reservoir pressure changes and overburden strain that could be exploited in a simple, computationally inexpensive way so that we can directly invert observations for reservoir changes.

Possibly the simplest geomechanical model that represents a depleting reservoir is a nucleus of strain in a linear poroelastic halfspace. The mathematical description the displacement due to a nucleus of strain under such conditions had been reported by several authors. In this chapter, I described how this model can be used to construct reservoirs of arbitrary shapes, by the superposition of a number of depleting cuboids.

Next I showed how the problem can be cast as linear, allowing forward modelling of deformation given a known pressure distribution, and allowing inversion given strain observations outside the reservoir.

Crucially I demonstrated through several examples that it is the distance between the reservoir and the observations that determines the resolving power of the inversion. This 4D seismic offers greater potential than surface deformation measurements because of the ability to 'see' the deformation in the subsurface closer to the reservoir.

Poisson's ratio was identified as the key geomechanical factor in a homogeneous linear elastic halfspace, with the shear modulus and Biot coefficient simply scaling the solution. Therefore, errors in these parameters can be fixed if calibration is possible. Errors due to uncertainty in the Poisson's ratio, however, cannot be generalised.

To test the inversion I took the output from a heterogeneous, iteratively coupled, finite element model based on a sector of the Valhall field provided by Margarita Corzo (Corzo and MacBeth, 2006). From this model I successfully inverted the reservoir pressure changes given the overburden strain. The reservoir depletion is

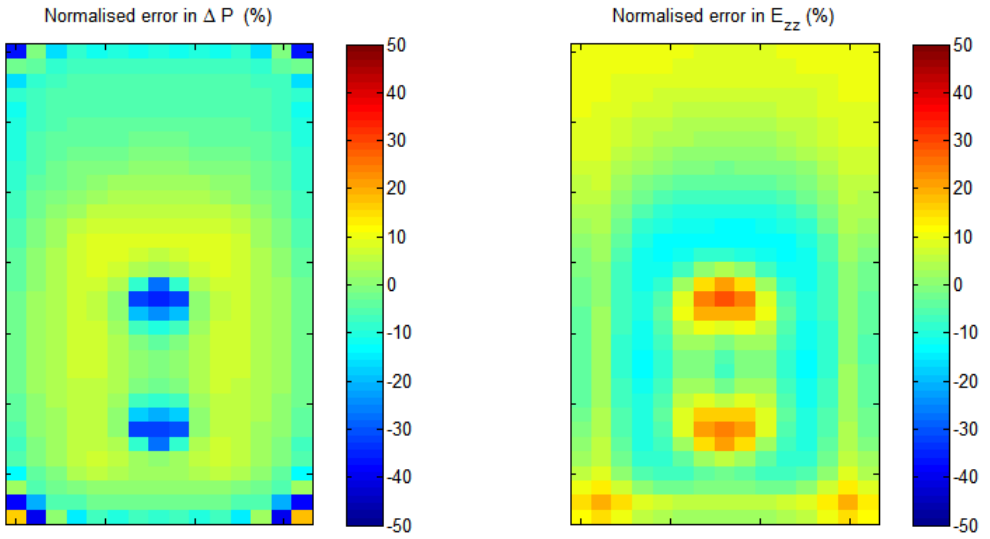

Figure 4.18: *A comparison of the normalized difference between the vertical strain predicted by the semi-analytical model to that predicted by the FEM model with the normalized errors between predicted and inverted pressure. Errors in strain are clearly correlated to errors in the inverted pressure.*

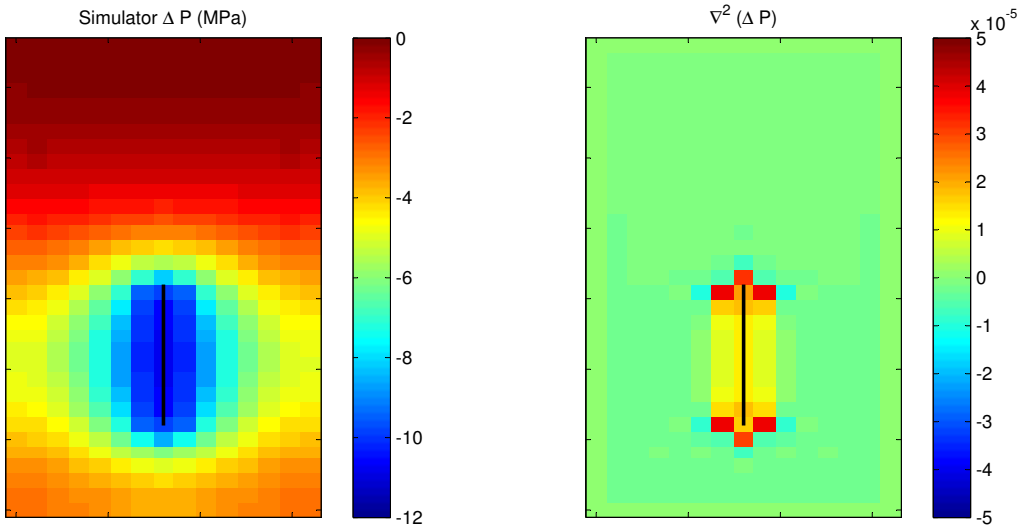

Figure 4.19: *The Laplacian of the Valhall depletion pattern. Clearly the assumption that the Laplacian is zero is invalid in the near-well region.*

recovered to within ±10% normalized RMS difference. Some larger errors were found that can be attributed to the large drawdown at the well being inconsistent with the assumption used to regularize the inversion.

Although, I have chosen to relate velocity changes to vertical strain, providing a simple and pragmatic approach, this linear inversion formulation can be extend to allow changes in velocity to be related to any any linear combination of the components of the stress and strain tensor. I have described this fully in Appendix C.

CHAPTER

FIVE

Inverting for reservoir compaction at Valhall field, North Sea

This chapter will bring together the material presented thus far by studying a sector of the Valhall Field. First, a time shift analysis will be presented which will reinforce some of the observations made in Chapter 3 about the difficulty of measuring time shifts in the reservoir zone. Next, time shifts in the overburden will be analyzed for their suitability as input to the inversion scheme suggested in Chapter 4. Finally, I will present an inversion for reservoir strain from overburden time-lapse time shifts.

5.1 Description of Valhall Field

5.1.1 Background

The history of Valhall is well documented in the literature. I will give a brief description relevant to the contents of this chapter. For more on the general background, see "Valhall field - still on plateau after 20 years of production" by Barkved et al. (2003).

Valhall is situated in the south-west of the Norwegian sector of the North Sea (see Figure 5.1), under an initial water depth of approximately 70m. The reservoir is an asymmetric NNW-SSE trending anticline which has an average depth of 2500m and covers an area of approximately 6×13km.

The reservoir is formed of Upper Cretaceous chalk. The primary reservoir is the Tor Formation which provides the greatest reservoir volume, although a secondary reservoir is also located in the lower Hod Formation. The thickness of the Tor formation varies abruptly and ranges from 0 to 80m, with an average thickness of 30m. There is a general correlation between the thickest areas and the highest porosities (up to 50%) and permeability (1 to 10 mD). Barkved et al. (2003) note that the variability of initial thickness and reservoir quality makes planning and drilling horizontal wells a considerable challenge.

5.1.2 Compaction

The reservoir is substantially over-pressured. The initial pore pressure at the crest of the Tor formation was 45MPa. With an overburden stress of approximately 50MPa the effective stress felt by the reservoir matrix (assuming a Biot coefficient of 1) is only 5MPa, some 20MPa over pressured. The reservoir chalk is mechanically weak, high porosity chalk, displaying porosities of above 50%. With such a low effective stress, significant compaction and associated porosity and permeability loss occurs upon depletion.

The evidence for reservoir compaction has been seen at surface, where the sea floor has compacted several metres since the field was brought on stream in 1985. Subsidence of 0.5m was measured only 3 years after first oil. Maximum sea floor

Figure 5.1: *The location of Valhall Field. After Barkved et al. (2003).*

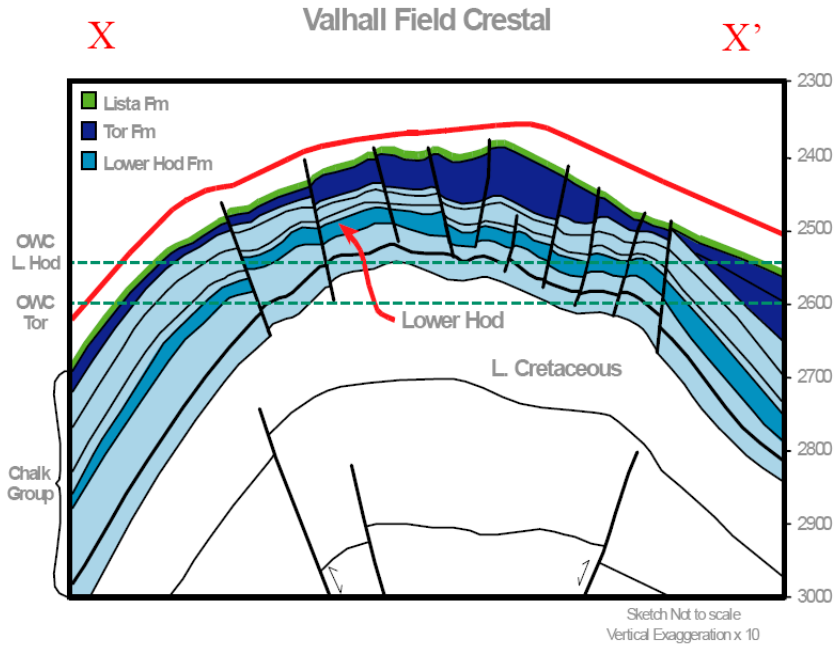

Figure 5.2: *A simplified geological cross-section of Valhall Field. After Barkved et al. (2003).*

subsidence has continued to increase at a rate of approximately 0.25 m/year. As of March 2004 subsidence was 4.9m.

5.1.3 Life of Field Seismic

The Valhall Life of Field Seismic (LoFS) project is the world's first permanently installed Ocean Bottom Cable (OBC) system. More than 120km of seismic cables cover an area of 45km^2 - approximately 70% of the field - with around 2500 4-component (4C) sensors. Each sensor consists of three geophones, which record compressional waves and converted waves, and a hydrophone which measures P-waves.

The LoFS project offers several advantages over traditional marine time-lapse data. As I discussed in Chapter 3, Calvert (2005) has shown that source and receiver position repeatability has a direct correlation with the time-lapse repeatability. Fixed receiver positions mean that time-lapse repeatability is greatly improved compared to traditional towed-streamer data, where cable feathering can be a significant issue. The LoFS data were found to have NRMS values a factor of two smaller than streamer time-lapse data recorded at Valhall before the LoFS installation (Kommedal et al., 2005).

Some intervals in the shallow overburden are charged with gas which makes imaging with traditional P-wave data challenging. Converted wave imaging provides a way to 'see through' the gas due to the insensitivity of shear waves to the fluid content of the rock.

From a reservoir management perspective, permanently installed sensors allow for continuous time-lapse seismic monitoring of the Valhall reservoir. Nine surveys in total were conducted over the period November 2003 to November 2007. This frequently acquired data is now an integral part of the field development, providing data that informs well planning decisions, helps monitor well performance and identify where well interventions are required, constrains the reservoir model history match and aids calibration and understanding of geomechanical models (van Gestel et al., 2008a).

5.2 Motivation

In Chapter 3 I argued that the time shift at reservoir level was difficult to measure and interpret. In this section I will give an example from the Valhall sector used in this study that supports this statement. Figure 5.4 shows a comparison of traces from the LoFS1 and LoFS6 surveys from a location in the south sector of the field. The BP interpreted pick of top and base reservoir is shown. Alongside the seismic traces is the time shift measured by cross correlation (using a 60ms Hanning window) and the normalized maximum cross correlation coefficient (CC_{max}) associated with that time shift.

Clearly, inside the reservoir zone the reflectivity is dramatically changed because of changes in the acoustic impedance of the reservoir. I make no attempt to interpret these changes, but simply show them as an example of how, in certain cases, time shift measurements based on matching the similarity of events become invalid. In this example the trough at $\approx 2600ms$ disappears, so that the peak-trough-peak combination that defines the reservoir is no longer visible. This change in reflectivity appears in the normalized values of CC_{max}. Outside the reservoir zone CC_{max} values are close to the maximum value of 1 (-1 being a perfect anti-correlation). In the reservoir zone they drop down to below zero, indicating that there is little similarity in the shape of the windowed events. In such circumstances it is meaningless to measure a time shift based on a similarity measurement (such as cross-correlation or least-squares, which were discussed in Chapter 3).

A more appropriate approach accounting for the changes in the seismic data is through an acoustic impedance inversion, which will correctly account for both time shifts and changes in reflectivity. Time-lapse acoustic impedance inversions are additionally challenging in compacting reservoirs due to extra degrees of freedom required to capture the compaction effect. Layer thickness, as well as density and velocity, must be allowed to vary. In addition, as discussed by Pettersen et al. (2006), the low frequency background model that is often assumed to be constant for time-lapse inversions must also change to capture the changes in the non-reservoir rocks.

The method of inversion of overburden time-lapse time shifts presented offers a potentially quick inversion to estimate reservoir strain compared to an acoustic impedance inversion.

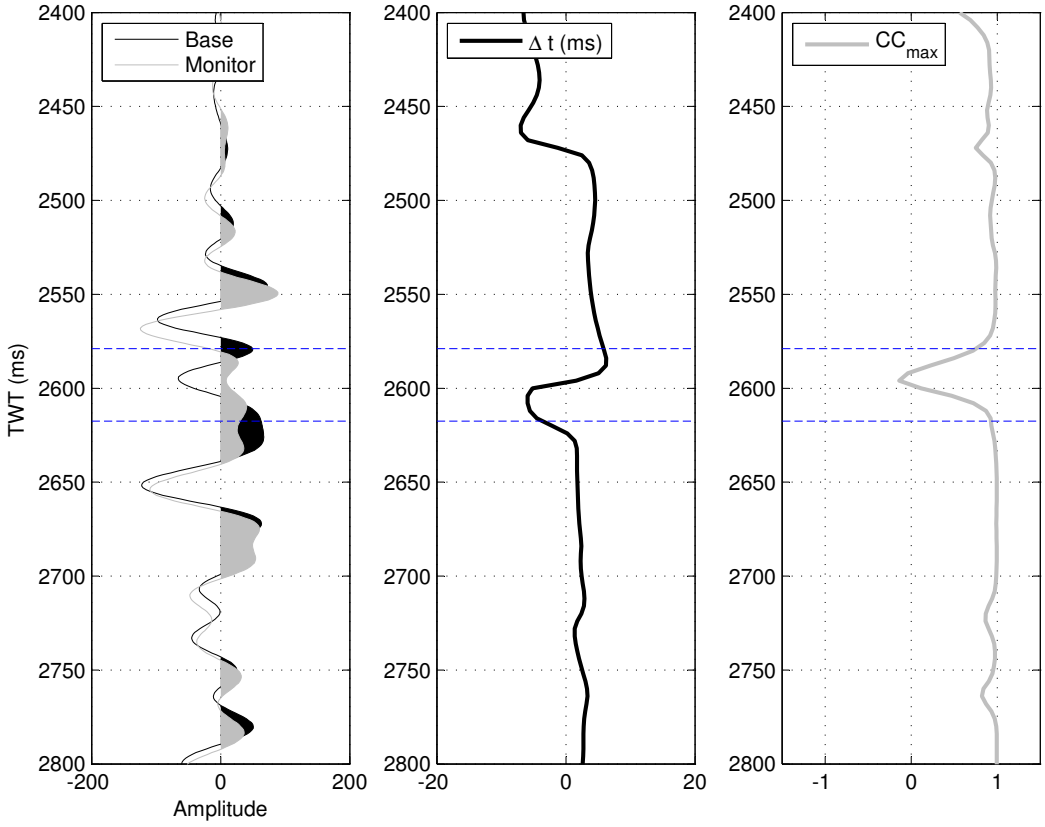

Figure 5.3: *Traces from the LoFS1 and (base) and LoFS6 surveys (monitor) showing reflectivity changes in the reservoir zone. The measured time shift is shown along with the maximum cross-correlation coefficient (CC_{max}) used to calculate the time shift (measured in a 60ms Hanning window). In the reservoir zone CC_{max} decreases as a result of the strong reflectivity change. In such circumstances measuring time shifts based on maximizing the similarity of two signals is inappropriate.*

5.2.1 Scope of the study

Since the inversion technology presented thus far is untested, the aim of this study is to see what the results are possible with limited *a priori* knowledge. This provides a way of evaluating the proposed inversion technique without imposing too many preconceptions about what the answer should be. I will conduct the inversion with only the most basic information required, which is top and base reservoir horizons (in depth) and the time-lapse seismic volumes at the times of interest. Note that no other information such as well-log data is required, which is a distinct advantage over seismic inversion, for example.

5.2.2 Study area

Valhall is a large reservoir, so to make the study manageable a small subarea in the south of the field was chosen. This area is away from the central overburden gas cloud and had good quality P-wave seismic data. Figure 5.4 shows an estimated compaction map for the whole of the Valhall Field at the time of the LoFS6 survey. The study sub-area is identified in Figure 5.4.

5.3 Building a model of the area of interest

In this section I will describe the model building process for the Valhall sector. Once the model is constructed I will have the ability to (a) forward model time-lapse time shifts given a reservoir strain map and (b) invert time-lapse time shifts for reservoir strain.

The model building process involves constructing a block model of the reservoir. The summation of the independent contribution of each block can yield the total stress, strain or displacement at any point in the overburden if an appropriate Green's function is employed.

To build a block model of the sector of interest I was given depth horizons of top and base reservoir. These maps were based on seismic data and as such had a sampling of 25×25m. As discussed in Chapter 4, this sampling is inappropriate

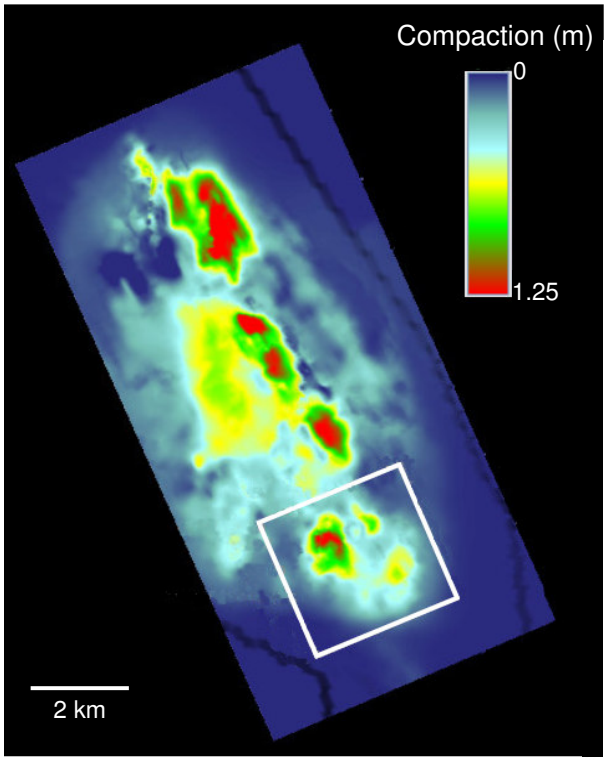

Southern Sector

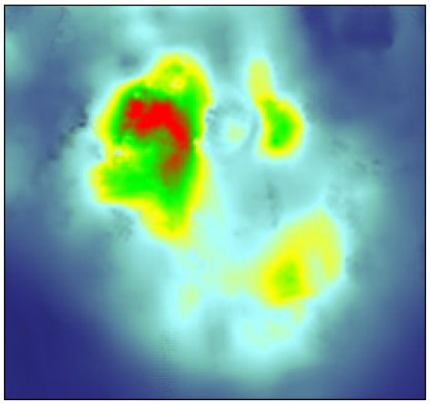

	No. of Lines	Spacing
Inline	110	25m
Crossline	142	25m

Figure 5.4: *The subarea selected for the study. The map shows the estimated compaction of the reservoir between the time of the LoFS 6 and LoFS 1 surveys. The zoom-in box shows the area of interest that will be studied in this thesis. The area consists of a 110 × 142 seismic bins, with a spacing of 25m in both the inline and crossline directions.*

for our inversion as we do not expect to be able to resolve changes to such a high resolution from overburden time shifts. To be consistent with the reservoir engineering and geomechanical modeling scale, I resampled the grid to 100×100m.

As described earlier in the chapter, there is some uncertainty in the initial thickness of the reservoir, because of the low acoustic impedance contrast at top reservoir, which makes the top reservoir difficult to pick on 3D seismic. This uncertainty will be explored later in the chapter as part of the study.

5.4 An linear equation relating time shifts to reservoir strain

In this section I define the equations for the forward modelling of time-lapse time shifts using a reservoir strain map and the inversion of reservoir strain from time-lapse time shifts. Recall that in Chapter 4 I outlined an equation relating time-lapse time strain to vertical strain:

$$\frac{\Delta t}{t} = (1 + R)\varepsilon_{zz} \tag{5.1}$$

This equation gives a linear relationship between the overburden vertical strain ε_{zz} and time strain $\Delta t/t$. The time shift at a given depth was found by integration of the above equation:

$$\Delta t(z) \approx 2(1 + R) \int_0^d \frac{\varepsilon_{zz}(z)}{V_o(z)} dz \tag{5.2}$$

In Chapters 3 and 4 I showed that time strains were convenient because they linearized the problem, allowing for a direct inversion of reservoir strain from the measured time strain. However, since time strains are the derivative of time shifts they are prone to be noisier. I stated that it was preferable to work with time shifts but that the linearization of Equation 5.2 was only possible for constant initial overburden velocity (V_0).

In the case of Valhall we have the special case of being able to assume the initial overburden velocity (V_o) is constant with depth. The overburden velocity model shows no strong deviations and can be approximated by constant mean velocity of

$2000ms^{-1}$ (Barkved, 2008). This assumption was also adopted by Hatchell et al. (2005) who used alternative methods to calculate time-lapse time shifts at Valhall. As I will outline, the assumption of constant velocity means that we can linearly relate time shifts to reservoir strain. As discussed in Chapter 3, time shifts are a more stable product than time strains and, if possible, it is preferable to work with them.

If the initial overburden velocity structure is sufficiently simple that it can be approximated as constant, then we can evaluate the integral between the surface and depth D:

$$\Delta t(D) \approx \frac{2(1+R)}{V_o} \int_0^D \varepsilon_{zz}(z) dz = \frac{2(1+R)}{V_0} [U_z(D) - U_z(0)] + \Delta t_0 \tag{5.3}$$

Equation 5.3 is a simple result, it allows us to think in terms of displacements (U) rather than strain. $U_z(D) - U_z(0)$ is simply the change in path length. The term Δt_0 is the constant of integration. In the case of time-lapse time shifts at an offshore field this would be a result of seafloor subsidence, which increases the travel time through the water layer. It is the case at Valhall and common practice to datum the seismic to the seafloor, which removes the surface subsidence-imprint. Therefore, from herein I remove this term.

In Chapter 3 I showed how displacements, stress, and strain in a linear poroelastic half-space can be written as Green's functions, which are a linear function of reservoir pressure change. Re-writing Equation 5.3 in terms of a discrete Green's function matrix, where the reservoir is described as a series of blocks (see Chapter 4), I arrive at the following expression:

$$\Delta t_M \approx \frac{2000(1+R)C_m}{4\pi V_0} \sum_{n=1}^{N} \Delta p_n G_{n,M} \tag{5.4}$$

where I have defined a new Green's function matrix $G(x, y, z = D) = [U_z(x, y, z = D) - U_z(x, y, z = 0)]$ that describes the overburden stretch (between the surface and the point of interest) at a location, $M = (x, y, z = D)$, due to unit pressure change in the nth reservoir block. The multiplier of 2000 converts the time shift from one way travel time in seconds to two way time in milliseconds. The time shift at a location M is given by the sum over all n pressure sources (see Chapter 4, Figure 4.3). The

term $C_m \Delta P$ gives the volumetric strain ε_v and therefore the above equation can be written in terms of the volumetric strain of each block:

$$\Delta t_M \approx \frac{2000(1+R)}{4\pi V_0} \sum_{n=1}^{N} \Delta\varepsilon_{v,n} G_{n,M} \tag{5.5}$$

5.5 Forward modelling overburden time-lapse time shifts

As what some may describe as a "sanity check" it makes sense to conduct deterministic modelling with a current estimate of reservoir strain. In general, unless our current estimate is in gross error or our modelling assumptions are too limiting, then one might expect a reasonable agreement.

5.5.1 Reservoir strain estimate

A top reservoir displacement map was provided by BP for the time of the LoFS6 survey. Since no information on the displacement of the base reservoir was available I calculated a reservoir strain map assuming uniaxial displacement and no movement of base reservoir. In this case my *a priori* strain estimate is simply $\varepsilon_{zz} = \Delta h/h$, where h is the initial thickness and Δh is the top reservoir displacement. The resulting strains show values as high as several percent.

5.5.2 Visual comparison

Figure 5.6 shows the modelled and predicted time shifts using $R = 5$, $V_0 = 2000 ms^{-1}$ and $\nu = 0.25$ for a depth-slice 100m above the reservoir and for a cross-section through the central time shift anomaly. I will investigate further the sensitivity of the value of R and ν in the next section.

As expected, the qualitative match is good. The anomalies clearly match in location and general shape, even if their magnitude differs slightly. Clearly, increasing the LSF window size reduces the noise without reducing resolution, since the spatial wavelengths in the modelled time shift are also very low. In the following sections I will quantify the goodness of the match.

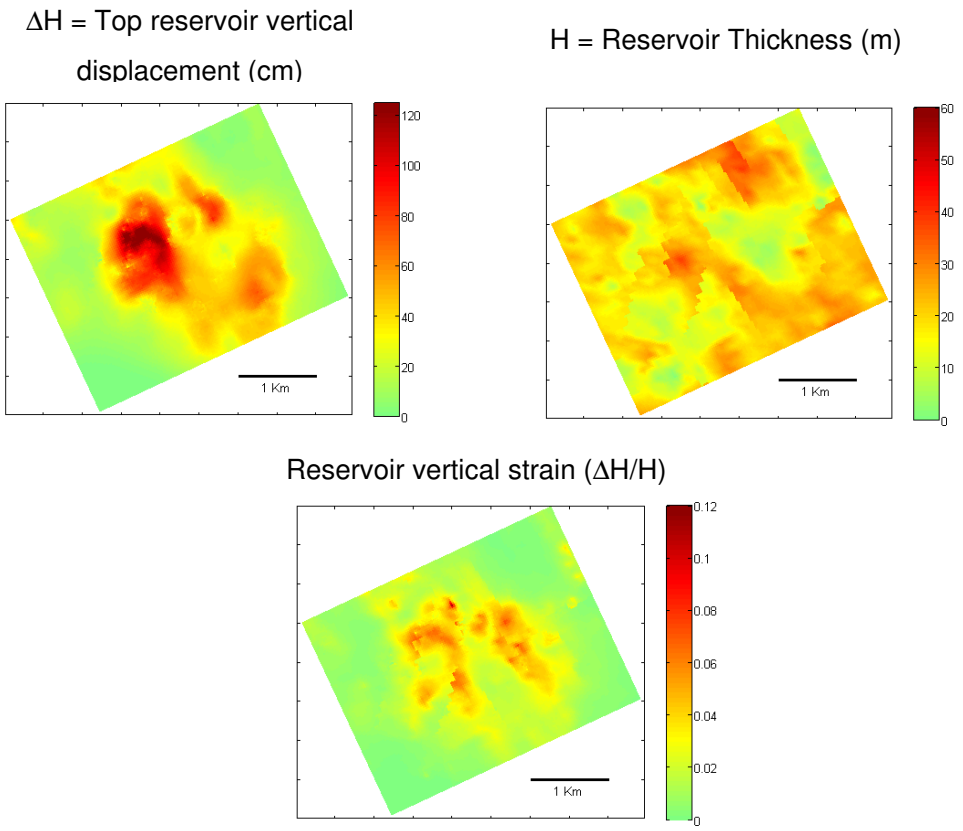

Figure 5.5: *The strain in the area of interest. A map of top reservoir vertical displacement was provided by BP along with the depths of top and base reservoir, from which the reservoir thickness was calculated. The strain was calculated assuming no movement of base reservoir, so that* $\varepsilon_{zz} = \Delta h/h$.

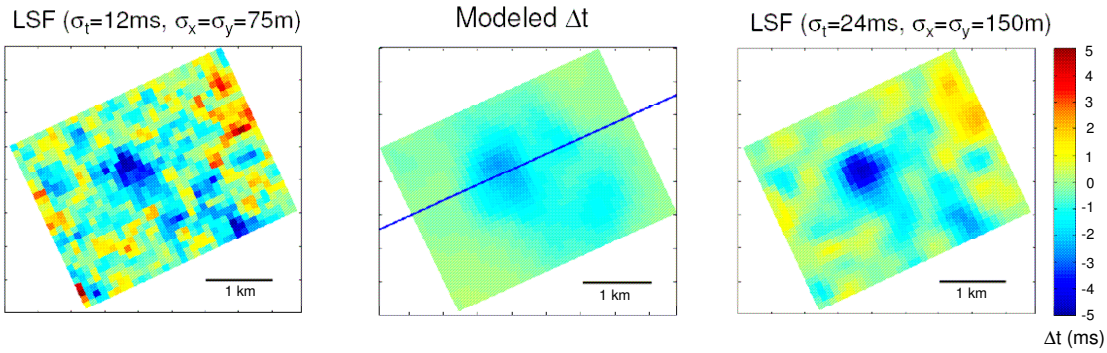

(a) Modelled (centre) and measured time shifts on a horizon 100m above the reservoir. The measured time shifts are for two different LSF parameterizations. The blue line indicates the location of the cross-section below.

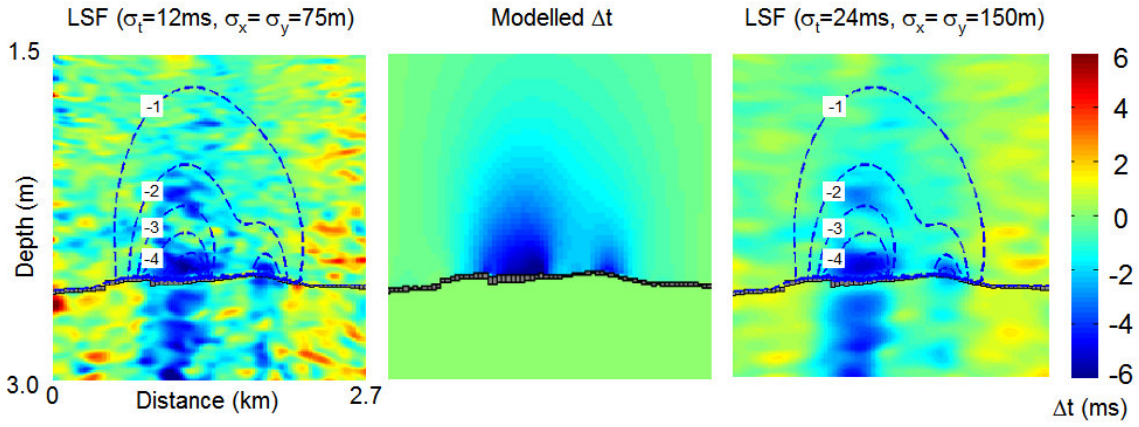

(b) Modelled and measured time shifts shown on a cross-section. The contour lines show the predicted time shift at 1, 2, 3 and 4ms. Note that underburden time shifts were not modelled.

Figure 5.6: *A comparison of modelled and measured time shifts at the area of interest in Valhall using $C = 0.48$ and $\nu = 0.25$. In general the agreement is very good. Note the apparent 'hole' in the centre of the time shift anomaly.*

I chose to show this particular cross-section because during the course of the study I noticed a 'hole' in some areas of the time shift signal (located at approximately 2300m) that is inconsistent with the forward modeled data. I will discuss this further in Section 5.6.

5.5.3 Investigating the sensitivity to R and ν

In order to forward model we have to assess the value of the constants that characterize the problem. As described in Chapter 4, the only parameter that controls the shape of the deformation around the reservoir is the Poisson's ratio, all the other factors simply scale the deformation pattern. In the case of Equation 5.5 we can define a scaling factor C that is given by:

$$C = \frac{2000(1+R)}{4\pi V_o} \tag{5.6}$$

The previous figures show a good qualitative match was achieved with $R = 5$, $V_0 = 2000ms^{-1}$, giving $C = 0.48$. However, as we have an estimate of the reservoir strain, then for any given Poisson's ratio I am able to calculate the value of C that minimizes the misfit between the observed and calculated time shifts. The time shifts were calculated between the LoFS1 and LoFS6 surveys (which is the timing of the estimated compaction map) using a cross-correlation technique. The cross-correlation was performed using a method called Local Shift Finder (LSF) which was discussed in Chapter 3 (Hale, 2007). The technique calculates the time shift by cross-correlating local 3D patches of data which are tapered by Gaussian windows. The Gaussian tapers are defined by their half-widths in the time, inline and cross-line direction, σ_t, σ_x and σ_y respectively.

To calculate the value of C I forward model time shifts at three depth horizons with average distances of 100m, 300m and 500m above the reservoir for Poisson's ratios of 0.1 to 0.45 in steps of 0.05. In principle we could use the whole time shift cube, however using depth slices is convenient from a computational standpoint. Each horizon has 15,620 data points on it, given that the grid spacing is 25×25m and the area of interest is 2725×3525m.

For each forward model a value of C was found that minimized the least-squares misfit between the measured time shifts and the forward modelled time shift. I then

	LSF(σ_t =24ms, σ_x=σ_y=150m)			LSF(σ_t=12ms, σ_x=σ_y=75m)		
		Residuals			Residuals	
ν	C	mean(r)	1 $\sigma_{s.d.}(r)$	C	mean(r)	1 $\sigma_{s.d.}(r)$
0.10	0.50	-0.13	0.62	0.49	-0.12	1.15
0.15	0.48	-0.13	0.62	0.47	-0.12	1.15
0.20	0.46	-0.13	0.62	0.46	-0.12	1.15
0.25	0.45	-0.14	0.62	0.44	-0.13	1.15
0.30	0.43	-0.14	0.63	0.43	-0.13	1.15
0.35	0.42	-0.15	0.63	0.41	-0.14	1.16
0.40	0.41	-0.15	0.63	0.40	-0.14	1.16
0.45	0.39	-0.15	0.64	0.39	-0.14	1.16

Table 5.1: *For each Poisson's ratio ν the scaling factor C which gave the lowest least-squares error between the forward modeled time shifts and the measured time shifts. Two sets of time shift measurements were made using the Local Shift Finder algorithm with two sets of parameterizations for the Gaussian tapers. The mean and 1 standard deviation of the residuals ($r = \Delta t_{modeled}$ - $\Delta t_{measured}$) are also presented.*

characterize the goodness-of-fit of a particular combination of Poisson's ratio and C by examining the mean and 1 standard deviation ($\sigma_{s.d.}$) of the residuals. The results are reported in Table 5.1.

The results presented in Table 5.1 show that the value of C is reasonably consistent and lies between 0.39 and 0.5. An analysis of the residuals shows that the mean and standard deviations are also consistent between each Poisson's ratio tested. Intuitively one can see that no distinction can be made between any of the combination of Poisson's ratio ν and the C value. It is also clear that the larger windows used to calculate the time shift substantially decrease the standard deviation of the residuals.

Two standard statistical tests are appropriate to give a firmer basis to these observations. First, a series of F-tests (see Davis and Sampson, 1986, for example) reveal that for each separate LSF parametrization we can not distinguish between the variances of the models with a significance level of 99%. Second, a series of t-tests are used to test the hypothesis that we can not distinguish between the means of the models. The t-test assumes (see Davis and Sampson, 1986, for example) equal variances, which the F-test showed to be an acceptable assumption. The result of the t-tests showed that we can not distinguish the means of the models within a significance level of 99%. These two statements together suggest that for the current estimated strain distribution all models fit the data equally well. Clearly,

the sensitivity of the model to Poisson's ratio is less than the noise observed in the time shift data.

A further observation is that the best fit to the time shift data gives residuals that are slightly biased below zero. This may be due to the presence of some areas of positive time shift which the current model does not predict. These are thought to be acquisition related (see Figure 5.6 for more detail).

If we examine the standard deviations of the two different LSF parameterizations then it is clear that using a larger window has the desired effect of reducing the noise without biasing the result. The standard deviations are reduced by approximately half without significantly changing the mean.

5.5.4 Interpreting the value of C

So how does our range of C values derived from the matching process compare with the value of C we might predict using our current estimate of R and V_0? The value of R at the Valhall field has been independently estimated as 5 by Hatchell et al. (2005) and 5.7 by van Gestel et al. (2008a). These would give theoretical values of C=0.48 and C=0.53 respectively, assuming $V_0 = 2000ms^{-1}$, which are consistent with the observed values over the range of Poisson's ratios.

5.6 The effect of residual multiple energy on overburden time-lapse time shifts

The 'hole' in the time shift data which can clearly be observed in Figure 5.6(b) requires some further investigation. Several hypotheses were considered such as whether the geomechanical model is too simple (e.g. the anomaly could be explained by material contrasts), or if there are fluid effects in the overburden such as migrating gas or pore pressure changes in the shales overlying the reservoir offered an explanation. However, a paper by Hatchell and Wills (2007) suggested that these data may be explained by time-lapse multiple interference. Hatchell and Wills (2007) looked at the behaviour of time-lapse time shifts inside the central gas cloud region and found that these were strongly correlated to the water velocity variations between

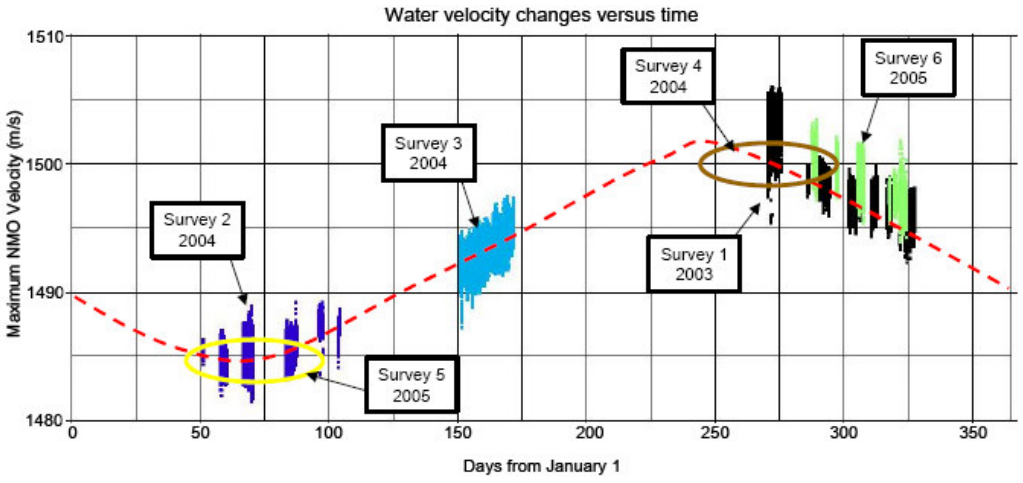

Figure 5.7: *Seasonal variations in water velocity at Valhall as measured and presented by Hatchell and Wills (2007).*

time-lapse surveys. Subtle differences in acoustic velocity of the water column occur mainly because of seasonal variations in water temperature (Kommedal et al., 2005). Figure 5.7 shows the seasonal variations in water velocity as reported by Hatchell and Wills (2007). A correlation between time shifts and water velocity variations indicates a relationship to residual multiple energy that has not been removed from the seismic data. In this section I carry out a similar analysis to Hatchell and Wills (2007) on the data from the area of interest covered by this chapter.

As I discussed in the introduction, the acquisition of multiple time-lapse surveys over the Valhall field offers new possibilities for time-lapse seismic. Not only does it allow us to gain even more insight into the dynamic evolution of the reservoir (Floricich, 2006, e.g.), but it also enables us to approach traditional seismic processing problems in a new light. For example, Calvert (2005) identifies a multiple suppression technique that is only possible using three or more time-lapse surveys. With six LoFS surveys available at Valhall we have a unique opportunity to study certain phenomena.

Figure 5.8(a) shows a cross-section of the modelled and estimated time shifts with three areas of interest marked on them, one just above the reservoir, one where the multiple interference is suspected and a third area above this. First, I will examine the evolution of the time shifts relative to the first LoFS survey (LoFS1). I examine the average time shift in a small 16ms×250m×250m patch of data. Figure 5.8(b) shows the evolution of these time shifts with each LoFS survey.

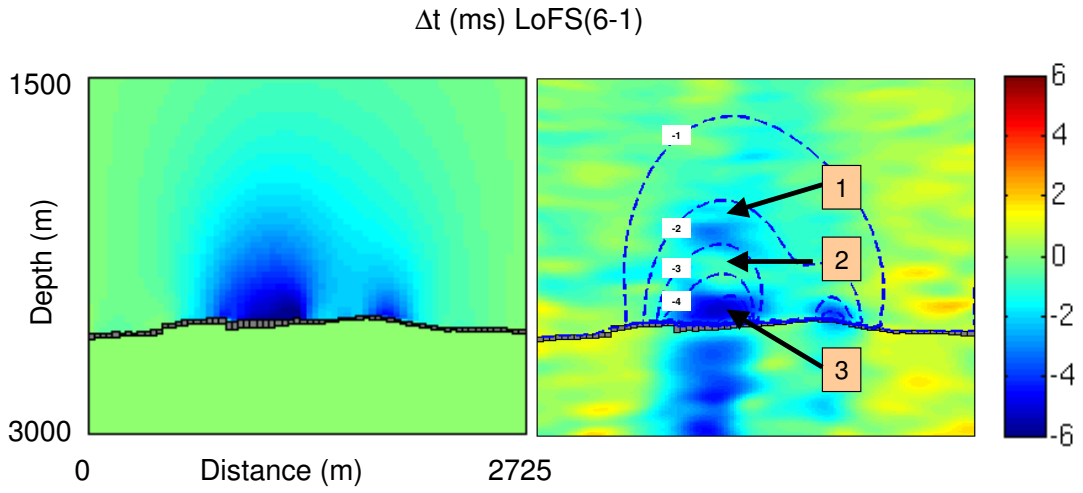

(a) A cross section of the time shift between LoFS1 and LoFS6. Three regions are identified for analysis: 16ms×250m×250m windows centered at 2566ms, 2400ms and 2200ms.

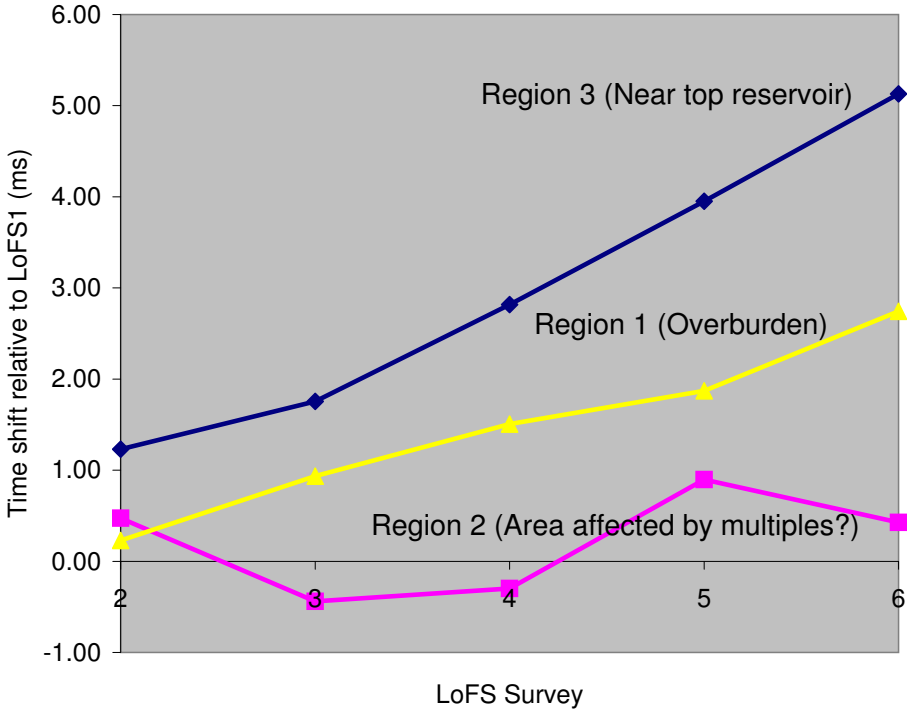

(b) The time-lapse time shift in each of the three regions relative to LoFS1.

Figure 5.8: *Investigating the overburden time-lapse time shift anomaly.*

Regions 1 and 3 show increasing time-lapse time shifts with time (note they are plotted as a function of LoFS survey, not as a function of real time between surveys). Region 2 lies in between regions 1 and 3 in depth. Geomechanical principles dictate that deformation will decay with distance from the reservoir, assuming a linear-elastic overburden. Even if strong material contrasts were introduced in the overburden this would only change the *rate* of decay. Therefore, we would expect the magnitude of time shifts in region 2 to lie between the time shifts above and below it, assuming the R factor model holds, which is reasonable given the quantitative match I showed in the earlier section.

Next I examine the theory that the mismatch is caused by time lapse multiple interference. Using a Taylor expansion for the theoretical trend line for time shift caused by water velocity changes for a water column of depth D, initial water velocity V_0 and a change in velocity of ΔV is given by:

$$\Delta t = 2000D\left[\frac{1}{V_0} - \frac{1}{V_0 + \Delta V}\right] \approx -\frac{2000D}{V_0^2}\Delta V \tag{5.7}$$

where the value 2000 converts from one-way travel time in seconds to two-way travel time in milliseconds. To examine if the time shifts in a particular region are correlated to the water velocity variations I will calculate the value of Δt in each of the three regions over a range of water velocity variations. This is only possible because we have six LoFS surveys with which to work with. I calculate time shifts for the following combinations of surveys:

- LoFSn LoFS1 (for n = 2, 3, 4, 5, 6)
- LoFSn LoFS2 (for n = 1, 3, 4, 5, 6)
- LoFSn LoFS3 (for n = 1, 2, 4, 5, 6)

The value of the water velocity change ΔV between the above combinations of surveys will be calculated from Table 5.2, which was derived from the data in Figure 5.7.

The plots in Figure 5.9 clearly suggest that the time shifts in region 2 show a correlation to water velocity changes. Although the correlation coefficient (R^2 value)

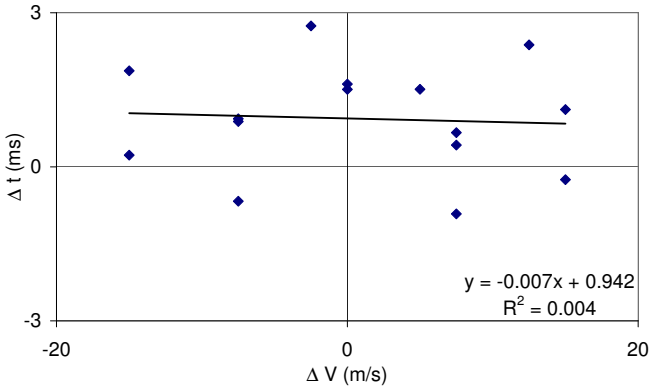

(a) Region 1

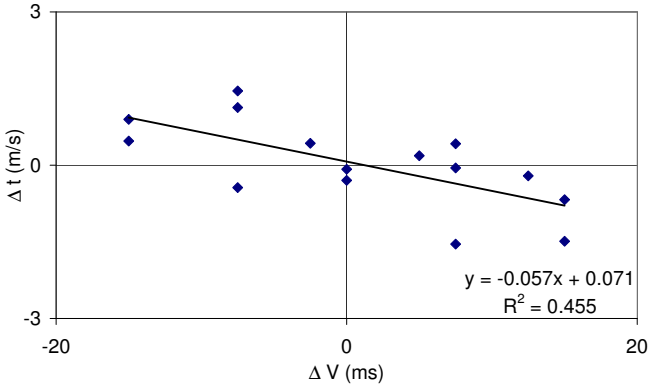

(b) Region 2

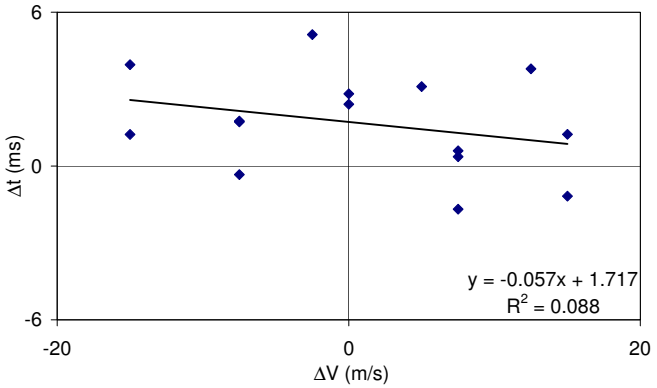

(c) Region 3

Figure 5.9: *A plot of time shift against water velocity variations in the three regions of interest identified in Figure 5.8. Note there is a clearer correlation between water velocity changes and measured time shift in region 2 compared to regions 1 and 3. The least-squares fit to a straight line is shown for each region, along with the equation and R^2 value*

LoFS survey	Water Velocity (m/s)
1	1500.0
2	1485.0
3	1492.5
4	1500.0
5	1485.0
6	1497.5

Table 5.2: *Water velocities at the time of the Valhall LoFS surveys as derived from Figure 5.2.*

is only 0.46, it is an order of magnitude higher that the other two regions (0.089 and 0.004). The theoretical trend, based on a water depth of 69m and an average reference water velocity of 1492m/s is $\Delta t = -0.062\Delta V$. The measured best fit line, with standard errors is $\Delta t = (-0.057 \pm 0.017)\Delta V + (0.07 \pm 0.17)$. I conclude that the measured time shifts in the region 2 are consistent with time shifts generated by residual multiple energy.

Summary

The objective of this section is to demonstrate an example of the uncertainties and errors involved in the estimation of overburden time shifts which were raised but not specifically addressed in Chapter 3. The work in this section has demonstrated that:

- Forward modelling using the current reservoir strain estimate provided a good match to the observed time shift, despite the use of a simple geomechanical model based on a homogeneous half-space.
- Where the modelled and observed data showed a mismatch I was able to identify an area for further investigation.

These two points show that simple, quick and cheap geomechanical modelling can be useful for deterministic forward modelling.

Methods of multiple removal are beyond the scope of this thesis and so I do not address ways to correct for the multiple contamination observed. For the inversion of time shift data, I propose a horizon-based approach, which will allow me to simply avoid the contaminated area, by selecting horizons above or below it.

5.7 Inversion for reservoir strain from time-lapse time shifts

Equations for forward modelling time shifts have been presented earlier in this chapter. The same equations can also be used to invert observed time shifts. There are three main processes involved in the inversion: Defining the reservoir geometry, geomechanical parameters and velocity strain relationship; Defining the time shift data that will be used as an input to the inversion; and finally defining the inversion algorithm and parametrization. I will discuss each of these areas in more detail below.

Model parametrization

The reservoir geometry is the same as outlined for the forward modelling process. The reservoir is defined by splitting it into blocks with a lateral extent of 100×100m. The thickness is given by the average thickness of the reservoir over the block, which is derived from a map provided by depth-converted seismic interpretation. As discussed earlier, there is some uncertainty about the thickness of the reservoir because the top reservoir reflectivity is difficult to interpret on the seismic data. I will address these uncertainties in reservoir thickness in a later section. For the first inversion run I will assume that the reservoir geometry provided by BP is accurate.

In addition to the geometry, three further parameters are required for Equation 5.5: R which couples the strain in the overburden to the change in velocity; the initial velocity of the overburden V_0; and Poisson's ratio ν which controls the geomechanical deformation. By forward modelling based on the current reservoir strain estimate provided by BP, I found the data was consistent with other published observations giving $R = 5$ and an initial overburden velocity of $2000ms^{-1}$. These factors only scale the magnitude of the solution and have no influence on the spatial distribution of the reservoir strain, therefore, it is not critical to have these values correct to a high degree of accuracy. However, it is crucial that these parameters are of the correct order of magnitude, otherwise the inversion may be badly scaled. The choice of Poisson's ratio was found to have a limited impact on the goodness-of-fit to the observed time shift data in the range $0.1 \geq \nu \leq 0.45$, implying that the sensitivity of the model to Poisson's ratio is less than the noise observed in the time shift data, making the choice of Poisson's ratio essentially arbitrary in this range. I therefore

chose $R = 5$, $V_0 = 2000ms^{-1}$ and $\nu = 0.25$ as my modelling parameters.

Choice of time shift data

As demonstrated in Chapter 4, data closest to the reservoir will control the highest frequencies of the inversion result. Therefore, it is best to choose a horizon which is parallel to the reservoir. Since the area of interest is dipping, I extract a horizon that is simply the top reservoir horizon moved up by 100m. I chose 100m because it is outside the zone which was identified as being contaminated by multiples, but also far enough away from the reservoir to not feel the influence of near field effects, such as the bias of time shift measurements or inaccuracies with the geomechanical model which where discussed in Chapter 3.

Inversion

For the inversion I use a least-squares algorithm with a non-negative constraint, i.e. a least-squares solution is found under the conditions that all strains are positive. This is reasonable given that the area is depleting and we expect only compaction. I stabilize the spatial distribution of the solution using weighted second order Tikhonov regularization. The weight given to the regularization is determined by the L-curve method as described in Chapter 4.

5.7.1 Inversion results

The results of the inversion are presented in Figure 5.10. The inverted volumetric reservoir strains are shown alongside the current strain estimation map for comparison. In addition to the reservoir strain, well paths are included, with perforations marked as diamonds.

In general the agreement is good, especially the shape of the depletion pattern. The magnitudes are clearly different, but, as discussed, the scaling of the inversion does not alter the resulting shape of the inverted solution. The cause of the differences in the magnitude could lie with a number of problems:

- The original assumption of uniaxial strain conditions used to create the reservoir strain from the top reservoir vertical displacement map provided by BP.
- The assumption of an isotropic homogenous half-space.
- Uncertainties in the values of R and V_0.

Table 5.1 shows that forward modelling using the current simulator estimate underestimated the overburden time shifts by approximately 0.13ms (the mean of the residuals was -0.13ms) with standard deviation of 0.62ms. The residuals for the inverted data have a mean of -0.2ms with a standard deviation of 0.38ms. The inverted strain map fits the observations with more confidence (the standard deviation is approximately one third lower). However, the mean of the residuals is still biased. This is a result of putting a non-negative constraint on the inverted strains, which will have the effect of not allowing the prediction of positive time shifts in the overburden. This is a reasonable constraint as we expect only compaction in the reservoir and only negative time shifts based on our forward modelling earlier in the chapter. Figure 5.11 compares the measured time shift data to time shifts modeled using the inverted strain map, along with the difference between the two. An area affecting the residuals is in the top right corner which shows an area of positive time shifts. Further investigation showed that this is most likely related to problems with acquisition and processing.

Figure 5.12(b) shows a depth slice through the time shift cube at 300m which has the receiver lines plotted in addition. Striping is observed in the direction of the receiver lines. The cross section (Figure 5.12 (a)) shows that the striping is more prominent in the shallow overburden, and appears to attenuate with depth, although the effects are still seen at reservoir level.

Removing the biased data (15% of the total number of data points) from the calculation of mean and standard deviation of the residuals shows that it does indeed have an impact. The mean and standard deviation are reduced to -0.07ms and 0.19ms respectively.

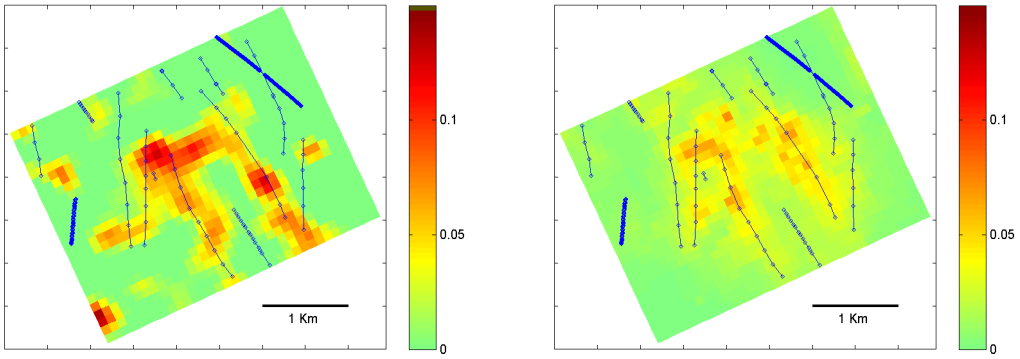

(a) Inverted volumetric strain.

(b) Current simulator estimate of volumetric strain.

Figure 5.10: *Results of the inversion for volumetric reservoir strain (a) compared with the current strain estimate based on geomechanical modelling (b). The color scale shows the fractional volumetric strain.*

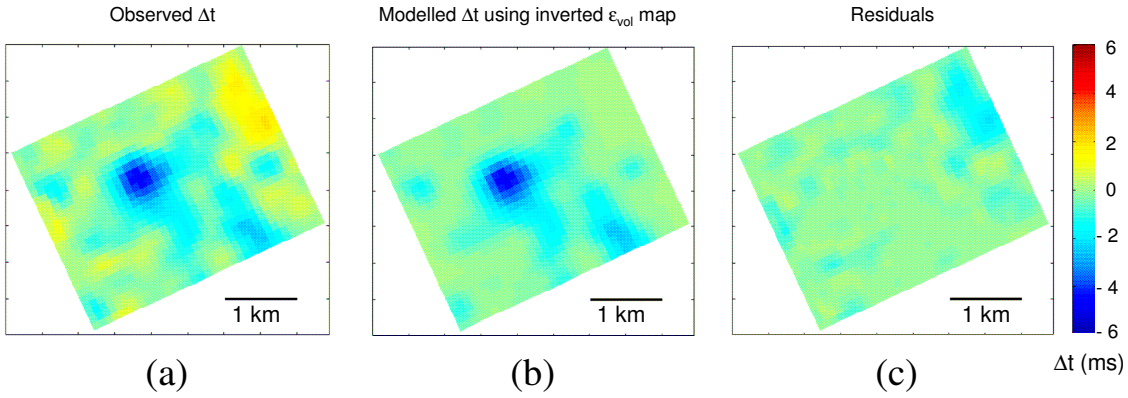

Figure 5.11: *The measured time shift data (a), time shifts modeled using the inverted strain map (b) and the difference between the two (c).*

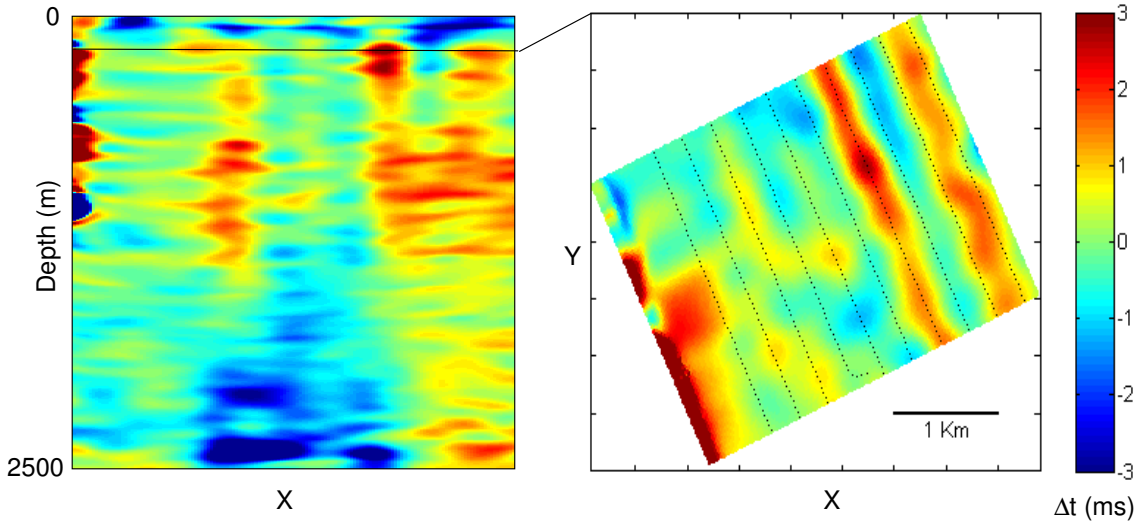

Figure 5.12: *A cross-section through the time shift data (a) clearly shows striping of positive time shifts. Figure (b) shows a depth slice at 300m with the receiver lines marked. Clearly the striping is in the direction of the receiver lines, inferring that they are related to acquisition and/or processing.*

5.7.2 Investigating uncertainty in reservoir thickness

As mentioned earlier in the chapter, a key uncertainty is the thickness of the reservoir, which may be in error because of the difficult interpretation of the top reservoir horizon on the seismic data.

What happens if the reservoir thickness is incorrect? In Chapter 4 I showed that, under the assumption of a linear elastic deformation in a half-space, deformation outside a reservoir can be described by summing the contributions of depletion in a series of cuboids:

$$u_i = \sum_{n=1}^{N} \varepsilon_{v,n} \int_{V_n} G_i(\boldsymbol{x}, \zeta) dV_n \tag{5.8}$$

where V_n and $\varepsilon_{v,n}$ are the volume and average volumetric strain over the nth cuboid respectively. Thus, if two cuboids experience the same change in volumetric strain, a larger one will produce larger overburden deformation, since the integration is over a bigger volume. In general, our reservoir will be made of cuboids that are evenly

spaced laterally (e.g. 100×100m in this case) but vary in thickness. Therefore, variations in the integration volume come from variations in the reservoir thickness.

Imagine a reservoir of constant thickness with uniform depletion. If the thickness of one reservoir block is in error we may not necessarily find that the inversion returns an anomalous result at that cuboid, especially if smoothing constraints have also been imposed. Instead, because the overburden deformation at any given point is the sum of the contributions of all blocks, then the error can be distributed over the other cuboids in the reservoir.

To demonstrate this I invert the Valhall data, assuming a constant reservoir thickness of 19m - the average reservoir thickness. Figure 5.13(a) shows the ratio of the constant thickness to the previous reservoir geometry and, therefore, highlights areas where the thickness is much greater or smaller. Two areas of interest are highlighted where, by assuming a thickness of 19m, the thickness of those cells is increased by up to a factor of four, relative to the original thickness. However a comparison of the inversion results (Figures 5.13(b) and (c)) shows that the change in reservoir geometry has very little effect in the visual appearance of the reservoir strain. An examination of the least-squares error between the modelled and observed overburden time shifts gives a root mean squared error of 0.43ms using the original reservoir geometry, and 0.63ms using a uniform thickness, so mathematically we can conclude that the original geometry fits the data more accurately.

A suggestion for inverting reservoir strain when the reservoir thickness is uncertain, would be to conduct a probabilistic joint inversion for reservoir strain and initial thickness. In this case a probability density functions (pdf's) would be defined for reservoir thickness and strain. An approach such as Monte-Carlo simulation could then be used to find, in a probabilistic framework, the initial thickness and volumetric strain that best fit the observed time shift data. I leave this as a suggestion for future work, since the approach of this thesis has been to concentrate on linear inversion.

5.8 Summary

This chapter has combined the material presented in Chapters 3 and 4, culminating in the inversion for reservoir strain at a sector of the Valhall field.

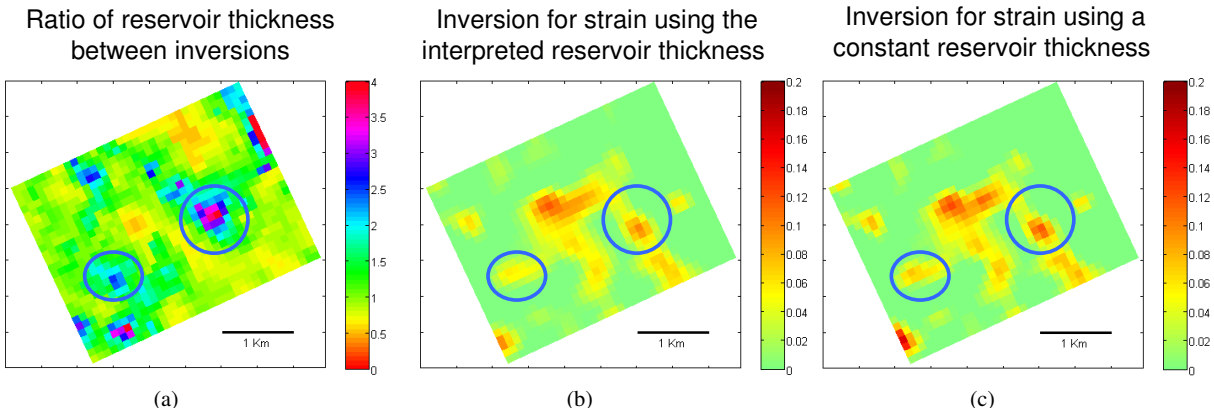

Figure 5.13: *Investigating the effect of uncertainty of the reservoir thickness. Two inversions are conducted: (b) using the reservoir geometry provided by BP; and (c) one that assumes the reservoir has a uniform thickness. Figure (a) shows the ratio of the uniform thickness (19m) to the original thickness.*

First, a time shift analysis was presented. Some observations made in Chapter 3 about the difficulty of measuring time shifts in the reservoir zone were highlighted. It was found that reflectivity changes in the reservoir zone compromised the integrity of the time shift estimate using similarity-based algorithms. More complex processing, such as acoustic impedance inversion, would be needed to unravel the combination time shifts in the overburden, underburden and reservoir along reflectivity changes. The motivation for this thesis is to present an inversion for reservoir strain from overburden time lapse time shifts, which is simple to apply and requires substantially less *a priori* information than current alternatives.

Next, a formulation for linking time-lapse time shifts directly to reservoir strain was presented. This took advantage of the relatively homogenous properties of the overburden at Valhall that allow the approximation of a uniform initial velocity.

Forward modelling using an existing reservoir strain estimate revealed that the approximation of a homogenous linear elastic half-space was able to produce a good match to the observed time-lapse time shifts. An investigation into the sensitivity to the choice of Poisson's ratio revealed the sensitivity of the model to Poisson's ratio to be less than the uncertainty observed in the time shift data.

Forward modelling also suggested that the overburden time-lapse time shifts showed

areas of correlated noise. First, an analysis of an anomalous region of time shifts suggested a relationship to residual multiple energy. This section of the chapter was able to capitalise on the availability of frequently acquired data at Valhall. Other anomalous time shifts were observed that correlated very well with the receiver lines, suggesting the origin of the noise is related to acquisition and/or processing.

Time-lapse time shifts from a horizon 100m above and parallel to the top reservoir were chosen as an input to an inversion for reservoir volumetric strain. The inversion results are promising, showing good similarity to the current strain estimate. An analysis of the sensitivity to the reservoir thickness was also examined, in light of concerns about uncertainties in the seismic interpretation of top reservoir. I compared two inversions: One using the reservoir geometry provided; and one that assumed the reservoir had a uniform thickness. The results were visually similar, although the inversion which assumed uniform thickness showed a larger least-squared error.

The method presented shows considerable promise. The goal of this chapter was to verify that the theoretical basis for the inversion and forward modelling of time-lapse time shifts produced reasonable results when used with real data. This chapter has shown that in the geological setting of Valhall the framework proposed gives promising results.

As highlighted earlier in the chapter, the semi analytical formulation, when compared to finite element modeling for example, make the approach simple, fast and cheap for both forward modeling and inversion. The forward modeling has shown some practical value, by identifying anomalous areas of time-lapse time shift for further investigation. The next step, once we have more confidence in the inversion result, is to understand how or if the inversion results can contribute to answering any unresolved questions about reservoir performance. Of course, in that respect the results of such an inversion are only a small part of a much larger puzzle.

CHAPTER

SIX

Inverting for reservoir compaction using time-lapse time strains: Application to the Genesis Field

In the previous chapter I studied a sector of the of the Valhall field in the North Sea. In this chapter I will apply a similar inversion approach in a very different geological setting: the Genesis Field, a stacked deepwater turbidite reservoir located in the Gulf of Mexico.

6.1 Introduction

In the previous chapter I studied a sector the of the Valhall field in the North Sea. The setting was a weak chalk reservoir with compaction confined to a single layer of 20m average thickness. I used overburden time-lapse time shifts as input to an inversion for reservoir strain. In this chapter I will apply a similar inversion approach in a very different setting: the Genesis Field, a stacked deepwater turbidite reservoir located in the Gulf of Mexico.

6.2 The Genesis Field

6.2.1 Location and geology

Genesis Field lies 150 miles southwest of New Orleans in the Gulf of Mexico and encompasses parts of Green Canyon Blocks 160, 161, and 205. The operator is Chevron, with ExxonMobil and BHP Billington as partners. Water depth across the field varies between 750 and 850m. The reservoir is at a depth of approximately 4000m.

Figure 6.1: *Map showing the location of the Genesis Field, which lies approximately 150 miles southwest of New Orleans, USA.*

Genesis field consists of several stacked Plio-Pleistocene turbidite sandstone reservoirs which lie on the eastern flank of a salt-cored anticline. There are three main producing intervals, named N1, N2, and N3, which are part of a group of

sands labelled the N-series. The sand-rich intervals in the N-series are in the range of approximately 0-33m thick, contain intra-reservoir shales in the ranging of approximately 15-45m thick. The producing N-sands are located on the hanging wall of an east-dipping normal fault on the eastern flank of the anticline. Reservoirs dip between 15° and 40° and pinch out towards the fault, which forms the updip limit of the hydrocarbon accumulation. In addition, there are two deeper late-Pliocene age reservoirs, called the 14200ft sand and the 14800ft sand. The sands are unconsolidated and have high-porosity (23 to 32%), high net-to-gross (0.7 - 1.0), and high permeability (over 1 darcy). The very high porosities are a consequence of rapid burial, which caused the development of overpressure that inhibited normal compaction, along with reservoir temperatures that are too low for the initiation of quartz cementation (Sweet and Sumpter, 2007). Figure 6.2(a) shows a schematic cross-section through the reservoir and Figure 6.2(b) shows an example log.

6.2.2 Production history and compaction

Since first oil in 1999, the field has been produced under primary depletion drive. Although there is a moderate natural water drive in parts of the field, there have been large pressure declines. The initial reservoir pressure was between 55-60 MPa, with a typical bubble point pressure of 40MPa. By the time of the monitor survey, the reservoirs had depleted by up to 30 MPa around some of the wells, with an average depletion of around 20MPa. Sands are over-pressured by approximately 15MPa. The combination of overpressure and the unconsolidated, weak nature of the sands means that reservoir compaction is likely. Unfortunately, there are no physical measurements of reservoir compaction at Genesis. Radioactive bullets were installed during the initial completion of the shales just above the reservoir interval. However, a baseline log for the bullets was never run (Pourciau et al., 2005).

Reservoir compaction has been inferred from three major sources of data: Permeability loss; time-lapse seismic; and well failures. Pourciau et al. (2005) reports that, in the first four years of production, many wells displayed decreasing permeability, which, after ruling out other possible causes, was determined to be caused by compaction. In some cases permeability losses as high as 80-95% of the initial permeability were implied. As I will discuss in the next section, time-lapse seismic observations of overburden time shifts supported the theory of strong reservoir compaction, with significant time shifts outside the reservoir suggesting overburden

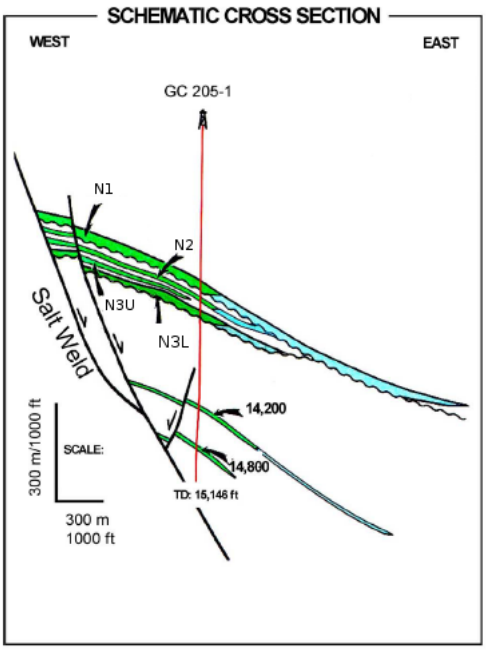

(a)

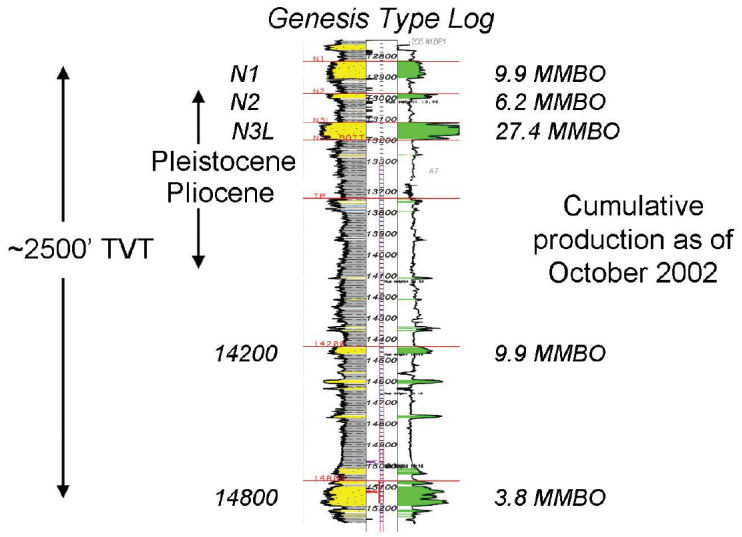

(b)

Figure 6.2: *(a) Schematic cross section of the Genesis Field showing main reservoir intervals (N1, N2, N3L, 14,200-ft sand and 14,800-ft sand), faults, and the salt weld that lies west of the field. Adapted from Sweet and Sumpter (2007). (b) Genesis type log showing gamma ray log (left, yellow), which indicates areas of high-quality reservoir sand and resistivity (right, green) with indicates the presence of hydrocarbons, alongside cumulative production in each of the sands at October 2002, the time of the time-lapse monitor survey.*

stretching. Hudson et al. (2005) report that within nine months of the time-lapse seismic observations four wells failed due to compaction-related shear failure. The failed wells were all completed in areas of pure depletion drive and had high inclinations (between 20 ° and 50 °).

6.2.3 Description of the time-lapse surveys

Time-lapse seismic data at Genesis consists of a pre-production base survey shot in 1991 and a monitor survey acquired in October 2001, three years after production started. An overview of the time-lapse acquisition and processing at Genesis is given by Magesan et al. (2005). The monitor survey was acquired with the time-lapse product in mind, so the monitor acquisition parameters were chosen to replicate the base survey as closely as possible. However, since the monitor was shot 10 years after the base survey, acquisition choices were also made to maximize the potential of the monitor survey as a high resolution 3D survey, in addition to its use as a time-lapse survey. The intention was to use the improved 3D seismic data to improve static reservoir characterization. For example, larger offsets allowed AVO (amplitude verses offset) signatures to be used, because the farthest offsets of the monitor survey extend to 45 ° compared to the baseline which only went out to 30 ° (Hudson et al., 2005). In addition, the monitor survey was acquired with smaller capacity sources and shallower source/streamer depths, resulting in broader frequency content for the acquired data (Magesan et al., 2005). A summary of survey parameters is provided in Table 6.2.3.

To account for these differences in acquisition parameters, pre-stack co-processing and cross-equalization of the base and monitor seismic data were performed.

6.2.4 Initial 4D observations

The initial 4D observations were reported in Hudson et al. (2006) and Hudson et al. (2005). Alongside some reservoir level 4D differences related to depletion and saturation changes, time-lapse differences were also observed in the overburden. Figure 6.3 shows a line through the time-lapse difference cube. Along with the large differences seen at reservoir level, differences are observed at the Wet Illinoian Sands, a good reflector approximately 300m above the reservoir. These differences

Parameter	Baseline	Monitor
Acquisition year	1991	2001
No. of steamers	2	8
No. of sources	1	2 (dual boat)
Max. offset	5000m	7200m
Channel / streamer	180	576
Bin size	12.5×37.0m	12.5×37.0m
Fold	90	96
Gun depth	7.5 m	6.0m
Streamer depth	10.0 m	8.0m
Gun volume	6324in^3	3090in^3
Direction	N-S	N-S

Table 6.1: *Acquisition parameters for the base and monitor surveys at Genesis. After Magesan et al. (2005)*

are attributed to reservoir compaction causing overburden dilation and a reduction in overburden velocities. These observations were published about the same time that other authors were reporting similar compaction-related 4D differences outside compacting reservoirs (e.g. Hatchell and Bourne, 2005b; Kristiansen et al., 2005; Tura et al., 2005), lending further weight to the argument that reservoir compaction caused observable non-reservoir time-lapse changes.

6.2.5 Cross-equalization over compacting reservoirs

In the previous section I described the acquisition and processing of the Genesis time-lapse data. Interestingly, the article by Magesan et al. (2005) does not discuss these overburden changes in the context of cross-equalization. Initially, the cross-equalization produced an unsatisfactory time-lapse product when the matching operators were derived in the overburden above the reservoir. A much better time-lapse product was achieved when matching operators where derived in an area down dip of the reservoir, but, this left overburden time shifts above the reservoir. At the time the reason was not clearly understood (Hudson, 2005, pers. comm.).

In Chapter 2 I performed a literature search showing that there are now many examples where time-lapse time shifts are observed above compacting reservoir. In this context, these time shifts are now accepted as a production-related change and not an artifact of acquisition and/or processing. This above anecdote about

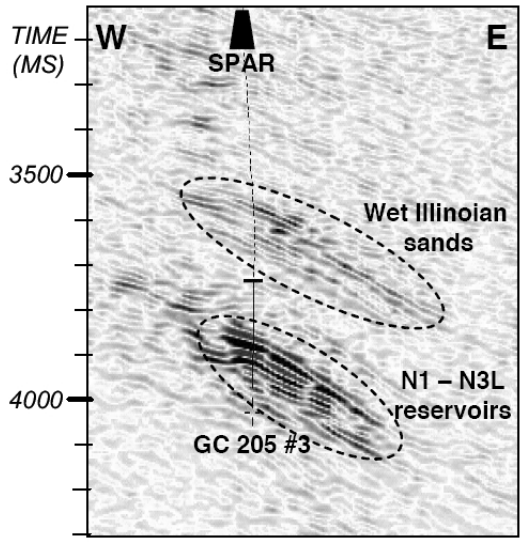

Figure 6.3: *Initial published time-lapse differences (raw substraction of the seismic data) at Genesis Field from Hudson et al. (2005). Significant time-lapse differences where observed in the overburden in addition to the expected time shifts observed at reservoir level. The differences in the overburden are attributed to time shifts caused by reservoir compaction and overburden dilation.*

the discovery of overburden time shifts at Genesis reveals two points. First, and most importantly, it reveals that there may be data in time-lapse surveys that we may simply miss because it is processed away as noise. Secondly, it shows that if cross-equalization is required on time-lapse surveys over compacting fields, there must be sufficient good quality data away from the reservoir in which to derive the cross-equalization parameters. In general, however, repeat surveys will cover a more limited area than a base survey, focusing on the lateral extent of the reservoir, making time and cost savings in acquisition and processing. As such, a suitable control area may not be available, unless compaction and overburden expansion was previously considered.

6.3 Time shifts and time strains at Genesis

Since the initial observation of overburden time-lapse time shifts the desire to maximize the potential of the Genesis time-lapse data has led to significant developments in time-lapse time shift analysis. First, a recursive algorithm for cross-correlation was developed, which provided a computationally efficient algorithm for

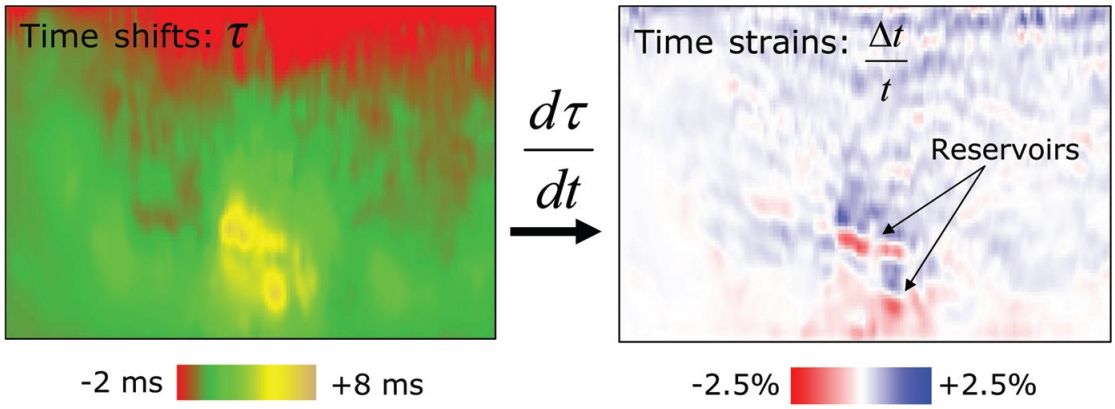

Figure 6.4: *(a) Time shifts calculated at a cross-line through the Genesis reservoir (b) time strains. Note how the time strain is instantly more interpretable. A clear distinction can be made between velocity slow-down in overburden (blue) and the speed-up in the reservoir (red). After Rickett et al. (2007a).*

cross-correlating 3D patches of data in the vertical (time) direction (see Rickett et al., 2006). However, as discussed in Chapter 3, the approach has its limitations. A second approach, which was also introduced in Chapter 3, of non-linear time shift inversion was applied, which finds the time shift $\tau(t)$ that maps the base $x_1(t)$ to the monitor data $x_2(t)$ by minimizing the least squared difference $E = |x_1(t) - x_2(t + \tau(t))|^2$. Crucially, the inversion uses spatial constraints to favour trace to trace consistency and a stable first time derivative of the time shifts.

The advantage of this new approach is the ability to produce stable estimates of time strains in comparison to cross-correlation based measurements. As identified in Chapters 3 and 4, time strains have the advantage of being instantaneous measurements, which avoids the non-linearity introduced by working with time shifts. These time strains form the input to our inversion for reservoir pressure changes. Figure 6.4 shows the time shift and time strain at a cross-line through the Genesis reservoir.

6.3.1 Time shift resolution at reservoir level

A stacked turbidite system such as Genesis, which is a common geological setting for hydrocarbon accumulations, present challenges for seismic imaging. Typically, the

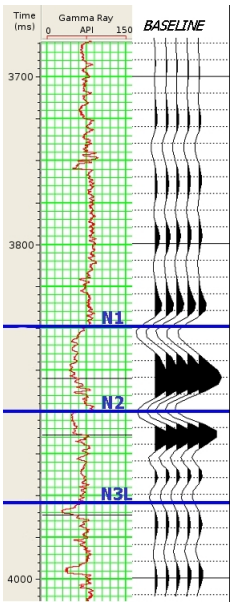

Figure 6.5: *A gamma log from a vertical Genesis well with the baseline seismic plotted along side. The formation tops are marked. The sands are low impedance compared to the surrounding shales, so the top N1 formation is a trough under normal polarity. The sand/shale sequences are clearly represented by a trough/peak combination.*

vertical resolution of surface seismic data is in the order of tens of meters. At Genesis using the assumption of an RMS velocity of approximately 2500ms^{-1} in the reservoir zone and a peak frequency of 25Hz for the seismic wavelet, the resolution given by the Rayleigh criteria is approximately 45m. Since the sands have an average thickness of 20m, it is clear that they are below seismic resolution. This further complicates time shift analysis in the reservoir zone. Figure 6.5 shows a gamma log from a vertical Genesis well in the centre of the field with the baseline seismic plotted alongside. The formation tops are marked. The sands are low impedance compared to the surrounding shales, so the top N1 formation is a trough under normal polarity. The sand/shale sequences are clearly represented by a trough/peak combination.

Compacting stacked reservoirs present new time-lapse challenges. In addition to the recognition of overburden and underburden stretching, the inter-reservoir shales are predicted to respond to the compaction of the reservoirs. Geomechanical modelling suggests that, just as in the overburden, the inter-reservoir shales will expand. Figure 6.6 shows the vertical strain computed for an unconsolidated deep water Gulf of Mexico turbidite by Sayers (2006). Here the sands are compacting while the intra reservoir shales and the shales overlying and underlying the reservoir are in

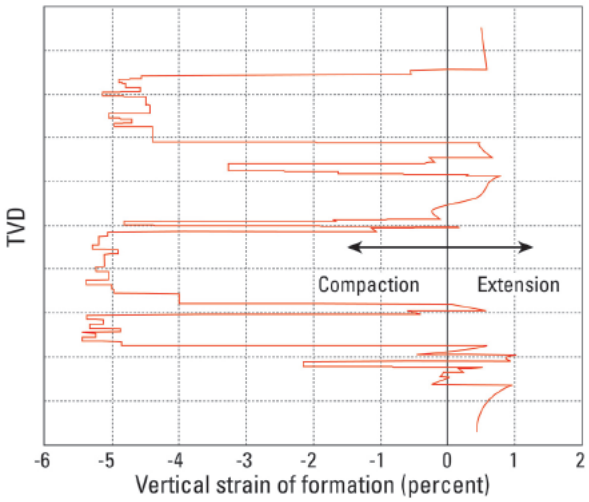

Figure 6.6: *Modelled vertical strain alternation at the location of a well in a deepwater Gulf of Mexico turbidite as a function of TVD (After Sayers et al., 2006)*

extension.

The geomechanical modelling presented by Sayers et al. (2006) assumes that there is no pressure communication between the shales and the sands due to the low permeability of the shales, which is typically in the order of 1mD to 1nD. Recent research by MacBeth et al. (2008) shows that the shale response will be time-dependent. Over short timescales the shale is expected to dilate as though it were impermeable, as an elastic rebound response to the compaction of the sands. However, over large timescales it is expected that the pressure in the shales will equilibrate with the depleted sands, resulting in eventual compaction of the shale.

The exact length of these time-scales will depend on a number of factors, such as the permeability, mineral makeup and thickness of the shale unit. Further research is required into the poro-mechanical properties of shale in order to properly understand these effects. However, assuming the intra-reservoir shales behave elastically and expand over the timescale of seismic surveys, then it is reasonable to expect this to lead to a decrease in velocity in the same way that we observe velocity changes in the overburden. This means that there are potentially two counteracting effects in the reservoir zone: A decrease in travel time in the reservoir sands because of compaction and velocity increase; and an increase in travel time between the compacting layers due to the expansion of the shales. The time strain cross-section (Figure 6.4) clearly shows that a decrease in the time shift decrease is observed across the reservoir,

suggesting that velocity increase due to compaction is the dominant effect.

6.4 Inversion for reservoir pressure change

In this section I describe the process of an inversion for reservoir pressure change. The workflow is very similar to that used for the inversion of the Valhall data. However, there are two major differences. First, the velocity of the overburden increases approximately linearly with depth, unlike the Valhall overburden velocity which could be approximated as constant. The presence of a velocity gradient breaks the linearity between time shifts and reservoir strain. Instead, as described in Chapter 3, we can use time strains, which localise the measurement. Secondly, unlike the Valhall reservoir, which could be approximated as a single compacting layer, Genesis is made up of a series of vertically stacked sands. I will show that one cannot resolve individual pressure distributions in a stacked system from overburden measurements alone. I will, therefore, create a single composite reservoir and invert for the total pressure change. I will discuss this issue in more detail.

6.4.1 Inversion of a vertically stacked reservoir

The synthetic modelling conducted in Chapter 4 showed that the inversion is stable where the reservoir is confined to a single layer. However, a problem arises when attempting to resolve vertical layers: There is a trade-off between pressure changes in layers at different depths.

I explore this problem by examining the model resolution matrix of a simple three layer reservoir. Details about the model resolution matrix were given in Chapter 4 (Section 4.7). The reservoir has lateral dimensions of 2×4km and consists of three 20m thick layers, with the top of the each layer located at 4000m, 4050m and 4100m respectively. I make a horizontal observation horizon 250m above the top reservoir. The forward operator is the discrete vertical strain Green's matrix for an poroelastic halfspace. I assume no vertical connectivity between layers and as such employ regularisation to each layer individually i.e. I favor spatial consistency in the horizontal direction in each layer, but do not expect that the any consistency in the vertical direction. Figure 6.7 shows the results of this test. The resolution is tested

by multiplying the resolution matrix with a unit spike located at the centre of the uppermost layer. If resolution were perfect then the spike test would return the input.

Figure 6.7 reveals that there is substantial leakage between the layers. For the input spike located in the centre of the upper layer components of that spike are found in the middle and lower layers, showing the trade-off between layers.

To avoid this problem I take the pragmatic approach of creating a single equivalent unit representing the three sand units. The consequences of adopting this approach will be discussed later.

Upscaling layers

In order to create a composite layer out of a series of vertically stacked layers we must understand how the pressure upscales, so that a single equivalent layer generates the correct equivalent overburden strain. This helps to interpret the physical meaning of the results, as well as provide a model to upscale the pressures from the layered reservoir model to the composite layer for use in forward modelling.

As I have done throughout this thesis I will assume a uniform linear poroelastic medium. For simplicity I assume a stack of layers of infinite lateral extent, so that the deformation is uniaxial. Figure 6.8 shows the simple case of a three-layered stacked reservoir where a barrier between the layers means that the pressure in each layer is different. These barriers represent the intra-reservoir shales. If we want to represent this as a single layer instead of three separate layers then what pressure change $\Delta\overline{P}$ should be used to replace the pressures changes in each of the layers?

We want to find a pressure $\Delta\overline{P}$ that when applied to the new volume, creates the same total vertical strain as the summation of the three independent vertical strains. For layers of infinite lateral extent (or reservoirs where the size >> depth) the vertical strain is related to pressure via the uniaxial compaction coefficient C_m

$$\varepsilon_{zz} = \frac{\Delta h}{h} = C_m \Delta P \tag{6.1}$$

To find the equivalent pressure for the composite layer we need to determine

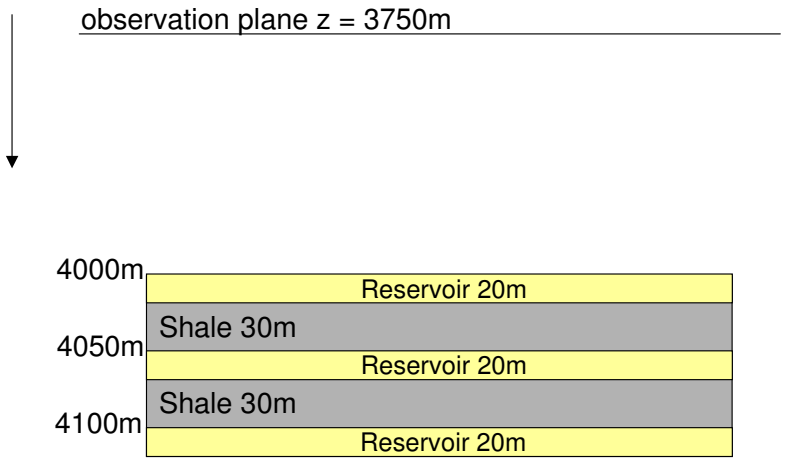

(a)

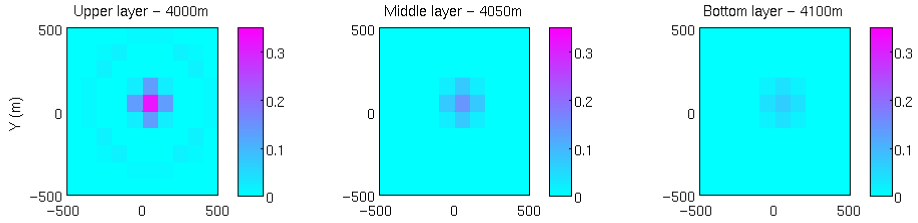

(b)

Figure 6.7: *A resolution spike test showing leakage between stacked reservoirs. (a) The model resolution matrix was formed for a three layer stacked reservoir model, with the top of each layers located at 4000m, 4050m and 4100m respectively. The model resolution matrix is multiplied by a unit spike located at the centre of the upper reservoir. If the resolution were perfect, the test would return a unit spike. As can seen, the returned spike is distributed in all three layers because an observation plane directly above the reservoir cannot distinguish in which layer the pressure change has taken place.*

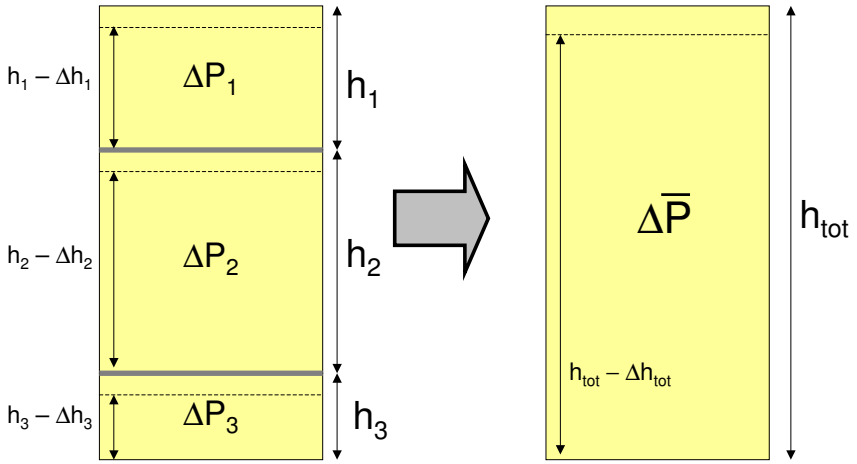

Figure 6.8: *By upscaling a vertically stacked reservoir one wishes to find a pressure* $\Delta\overline{P}$ *that when applied to the net volume, creates the same total vertical strain as the summing the individual vertical strains together.*

$\Delta h_{net}/h_{net} = C_m\Delta\overline{P}$. The total change in thickness of the three layers is given by $\Delta h_{net} = C_m(h_1\Delta P_1 + h_2\Delta P_2 + h_3\Delta P_3)$ from which we can calculate $\Delta\overline{P}$:

$$C_m\Delta\overline{P} = \frac{\Delta h_{net}}{h_{net}} = C_m\frac{(h_1\Delta P_1 + h_2\Delta P_2 + h_3\Delta P_3)}{h_{net}} \tag{6.2}$$

leading to the $\Delta\overline{P}$ being the thickness-weighted average of the pressure in all layers:

$$\Delta\overline{P} = \frac{(h_1\Delta P_1 + h_2\Delta P_2 + h_3\Delta P_3)}{h_{net}} \tag{6.3}$$

In fact, Equation 6.3 can be extended to n layers and is similar to the Backus averaging result (Backus, 1962), but with all layers having the same material properties.

Under the assumption of uniaxial compaction, the intra-reservoir shales will not strain in response to the reservoir. As discussed earlier, in reality the mode of deformation is most probably not uniaxial. The geometry of the reservoir along with material contrasts and poro-mechanical effects between the reservoirs, intra-reservoir shales, underburden and overburden will all play a role. However, this approach is consistent with the simple models I have used thus far and provides a first order upscaling routine.

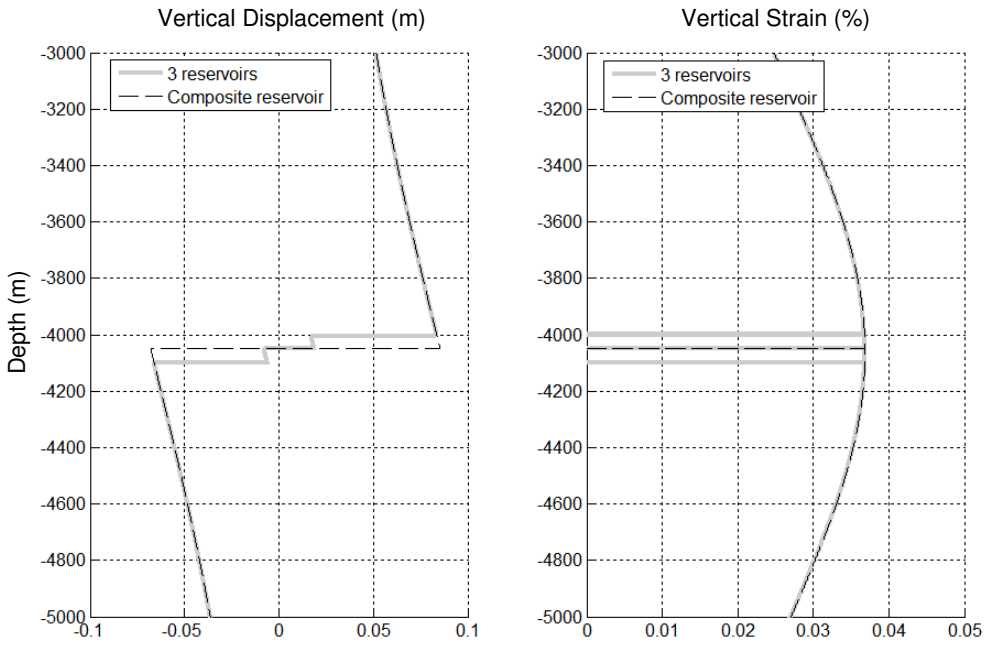

Figure 6.9: *Displacement and strain caused by a series of depleting vertically stacked sands compared to the displacement and strain due to an upscaled layer.*

To show that the overburden displacement and strain from a series of vertically stacked layers can be approximated by a single layer under the assumptions outlined above, I use Geertsma's solution for a disk-shaped reservoir (Geertsma, 1966). Figure 6.9 shows the displacement and strain through the centre of three vertically stacked reservoirs of thickness 20, 20 and 30m respectively that are undergoing 10, 4 and 6 MPa of depletion in a half-space with shear modulus = 1GPa and a Poisson's ratio of 0.25. This model is very loosely based on the layering of Genesis. The reservoirs are located at 4000, 4050 and 4100m depth and all have a radius of 2000m. The stretching of the intra-reservoir areas can clearly be seen. Plotted on top of those solutions is the solution for a composite layer located at the mean depth of 4050m and undergoing the thickness-weighed depletion $\overline{P} = 6.57$MPa. The two solutions are almost identical in the over and underburden (the error is less then 1% everywhere outside the reservoir), however, at reservoir level there are obvious differences. The fact that outside the reservoir we can not distinguish between these two systems is at the heart of the non-uniqueness identified in the spike test I performed earlier.

Conclusion

In a linear elastic homogeneous half-space we can approximate a stack of layers as a single layer with a thickness equivalent to the total thickness of all layers (depleting and non-depleting) and located at the mean depth of those layers. However, the assumption of a homogenous media and uniaxial compaction may be a limitation.

I will use this upscaling approach to invert for a thickness-weighted pressure distribution which we can not readily decompose back into individual layers. This knowledge is important for interpreting the inversion product.

6.4.2 Data preparation

Time strains

For the Genesis data I will work with time strains. A time strain volume was provided by Chevron and created using the non-linear inversion approach described in Chapter 3, earlier in this chapter and in greater detail in Rickett et al. (2007b). The time strain volume was converted from two-way time to depth using the velocity model resulting from seismic processing. From this depth-converted time strain cube I extract the time strain on a surface 350m parallel to the top N1 reservoir horizon. The seismic data were acquired at a sample interval of 12.5×18.5m (see Table 6.2.3). In order to reduce the number of data points in the inversion I resample this grid to 50×55.5m. This reduces the number of data points over the region of interest from ≈50,000 to ≈4,000, which has a significant impact on the computational time and memory requirements of the inversion for reservoir pressure change. As I will describe, the reservoir simulation grid onto which we will invert has a spatial sampling of 100×100m. Therefore, since the seismic data is at nearly half that sample rate we are over-sampled for the problem.

Figure 6.10 shows the observed time strains as a millistrain (i.e. 1000 $\Delta t/t$). Two major separate anomalies, one to the north and one to the south, are visible.

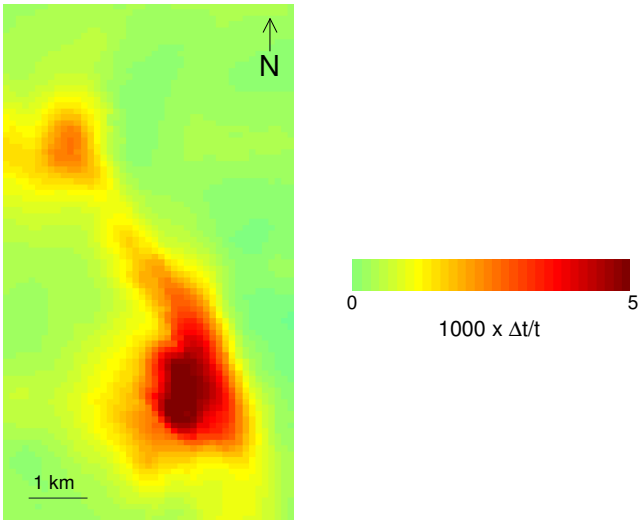

Figure 6.10: *Time strains at a horizon 350m above and parallel to the top N1 sands.*

Preparing the inversion grid

The next step of the preparation is to define a the reservoir geometry upon which we wish to invert to. Results of a reservoir model were provided by Chevron, with the dynamic data (pressures and saturations) at the time of the time-lapse surveys along with static data (grid geometry and porosity). For the inversion of overburden strain to reservoir pressure, the geometry of the sources, i.e. grid blocks, must be defined in relation to the observations. As discussed in the section on upscaling, I will invert for a the pressure change in a single layer equivalent layer which is a combination of the N1, N2 and N3 sands. In addition, I choose to place these grid blocks on a grid with regular lateral spacing of 100× 100m (although this is not strictly necessary, it makes computations easier). The spacing of the grid is consistent with the spacing used for reservoir simulations. In some places it is more dense than the simulation grid, since the the grid becomes less dense towards the edges of the reservoir. I define the thickness of the grid block at each location as the total thickness of the interval between the top N1 surface and the base N3 surface. For forward modelling and comparison purposes, the pressure is upscaled as defined

previously. Figure 6.11 shows pressure changes in each of the individual sands along with the upscaled pressure change.

Here it is clear that there have been some dramatic pressure declines. Compartmentalization and the influence of varying connectivity to the aquifer has had a significant impact on resulting the depletion.

Calibration of material properties

As described in Chapter 3 and the previous chapter on the Valhall data, two material properties characterize the linear elastic half-space: The Poisson's ratio ν and the shear modulus μ. Together these material properties can be used to relate pressure changes to the volumetric strain of each block. As discussed in Chapter 3, the shear modulus plays no role in the shape of the predicted overburden strain, it simply scales the magnitude of the solution. Therefore, additional information is required to constrain the magnitude of the inverted solution. Fortunately, almost all of the development wells were fitted with downhole pressure gauges, so pressure data are abundant and pressure measurements at the times of the seismic surveys are available. The calibration of the data will be performed as part of the inversion and described in the coming section. The Poisson's ratio does have some influence over the spatial distribution of overburden strain. However, as we saw with the analysis of the Valhall data, the influence of Poisson's ratio was below the noise level of the measured data, i.e. a range of Poisson's ratio's fitted the data with equal goodness-of-fit. I will perform the same test for Poisson's ratio when inverting the Genesis data.

6.4.3 Results

The time-lapse time strain data shown Figure 6.10 were used as input into the inversion. To regularise the solution, first-order Tikhonov regularisation was found to give the most stable result. I use the same approach as with the Valhall data and use a bounded least squares solver, which assumes that pressure changes are negative everywhere. This is consistent with the production in the field, which is primary depletion drive with no injection support.

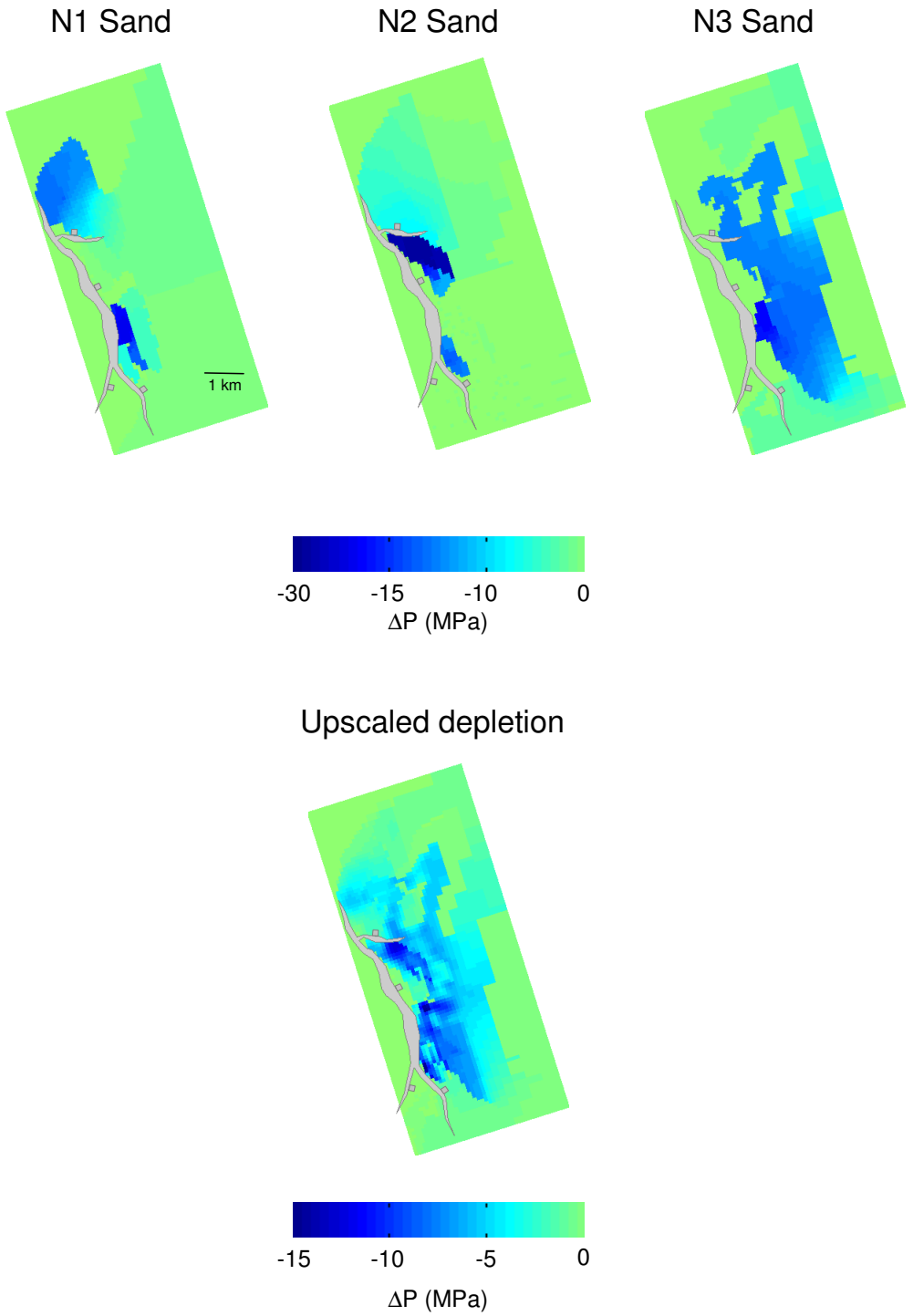

Figure 6.11: *Above, one history-matched reservoir simulation of the pressure depletion in the N1, N2 and N3 sands (provided by Chevron). Below, depletion upscaled to a single layer based using the upscaling scheme described in Equation 6.3.*

ν	Scaling factor $C \times 10^5$	mean(r)	1 $\sigma_{s.d.}(r)$
0.05	4.99	0.69	0.51
0.10	6.55	0.69	0.51
0.15	6.92	0.70	0.49
0.20	7.07	0.68	0.49
0.25	7.67	0.68	0.50
0.30	7.16	0.67	0.50
0.35	6.25	0.67	0.50
0.40	4.85	0.67	0.50
0.45	2.64	0.68	0.49
0.48	0.61	0.67	0.49

Table 6.2: *Comparison of the mean and standard deviations of the residuals (r = observed - modelled) for inversions parameterized by different Poisson's ratio for the half-space used in the Genesis inversion. The optimal scaling factor C is then found for each Poisson's ratio.*

The inversion was carried out several times, with Poisson ratios ranging between 0.2 and 0.49 in steps of 0.05. In addition, for each Poisson's ratio a range of scaling factors where tested to find the best least squares fit. This is done in two stages. First, by using depletion estimates from the reservoir simulator, I forward model overburden strains and compare them to the observed time strains and calculate a scaling factor which equalizes the root mean squared (RMS) energy between the predictions and observations. While the forward-modelled strains may be inaccurate, because the simulator input is only one estimate, unless it is wildly different from the real depletion field, it allows an order-of-magnitude calculation. Next, the a range of calibration factors can be tested around this first estimate, to find the one that minimizes the least-squares error between the observations and the observations predicted using the inverted result.

Poisson's ratio ν and scaling factor, C, along with mean and standard deviations of data residuals are reported in Table 6.2.

Formally, in this case, the scaling factor C relates to the shear modulus and R-factor by:

$$C = \frac{(1+R)}{8\pi\mu} \tag{6.4}$$

I do not attempt to interpret these scaling factors in terms of R and μ because,

as discussed in Chapter 3, instead of representing an actual elastic property of the material, it is in fact a pseudo-property which will include a correction to account for the contrast in material properties between the overburden and the reservoir. In addition, the value of R is uncertain. We can not meaningfully separate the value C into its constituent components.

As can be seen the mean and standard deviations of the various models are very similar and we can not say that one scaling-factor/Poisson's ratio combination is better than any other. This is confirmed by statistical tests (f-test followed by a t-test as described in the previous chapter).

As can be seen, all models generally under-predict the magnitude of the time-lapse time strain signal, as the mean of the residuals is positive.

These results show that, under the geomechanical assumptions made, the choice of Poisson's ratio is irrelevant. I therefore show results for $\nu = 0.48$, which was the average Poisson's ratio in the overburden determined by Chevron, from empirical relationships between dynamic measurements (sonic log data) and static measurements (rock mechanical tests). Figure 6.12 shows the inverted pressure change in the composite layer alongside the upscaled pressure changes from the reservoir simulator.

The agreement between the two maps is favourable. As expected, the inverted depletion does not contain the high spatial frequencies seen in the upscaled result. The major depleted area in the south of the field is in good agreement. In particular the inversion appears to capture a linear baffle running parallel to the main fault which is evident on the simulator result (highlighted by an arrow). In the north at the G1 well the result is also in good agreement. There are two notable areas of disagreement, one around the G2 and G3 wells and the area to the north-east.

Area around the G2 and G3 wells

The most obvious discrepancy between the simulated pressure changes and inverted pressure changes is in the centre of the field around the G3 well. The production in this well is from the N2 sands (see Figure 6.11). As indicated earlier the reservoir pressure changes provided by the reservoir simulator are history matched to pressure changes measured by downhole gauges. Figure 6.13 shows the maximum shut-in

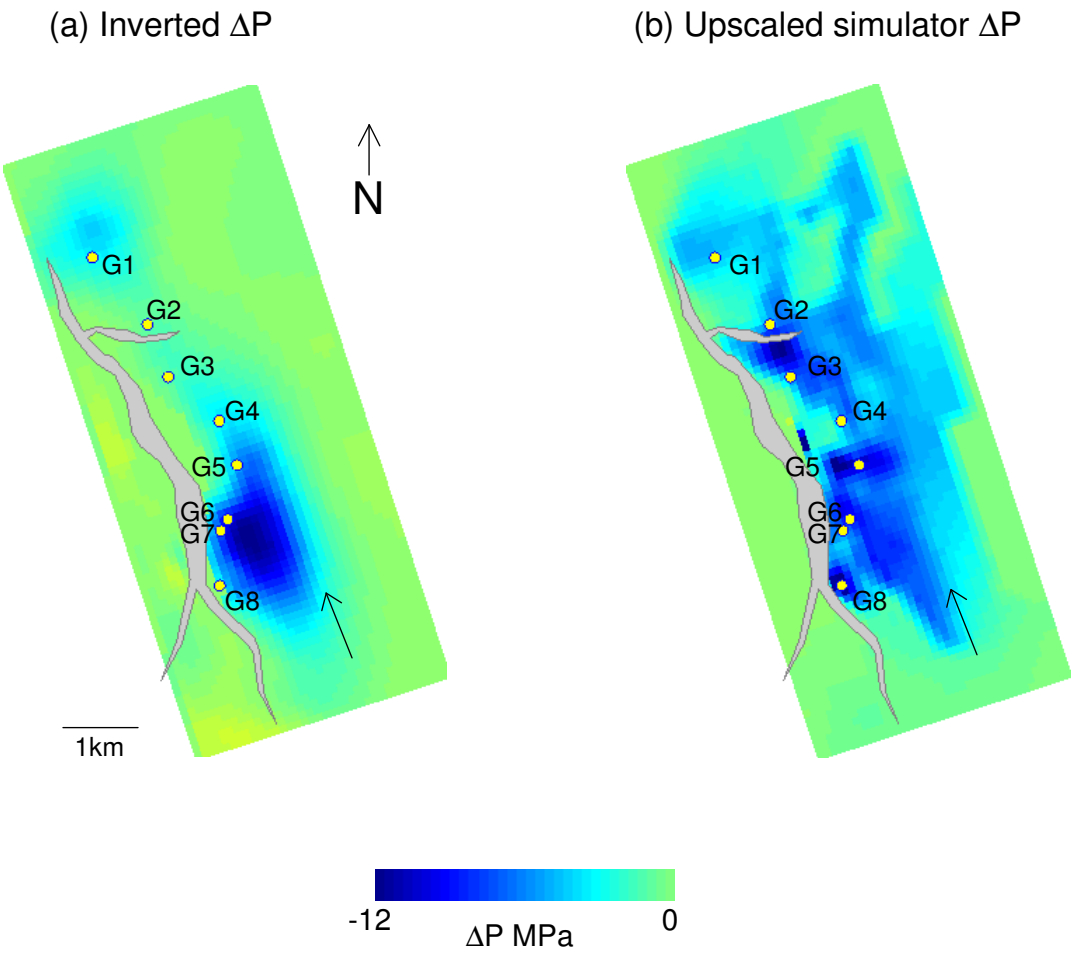

Figure 6.12: *(a) The result of the inversion for pressure change in a layer combining the N1, N2 and N3 sands. (b) The pressure depletion from one reservoir simulation, upscaled to the same single layer.*

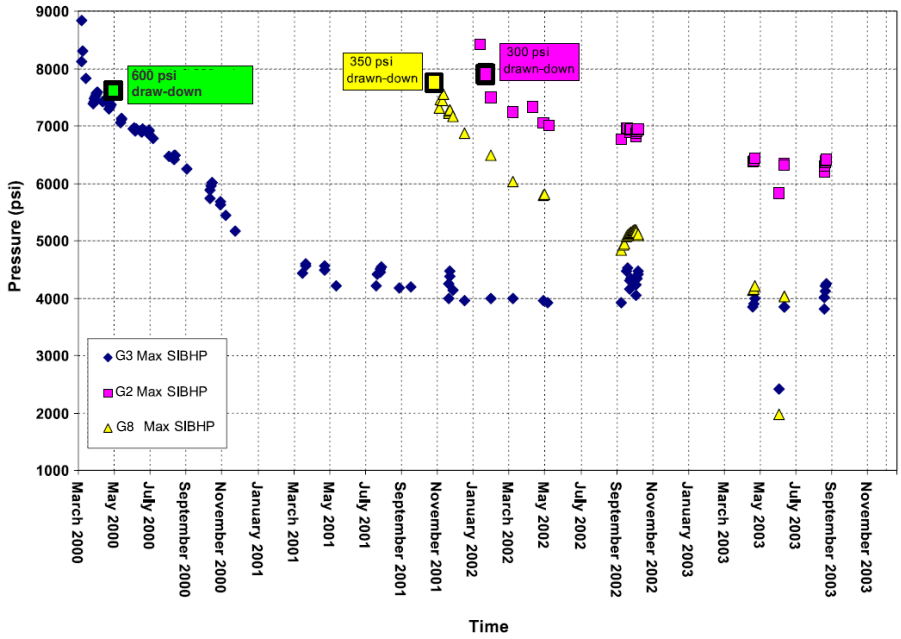

Figure 6.13: *Maximum shut-in bottom-hole pressure (SIBHP) from downhole gauges plotted against time for the G2, G3 and G6 wells, all completed in the N2 sand. Initial pressure in each completion is shown by data points outlined with thick black lines. Text shows draw down from virgin reservoir pressure. Adapted from Sweet and Sumpter (2007).*

bottom-hole pressure (SIBHP) from downhole gauges plotted against time for the G2, G3 and G6 wells, which were all completed exclusively in the N2 sand.

The downhole measurements show that there has indeed been a large depletion at the G3 well, and that it appears there a large difference in the depletion between the G2 and G3 wells. The G3 well has shown depletion of approximately 28MPa in the period March 2000 to September 2003. The G2 well was brought on stream in January 2002 and found virgin pressures, indicating that although the two wells reached equilibrium in a single pressure compartment over geologic time, the connections between the two wells and between each well and the aquifer are not effective over production time-scales (Sweet and Sumpter, 2007).

So why do we not see a large depletion around the G3 well? Figure 6.14 shows the measured overburden time strain with the overburden time strain calculated using the reservoir simulator pressure. From this figure it is clear that if our assumptions are correct, then there should indeed be a distinct overburden time strain that is of similar magnitude to the time strain anomalies in the north and the south. This suggests that the time strain in this area should be measurable above any noise.

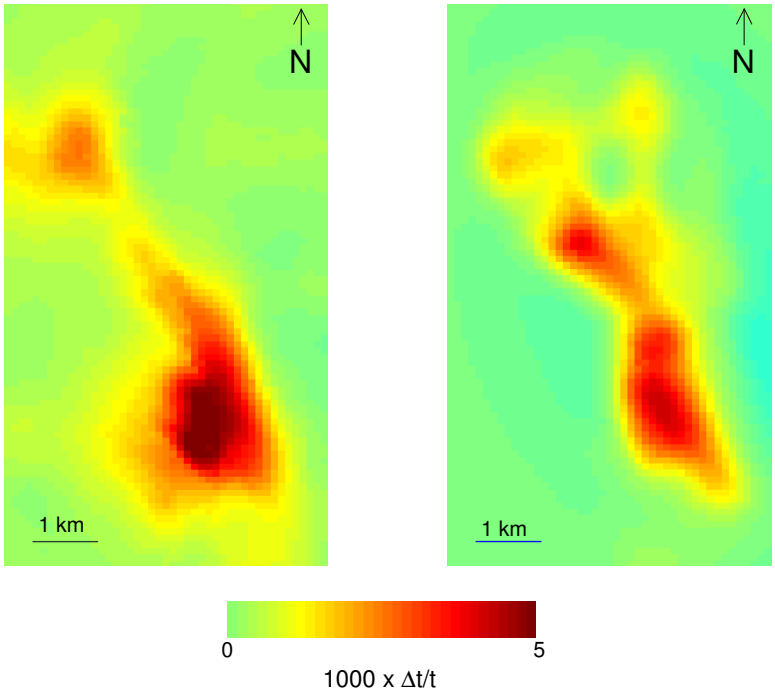

Figure 6.14: *Left, measured time strains from the Genesis seismic data. Right, modelled time strains using the depletion from the reservoir simulator.*

So we have an area that has seen the largest depletions yet clearly does not appear to have caused significant time strain in the overburden. The absence of this anomaly and the lack of an indication of any pressure change in the inversion is not one that I have a definitive explanation for. In the coming discussion I suggest a range of factors that might lead to inaccuracies in the inverted result.

Area to the east

A significant area of depletion in the east of the field does not seem to have been captured by the inversion. Referring back to Figure 6.11 one can see that all of the depletion in this area comes from the deepest sand the N3. From the time strains predicted by the current simulator depletion estimate (Figure 6.14) it is clear that the time strains are small to the east, on the order of 0.5-1 millistrain. Comparing the observed strains it is probable that they are below the noise have been lost during the time strain calculation.

6.4.4 Discussion

The Genesis field was an challenging field on which to test this inversion scheme to work. Below I discuss several reasons why we should be surprised at the quality result as it stands. Further investigation of these effects may provide ways to improve the inversion result.

The relationship between pressure and strain

As already discussed, the inversion scheme presented assumes that the relationship between pressure and strain is linear, under the framework of linear poroelasticity. In a general case, however, we might reasonably expect the deformation of the sands to be a non-linear function of pressure. Ostermeier (2001) explains that the pore-volume compressibility of deepwater Gulf of Mexico turbidite sands exhibits large variations in both magnitude and stress dependency. Field and laboratory examples are given for geologically young, over-pressured sands that show larger initial compressibility, which decreases as a function of increasing stress (stress hardening). The introduction of a non-linear relationship between pressure and strain (reservoir

compaction) may improve our results. Unfortunately, while suitable constitutive models exist, the parametrisation of such models is often highly uncertain.

Uncertainties in thickness and vertical resolution

The role of thickness in the inversion for reservoir strain was also explored in the previous chapter on Valhall. The inversion requires the reservoir geometry as *a priori* information for the calculation of the Green's function. As mentioned in the introduction to the field, there is some uncertainty in the thickness of the individual sands because they are below the the vertical resolution of the seismic data.

Upscaling and the effect of intra-reservoir shales

The upscaling scheme presented was extremely simple and assumes uniaxial compaction, resulting in no deformation of the intra-reservoir shales. Earlier I discussed some work being undertaken to understand the effects of intra reservoir shales (e.g. MacBeth et al., 2008). An extension to the upscaling scheme would be to account for material contrasts and non-uniaxial behavior. It is also of note that the upscaling depends upon the layer thicknesses, which, as highlighted in the previous section, are also a source of uncertainty.

Faults

The presence of faults is not considered in the model or inversion. Intuitively, however, one feels faults must play a role. Stress effects on faults will effect the distribution of stress and strain in the reservoir and into the overburden. These effects are not well understood at present because defining and parameterising the constitutive mechanical models for faults is highly uncertain. Stress effects around faults will also have a important role for fluid flow modelling, for example, where transmissibilities may change as a function of stress. It is interesting to note that the main area of disagreement between the inversion result and the simulated pressures is around a fault. One possibility is that the fault may be reacting to the depletion in this area and effecting the transference of stress into the overburden. At present this is mere speculation and offers one possible avenue of further investigation.

6.4.5 Conclusion

The results of the Genesis inversion are promising given the major simplifications used to arrive at the result. In the discussion above I introduced several good reasons why one might believe that such a simple approach was unlikely to give any reasonable solution. Interestingly, the issues raised in the discussion are not restricted to the inversion scheme presented in this thesis, but are problems also faced by geomechanicists conducting finite element (FE) modelling to forward predict reservoir compaction and deformation outside the reservoir. For example, upscaling is a major issue for FE modelling of Genesis-type reservoirs, where it is nearly impossible to model thin sands individually because of the computational burden (Schutjens, 2005). Similarly, the discussion on the relationship between pressure and strain is an important one and still on going in the literature. Many constitutive models exist that can describe non-linear deformation, however choosing and parameterising these models is often a very sparsely constrained problem.

The ultimate goal would be to inform a reservoir simulator update. However, it is clear at this stage that, while the results are extremely promising, there are too many uncertainties to give full confidence to the inversion result. We cannot confidently at this stage say whether discrepancies between the inverted result and simulated data are because of problems with the time-lapse data, simplified geomechanical model, or reservoir simulation itself.

CHAPTER

SEVEN

Conclusions and recommendations for future research

7.1 Conclusions

This thesis has presented a method to relate overburden time-lapse time shifts, or their derivative time-lapse time strains, directly to the deformation in and around compacting hydrocarbon reservoirs.

This method is a significant departure from the approach of other published methods which generally assume a pancake-like uniaxial deformation of the reservoir and surrounding rock (e.g. Guilbot and Smith, 2002; Røste et al., 2006; Hawkins et al., 2007), or use complex finite-element modelling (e.g. Minkoff et al., 1999; Herwanger and Horne, 2005; Staples et al., 2007; Schutjens, 2005).

The approach I adopted was to find a model to relate pressure change to overburden deformation that was simple and computationally fast to implement. Under the framework of linear poro-elasticity I take a semi-analytical route by numerically integrating the solution for a nucleus of strain in a homogeneous half-space. This approach has the obvious limitation of not allowing mechanical stratigraphy, but it does allow for the geometrical effects and and spatial distribution of reservoir compaction.

I draw on the work of Hatchell and Bourne (2005a) and use the assumption of a linear relationship between overburden vertical strain and relative changes in seismic velocity, which are visible on time-lapse seismic surveys as time shifts. In Chapter 3 I described in detail why using the overburden time-lapse seismic signature presented complimentary information to the reservoir-level signature, which is often more complex to interpret. I also presented a review of several techniques for measuring time-lapse time shifts and showed that we can be more confident of the overburden signature. The reason for this is that time shift estimation techniques work best when the time shift is varying slowly, which we expect to be the case in the overburden based on geomechanical modelling. At the reservoir level this assumption is invalid, because we expect a sharp change in the time shift gradient, where there is a switch between extension of the overburden and compaction of the reservoir.

Using this simple geomechanical approach and the linear rock physics model, I proposed a linear inversion for reservoir strain using time-lapse time strains (the derivative of time-lapse time shifts) as the input data. In Chapter 4 I tested this method on synthetic data. For this synthetic test I chose to invert data created using

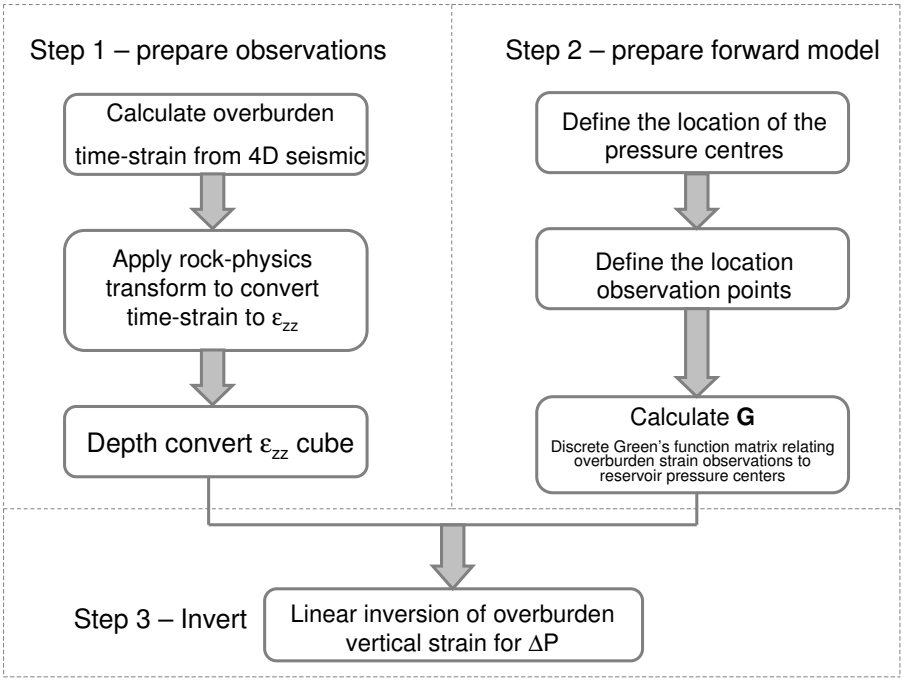

Figure 7.1: *The work flow for inverting for reservoir pressure from time-lapse time strains as outlined in this thesis.*

a different geomechanical model to one I adopted, avoiding the so-called inverse-crime, where one uses the same model to create synthetic data for an inversion. The data I inverted was created using a finite-element simulation, which modelled realistic subsurface geology and stratified mechanical properties. This inversion test successfully recovered the reservoir pressure changes within a normalized root-mean-squared error of $\pm 10\%$. Figure 7.1 summarizes the workflow.

Although, I have chosen to draw in the work of Hatchell and Bourne (2005a) and relate velocity changes to vertical strain, which is possibly the simplest possible approach, the inversion formulated in this thesis and summarized in Figure 7.1 can be extended to so that velocity changes can be related to any linear combination of the stress and strain tensor. I have the described this fully in Appendix C.

Two real data applications of this technique were presented in this thesis:

Valhall Field, North Sea

In Chapter 5 a sector of the Valhall field was studied. The relatively benign geology of the overburden is such that to first-order the initial seismic velocity can be assumed to be constant. This allowed the inversion method presented in Chapter 4 to be recast in terms of time-lapse time shifts and vertical displacements instead of time-lapse time strains and vertical strain. It was discussed in Chapter 3 that time-lapse time shifts are a more stable attribute to work with.

Forward modelling using an existing reservoir strain estimate revealed that the approximation of a homogenous linear elastic half-space was able to produce a good match to the observed time-lapse time shifts. An investigation into the sensitivity to the choice of Poisson's ratio revealed the sensitivity of the model to Poisson's ratio to be less than the uncertainty observed in the time shift data. Forward modelling also suggested that the overburden time-lapse time shifts showed areas of correlated noise. First, an analysis of an anomalous region of time shifts suggested a relationship to residual multiple energy. This section of the chapter was able to capitalise on the availability of frequently acquired data at Valhall. Other anomalous time shifts were observed that correlated very well with the receiver lines, suggesting the origin of the noise is related to acquisition and/or processing.

Time-lapse time shifts from a horizon 100m above and parallel to the top reservoir were chosen as an input to an inversion for reservoir volumetric strain. The inversion results are promising, showing good similarity to the current strain estimate predicted by complex finite element modelling. The sensitivity to the reservoir thickness was also examined, in light of concerns about uncertainties in the seismic interpretation of top reservoir. I compared two inversions: one using the reservoir geometry provided; and one that assumed the reservoir had a uniform thickness. The results were visually similar, although the inversion which assumed uniform thickness showed a larger least squared error.

Genesis Field, Gulf of Mexico

The Genesis Field in the Gulf of Mexico presented considerably greater challenges than the sector of the Valhall Field. First, the presence of a linear overburden velocity gradient meant that it was necessary to work with time strains, which is

and instantaneous property, rather than time-strains. Time-strains are generally noisier to work with, but a new method presented by Rickett et al. (2007b) provided stable results. Second, the geology of the Genesis field was also more complex than Valhall. The inversion focused on three vertically stacked thin reservoirs. Vertical resolution was identified as a limitation of the proposed inversion scheme. To tackle this I adopted an approach of inverting for the pressure in an upscaled layer. Taking a uniaxial approach in a homogeneous half-space, I showed that the upscaled pressure is the thickness weighted average of the pressure changes in the individual layers.

An inversion for reservoir pressure change of the time-lapse data revealed that there is broad agreement in two areas. However, a large pressure depletion in a small compartment in the centre of the field was not predicted by the inversion. Down-hole pressure measurements reveal that the reservoir model in this are was expected to be broadly correct. So what caused this mismatch? In the conclusions of the chapter I discussed many areas of further investigation based around the limitations of the current geomechanical formulation. Although the inversion result is favourable, showing many of the key features of the pressure distribution, additional complexity, such as layering and faults, may be required to explain some of the discrepancies.

7.2 Suggestions for further research

7.2.1 Further investigation of the limitations of the geomechanical model

In this thesis I set out to relate reservoir pore pressure changes to time-lapse seismic observations. In Chapter 4 I showed that poroelasticity does indeed allow this connection and holds true for any heterogeneous linear elastic medium. However, calculation of the Green's function for a fully heterogenous medium would require computation using a numerical method such as finite elements. I opted for a simple semi-analytic solution that is simple to implement and computationally fast. With this choice comes a compromise; the medium is a homogenous linear elastic halfspace.

In the case of the inversion test of the Valhall FEM model in Chapter 4, we saw that a simple scaling factor was able to largely account for the difference in observed overburden strains and those predicted by the homogenous model. In the field data study of the Valhall Field, we also saw how we were able to model time-shifts within

the noise level of the data with the assumption of a homogeneous media. However, in the case of Genesis there was more uncertainty. A combination of upscaling layers and contrasts in material properties, along with possible non-linear effects, meant that relating the inverted strain product to reservoir pressure changes was challenging.

Further investigation is required in this area to better define the cases where the assumption of a homogeneous media is no longer adequate. An analytical model by Rudnicki (1999) goes part of the way. The model is of an ellipsoidal inclusion inside an infinite material. In this model the material properties of the inclusion are allowed to differ from those of the surroundings, but only the deformation of the inclusion (i.e. the reservoir) can calculated. In general, one can make the statement that the reservoir geometry (i.e. the aspect ratio of the ellipsoid) and the magnitude of the contrast between the reservoir and the surroundings affect the reservoir strain. However, this general statement can only provide partial understanding. For this model, because an the inclusion is in an infinite medium, we are restricted to reservoirs whose depth is much greater than width, so that the effect of the free surface is negligible. Also, in relation to the work presented in this thesis, we are more specifically interested in how material contrasts and geometrical effects affect the overburden deformation, which the model does not allow us to investigate. In addition to a simple material contrast between the reservoir and the surroundings, we wish to understand the affect of multiple layers, for example, the case of reservoir sand and intra reservoir shale interaction.

These topics are non-trivial and substantial, requiring finite element modelling of the mechanical interaction of layers and, where appropriate, the poromechanical interaction between layers via the coupled flow-deformation equations presented in Chapter 4.

I suggest we should try to find the appropriate limits of applicability of our current model, before extending the simple model to something more complex. For example, it would be possible to pre-compute the Green's function of a linearly elastic heterogenous media using a fully numerical approach such as finite elements or finite difference. However, depending on the complexity of the scenario we wish to calculate, the computational power required could be potentially prohibitive.

In conclusion, this thesis has shown simple semi-analytical modelling of a homogeneous half space to give good approximations in several cases. However, more

research is needed to define cases in which we expect these models will fail to adequately approximate the physics of the situation.

7.2.2 Understanding the reservoir level signal

In Chapter 3 I made the case that the reservoir level signal is more complex to interpret than overburden observations, because the reflectivity changes at reservoir level mean that both amplitude changes, caused by compaction and fluid changes, and time shifts, which are difficult to measure, must be understood. In this thesis I have identified a link between reservoir strain changes and overburden deformation. This allows the possibility of this technique being used to decouple the two effects at reservoir level, in a joint inversion. The overburden is related only to the volume change in reservoir, where as the reservoir level amplitude, or other seismic attribute derived at reservoir level, will be effected by both. Therefore, a joint inversion of the two complimentary data sources might be able to separate the two effects.

7.2.3 Geomechanically consistent seismic warping

This thesis is built on the fundamental principle that, when a reservoir compacts, some overburden deformation will occur. This then causes a change in seismic velocity that, if sufficiently large, we can measure using the method of time-lapse seismic imaging.

The approach of this thesis has been one of linear least-squares inversion, in which a linear forward model connects our unknown reservoir strain to the observed data. The observed data is then inverted for the unknowns in the model to find the solution with the smallest L2-norm fit to the data.

In Chapter 3 I reviewed how those observations (time-lapse time shifts and time strains) are made. I showed that the way we make these measurements has some inherent limitations, mostly that we only make the most stable measurements when the underlying time shift signal is slowly varying.

An alternative approach is to make the time-shift estimation part of the inversion. An approach like this would be a non-linear stochastic inversion, in which reservoir

strains are estimated, then overburden deformation is calculated. Using the overburden deformation the resultant time shifts are calculated and applied to the seismic data. Next, the residuals between the time shifted monitor data and base are examined and the reservoir strain estimate is updated accordingly. For example, a global optimization scheme such as simulated annealing could be used.

The key difference between this approach and the one outlined in this thesis is that instead of first processing the seismic data, i.e. measuring time shifts and then using the time shift product to invert for reservoir strain, we would instead find a geomechanical model that was *directly* consistent with the seismic data and therefore not subject to the pitfalls involved in the measurement of time shifts.

In addition to vertical shifts, Cox and Hatchell (2008) show that overburden deformation and velocity change can cause apparent lateral shifts in the time-lapse seismic images. This is a result of seismic ray bending through the overburden velocity perturbation which is not accounted for in the migration of the time-lapse datasets. These lateral shifts can be included in such an inversion scheme. If we account for both time shifts and lateral shifts then I would call this concept *"geomechanically consistent warping"*.

For reservoirs where the effect of fluid saturation is small and the change in seismic velocity is related mainly to the reservoir strain (such as a compacting gas reservoir for example), this would address the issue of resolving the sharp change at reservoir level, since this approach would not require the gradient of the time-shift to be smooth in order to stabilize the result. In reservoirs where changes in saturation cause significant changes in velocity, then we would be restricted to looking at only the overburden warp.

In order to conduct such an inversion, however, the geomechanical model needs to be simple and quick to compute, because at every update of the reservoir strain, a new geomechanical model must be run and from this the warp vectors calculated. Assuming linear elasticity this amounts to a simple convolution of the Green's function matrix with the current strain estimate. Therefore the computation cost is mostly in the initial building the of the Green's function matrix. As I indicated earlier the balance would lie in finding a geomechanical model that was simple enough to be of practical use, but complex enough to define the gross features seen in the data. For this reason the earlier recommendations of further research into geomechanical

modelling are even more relevant.

APPENDIX

A

Time shift estimation by non-linear inversion

This appendix describes in detail the method of time shift estimation by non-linear inversion.

In the case of time-lapse time shifts we have two seismic traces, $x_1(t)$ from the base survey and $x_2(t + \tau(t))$, where $\tau(t)$ is a time shift function that describes the time-lapse time shifts. Our goal is to estimate the function $\tau(t)$ given the two time-lapse traces.

To pose this as an inversion problem we wish to find the function $\tau(t)$, which, once applied, minimizes the difference between the traces in a least-squares sense:

$$min|x_1(t) - x_2(t + \tau(t))|^2 \tag{A.1}$$

An interpolation algorithm is typically used to apply the time shifts to the monitor trace. Applying a time shift to a seismic trace involves first shifting the amplitudes by the time shift then, reconstructing the trace at the regular sampling interval. This reconstruction is usually done by numerical interpolation such as cubic spline

interpolation or sinc interpolation. The objective function can generally be written as:

$$min|\mathbf{d} - f(\mathbf{m})|^2 \tag{A.2}$$

where the data vector, $\mathbf{d}$, contains the baseline seismic data volume, $x_1(t)$; the model vector, $\mathbf{m}$, contains the time shift volume, $\tau(t)$; and the function, $f(\mathbf{m})$, applies these shifts to the monitor survey to give $x_2(t + \tau(t))$.

Since the time shift itself is a function of time, the objective function is non-linear. Several approaches can be taken to solving non-linear inversion problems. Here I describe the regularised Gauss-Newton method, which I have used for the examples in this thesis.

The Gauss-Newton algorithm works by linearizing the problem and taking iterative steps towards the solution. At each iteration a linear system of equations is solved:

$$(\mathbf{J}^T\mathbf{J})\Delta\mathbf{m} = -\mathbf{J}^T\mathbf{r} \tag{A.3}$$

where $\mathbf{J}$ is the Jacobian, which linearises the non-linear problem; $\Delta\mathbf{m}$ is the model update at a given iteration; and $\mathbf{r}$ is a vector of the residuals at that iteration.

The Jacobian is found by taking the derivative of the residuals with respect to the time shift, $\tau(t)$. Since only the monitor trace is affected by the time shift, the Jacobian is given by:

$$J_{ii} = \left.\frac{\partial x_2}{\partial t}\right|_{t=t_i+\tau_i^{(0)}} \tag{A.4}$$

Since many time shift models may match the monitor to the base the problem is non-unique and may become singular. To avoid this we may regularise the problem. One desirable way of regularising the problem is to add the minimisation of a derivative to the objective function. This ensures that the time shift is consistent from sample to sample. The regularised objective function may be written as:

$$min|\mathbf{d} - f(\mathbf{m})|^2 + \alpha^2|\mathbf{Lm}| \tag{A.5}$$

where $\mathbf{L}$ takes the derivative of the model $\mathbf{m}$. In the case of the time shift estimation problem $\mathbf{L}$ will take the form of the second derivative, since we want to minimize the first derivative of the time shifts in order to estimate stable time strains.

Equation A.5 can be rewritten as:

$$min \left| \begin{array}{c} \mathbf{d} - f(\mathbf{m}) \\ \alpha^2 \mathbf{L}\mathbf{m} \end{array} \right|^2 \tag{A.6}$$

For each iteration step k the Jacobian for the regularised least-squares problem then becomes:

$$\mathbf{K}(\mathbf{m}^k) = \left[\begin{array}{c} \mathbf{J}(\mathbf{m}^k) \\ \alpha^2 \mathbf{L}\mathbf{m}^k \end{array} \right] \tag{A.7}$$

The model update at each Gauss-Newton iteration is then given by solving the following equation for $\Delta\mathbf{m}$:

$$\mathbf{K}(\mathbf{m}^k)^T \mathbf{K}(\mathbf{m}^k) \Delta\mathbf{m} = -\mathbf{K}(\mathbf{m}^k)^T \left[\begin{array}{c} f(\mathbf{m}) - \mathbf{d} \\ \alpha^2 \mathbf{L}\mathbf{m}^k \end{array} \right] \tag{A.8}$$

This can be simplified and solved as the linear system of equations $\mathbf{A}\Delta\mathbf{m} = \mathbf{b}$ where:

$$\mathbf{A} = \mathbf{J}(\mathbf{m}^k)^T \mathbf{J}(\mathbf{m}^k) + \alpha^2 \mathbf{L}^T \mathbf{L} \tag{A.9}$$

$$\mathbf{b} = -\mathbf{J}(\mathbf{m}^k)^T \mathbf{r} - \alpha^2 \mathbf{L}^T \mathbf{L}\ \mathbf{m}^k \tag{A.10}$$

which can be solved for $\Delta\mathbf{m}$, the model update, in a least squares sense using the normal equations $\Delta\mathbf{m} = (\mathbf{A}^T\mathbf{A})^{-1}\mathbf{A}^T\mathbf{b}$.

APPENDIX

B

Strain field around a nucleus of strain in a poroelastic half-space

B.1 Introduction

Expressions for the internal displacement due to a nucleus of strain in a poroelastic half-space with a traction-free surface are provided by Geertsma (1966). In this document, equations to calculate the *full strain tensor* due to a nucleus of strain are given by taking the appropriate derivatives of the x, y and z components of displacement.

B.2 Displacements

The coordinate system used by Geertsma is shown below in Figure B.1. Note that the z-axis is taken as *positive* in the downwards direction.

The expression for displacement due to a unit pressure change outside a nucleus at depth $z = c$ and a radial distance $r^2 = (x - a)^2 + (y - b)^2$ from the nucleus located

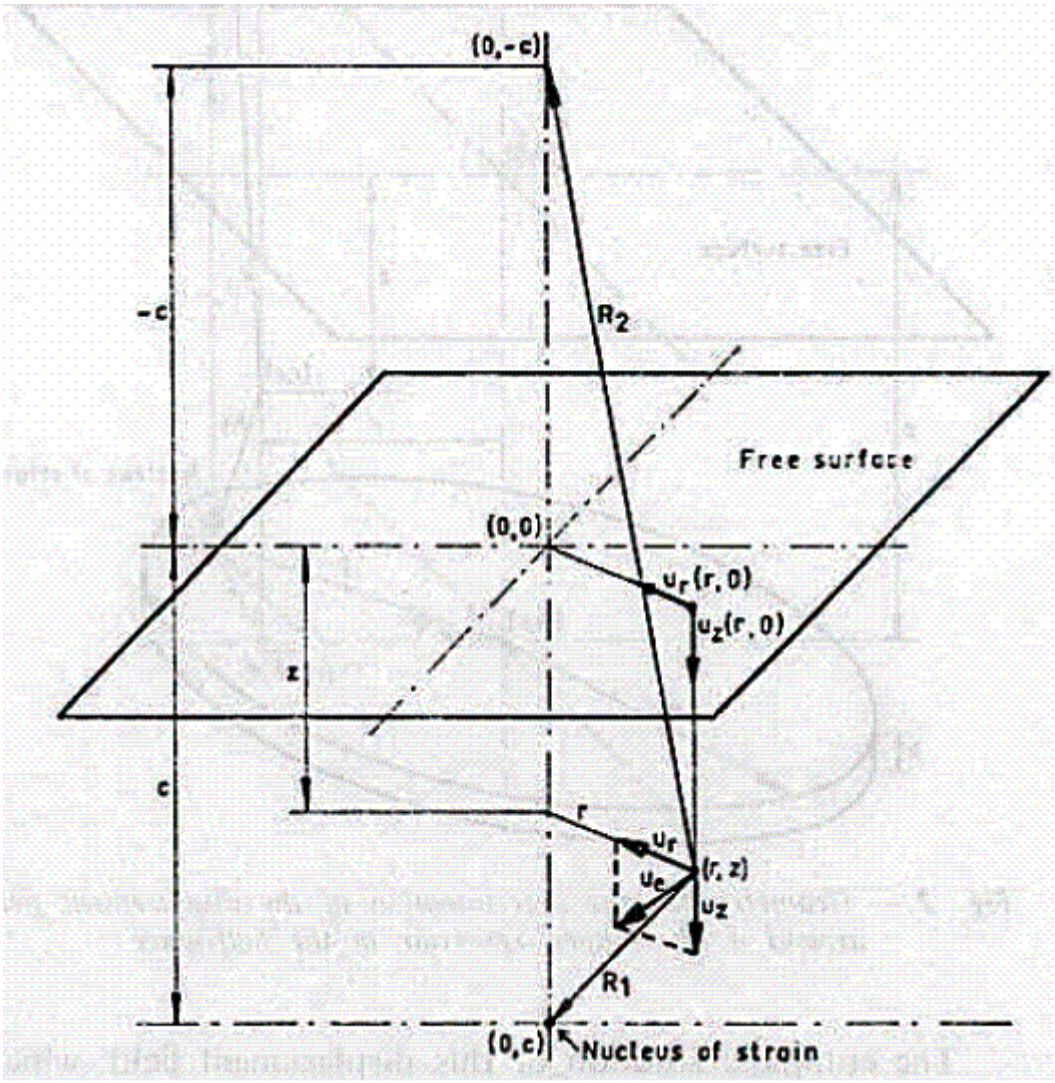

Figure B.1: *Figure taken from Geertsma (1966) defining the geometry used in subsequent equations*

at (a, b, c) as:

$$\overrightarrow{u_l^*} = \frac{C_m}{4\pi}\left[\frac{\overrightarrow{R_1}}{R_1^3} + \frac{(3-4\upsilon)\overrightarrow{R_2}}{R_2^3} - \frac{6z(z+c)\overrightarrow{R_2}}{R_2^5} - \frac{\overrightarrow{2k}}{R_2^3}\left\{(3-4\upsilon)(z+c) - z\right\}\right] \quad \text{(B.1)}$$

where:

$$R_1^2 = (x-a)^2 + (y-b)^2 + (z-c)^2,$$

$$R_2^2 = (x-a)^2 + (y-b)^2 + (z+c)^2,$$

$$\overrightarrow{R_1} = (x-a)\,\overrightarrow{\mathrm{i}} + (y-b)\,\overrightarrow{\mathrm{j}} + (z-c)\,\overrightarrow{\mathrm{k}},$$

$$\overrightarrow{R_2} = (x-a)\,\overrightarrow{\mathrm{i}} + (y-b)\,\overrightarrow{\mathrm{j}} + (z+c)\,\overrightarrow{\mathrm{k}}$$

where $\overrightarrow{\mathrm{i}}$, $\overrightarrow{\mathrm{j}}$, $\overrightarrow{\mathrm{k}}$ are the unit vectors in the x, y and z directions respectively. The constant C_m is the uniaxial compressibility coefficient which is given by:

$$C_m = \frac{(1-\beta)(1-2\upsilon)}{2G(1-\upsilon)} \quad \text{(B.2)}$$

where β is given by the ratio of rock bulk compressibility to rock matrix compressibility C_b/C_r. Redefining $x = (x-a)$ and $y = (y-b)$ for ease of notation, the individual components of the displacement are:

$$u_x = \frac{C_m}{4\pi}\left[\frac{x}{R_1^3} + \frac{(3-4\upsilon)x}{R_2^3} - \frac{6z(z+c)x}{R_2^5}\right] \quad \text{(B.3)}$$

$$u_y = \frac{C_m}{4\pi}\left[\frac{y}{R_1^3} + \frac{(3-4\upsilon)y}{R_2^3} - \frac{6z(z+c)y}{R_2^5}\right] \quad \text{(B.4)}$$

$$u_z = \frac{C_m}{4\pi}\left[\frac{z-c}{R_1^3} + \frac{4\upsilon(z+c) - (z+3c)}{R_2^3} - \frac{6z(z+c)^2}{R_2^5}\right] \quad \text{(B.5)}$$

B.3 The strain tensor

The strain tensor is defined as:

$$\varepsilon = \begin{bmatrix} \varepsilon_{xx} & \varepsilon_{xy} & \varepsilon_{xz} \\ \varepsilon_{xy} & \varepsilon_{yy} & \varepsilon_{yz} \\ \varepsilon_{xz} & \varepsilon_{yz} & \varepsilon_{zz} \end{bmatrix} \tag{B.6}$$

and the individual components of the strain tensor are given by:

$$\varepsilon_{ij} = \frac{1}{2}\left(\frac{\partial u_i}{\partial x_j} + \frac{\partial u_j}{\partial x_j}\right) \tag{B.7}$$

where the subscripts i and j can be the numbers 1, 2, 3, representing the x-, y- and z-axis respectively.

To populate the strain tensor nine derivatives are required (the derivatives with respect to x, y and z of all three components of displacement). These derivatives are set out on the following pages.

B.4 The stress tensor

The stress tensor is easily calculated by combining elements of the strain tensor and the elastic properties of the material. Assuming undrained conditions (i.e. no pore pressure change in the material surrounding the nucleus) the stress tensor related to strain by:

$$\sigma_{ij} = 2\mu\varepsilon_{ij} + \frac{2\mu\upsilon}{1-2\upsilon}\varepsilon_{kk}\delta_{ij} \tag{B.8}$$

The effective stress is given by:

$$\sigma_{ij}^{eff} = 2\mu\varepsilon_{ij} + \frac{2\mu\upsilon}{1-2\upsilon}\varepsilon_{kk}\delta_{ij} - \alpha\Delta p\delta_{ij} \tag{B.9}$$

B.5 Numerical Tests

To test that the analytical derivatives have been derived, presented, and coded without error, the numerical derivatives of u_x, u_y and u_z with respect to x, y and z were taken and plotted against the analytical derivatives. The results are presented in Figures B.2, B.3 and B.4.

Component	Expression	
$\frac{\partial u_x}{\partial x}$	$\frac{1}{R_1^3} - \frac{3x^2}{R_1^5} - 6z(c+z)\left\{\frac{1}{R_2^5} - \frac{5x^2}{R_2^7}\right\} + (3-4\upsilon)\left\{\frac{1}{R_2^3} - \frac{3x^2}{R_2^5}\right\}$	(B.10)
$\frac{\partial u_x}{\partial y}$	$-\frac{3xy}{R_1^5} - \frac{3(3-4\upsilon)xy}{R_2^5} + \frac{30xz(c+z)y}{R_2^7}$	(B.11)
$\frac{\partial u_x}{\partial z}$	$-\frac{3x(z-c)}{R_1^5} - 6x\left\{\frac{c+2z}{R_2^5} - \frac{5z(z+c)^2}{R_2^7}\right\} - \frac{3(3-4\upsilon)x(c+z)}{R_2^5}$	(B.12)

Table B.1: *Derivatives of u_x. All expressions require multiplication by a factor of $C_m/4\pi$ which is omitted for ease of notation*

Component	Expression	
$\frac{\partial u_y}{\partial x}$	$-\frac{3xy}{R_1^5} - \frac{3(3-4\upsilon)xy}{R_2^5} + \frac{30xz(c+z)y}{R_2^7}$	(B.13)
$\frac{\partial u_y}{\partial y}$	$\frac{1}{R_1^3} - \frac{3y^2}{R_1^5} - 6z(c+z)\left\{\frac{1}{R_2^5} - \frac{5y^2}{R_2^7}\right\} + (3-4\upsilon)\left\{\frac{1}{R_2^3} - \frac{3y^2}{R_2^5}\right\}$	(B.14)
$\frac{\partial u_y}{\partial z}$	$-\frac{3y(z-c)}{R_1^5} - \frac{3(3-4\upsilon)y(c+z)}{R_2^5} - 6y\left\{\frac{c+2z}{R_2^5} - \frac{5z(c+z)^2}{R_2^7}\right\}$	(B.15)

Table B.2: *Derivatives of u_y. All expressions require multiplication by a factor of $C_m/4\pi$ which is omitted for ease of notation*

Component	Expression
$\frac{\partial u_z}{\partial x}$	$-\frac{3x(z-c)}{R_1^5} - \frac{3x(-3c-z+4\upsilon(c+z)}{R_2^5} + \frac{30xz(c+z)^2}{R_2^7}$ (B.16)
$\frac{\partial U_z}{\partial y}$	$-\frac{3y(z-c)}{R_1^5} - \frac{3y(-3c-z+4\upsilon(c+z)}{R_2^5}\frac{30yz(c+z)^2}{R_2^7}$ (B.17)
$\frac{\partial u_z}{\partial z}$	$\frac{1}{R_1^3} - \frac{3(z-c)^2}{R_1^3} + \frac{4\upsilon-1}{R_2^3} + \frac{3(c+z)(-3c-z+4\upsilon(c+z))}{R_2^5} - \frac{6(z+c)^2}{R_2^5}$ (B.18) $-6z\left\{\frac{2(z+c)}{R_2^5} + \frac{5(z+c)^3}{R_2^7}\right\}$

Table B.3: *Derivatives of u_z. All expressions require multiplication by a factor of $C_m/4\pi$ which is omitted for ease of notation*

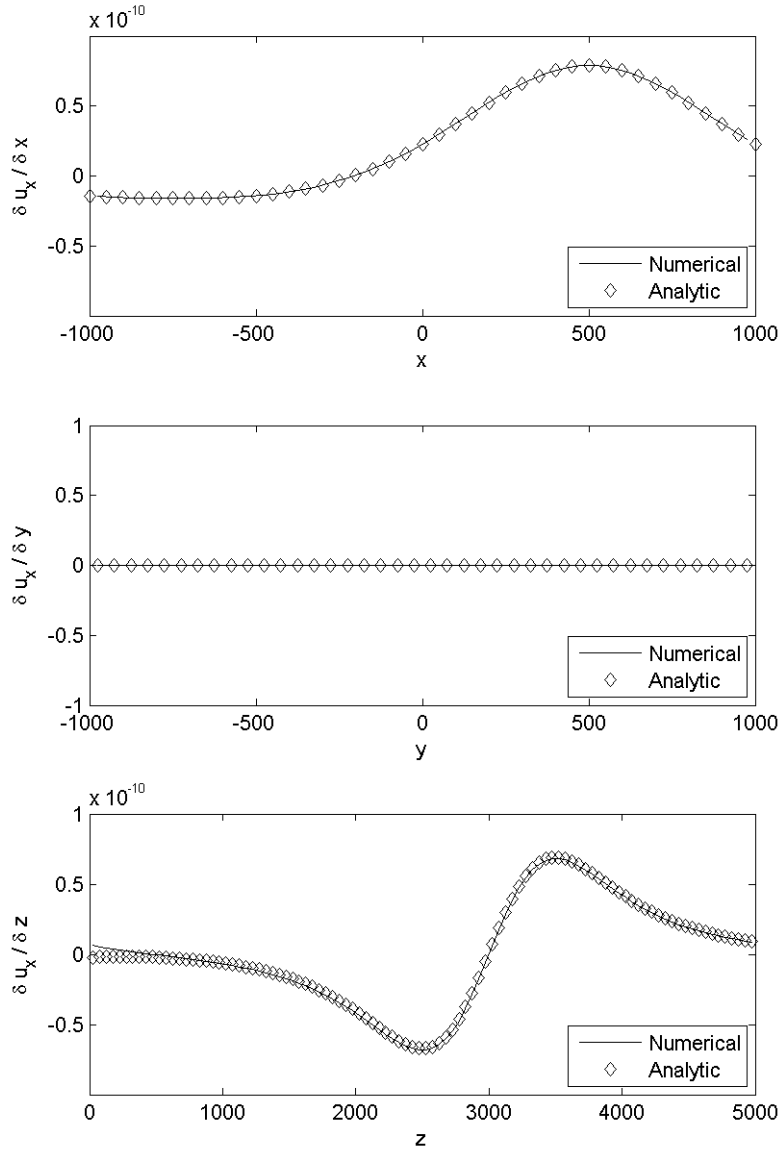

Figure B.2: *Numerical and analytical derivatives of* u_x *due to a nucleus of strain located at* $(500, 500, 3000)$ *for observation points at (a)* $(x, 500, 200)$*, (b)* $(500, y, 2000)$ *and (c)* $(-500, 500, z)$*.* $C_m = 1$ *and* $\upsilon = 0.25$

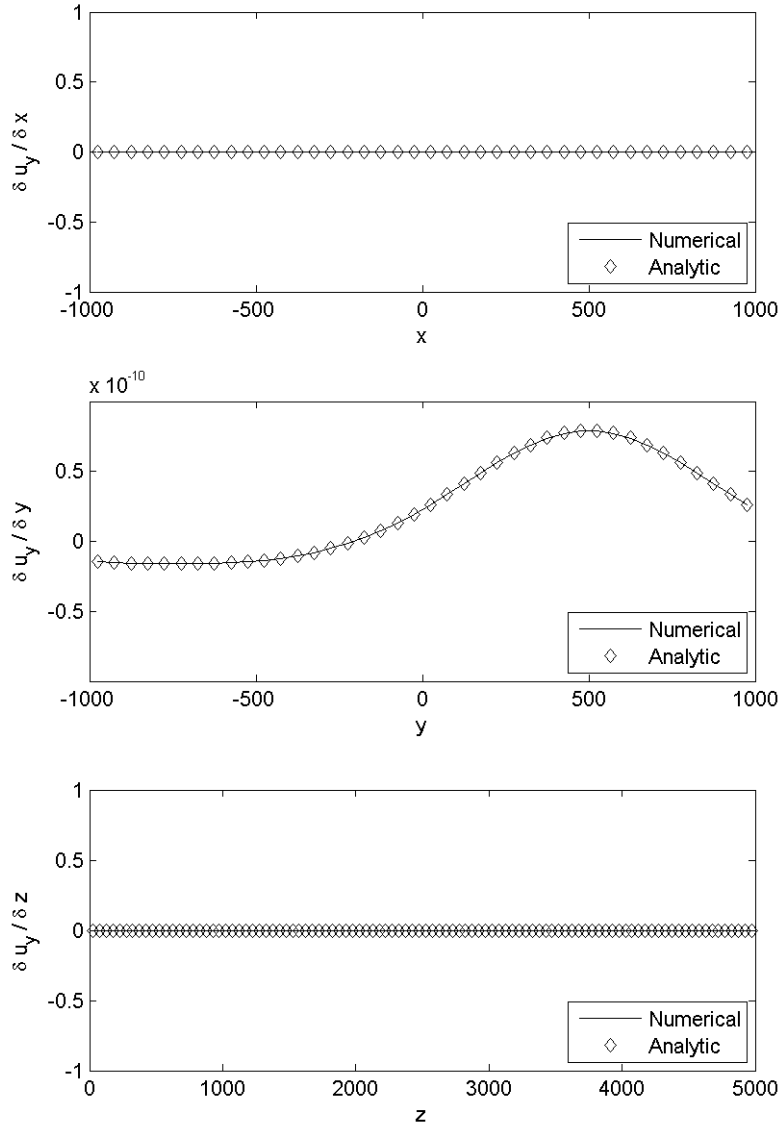

Figure B.3: *Numerical and analytical derivatives of* u_y *due to a nucleus of strain located at* $(500, 500, 3000)$ *for observation points at (a)* $(x, 500, 200)$*, (b)* $(500, y, 2000)$ *and (c)* $(-500, 500, z)$*.* $C_m = 1$ *and* $\upsilon = 0.25$

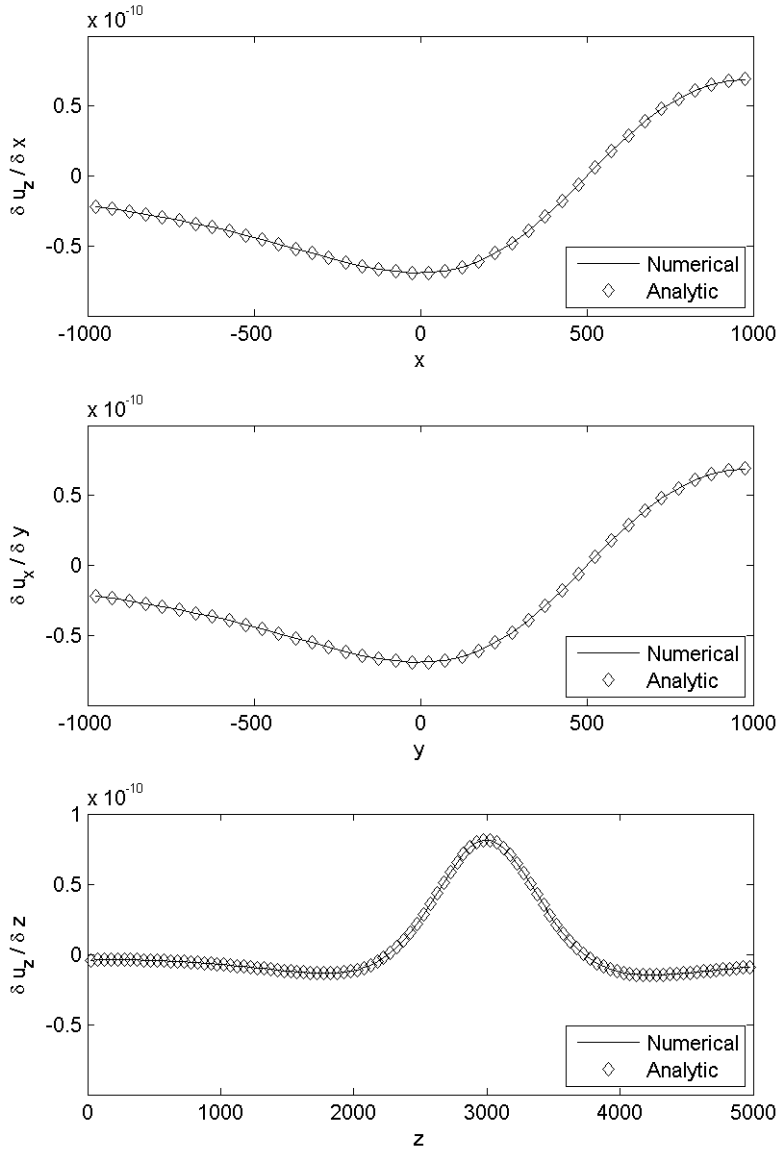

Figure B.4: *Numerical and analytical derivatives of* u_z *due to a nucleus of strain located at* $(500, 500, 3000)$ *for observation points at (a)* $(x, 500, 200)$*, (b)* $(500, y, 2000)$ *and (c)* $(-500, 500, z)$*.* $C_m = 1$ *and* $\upsilon = 0.25$

APPENDIX

C

Beyond the R-factor

C.1 Introduction

In this thesis I have made the practical assumption that observed zero-offset time-strains are related to vertical strain by a single parameter, the R-factor, as follows:

$$\frac{\Delta t}{t} = (1 + R)\varepsilon_{zz} \tag{C.1}$$

The reasons for using the 'R-factor' approach where discussed extensively in Chapter 4. From this equation we can relate the time-strain directly to reservoir pressure via a Green's function, relating reservoir pressure change to overburden vertical strain:

$$\left(\frac{\Delta t}{t}\right)_M = (1 + R)\sum_{n=1}^{N} \Delta p_n G^{\varepsilon_{zz}}_{n,M} \tag{C.2}$$

For details of the notation see Chapter 4. In this appendix I explicitly show how this approach can be extended so that changes in velocity can be related to any linear combination of stress or strain, provided we maintain the assumption of a linear elastic material.

C.2 Example: Relating velocity to vertical stress

First, recall that:

$$\frac{\Delta t}{t} = \varepsilon_{zz} - \frac{\Delta V}{V} \tag{C.3}$$

Instead of relating velocity changes to vertical strain, we instead relate it to changes in vertical stress via a constant of proportionality U, so that:

$$\frac{\Delta V}{V} = U\Delta\sigma_{zz} \tag{C.4}$$

The equation for time-strain now becomes:

$$\frac{\Delta t}{t} = \varepsilon_{zz} - U\Delta\sigma_{zz} \tag{C.5}$$

Using the framework set out in Chapter 4 we can replace ε_{zz} and $\Delta\sigma_{zz}$ with Green's functions that relate reservoir pressure change, Δp, to overburden strain and changes in vertical stress. For a reservoir made of n discrete blocks, as described in Chapter 4, the time-strain at a point M in the overburden can be written as:

$$\left(\frac{\Delta t}{t}\right)_M = \sum_{n=1}^{N} \Delta p_n G_{n,M}^{\varepsilon_{zz}} + U \sum_{n=1}^{N} \Delta p_n G_{n,M}^{\sigma_{zz}} \tag{C.6}$$

which can be rewritten as:

$$\left(\frac{\Delta t}{t}\right)_M = \Delta p_n \left(\sum_{n=1}^{N} G_{n,M}^{\varepsilon_{zz}} + U \sum_{n=1}^{N} G_{n,M}^{\sigma_{zz}} \right) \tag{C.7}$$

Clearly we have maintained a linear relationship between the overburden time-strain and change in reservoir pressure. The 'composite' Green's function is a weighted sum of the strain vertical strain and vertical stress Green's function, with the U-factor determining the relative weighting.

It is clear to see how this approach can be extended. Any relationship that describes the change in velocity as a *linear* combination of elements of the stress and strain tensors can be used in Equation C.3.

References

Aki, K. and Richards, P. (2002). Quantitive Seismology.

Allen, D. and Mayuga, M. (1969). The mechanics of compaction and rebound, Wilmington oil field, Long Beach, California, USA. *Land subsidence: International Association of Hydrological Sciences Publication*, 89:410–423.

Aster, R., Borchers, B., and Thurber, C. (2005). *Parameter Estimation and Inverse Problems*. Elsiver Academic Press.

Backus, G. (1962). Long-Wave Elastic Anisotropy Produced by Horizontal Layering. *Journal of Geophysical Research*, 67:4427.

Barkved, O. (2008). Personal communication.

Barkved, O., Heavey, P., Kjelstadli, R., Kleppan, T., and Kristiansen, T. (2003). Valhall Field-Still on Plateau after 20 Years of Production. *Society of Petroleum Engineers*, 83957.

Bauer, A., Lehr, C., Korndorffer, F., van der Linden, A., Dudley, J., Addis, T., and Love, K. (2008). Stress and pore-pressure dependence of sound velocities in shales: Poroelastic effects in time-lapse seismic. In *SEG International Exposition and Annual Meeting*.

Biot, M. (1941). General Theory of Three-Dimensional Consolidation. *Journal of Applied Physics*, 12:155–164.

Biot, M. and Willis, D. (1957). The elastic coefficients of the theory of consolidation. *J. Appl. Mech*, 24(4):594–601.

Bourne, S. and Hatchell, P. (2005). Monitoring reservoir compaction by joint inversion of seafloor subsidence and timelapse seismic timeshift data. In *EAGE Conference and Technical Exhibition*.

Boutte, D. (2007). Through the continuous life cycle of reservoir, geophysics makes its mark. *The Leading Edge*, 26.

Brown, A. R. (2004). *Interpretation of three-dimensional seismic data*. Datapages.

Bruno, M. (2002). Geomechanical and decision analyses for mitigating compaction-related casing damage. *SPE drilling & completion*, 17(3):179–188.

Calvert, R. (2005). *Insights and methods for 4D reservoir monitoring and characterization: 2005 Distinguished Instructor Short Course*. Society of Exploration Geophysics.

Corzo, M. and MacBeth, C. (2006). Towards accurate quantitative monitoring of compacting reservoirs using time-lapse seismic. In *SEG International Exposition and Annual Meeting*.

Couples, G., Ma, J., Lewis, H., Olden, P., Quijano, J., and Fasae, T. (2007). Geomechanics of faults: impacts on seismic imaging. *First Break*, 25.

Cox, B. and Hatchell, P. (2008). Straightening out lateral shifts in time-lapse seismic. *First Break*, 26.

Davis, J. and Sampson, R. (1986). *Statistics and data analysis in geology*. Wiley New York et al.

De Gennaro, S., Onaisi, A., Grandi, A., Ben-Brahim, L., and Neillo, V. (2008). 4D reservoir geomechanics: a case study from the HP/HT reservoirs of the Elgin and Franklin fields. *First Break*, 26.

Domenico, S. (1977). Elastic Properties of Unconsolidated Porous Sand Reservoirs. *Geophysics*, 42:1339–1368.

Du, J. and Olson, J. (2001). A poroelastic reservoir model for predicting subsidence and mapping subsurface pressure fronts. *Journal of Petroleum Science and Engineering*, 30(3):181–197.

Dusseault, M., Bruno, M., and Barrera, J. (2001). Casing Shear: Causes, Cases, Cures. *SPE Drilling & Completion*, 16(2):98–107.

Eiken, O., Aronsen, H., Furre, A., Klefstad, L., Nordby, L., Osdal, B., and Skaar, M. (2003). Seismic Monitoring of the Heidrun, Norne and Midgard fields using streerable streamers. In *EAGE Conference and Technical Exhibition*.

Eiken, O. and Tøndel, R. (2005). Sensitivity of time-lapse seismic data to pore pressure changes: Is quantification possible? *The Leading Edge*, 24:1250.

El Ouair, Y. and Strønen, L. (2006). Value creation from 4D seismic at the Gullfaks Field: achievements and new challenges. In *SEG International Exposition and Annual Meeting*.

Fielding, E., Brink, J., Patzek, T., and Silin, D. (2002). Lost Hills Field Trial-incorporating new technology for resevoir management. In *SPIE Annual Technical Conference and Exhibition*.

Fjær, E., Holt, R., Horsrud, P., Raaen, A., and Risnes, R. (1992). *Petroleum related rock mechanics*, volume 33 of *Developments in petroleum science*. Elsevier, 1 edition.

Fjær, E., Holt, R., Horsrud, P., Raaen, A., and Risnes, R. (2008). Petroleum related rock mechanics. 53.

Floricich, M. (2006). *An engineering-consistent approach for pressure and saturation estimation from time-lapse seismic data*. PhD thesis, Institute of Petroleum Engineering, Heriot-Watt University.

Floricich, M., MacBeth, C., Stammeijer, J., Staples, R., Evans, A., and Dijksman, N. (2006). Determination of a seismic and engineering consistent petro-elastic model for time-lapse seismic studies: Application to the Schiehallion Field. In *SEG International Exposition and Annual Meeting*.

Freund, D. (1992). Ultrasonic compressional and shear velocities in dry clastic rocks as a function of porosity, clay content and confining pressure. *Geophysical Journal International*, 108:125–135.

Fuck, R., Bakulin, A., and Tsvankin, I. (2007). Time-lapse traveltime shifts above compacting reservoirs: 3D solutions for prestack data. In *SEG International Exposition and Annual Meeting*.

Furre, A., Bakken, E., Kløv, T., and Nordby, L. (2006). Heidrun 2001-2004 time-lapse seismic project: integrating geophysics and reservoir engineering. *First Break*, 24:33.

Gassmann, F. (1951). Uber die elastizitt poroser medien: Vierteljahrsschr. *Naturforrsh. Ges. Zuerich*, 96:1–23.

Geertsma, J. (1966). Problems of rock mechanics in petroleum production engineering. In *Proceedings of 1st Congress on International Society of Rock Mechanics*.

Geertsma, J. (1973a). A basic theory of subsidence due to reservoir compaction: the homogeneous case. *Trans. Royal Dutch Soc. Geol. & Mining Eng*, 22:43–62.

Geertsma, J. (1973b). Land subsidence above compacting oil and gas reservoirs. *Journal of Petroleum Technology*, 25:734–744.

Gubbins, D. (2004). *Time Series Analysis and Inverse Theory for Geophysicists*. Cambridge University Press.

Guilbot, J. and Smith, B. (2002). 4-D constrained depth conversion for reservoir compaction estimation Application to Ekofisk Field. *The Leading Edge*, 21(3):302–308.

Hale, D. (2007). A method for estimating apparent displacement vectors from time-lapse seismic images. *Center for Wave Phenomena Report*, 566.

Hall, S., , MacBeth, C., Barkved, O., and Wild, P. (2002). Time-lapse seismic monitoring of compaction and subsidence at Valhall through cross-matching and interpreted warping of 3D streamer and OBC data. In *SEG International Exposition and Annual Meeting*.

Hall, S. (2006). A methodology for 7D warping and deformation monitoring using time-lapse seismic data. *Geophysics*, 71:O21.

Han, D., Nur, A., and Morgan, D. (1986). Effects of porosity and clay content on wave velocities in sandstones. *Geophysics*, 51(11):2093–2107.

Hansen, P. (1998). *Rank-Deficient and Discrete Ill-Posed Problems: Numerical Aspects of Linear Inversion*. Society for Industrial Mathematics.

Hatchell, P. and Bourne, S. (2005a). Measuring reservoir compaction using time-lapse timeshifts. In *SEG International Exposition and Annual Meeting*.

Hatchell, P. and Bourne, S. (2005b). Rocks under strain: Strain-induced time-lapse time shifts are observed for depleting reservoirs. *The Leading Edge*, 24(12):1222–1225.

Hatchell, P., Jorgensen, O., Gommesen, L., and Stammeijer, J. (2007). Monitoring reservoir compaction from subsidence and time-lapse time shifts in the Dan field. In *SEG International Exposition and Annual Meeting*.

Hatchell, P., Kawar, R., and Savitski, A. (2005). Integrating 4D seismic, geomechanics and reservoir simulation in the Valhall Oil field. In *EAGE Conference and Technical Exhibition*.

Hatchell, P., van den Beukel, A., Molenaar, M., Maron, K., Kenter, C., Stammeijer, J., van der Velde, J., and Sayers, C. (2003). Whole earth 4D: Reservoir monitoring geomechanics. In *SEG International Exposition and Annual Meeting*.

Hatchell, P. and Wills, P. (2007). Time-lapse multiple removal technique to improve 4D interpretation in the gas cloud region at Valhall. In *EAGE Conference and Technical Exhibition*.

Hawkins, K., Howe, S., Hollingworth, S., Conroy, G., Ben-Brahim, L., Tindle, C., Taylor, N., Joffroy, G., and Onaisi, A. (2007). Production-induced stresses from time-lapse time shifts: A geomechanics case study from Franklin and Elgin fields. *The Leading Edge*, 26:655.

Hermansen, H., Thomas, L., Sylte, J., and Aasboe, B. (1997). Twenty Five Years of Ekofisk Reservoir Management. *Society of Petroleum Engineers*, 38927:5–8.

Herwanger, J. (2007). Linking geomechanics and seismics: Stress effects on time-lapse seismic data. *EAGE: Distinguished Lecture Program Course Notes*.

Herwanger, J. and Horne, S. (2005). Linking geomechanics and seismics: Stress effects on time-lapse seismic data. In *EAGE Conference and Technical Exhibition*.

Herwanger, J., Palmer, C., and S., C. R. (2007). Anisotropic velocity changes in seismic time-lapse data. In *SEG International Exposition and Annual Meeting*.

Hettema, M., Schutjens, P., Verboom, B., and Gussinklo, H. (2000). Production-Induced Compaction of a Sandstone Reservoir: The Strong Influence of Stress Path. *SPE Reservoir Evaluation & Engineering*, 3(4):342–347.

Hodgson, N., MacBeth, C., Duranti, L., Rickett, J., and Nihei, K. (2007). Inverting for reservoir pressure change using time-lapse time strain Application to Genesis Field Gulf of Mexico. *The Leading Edge*, 26:649.

Holt, R., Bakk, A., Fjær, E., and Stenebråten, J. (2005). Stress sensitivity of wave velocities in shale. In *SEG International Exposition and Annual Meeting*.

Hudson, T. (2005). Personal communication. Edinburgh Time-Lapse Project Sponsor's Meeting.

Hudson, T., Regel, B., Bretches, J., Condon, P., Rickett, J., Cerney, B., Inderwiesen, P., and Ewy, R. (2006). Preliminary results of the Genesis Field Time-Lapse-Seismic project, Gulf of Mexico. *Offshore Technology Conference: (OTC 18376)*.

Hudson, T., Regel, B., Bretches, J., Rickett, J., Cerney, B., and Inderwiesen, P. (2005). Genesis field, Gulf of Mexico, 4-D project status and preliminary lookback. In *SEG International Exposition and Annual Meeting*.

Kloosterman, H., Kelly, R., Stammeijer, J., Hartung, M., van Waarde, J., and Chajecki, C. (2003). Successful application of time-lapse seismic data in Shell Expros Gannet Fields, Central North Sea, UKCS. *Petroleum Geoscience*, 9:25–34.

Kommedal, J., Barkved, O., and Henneberg, K. (2005). Repeatability using a permanently installed seismic array: 67th Annual Conference and Exhibition, EAGE. In *EAGE Conference and Technical Exhibition*.

Kragh, E. and Christie, P. (2002). Seismic repeatability, normalized rms, and predictability. *The Leading Edge*, 21(7):640–647.

Kristiansen, T., Barkved, O., Buer, K., and Bakke, B. (2005). Production-induced deformations ouside the reservoir and their impact.

Kuster, G. and Toksöz, M. (1974). Velocity and Attenuation Of Seismic Waves In Two-Phase Media: Part I. Theoretical Formulations. *Geophysics*, 39:587.

Landrø, M., Digranes, P., and Strønen, L. (2001). Mapping reservoir pressure and saturation changes using seismic methods–possibilities and limitations. *First Break*, 19:671–677.

Landrø, M. and Janssen, R. (2002). Estimating compaction and velocity changes from time-lapse near and far offset stacks. In *EAGE Conference and Technical Exhibition*.

Landrø, M. and Stammeijer, J. (2004). Quantitative estimation of compaction and velocity changes using 4D impedance and traveltime changes. *Geophysics*, 69.

Lumley, D. (2004). Business and technology challenges for 4D seismic reservoir monitoring. *The Leading Edge*, 23(11):1166–1168.

MacBeth, C. (2004). A classification for the pressure-sensitivity properties of a sandstone rock frame. *Geophysics*, 69:497.

MacBeth, C., Stephen, K., and Gardiner, A. (2008). The impact of sub-seismic shale layers on the reservoirs stress sensitivity. In *SEG International Exposition and Annual Meeting*.

Magesan, M., Depagne, S., Nixon, K., Regel, B., Opich, J., Rogers, G., and Hudson, T. (2005). Seismic processing for time-lapse study Genesis Field, Gulf of Mexico.

Mindlin, R. (1949). Compliance of elastic bodies in contact. *J. Appl. Mech*, 16(3):259.

Mindlin, R. and Cheng, D. (1950). Nuclei of Strain in the Semi-Infinite Solid. *Journal of Applied Physics*, 21:926.

Minkoff, S., Stone, C., Arguello, J., Bryant, S., Eaton, J., Peszynska, M., and Wheeler, M. (1999). Coupled geomechanics and flow simulation for time-lapse seismic modeling: 69th Annual International Meeting. In *SEG International Exposition and Annual Meeting*.

Nes, O., Holt, R., and Fjoer, E. (2002). The reliability of core data as input to seismic reservoir monitoring studies. *SPE Reservoir Evaluation & Engineering*, 5(1):79–86.

Nur, A. and Byerlee, J. (1971). An exact effective stress law for elastic deformation of rock with fluids. *J. Geophys. Res.*, 76(26):6414–6419.

Olden, P., Corbett, P., Westerman, R., Somerville, J., Smart, B., and Koutsabeloulis, N. (2001). Modeling combined fluid and stress change effects in the seismic response of a producing hydrocarbon reservoir. *The Leading Edge*, 20(10):1154–1163.

Osdal, B., Husby, O., Aronsen, H., Chen, N., and Alsos, T. (2006). Mapping the fluid front and pressure buildup using 4D data on Norne Field. *The Leading Edge*, 25:1134.

Ostermeier, R. (2001). Compaction Effects on Porosity and Permeability: Deepwater Gulf of Mexico Turbidite. *Journal of Petroleum Technology*, 53(2):68–74.

Pettersen, R., Barkved, O., and Haller, N. (2006). Time-lapse seismic inversion of data from a compacting chalk reservoir. In *SEG International Exposition and Annual Meeting*.

Pourciau, R., Fisk, J., Descant, F., and Waltman, R. (2005). Completion and Well Performance Results, Genesis Field, Deepwater Gulf of Mexico. *SPE Drilling & Completion*, 84415:5–8.

Prioul, R., Bakulin, A., and Bakulin, V. (2004). Non-linear rock physics model for estimation of 3-D subsurface stress in anisotropic formations: Theory and laboratory verification. *Geophysics*, 69(2):415–425.

Rice, J. and Cleary, M. (1976). Some Basic Stress Diffusion Solutions for Fluid-Saturated Elastic Porous Media With Compressible Constituents. *Reviews of Geophysics and Space Physics*, 14:227.

Rickett, J., Duranti, L., Hudson, T., and Hodgson, N. (2006). Compaction and 4-D time strain at the Genesis Field. In *SEG International Exposition and Annual Meeting*.

Rickett, J., Duranti, L., Hudson, T., Regel, B., and Hodgson, N. (2007a). 4D time strain and the seismic signature of geomechanical compaction at Genesis. In *EAGE Conference and Technical Exhibition*.

Rickett, J., Duranti, L., Hudson, T., Regel, B., and Hodgson, N. (2007b). 4D time strain and the seismic signature of geomechanical compaction at Genesis. *The Leading Edge*, 26(5):644.

Rickett, J. and Lumley, D. (2001). Cross-equalization data processing for time-lapse seismic reservoir monitoring: A case study from the Gulf of Mexico. *Geophysics*, 66:1015.

Ross, C. and Cunningham, G. (1996). Inside the cross-equalization black box. *The Leading Edge*, 15(11):1233–1240.

Røste, T., Stovas, A., and Landrø, M. (2005). Estimation of layer thicknessand velocity changes using 4D prestack seismic data. In *EAGE Conference and Technical Exhibition*.

Røste, T., Stovas, A., and Landrø, M. (2006). Estimation of layer thickness and velocity changes using 4D prestack seismic data. *Geophysics*, 71(6):219–234.

Rudnicki, J. (1999). Alteration of regional stress by reservoirs and other inhomogeneities: stabilizing or destabilizing? *Proc. 1999 Int. Cong. of Int. Soc. Rock Mechanics*, pages 25–28.

Sarout, J., Molez, L., Guéguen, Y., and Hoteit, N. (2007). Shale dynamic properties and anisotropy under triaxial loading: Experimental and theoretical investigations. *Physics and Chemistry of the Earth*, 32(8-14):896–906.

Sayers, C. (2006). Sensitivity of time-lapse seismic to reservoir stress path. *Geophysical prospecting*, 54(3):369–380.

Sayers, C. (2007). Asymmetry in the time-lapse seismic response to injection and depletion. *Geophysical Prospecting*, 55(5):699–705.

Sayers, C., den Boer, L., Hooyman, P., and Lawrence, R. (2006). Predicting reservoir compaction and casing deformation in deepwater turbidites using a 3D mechanical Earth model. *Society of Petroleum Engineers*, (103926).

Sayers, C. and Kachanov, M. (1995). Microcrack-induced elastic wave anisotropy of brittle rocks. *Journal of Geophysical Research*, 100(B3):4149–4156.

Schutjens, P. (2005). Reservoir monitoring with seismic time shifts: Geomechanical modeling for its application in stacked pay.

Scott Jr, T. (2007). The effects of stress paths on acoustic velocities and 4D seismic imaging. *The Leading Edge*, 26:602.

Segall, P. (1989). Earthquakes triggered by fluid extraction. *Geology*, 17(10):942–946.

Segall, P. (1992). Induced stresses due to fluid extraction from axisymmetric reservoirs. *Pure and Applied Geophysics*, 139(3):535–560.

Sen, B. (1943). Note on the stresses produced by nuclei of thermo-elastic strain in a semi-infinite elastic solid. *Quarterly of Applied Mathematics*.

Sen, V. and Settari, A. (2005). Coupled geomechanical and flow modeling of compacting reservoirs. *The Leading Edge*, 24:1284.

Setarri, A. (2002). Reservoir compaction. *Journal of Petroleum Technology*, (8):62–69.

Smith, I. and Griffiths, D. (2004). *Programming the Finite Element Method*. Wiley.

Stammeijer, J., Van Der Velde, J., Hatchell, P., Den Beukel, A., and Molenaar, M. (2004). Integrating 4D seismic and geomechanics: A case study. In *EAGE Conference and Technical Exhibition*.

Staples, R., Cook, A., Braisby, J., Hodgson, B., and Mabillard, A. (2006). Integration of 4D seismic data and the dynamic reservoir model reveal new targets in Gannet C. *The Leading Edge*, 25:1126.

Staples, R., Ita, J., Burrell, R., and Nash, R. (2007). Monitoring pressure depletion and improving geomechanical models of the Shearwater Field using 4D seismic. *The Leading Edge*, 26:636.

Stephen, K. and MacBeth, C. (2006a). Inverting for the petro-elastic model via seismic history matching. In *SEG International Exposition and Annual Meeting*.

Stephen, K. and MacBeth, C. (2006b). Seismic history matching in the Schiehallion UKCS Field. *First Break*, 24:43–49.

Stroud, A. (1971). *Approximate calculation of multiple integrals*. Prentice Hall.

Sulak, R. (1991). Ekofisk Field: The first 20 years. *Journal of Petroleum Technology*, 43(10).

Sweet, M. and Sumpter, L. (2007). Genesis field, Gulf of Mexico: Recognizing reservoir compartments on geologic and production time scales in deep-water reservoirs. *AAPG Bulletin*, 91(12):1701.

Tang, M., Ross, R., and Walker, R. (2007). Lessons through time in 4D seismic. *First Break*, 25.

Thurston, R. and Brugger, K. (1964). Third-Order Elastic Constants and the Velocity of Small Amplitude Elastic Waves in Homogeneously Stressed Media. *Physical Review*, 133(6A):1604–1610.

Tigrek, S. and Hatchell, P. (2006). Reservoir compaction quantification using geomechanical inversion of timelapse timeshifts. In *EAGE Conference and Technical Exhibition*.

Tura, A., Barker, T., Cattermole, P., Collins, C., Davis, J., Hatchell, P., Koster, K., Schutjens, P., and Wills, P. (2005). Monitoring primary depletion reservoirs using amplitudes and time shifts from high-repeat seismic surveys. *The Leading Edge*, 24(12):1214–1221.

van Gestel, J., Best, K., Barkved, O., and Kommedal, J. (2008a). Integrating Frequent Time-lapse Data into the Reservoir Simulation Modeling of the Valhall Field. In *EAGE Conference and Technical Exhibition*.

van Gestel, J., Clarke, R., and Barkved, O. (2008b). Rapid turn-around for processing and analysis of frequent time-lapse surveys. In *EAGE Conference and Technical Exhibition*.

Vasco, D. and Ferretti, A. (2006). On the use of quasi-static deformation to understand reservoir fluid flow. *Geophysics*, 70(4):13–27.

Vasco, D., Karasaki, K., and Doughty, C. (2000). Using surface deformation to image reservoir dynamics. *Geophysics*, 65(1):132–147.

Veeken, C., Hahleitner, J., and Keedy, C. (1994). Experimental Modelling of Casing Deformation in a Compacting Reservoir. *SPE/ISRM Rock Mechanics in Petroleum Engineering Conference*.

Vidal, S., Huguet, F., and Mechler, P. (2002). Characterizing reservoir parameters by integrating seismic monitoring and geomechanics. *The Leading Edge*, 21(3):295–301.

Walton, K. (1987). The Effective Elastic Moduli of a Random Packing of Spheres. *J. Mech. Phys. Solids*, 35(2):213–226.

Williamson, P., Cherrett, A., and Sexton, P. (2007). A new approach to warping for quantitative time-lapse characterisation. In *EAGE Conference and Technical Exhibition*.

Wyllie, M., Gregory, A., and Gardner, G. (1958). An experimental investigation of factors affecting elastic wave velocities in porous media. *Geophysics*, 23(3):459–493.

Xu, H. (2002). *Production induced reservoir compaction and surface subsidence, with applications to four-dimensional seismic*.

Yilmaz, Ö. and Doherty, S. (2001). *Seismic Data Analysis: Processing, Inversion, and Interpretation of Seismic Data*. Society of Exploration Geophysics.